INFORMATION TO USERS

This manuscript has been reproduced from the microfilm master. UMI films the text directly from the original or copy submitted. Thus, some thesis and dissertation copies are in typewriter face, while others may be from any type of computer printer.

The quality of this reproduction is dependent upon the quality of the copy submitted. Broken or indistinct print, colored or poor quality illustrations and photographs, print bleedthrough, substandard margins, and improper alignment can adversely affect reproduction.

In the unlikely event that the author did not send UMI a complete manuscript and there are missing pages, these will be noted. Also, if unauthorized copyright material had to be removed, a note will indicate the deletion.

Oversize materials (e.g., maps, drawings, charts) are reproduced by sectioning the original, beginning at the upper left-hand corner and continuing from left to right in equal sections with small overlaps. Each original is also photographed in one exposure and is included in reduced form at the back of the book.

Photographs included in the original manuscript have been reproduced xerographically in this copy. Higher quality 6" x 9" black and white photographic prints are available for any photographs or illustrations appearing in this copy for an additional charge. Contact UMI directly to order.

UMI

A Bell & Howell Information Company
300 North Zeeb Road, Ann Arbor MI 48106-1346 USA
313/761-4700 800/521-0600

COMMISSIONING OF 30 kVA VARIABLE-SPEED, DIRECT-DRIVE WIND POWER PLANT

by

DENİZ YILDIRIM

B.S., İstanbul Technical University, 1989

M.S., University of Colorado at Boulder, 1993

A thesis submitted to the

Faculty of the Graduate School of the

University of Colorado in partial fulfillment

of the requirements for the degree of

Doctor of Philosophy

Department of Electrical Engineering

1999

This thesis entitled:
COMMISSIONING OF 30 kVA VARIABLE-SPEED, DIRECT-DRIVE WIND POWER PLANT
written by Deniz Yıldırım
has been approved for the Department of Electrical Engineering

Ewald F. Fuchs

Ewald F. Fuchs

Carl T. A. Johnk

Carl T. A. Johnk

Date Feb. 14, 1999

The final copy of this thesis has been examined by the signatories, and we find that both the content and the form meet acceptable presentation standards of scholarly work in the above mentioned discipline.

Yıldırım, Deniz (Ph.D., Electrical Engineering)

COMMISSIONING OF 30 kVA VARIABLE-SPEED, DIRECT-DRIVE WIND POWER PLANT

Thesis directed by Professor Ewald F. Fuchs

Most wind turbines in service today employ induction generators together with a step-up mechanical gear so that the operational speed is close to the synchronous speed of two or four-pole generators. Because of the torque-speed characteristic of induction generators, the range of speed change is rather small; therefore, the operational speed can be considered to be nearly constant. Mechanical gears are subject to wear and tear, reduce reliability of the drive train and add to its weight. The maximum power that can be extracted from wind varies with its speed. Therefore, a direct-drive system, where a wind turbine is directly coupled to the generator shaft, is desirable along with a variable-speed operation.

The variable-speed, direct-drive train described in this thesis consists of a low-speed, permanent-magnet generator (60 to $120rpm$), a resonant rectifier and a pulse-width-modulated inverter. It supplies $30kVA/20kW$ apparent/real power to the utility system at leading and unity power factors for a given DC link voltage. The amplitude and phase (leading, unity) of the AC current delivered to the utility system are controllable and the voltage/current wave forms at the point of common coupling satisfy standard IEEE-519. The overall efficiency of the drive train is about 83% (excluding the generator), whereby the rectifier has an efficiency of 86% and the inverter efficiency is around 95%.

Using two different approaches (computer-aided and three-voltmeter methods), the losses of inductors are measured for the frequency range of 0 to $6kHz$. Measurement errors of both methods are less than 10% when measuring a few watts. The AC

resistance increase of a Litz-wire inductor without a core is smallest among all of the inductors being tested. Stranding of individual (uninsulated) wires to obtain a flexible cable results in more losses than using a solid cable having the same cross-sectional area as that of a stranded cable.

Nonsinusoidal voltages and currents in a power system can produce an additional power, called distortion power, generated from the cross products of voltage and current harmonics of different frequencies. This additional power increases system losses that cannot be easily compensated. Existing definitions of distortion power are not quite correct either from a numerical or a physical point of view because they involve voltage and current harmonics of the same frequency; therefore, a correct formulation is given which agrees well with experimental results.

When a transformer is operating under nonsinusoidal voltages and currents, its apparent power output must be reduced (derating) in order not to exceed the rated temperature. Comparison of measured derating values with ones obtained from $K-$ and $F_{HL}-$factor approaches reveals that the $K-$factor approach yields somewhat greater derating values than the $F_{HL}-$factor approach. The losses of conductive materials in the presence of magnetic fluxes are also investigated and it has been found that the maximum losses in these components occur at a specific (material-dependent) frequency. The losses are proportional to the power of 0.8 below this frequency and are inversely proportional to the power of 0.9 above this frequency.

DEDICATION

To my family and friends ...

ACKNOWLEDGEMENTS

I would like to express my sincere appreciation to my advisor, Prof. Ewald F. Fuchs, for his guidance and support throughout this work. Special thanks are due to Prof. Carl T. A. Johnk for reading this thesis word by word. I would also like to thank the committee members: Prof. R. W. Erickson, Prof. D. Maksimovic, Prof. M. Balas, and Prof. P. D. Elliott for their suggestions.

I would like to thank Turkish Government, Ministry of National Education for providing a four-year scholarship. Partial support for this work from the Electric Power Research Institute (EPRI) is also appreciated (Chapters 6, 8, and 9). I am very much obliged to the National Renewable Energy Laboratory (NREL) for providing necessary equipments and parts. Finally, I am indebted to my family and my student friends, here in Boulder, for their continuous support during my study.

CONTENTS

FIGURES

Figure

TABLES

Table

CHAPTER 1

INTRODUCTION

During the past ten years of research, design and construction of a 30 kVA variable-speed (60 to 120rpm) direct-drive wind power plant has been conducted in the Department of Electrical and Computer Engineering of the University of Colorado at Boulder. Most support for this project [1, 2] was provided by the National Renewable Energy Laboratory (NREL) in Golden. The primary work for design and construction of the low-speed permanent magnet generator is described in [3, 4, 5, 6]. This generator has been extensively tested [7] and mounted on a tower at the National Wind Technology Center (NWTC) of NREL. The $30kVA$ three phase PWM (pulse-width-modulated) inverter has been tested on the bench and reported in [6] for output powers of $20kW$ at about unity-power factor, without employing a transformer between the inverter and the power system of Public Service Company of Colorado, and without final mounting of the components within a steel cabinet. The zero-current-switch resonant rectifier has been assembled and tested [6] on the bench up to $3.2kW$ at low input and output voltages without control of the output voltage, and the components did not work properly within the environment of a steel cabinet.

Preliminary results of the above work have been reported in [8, 9, 10], and two invention disclosures were submitted to the Office of Intellectual Resources and Technology Transfer of the University of Colorado at Boulder [11, 12].

The goal of this dissertation was to resume the work on the design and testing

of the individual components of this project - the resonant rectifier, the PWM inverter including the current control for real/reactive/apparent powers - and to make all components work together so that, for a variable turbine speed varying from 60 to 120 rpm, a variable power at constant nominal frequency (e.g., 60 Hz) and at constant nominal voltage (e.g., 240 V_{L-L}) is supplied to the utility system, whereby the current wave shapes including the displacement factor and current amplitude are controllable.

The work of this dissertation encompasses the following topics:

1. 20 kW Three-Phase, Zero-Current-Switch (ZCS) Resonant Rectifier.
    - Redesign of the input filter for higher voltage ($600V$) and current ($40A$) stresses. A damping network is also added to the input filter.
    - Series connection of input bridge diodes to accommodate higher voltage (2000V) stresses.
    - Redesign of tank diodes and transistor (IGBT, insulated-gate-bipolar transistor) for higher voltage ($1400V$) and current ($200A$) stresses.
    - Design of the control circuit providing constant DC output voltage (e.g., 360 V) at variable AC input voltage (e.g., 300 V_{L-L} to 600 V_{L-L})
    - Mounting of rectifier components within a steel cabinet, and solution of EMI (electromagnetic interference) problems.
    - Debugging of the rectifier to deliver, at rated inputs, the rated output quantities.
2. 30 kVA Three-Phase Current-Controlled PWM Inverter.
    - Employment of a three-phase transformer between inverter and power system.
    - Debugging of the phase-lock-loop and gating circuits and to improve their operating stability.

- Addition of a harmonic tuned filter at the point of common coupling (PCC) to reduce the high frequency harmonic current flowing into the power system and to obtain a sinusoidal voltage waveform at the output of inverter before connecting it to the power system.
- Before connecting to the utility system, the required AC sinusoidal output voltage ($260V_{L-L}$ AC) for a given DC input voltage (340V DC) can be obtained by operating the PWM inverter with a modulation index greater than 1 ($m > 1$) - independent of the operating point of the inverter. This operating mode is novel: it improves the sinusoidal wave shape of the inverter output voltage and current, reduces switching losses, and reduces the input DC voltage required when compared to PWM with $m < 1$.
- Introduction of a phase-shifting input transformer, to make the displacement power factor of the inverter adjustable.
- Mounting the inverter components within a steel cabinet and to remove parasitic EMI problems.
- Establishing control surfaces for apparent power S and real power P as a function of the reference-current signal $V_{I_{ref}}$ varying between 0.9V and 7V.
- The real and reactive power flow generated by the PWM inverter and fed into the utility system is investigated using fundamental and harmonic phasor analyses.

3. Joint operation of the ZCS rectifier and the PWM inverter – mounted in steel cabinets – delivering rated power to the utility system.

4. Conceptual design of a Transversal Flux Machine (either motor or generator), providing high torques (5 kNm to 2.5 kNm) at low speeds (60 rpm to 120 rpm) based on alternating magnetic field theory. The work of [13] has been extended and two invention disclosures have been submitted [14, 15].

5. In a circuit where the load is nonlinear or the source has nonsinusoidal quantities. the apparent power is not simply $S = \sqrt{P^2 + Q^2}$: another type of power called distortion power (D) is generated by the cross products of voltage and current harmonics of different frequencies. For nonsinusoidal voltages and currents the apparent power is defined as $S = \sqrt{P^2 + Q^2 + D^2}$. This additional power D increases the load current (apparent power S gets larger) and causes additional losses. Past definitions of the distortion power are reviewed and most are found not to be correct either from a numerical or physical point of view. A proper formulation is derived for the computation of D from the individual voltage and current harmonics not containing voltages and currents of the same frequency. Experiments are performed to measure the distortion power for a variety of load conditions, i.e., for different THD_i and THD_v values.

6. Measurement of losses of inductors employed in different parts of the drive system, using two different approaches. Two methods for measuring losses of inductors at frequencies from 0 to $6kHz$ are discussed; the first involves the use of sampled inductor voltage and current wave forms through an A/D converter and a computer. The second, called three-voltmeter method, consists of recording the rms values of three sinusoidal voltages. Error analyses of the two approaches are presented.

7. Measurement of the derating of single-phase transformers operating at nonsinusoidal voltage and current wave forms, and comparison of the measured derating values with those obtained from K-factor and harmonic-loss factor (F_{HL}) approaches.

In the following it is assumed that the reader is familiar with the primary references of this work [1] to [16] and an effort will be made to complement and if necessary correct the statements and ideas of these references - thus repetition will be avoided.

Many of today's wind turbines employ standard, off-the-shelf induction generators, along with a step-up mechanical gear operating at nearly constant speeds. Mechanical gears are subjected to wear and tear, are expensive, reduce reliability [17], reduce efficiency of the drive train and add to its weight. Therefore, in wind power generating plants, direct-drive trains without any mechanical gears are desirable. Figure 1.1 illustrates the power curve of a wind turbine at two different wind speeds [18], where the

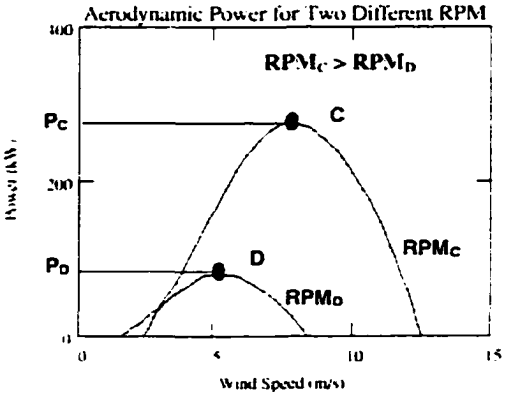

Figure 1.1: Power versus wind speed at two different rotor speeds [18].

output power of the wind turbine for a given wind speed peaks to a maximum value. Therefore, by allowing the rotor speed to vary with the wind speed, wind turbines can extract the maximum power available at different wind speeds [17].

Figure 1.2 shows the schematic diagram of a variable-speed, direct-drive wind

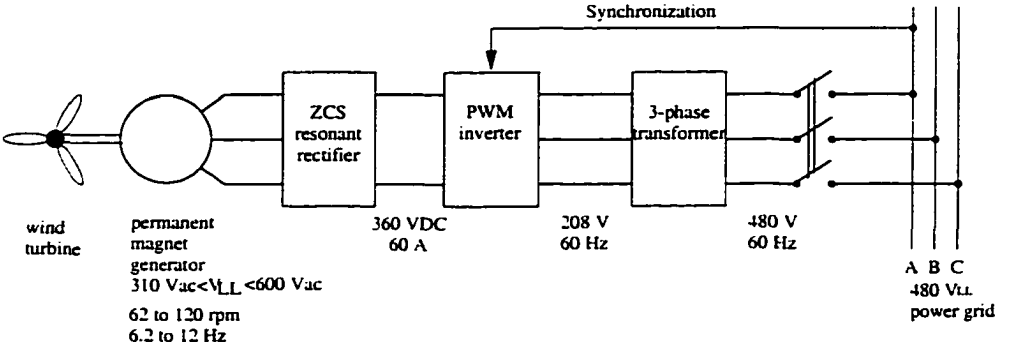

Figure 1.2: 30 kVA variable-speed, direct-drive wind power plant.

power plant. The permanent magnet (PM) generator operating at low speeds, e.g.,

$60 - 120rpm$, produces a three-phase variable AC voltage, $310V$ to $600V$ line-to-line, at a frequency of $6 - 12Hz$ and at a rated power of $20kW$ for some operating points. If a relatively heavy longitudinal PM generator or a transversal PM generator is used, the gear box between the turbine and the PM generator can be eliminated, resulting in reduced weight requirements for the tower. Three-phase AC voltage is then fed to the rectifier operating at slightly leading input power factor to produce a nearly constant DC voltage independent of input voltage amplitude and frequency variations and load changes. A current-controlled PWM inverter then converts the DC voltage to three-phase AC currents at a system line-to-line voltage of 240V. The output frequency of the inverter is locked to the nominal power-grid frequency of $60Hz$. The amplitude and the phase of the AC current fed into the power system are controllable through the adjustment of the three-phase reference currents, resulting in powers delivered at leading and lagging power factors to the power system. To provide an isolation and to ease the testing of the entire system, a three-phase transformer is placed between the inverter and the power grid. In later applications such a transformer can be omitted.

The total installed capacity of wind power plants has reached about 1.8 GW in North America in 1994 [19]. Most of these plants employ induction generators with a speed-up gear operating at nearly constant speed. There is no direct-drive variable-speed wind power train of this type on the market yet. Therefore, the work of this dissertation and the prior work [1] to [12] can considered to be novel and the first of its type.

CHAPTER 2

20 kW THREE-PHASE, ZERO-CURRENT-SWITCH, RESONANT RECTIFIER

2.1 Introduction

A zero-current-switch (ZCS), resonant rectifier is used to convert the three-phase AC voltage of variable amplitude and frequency to a constant DC voltage. As shown in Figure 2.1, the rectifier utilizes only one switch, an insulated gate bipolar transistor (IGBT), resulting in a relatively simple, however, nonlinear control circuitry. The operation of the rectifier is based on a resonant circuit between three tank inductors (L_R) and a tank capacitance (C_R), resulting in a zero-current-at-turn off property in the IGBT. The complete treatment of rectifier is explained in [20] and [21] for low power applications (a few hundred watts).

2.2 Series Connection of Diodes and IGBTs

When the peak voltage across a switching device is in the range of thousands of volts, it may be necessary to connect several switching devices in series because of two reasons: the unavailability of a device with such a high voltage rating, or it may not be economically feasible to go in some applications to a higher voltage rating device. To achieve an equal voltage sharing in a series connection, the voltage sharing during the off-state (steady state) and during transients (turn-on and turn-off) must be considered [22, 23].

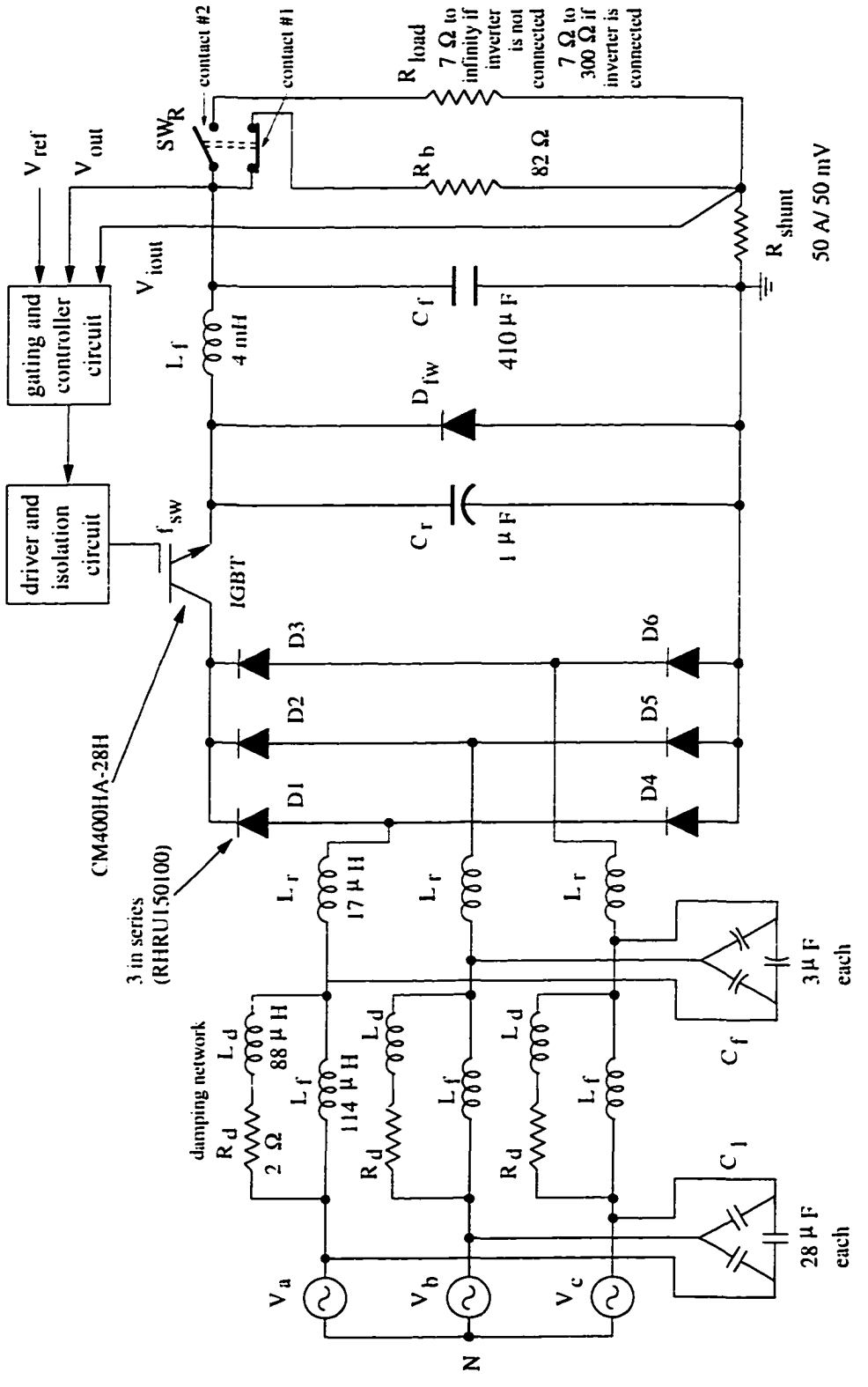

Figure 2.1: Zero-current-switch resonant rectifier; note the base-load resistor $R_b = 82\Omega$ can be disconnected when rectifier supplies power to inverter.

For the input diode bridge of the rectifier, fast 100 A/1200 V diodes were employed. The voltage stress across one diode was approaching its rated voltage at 400 V_{L-L} rms input voltage. Therefore, it was necessary to increase the voltage ratings of the input bridge diodes. It was not feasible to buy fast diodes with a higher voltage rating; instead to share the voltage, fast 150 A/1000 V diodes were connected in series. At the maximum generator output voltage of 600 V_{L-L} rms the voltage across one diode branch is equal to the maximum tank capacitor voltage [21], e.g., $V_{ak} = 2 \cdot \sqrt{2} \cdot 600 = 1697$ volts. To provide safety margins, it was decided to connect three fast 150A/1000 V diodes in series. The total voltage rating of one leg of the input bridge is, therefore, 3000 volts. Fast diodes (having low junction capacitance C_j) should be chosen such that their characteristics are matched as closely as possible to ensure that each diode shares equally one-third of the total voltage during their off state. Since diodes carry the same leakage current during their off state, unequal voltage sharing will be inevitable because of somewhat unmatched I-V characteristics.

Since it is not possible to find completely matched diodes, a parallel resistor is placed between the anode and cathode of each diode. The current in this resistor is chosen such that it is larger than the leakage current of diodes; then the voltage sharing at steady state will be independent of the leakage current. In addition, a capacitor with a capacitance of $10 \cdot C_j$ (where C_j is the junction capacitance of the diode) is connected in parallel to each diode, to ensure voltage sharing from a dynamic point of view. RC snubber circuits are also employed to ease the stresses on the diodes during turn-on and turn-off. The series connection of three diodes along with required resistors and capacitors are shown in Figure 2.2. The rectifier is operated with the diodes connected in series, and the peak voltage of one diode and total voltage across the series connected diodes are measured. Figure 2.3 shows that the maximum voltage across one diode is about 33% of the total voltage, showing an excellent voltage sharing. The oscillogram of the total voltage across the three series-connected diodes and that of the voltage across

one of the diodes are shown in Figure 2.4.

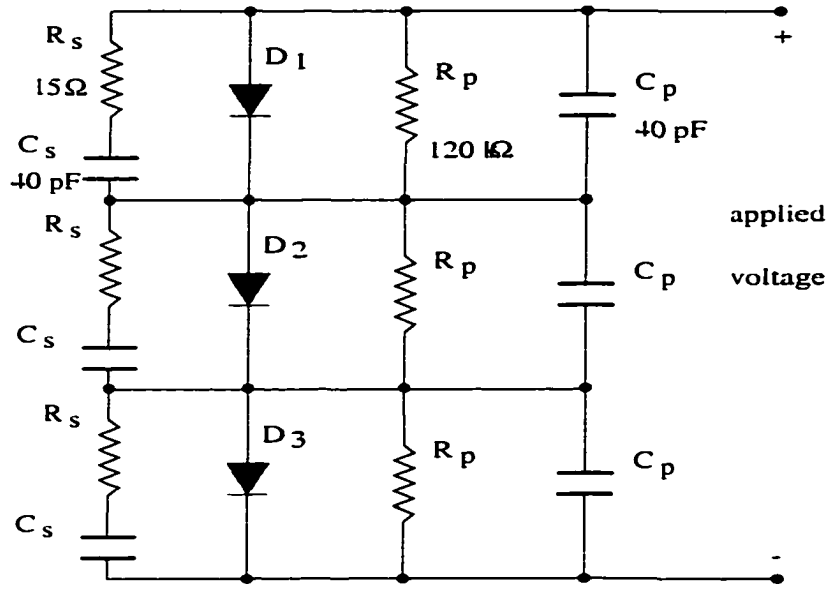

Figure 2.2: Series connection of three fast diodes.

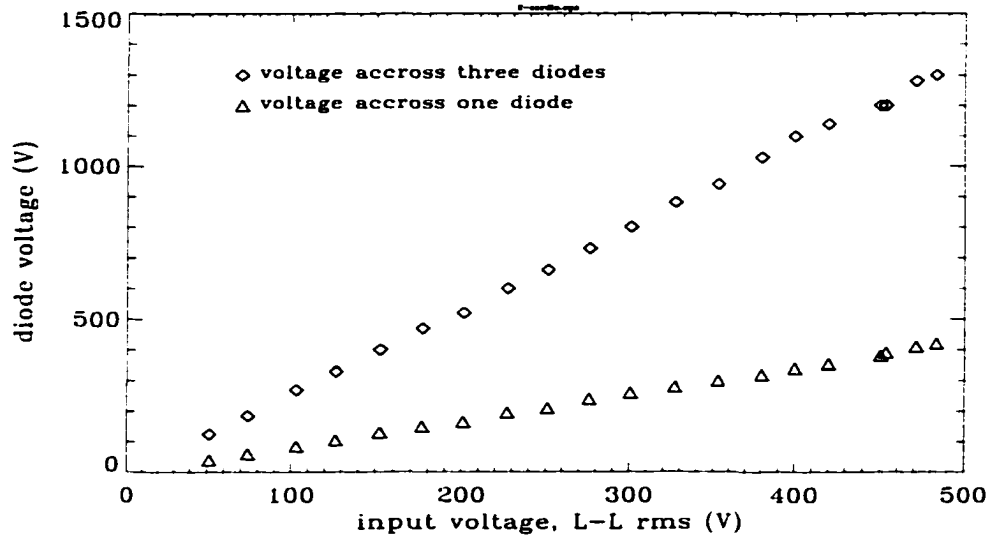

Figure 2.3: Voltage sharing of three fast diodes connected in series.

Numerous papers have been published about the series connection of IGBTs [24, 25, 26] to increase the power capability of a converter. Equal-voltage-sharing methods similar to those of diodes should be employed, as well as gate charge controlled

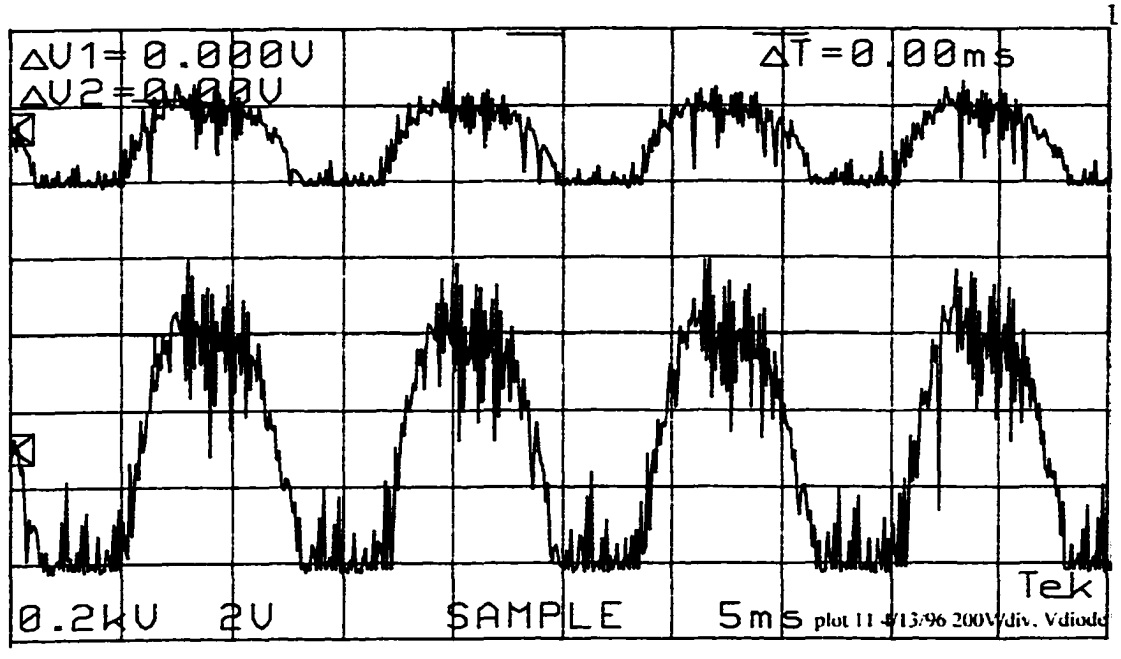

Figure 2.4: Voltage sharing of three series connected diodes, total voltage (lower trace) and voltage across one diode (upper trace), $V_{L-L}^{in} = 401VAC$, $V_{out} = 350VDC$, $I_{out} = 5ADC$, 200 V/div, 5 ms/div.

methods for voltage sharing. series. Equal voltage sharing at steady state is achieved by connecting a resistor between the collector and emitter of each transistor. The resistors are chosen such that the current through them is larger than the leakage current of a transistor ($1mA$). Although the gating circuits are the same. the turn-on and turn-off times of the IGBTs can be different because of different gate capacitance values and stray inductances and capacitances in the circuit layout. This will result in a voltage spike at the faster IGBT during turn-off, which may be high enough to destroy the device. Therefore, it is necessary to limit the voltage spike and its rate of rise, dv/dt, by connecting an RC snubber across each switching device [27], so that the rise of voltage in each device will be nearly equal.

2.3 Control Circuit of Rectifier

The rectifier is controlled such that the DC output voltage is nearly constant, independent of changes in load and input voltage/frequency variations. In ZCS type resonant rectifiers, an increase in the switching frequency will result in an increase in the

DC output voltage; therefore, the DC output voltage can be controlled by changing the switching frequency of the transistor. The switching frequency is changed between 6.5 kHz and 24 kHz, corresponding to minimum and maximum load, respectively. The block diagram of Figure 2.5 shows that the inputs to the control circuit are a DC reference voltage and the DC output voltage (negative feedback) and current (feed forward) of the rectifier; the block labeled as ZCS rectifier is given in Figure 2.1. The output voltage is compared with the reference voltage and the error voltage is fed to the limiter circuit, which limits the error voltage to a certain value, thereby limiting the maximum switching frequency.

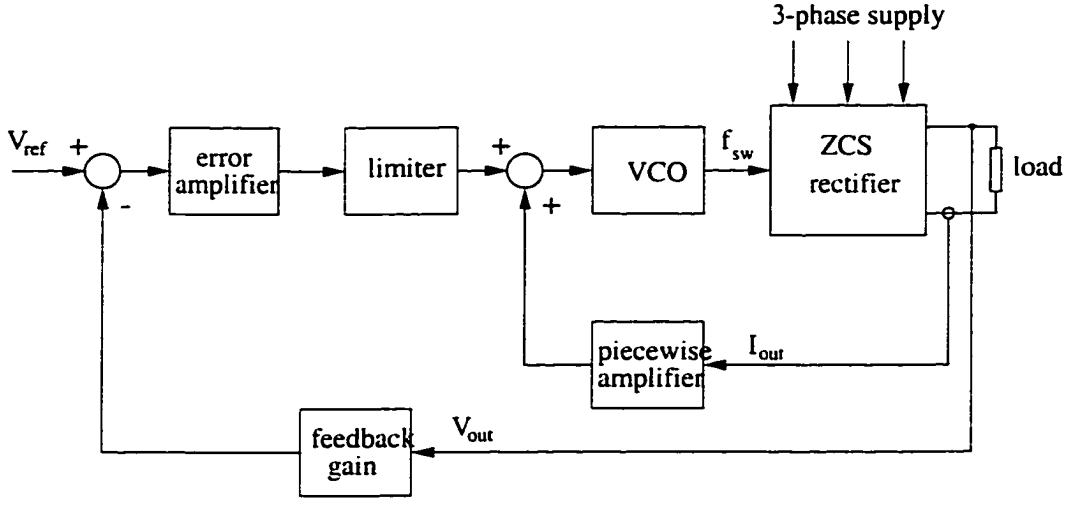

Figure 2.5: Block diagram of control circuit for rectifier.

The ground of the gating circuit is the same as the DC ground of the rectifier. The gating voltage is applied between gate and emitter of the IGBT. Since the emitter potential of the IGBT is at several hundreds of volts, applying the gating signal directly to the gate-emitter terminals of the IGBT will short-circuit the tank capacitor (C_R). Therefore, the gating signal applied to the IGBT is isolated from the rest of the circuit by using an optocoupler. The optocoupler requires a floating power supply which has output voltages of +16 and -11 volts. The ground of this power supply is connected to the emitter of IGBT and is called a floating ground because its potential referred to the

DC ground changes continually. Care should be taken to reduce the stray capacitance between this power supply and the DC ground of the rectifier, otherwise capacitively coupled currents will load the power supply above its rated current, and this will result in a failure of the power supply. One way to reduce the stray capacitance is by increasing the distance between the floating power supply and the DC circuit ground (e.g., cabinet in which rectifier is mounted). The zener diodes at the output of the optocoupler are employed to protect the gate of the IGBT from any overvoltages which might be occurring due to electromagnetic interference (EMI). The circuit diagram of the complete rectifier control circuit is documented in Appendix C.

When the transistor is turned on, its current starts to increase about linearly until it reaches the value of load current. At this time the freewheeling diode carries no current and L_R and C_R resonate together until the inductor current reaches zero. The input bridge diodes will prevent the inductor current from going negative. The transistor can be turned off at this time, but not necessarily: it can also be turned off during the interval when the capacitor voltage linearly discharges to zero [28]. Therefore, choosing a fixed on-time will turn off the transistor at zero current, reducing switching losses and achieving soft switching. The on-time of the gating signal is chosen as 24 μsec. The interval during which the capacitor voltage remains zero should be positive [28], resulting in a limitation on the maximum switching frequency for a given load. Figure 2.6 shows the possible switching frequencies for different load conditions while the tank capacitor voltage remains zero for an interval of $8\mu s$. An 8-step piecewise amplifier or A/D converter is used to approximate this frequency-versus-load nonlinear characteristic. This A/D converter adjusts the maximum switching frequency as a function of the rectifier load current: it was deemed to be accurate enough to perform this nonlinear adjustment in 8 steps (see Table 2.1). However, any new design should be based on at least 16 steps. At each step, the limit on the maximum switching frequency is increased, thus avoiding operation in the non-feasible region (Figure 2.6).

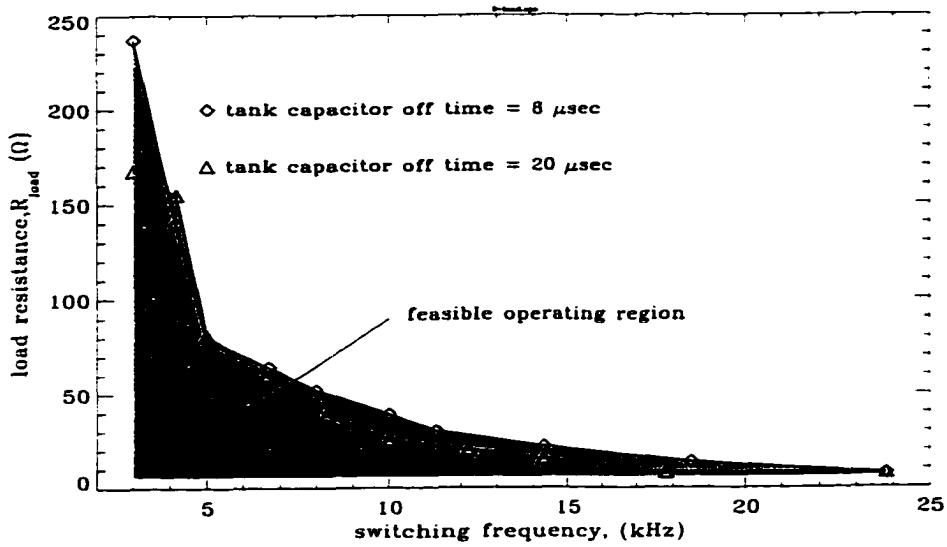

Figure 2.6: Measured feasible combinations of switching frequencies and rectifier loads.

The output of the piecewise amplifier and that of the limiter circuit are added together in a feed-forward manner and a voltage-controlled oscillator(VCO) is used to produce constant on-time, variable-frequency gating signals.

2.4 Input Filter

An input filter is placed between the rectifier and PM generator. The rectifier produces high-frequency pulsed currents which have a high amplitude. This is harmful to the generator. Therefore, the high-frequency currents must be eliminated and the low frequency component of the current should be supplied only by the generator.

Table 2.1: The switching points of 8-step amplifier (A/D converter)

step #	load current (A)	max. switching frequency (kHz)
0	0 - 6.60	6.61
1	6.60 - 9.20	7.97
2	9.20 - 12.28	9.91
3	12.28 - 16.70	11.93
4	16.70 - 23.50	13.14
5	23.50 - 29.76	14.29
6	29.76 - 37.68	17.30
7	37.68 - 44.30	20.72
8	44.30 and higher	23.98

The input filter is a L-C type filter as shown in Figure 2.7 with the corner frequency of around $f_0 = 5kHz$. The operation of the input filter, together with rectifier and

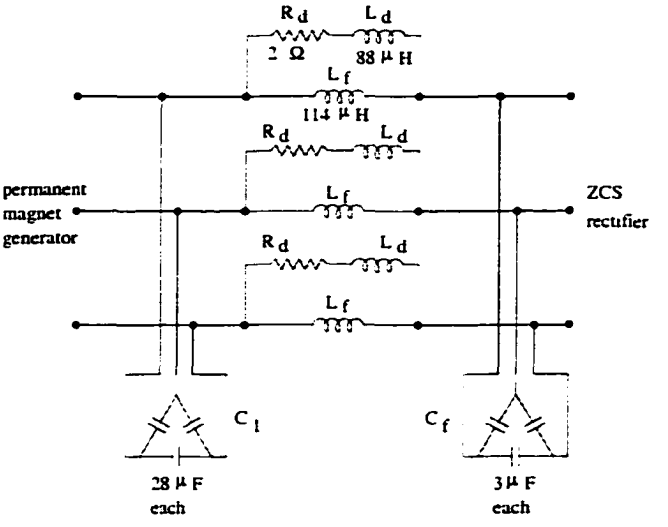

Figure 2.7: Input filter between ZCS rectifier and PM generator.

generator, indicated that a damping network might be beneficial in eliminating parasitic oscillations.

A single-phase representation of the low-pass input filter is illustrated in Figure 2.8. The transfer function of the filter with the damping network can be written as

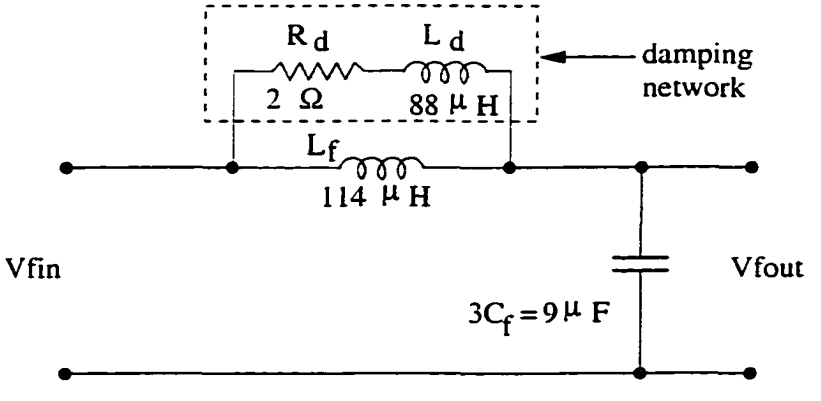

Figure 2.8: Single-phase representation of input filter of Figure 2.7.

$$H(s) = \frac{V_{fout}}{V_{fin}} = \frac{R_d + s(L_d + L_f)}{R_d + s(L_d + L_f) + R_d L_d L_f s^2 + L_d L_f C_f s^3} \quad . \tag{2.1}$$

Equation 2.1 is plotted in Figure 2.9 with and without a damping network. At the

corner frequency f_0, the transfer function peaks to a very high value, e.g., $50dB$, but

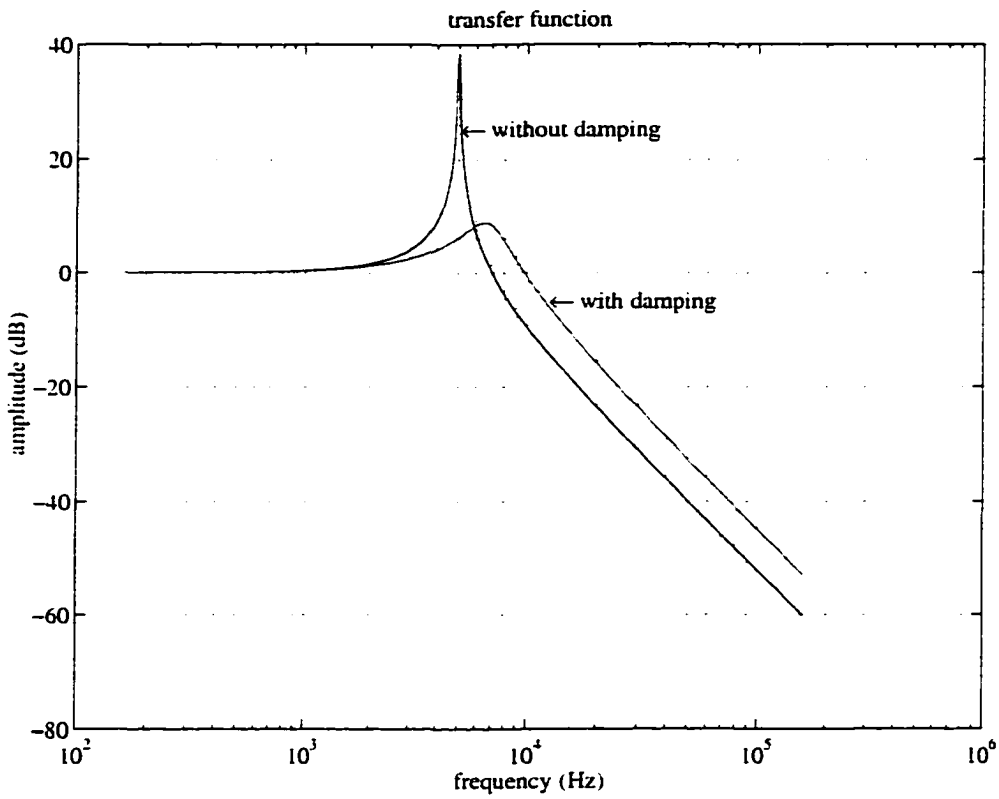

Figure 2.9: Transfer function of input filter.

addition of the damping network reduces the peak to about $10dB$. The use of a such a damping network reduces the efficiency of the rectifier significantly, and in future designs an attempt should be made to avoid such filter losses.

2.5 Commissioning of Rectifier

The ZCS rectifier was first tested in an open-loop connection, where no feedback signal was applied to the gating circuit, and as a result there was no control over the output voltage. The purpose of the open-loop test was to evaluate the voltage stresses experienced by the different components of the rectifier(e.g., tank capacitor, IGBT, input bridge diodes, etc.) for the specified input voltage range (e.g., $300V$ to $600V$). The switching frequency and the load are fixed throughout this experiment while the

input voltage is increased steadily to the maximum specified value. The maximum values of tank capacitor voltage, transistor voltage and output voltage for a load of 145 Ω and a switching frequency of $2.9kHz$ are shown in Figure 2.10.

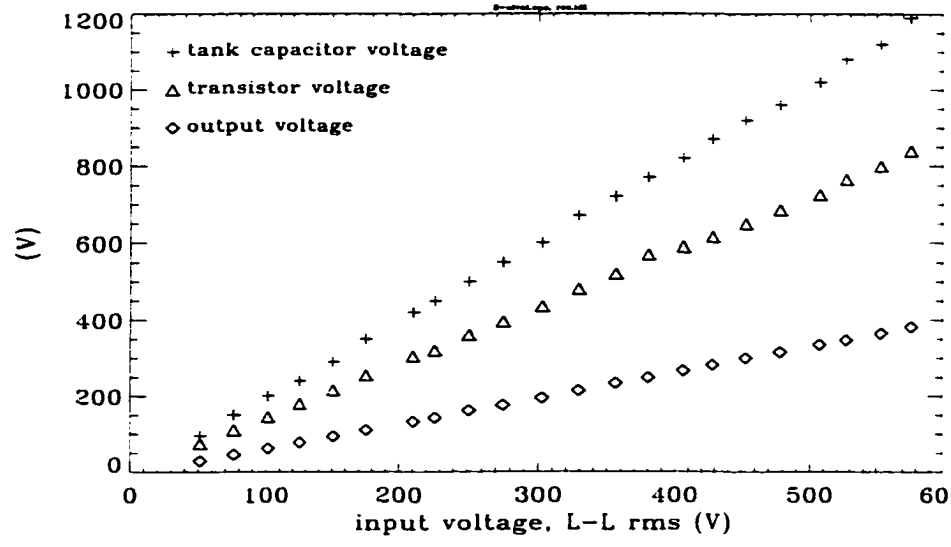

Figure 2.10: Output voltage, and voltage stresses for open-loop operation.

During startup of the rectifier, the switching frequency is limited to a maximum value of $6.5kHz$. As the input voltage increases, the switching frequency stays the same until the output DC voltage of the rectifier reaches the reference value, and any further increase in input voltage will result in a decrease in the switching frequency to maintain a constant output voltage. Figure 2.11 shows the DC output voltage and peak voltages of the tank capacitor (C_T) and those of the IGBT, up to a line-to-line input voltage of $380V$. The output voltage increases linearly with the input voltage until it is controlled, and then stays nearly constant; any change in the input voltage will be compensated by a change in switching frequency, making the output voltage constant and independent of changes in the input voltage. At this rectifier no-load condition, the piecewise amplifier has not yet reached the first step because of the low output DC current.

The load of the rectifier is a PWM inverter, which is emulated by a resistive load

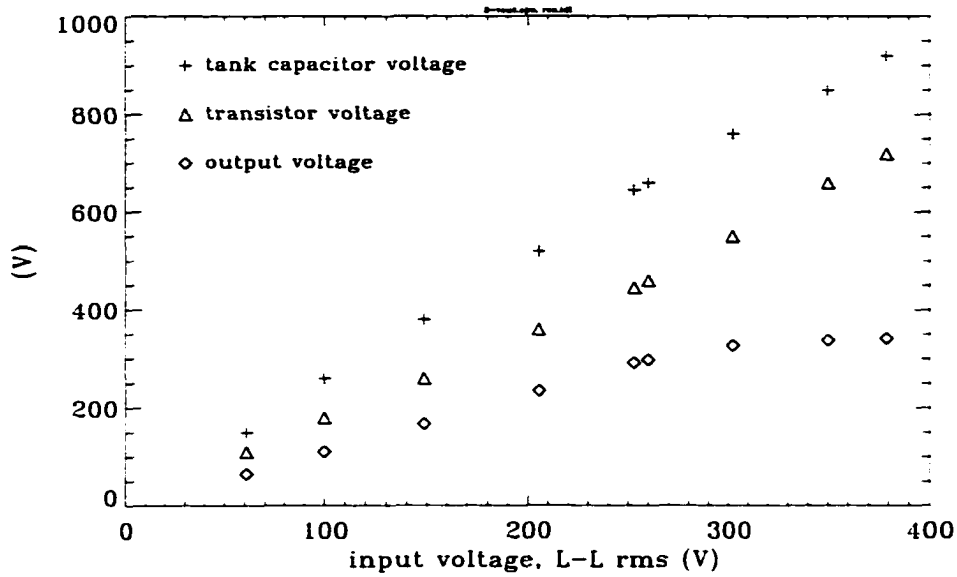

Figure 2.11: DC output voltage of rectifier and voltage stresses of IGBT and tank capacitor during startup.

during testing of the rectifier. As soon as load is connected to rectifier, the output current will increase and the output voltage will decrease. Depending on the value of the load current, the piecewise amplifier increases, in a step-wise manner, the maximum switching frequency according to Table 2.1; therefore moving to a different operating point. At this new operating point, the voltage-control loop adjusts the switching frequency to maintain a constant output voltage at the desired value (e.g. $350VDC$). The load is then increased to full load while the input voltage is maintained at its desired value. Figure 2.12 shows that the output voltage is nearly constant, independent of load current: by employing a 16-step A/D converter, this DC voltage control could be further improved. Note that when changing the above-mentioned operating point, the A/D converter must operate with a certain amount of hysteresis, otherwise instabilities can occur. The peak tank capacitor and transistor voltages increase linearly with the input voltage (Figure 2.11), and for a constant input voltage they stay nearly at the same value – independent of the load, as can be seen in Figure 2.12. Figure 2.13 shows how the switching frequency changes as the load current increases. An increase in load

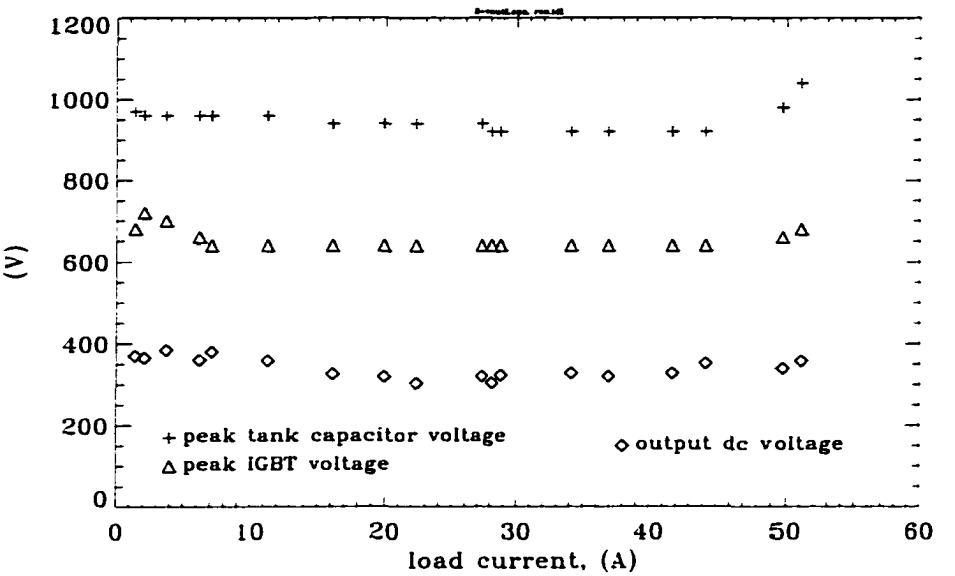

Figure 2.12: DC output voltage of rectifier and voltage stresses of IGBT and tank capacitor for an output power of up to $20kW$.

current will cause the switching frequency to increase, while, on the other hand, an increase in input voltage will result in a decrease of the switching frequency; this can be clearly seen in Figure 2.13. The efficiency of the rectifier is also shown in Figure 2.14. The nominal efficiency (at $20kW$ output) is about 89%. This is rather low, and

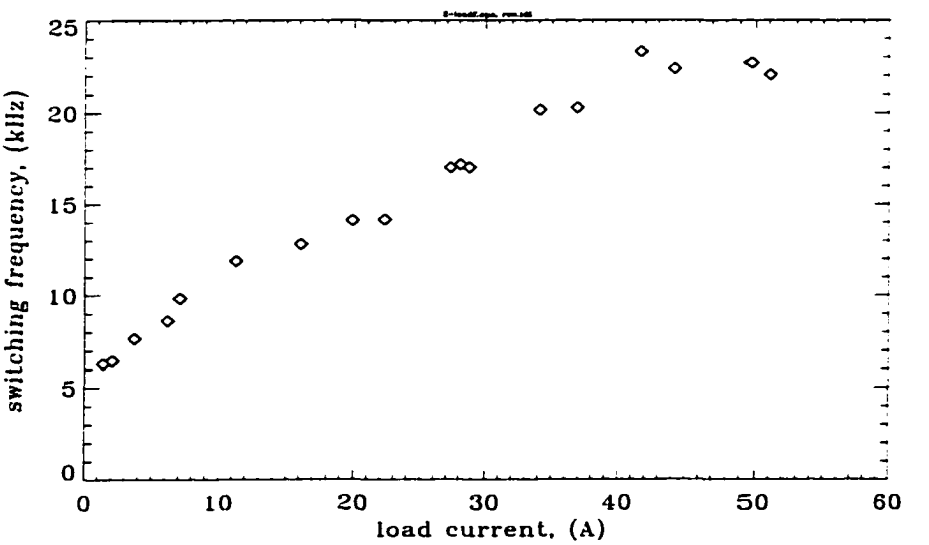

Figure 2.13: Switching frequency as a function of output current.

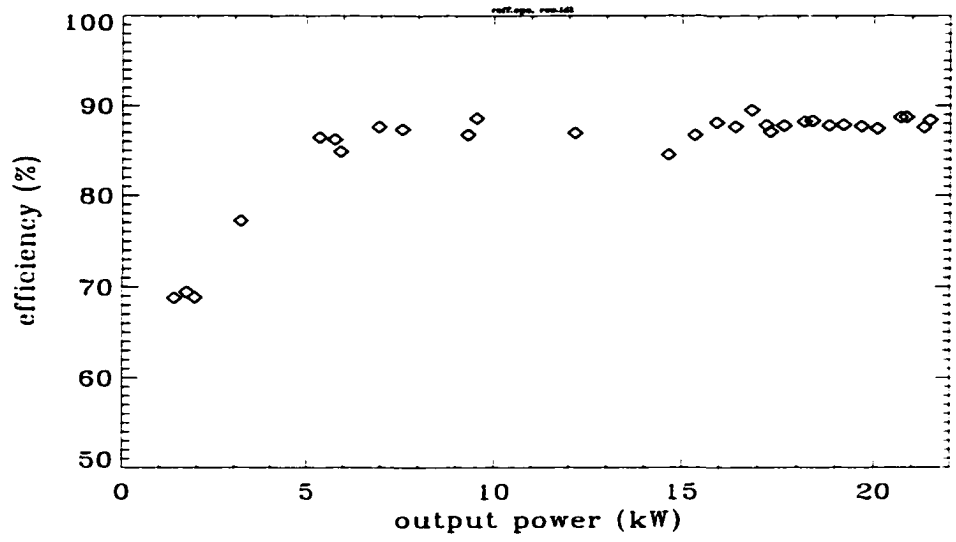

Figure 2.14: Efficiency of the ZCS rectifier versus output power.

one would require an efficiency of about 97%. Reasons for this low efficiency are the series-connected diodes, the damping of the input filter and the use of non-optimized inductors from a loss point of view.

The rectifier has been operated at full output power of 20 kW. The line-to-line output voltage and line current of the generator are illustrated in Figure 2.15, at $20kW$ power output. The line current slightly leads the generator voltage because of input capacitors connected across the line. This leading power factor is desirable in order to increase the generator voltage somewhat due to the supplied reactive (capacitive) power. A Fourier analysis is performed on the line current and line-to-line voltage of the generator, by use of the Fortran program listed in Appendix A. Harmonic amplitudes as a percentage of the fundamental are shown in Figure 2.16; the total harmonic distortion (THD) of voltage is $THD_v = 16.81\%$ at $V_{rms} = 378.75V$, $V_{1rms} = 376.24V$; and $THD_i = 13.04\%$ at $I_{rms} = 38.79A$, $I_{1rms} = 38.46A$.

Figure 2.17 presents the input current of the rectifier during 4.5 periods of the generator current and three switching cycles, at light-load conditions. The input current consists of pulses at switching frequency. As the frequency increases – this means an increase of the output current – the density of the current pulses is increased as shown in

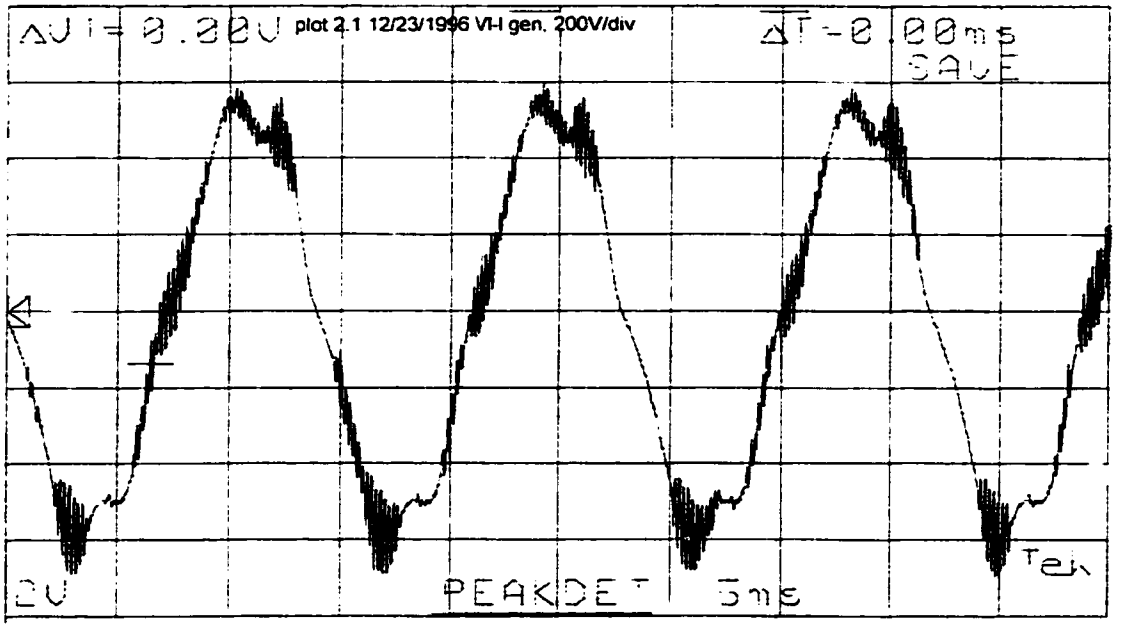

(a)

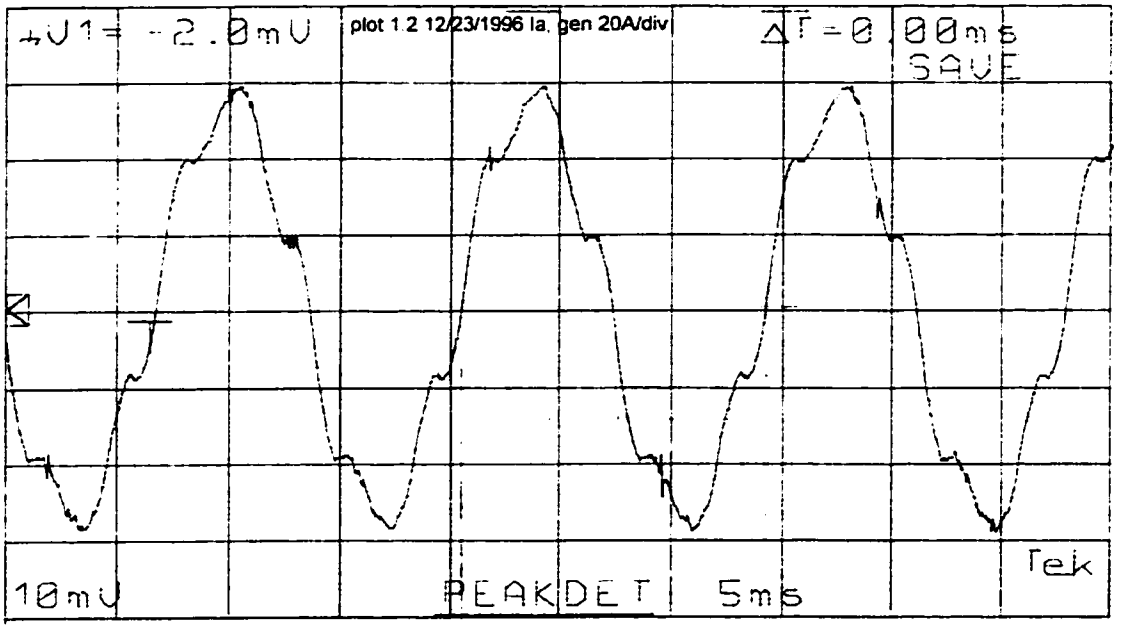

(b)

Figure 2.15: (a) Line-to-line output voltage, 200 V/div, 5 ms/div and (b) output current, 20 A/div, 5 ms/div of generator at full load (20 kW), $V_{L-L}^{in} = 382.6VAC$, $V_{out} = 362.6VDC$, $I_{out} = 60ADC$.

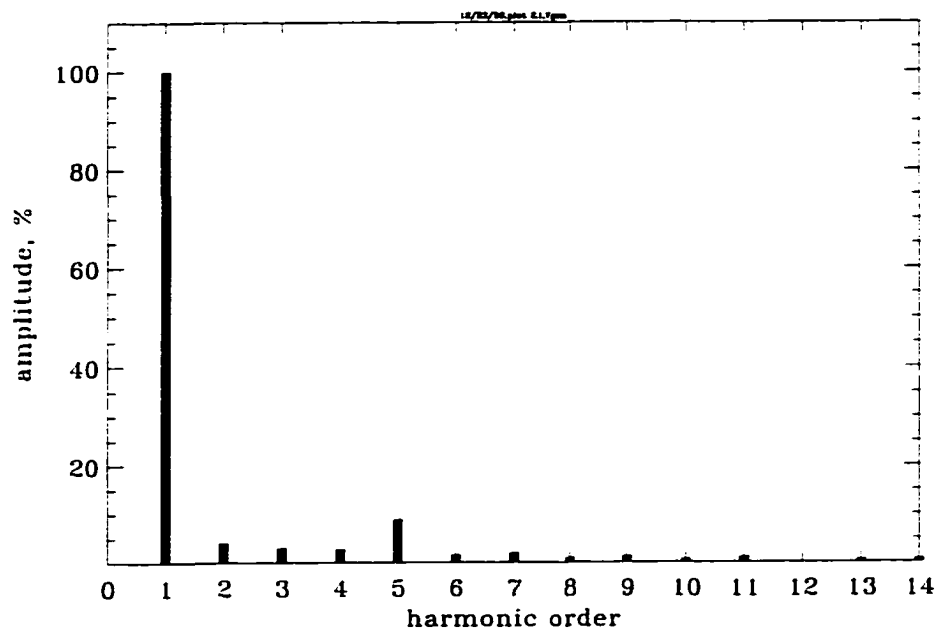

(a)

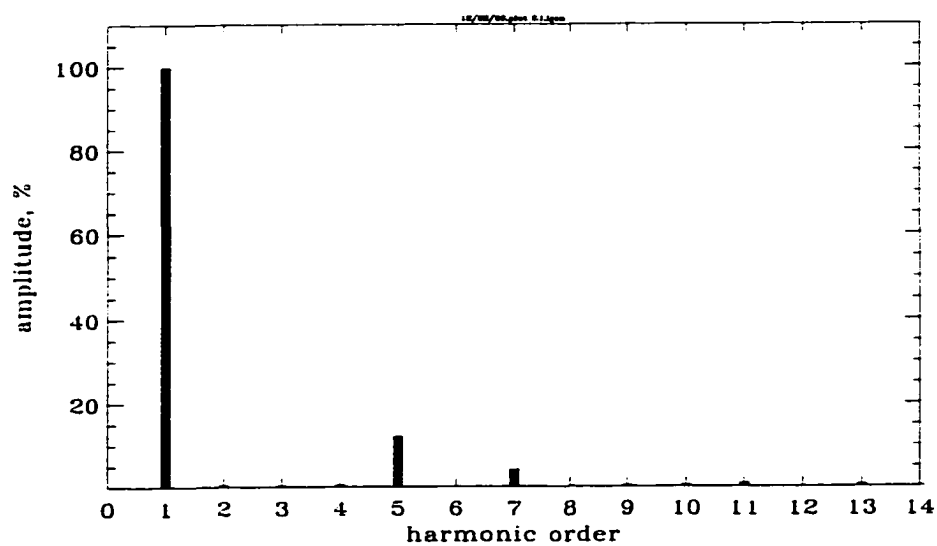

(b)

Figure 2.16: (a) Amplitudes of harmonics in the line-to-line voltage and (b) line current of generator.

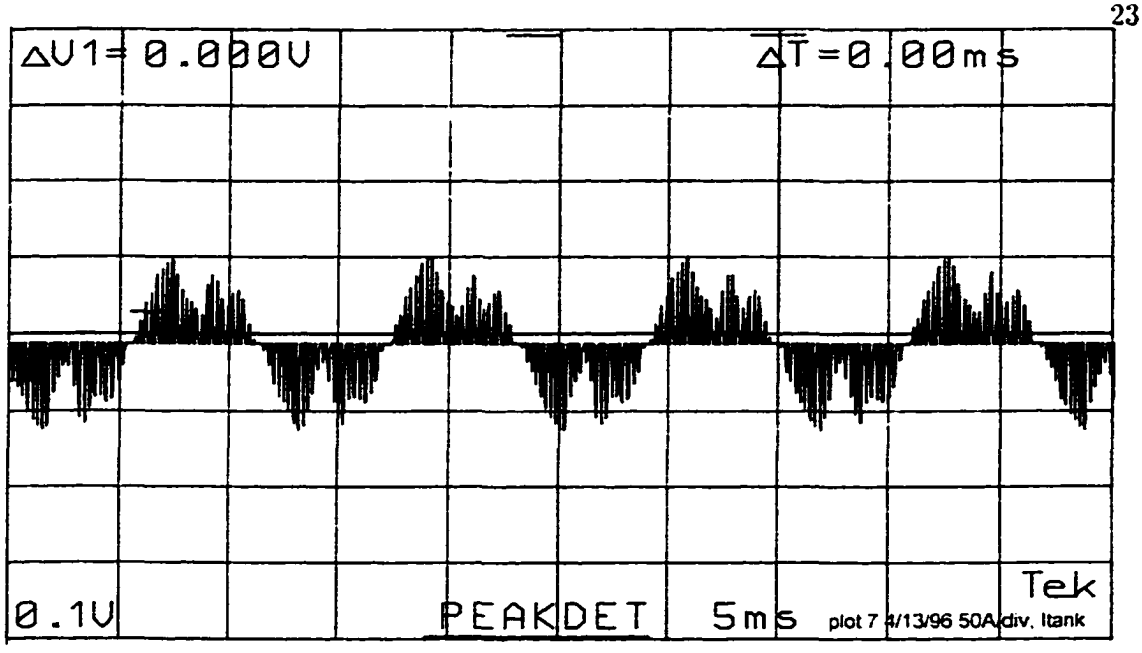

(a)

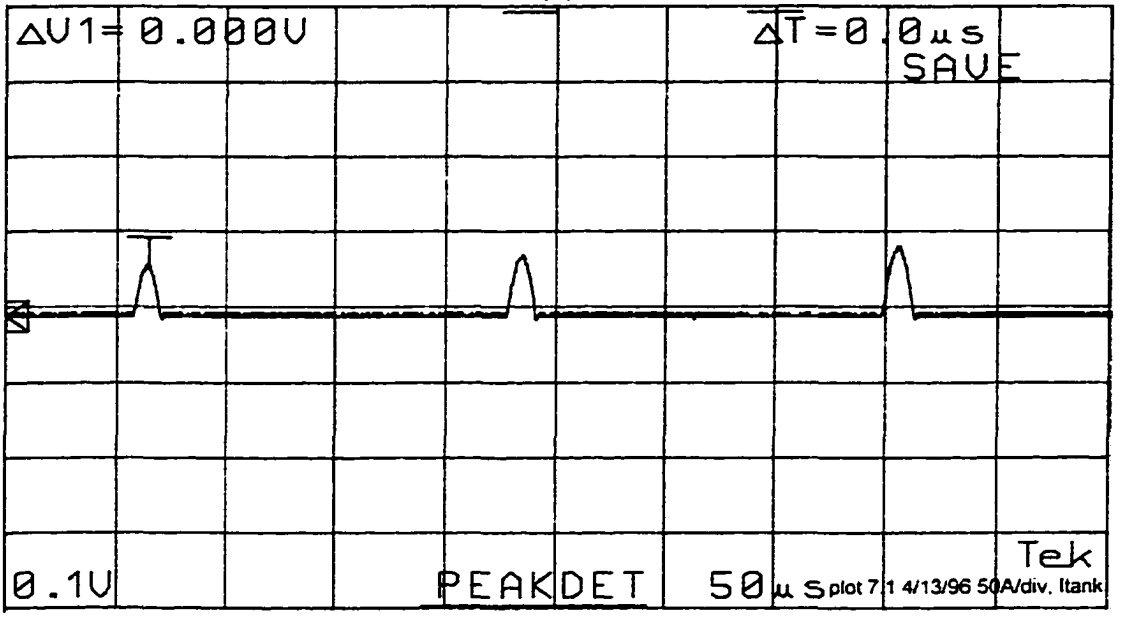

(b)

Figure 2.17: (a) Input current (or tank-inductance current) of rectifier, 50 A/div, 5 ms/div, and (b) detailed view, 50 A/div, 50 μs/div, at light load, $V_{L-L}^{in} = 397VAC$, $V_{out} = 347VDC$, $I_{out} = 5ADC$.

Figure 2.18. Figures 2.19 and 2.20 show the voltage across the tank capacitor and that of the IGBT at full load, for a few periods of the generator voltage and at the switching frequency. DC output voltage and current at rated load are illustrated in Figure 2.21 at the output of the rectifier.

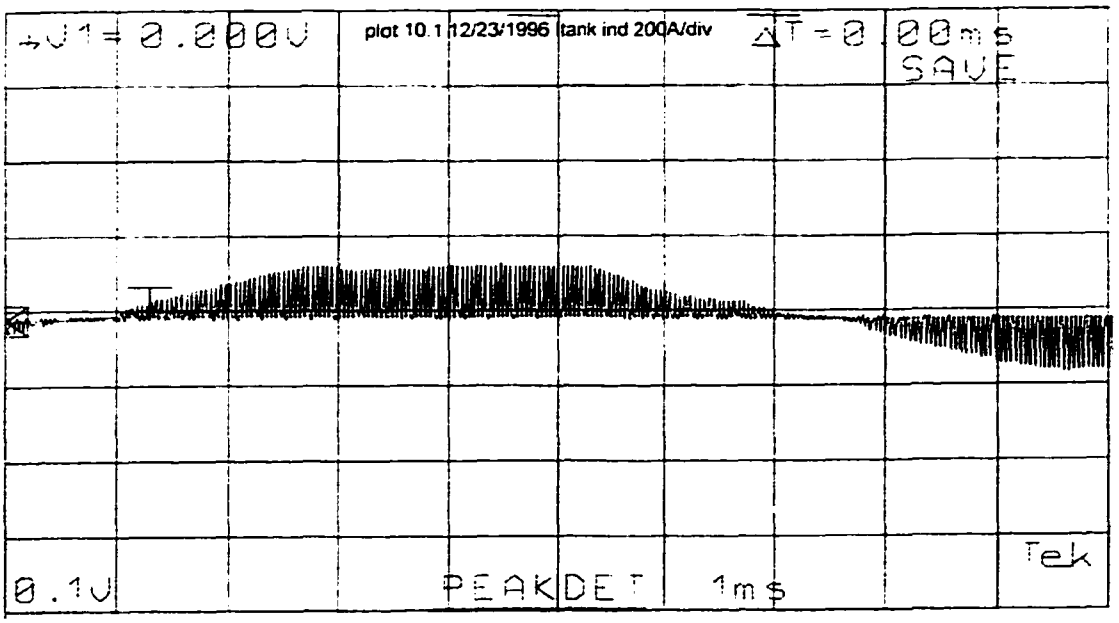

(a)

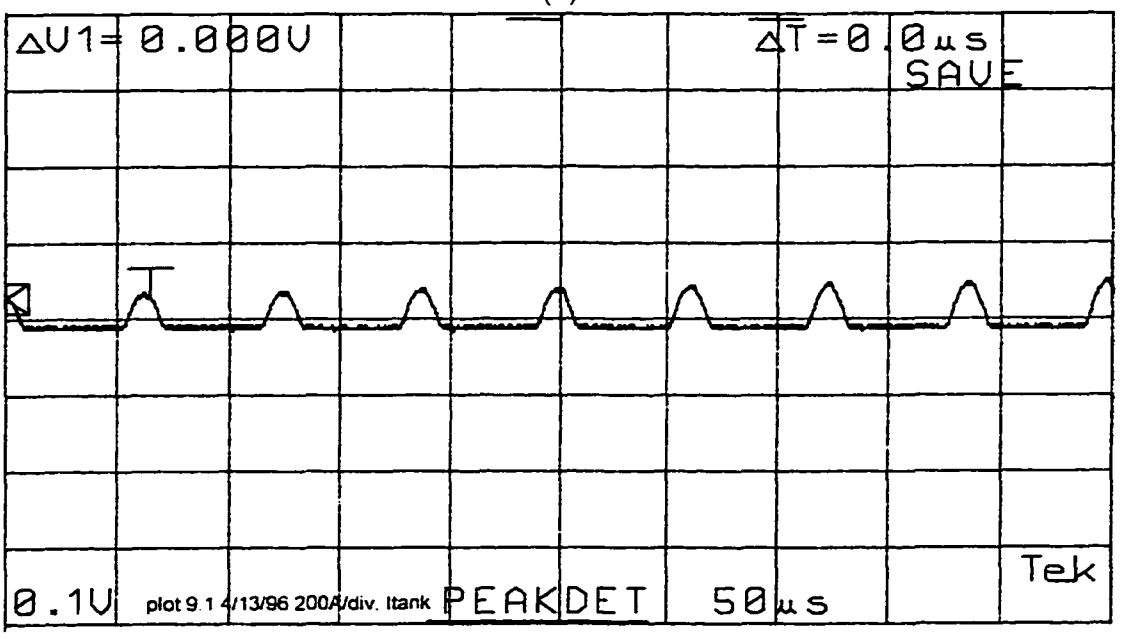

(b)

Figure 2.18: (a) Input current (or tank-inductance current) of rectifier at $V_{L-L}^{in} = 384.7VAC$, $V_{out} = 361VDC$, $I_{out} = 56ADC$, 200 A/div, 1 ms/div, and (b) at $V_{L-L}^{in} = 391VAC$, $V_{out} = 363VDC$, $I_{out} = 32.5ADC$, 200 A/div, 50 μs/div.

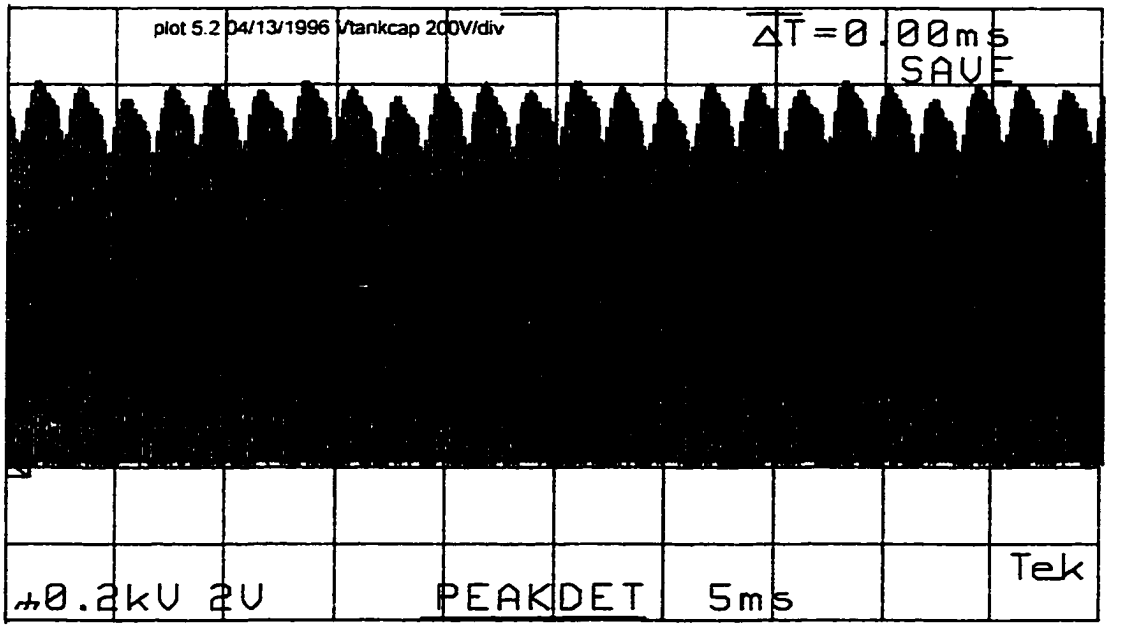

(a)

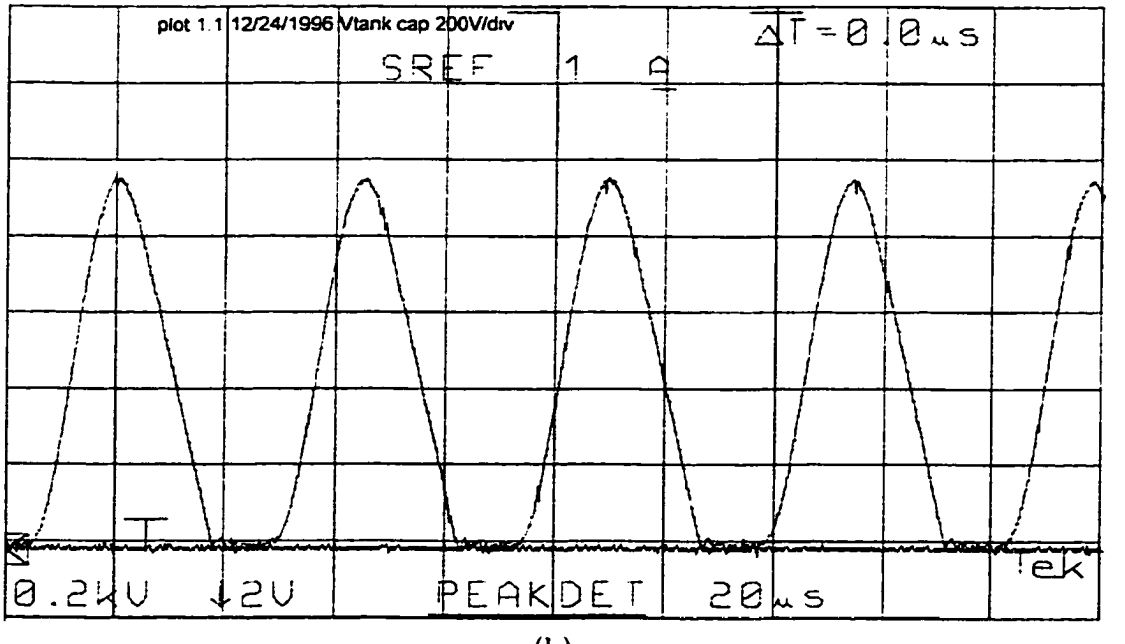

(b)

Figure 2.19: (a) Tank capacitor voltage at $V_{L-L}^{in} = 380VAC$, $V_{out} = 362VDC$, $I_{out} = 56.8ADC$, 200 V/div, 5 ms/div and (b) at $V_{L-L}^{in} = 384VAC$, $V_{out} = 366VDC$, $I_{out} = 59ADC$, 200 V/div, 20 μs/div.

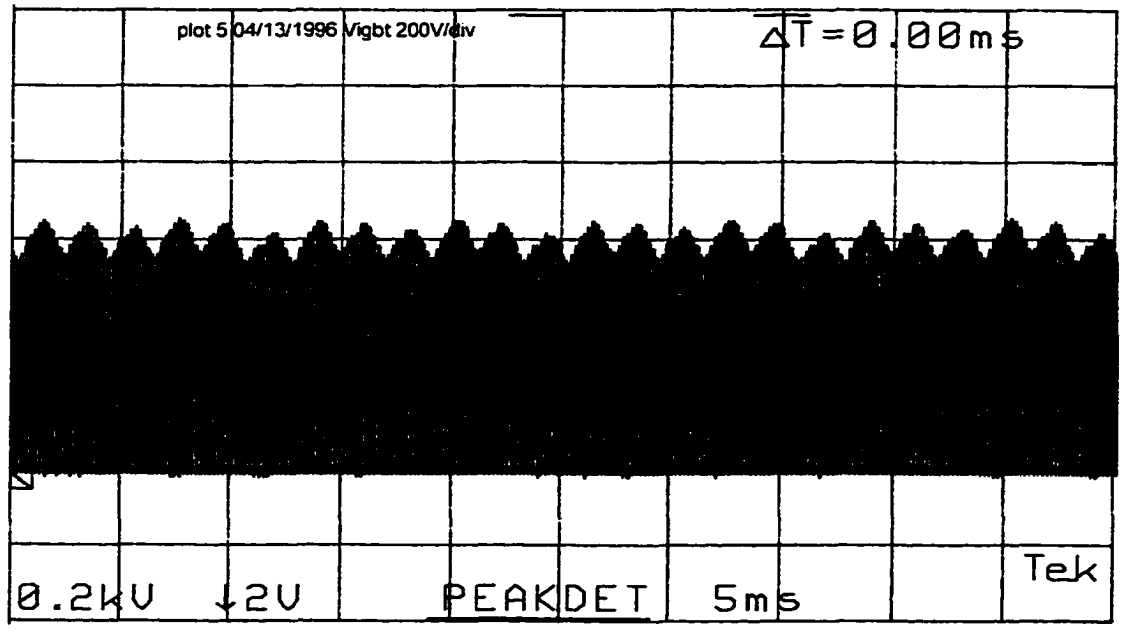

(a)

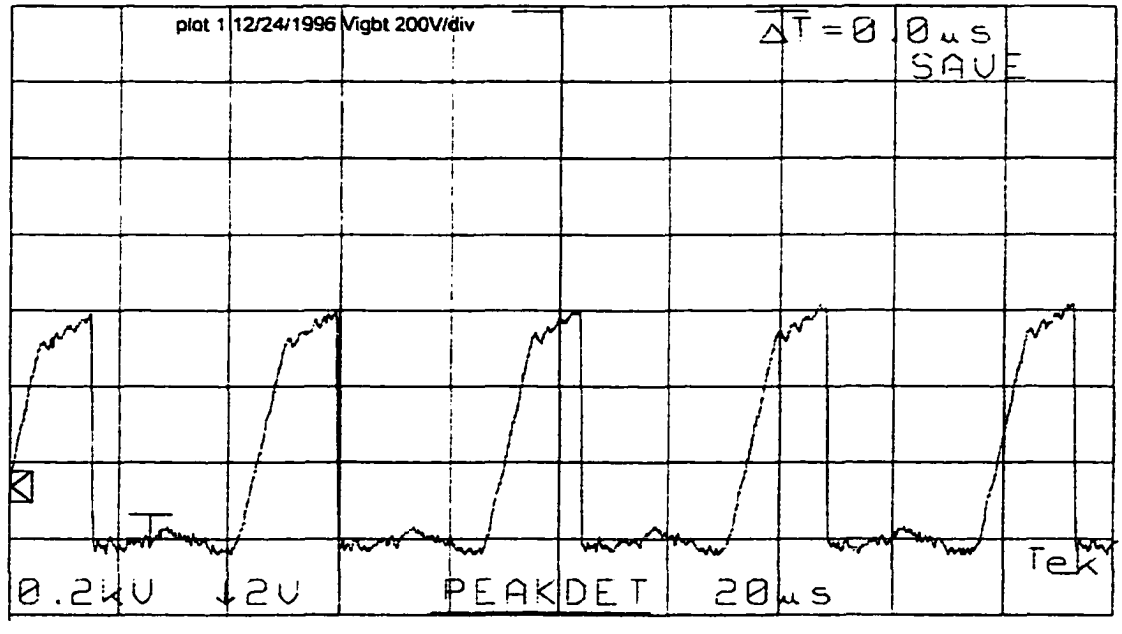

(b)

Figure 2.20: (a) Voltage stress across the IGBT at $V_{L-L}^{in} = 380VAC$, $V_{out} = 362VDC$, $I_{out} = 56.8ADC$, 200 V/div, 5 ms/div and (b) at $V_{L-L}^{in} = 384VAC$, $V_{out} = 366VDC$, $I_{out} = 59ADC$, 200 V/div, 20 μs/div.

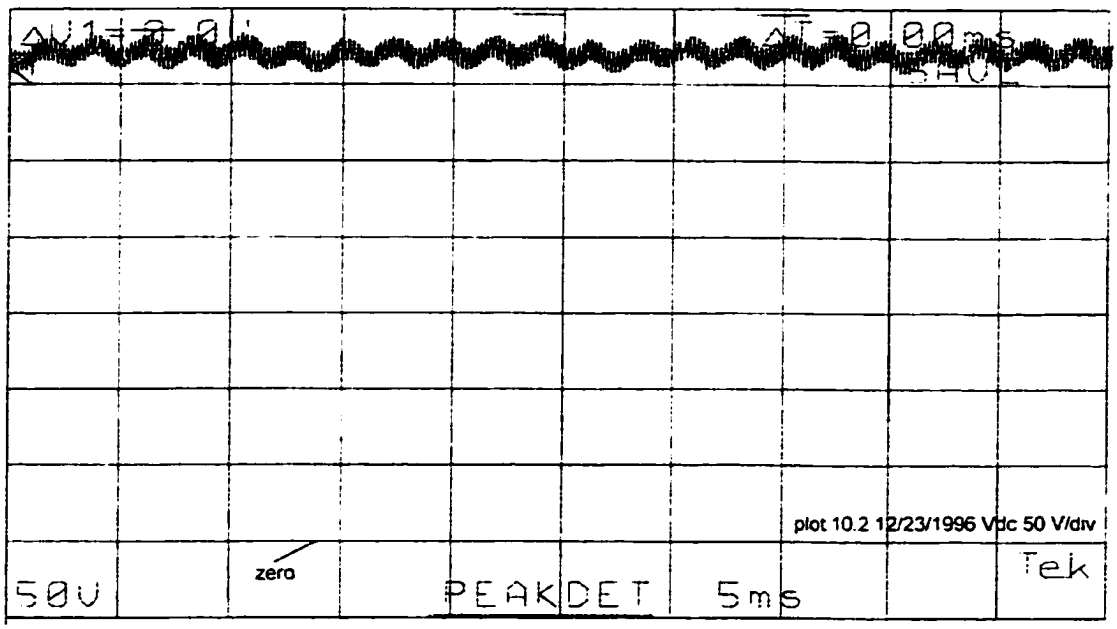

(a)

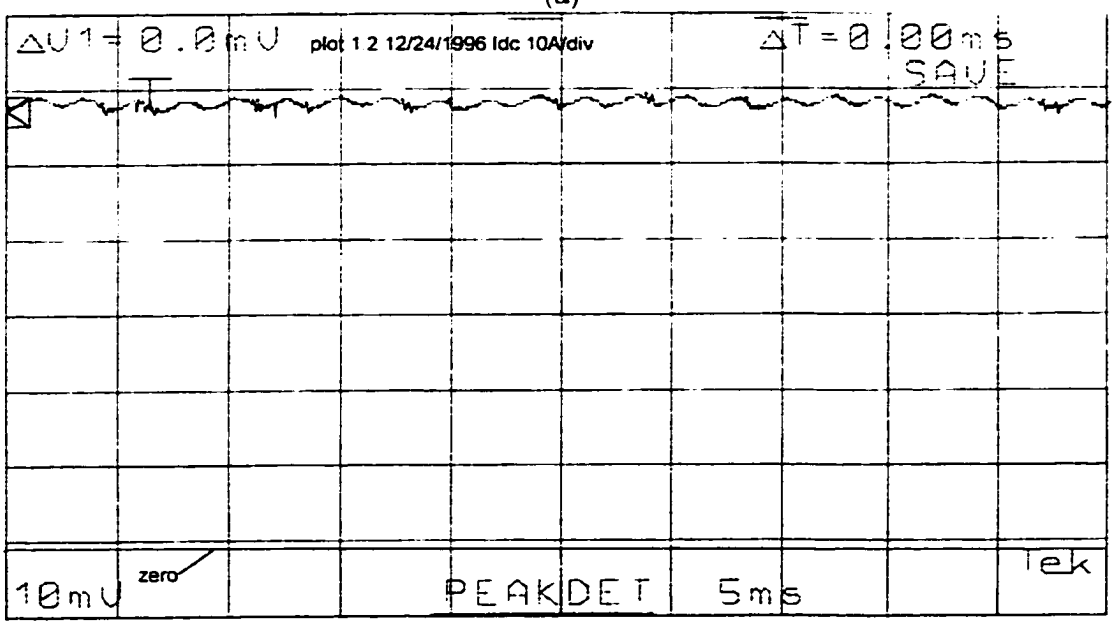

(b)

Figure 2.21: (a) Output DC voltage of the rectifier at $V_{L-L}^{in} = 378.3VAC$, $V_{out} = 354.4VDC$, $I_{out} = 59.2ADC$, 50 V/div, 5 ms/div and (b) output DC current of rectifier at $V_{L-L}^{in} = 384VAC$, $V_{out} = 366VDC$, $I_{out} = 59ADC$, 10 A/div, 5 ms/div.

CHAPTER 3

30 kVA PULSE-WIDTH-MODULATED (PWM) INVERTER

3.1 Introduction

The DC output power of the rectifier is converted to three-phase 60 Hz AC power by a current-controlled PWM inverter (Figure 3.1). The output currents of the inverter, measured by using Hall sensors, are compared with a sinusoidal reference current, and the current error is then compared with a fixed-frequency ($5.76kHz$) triangular carrier wave. The resulting PWM signal controls the inverter switching. There are three current controllers, one for each phase, but the high-frequency triangular carrier signal is common to all three phases, and each inverter leg switches at carrier frequency. The output current follows the reference current and as a result it is controlled by changing the reference current, while the output voltage of the inverter will be fixed by the power system's line-to-line voltage.

3.2 Commissioning of Inverter

The original gating circuit in [6] has been changed somewhat to reduce EMI problems, caused by mounting of components within a steel cabinet. The changes of the gating circuit are as follows:

- The capacitance connected to the Hall sensor output is reduced. The original 2.2 μF capacitor was causing low frequency oscillations of the output current of the inverter at certain (high) DC input voltages.

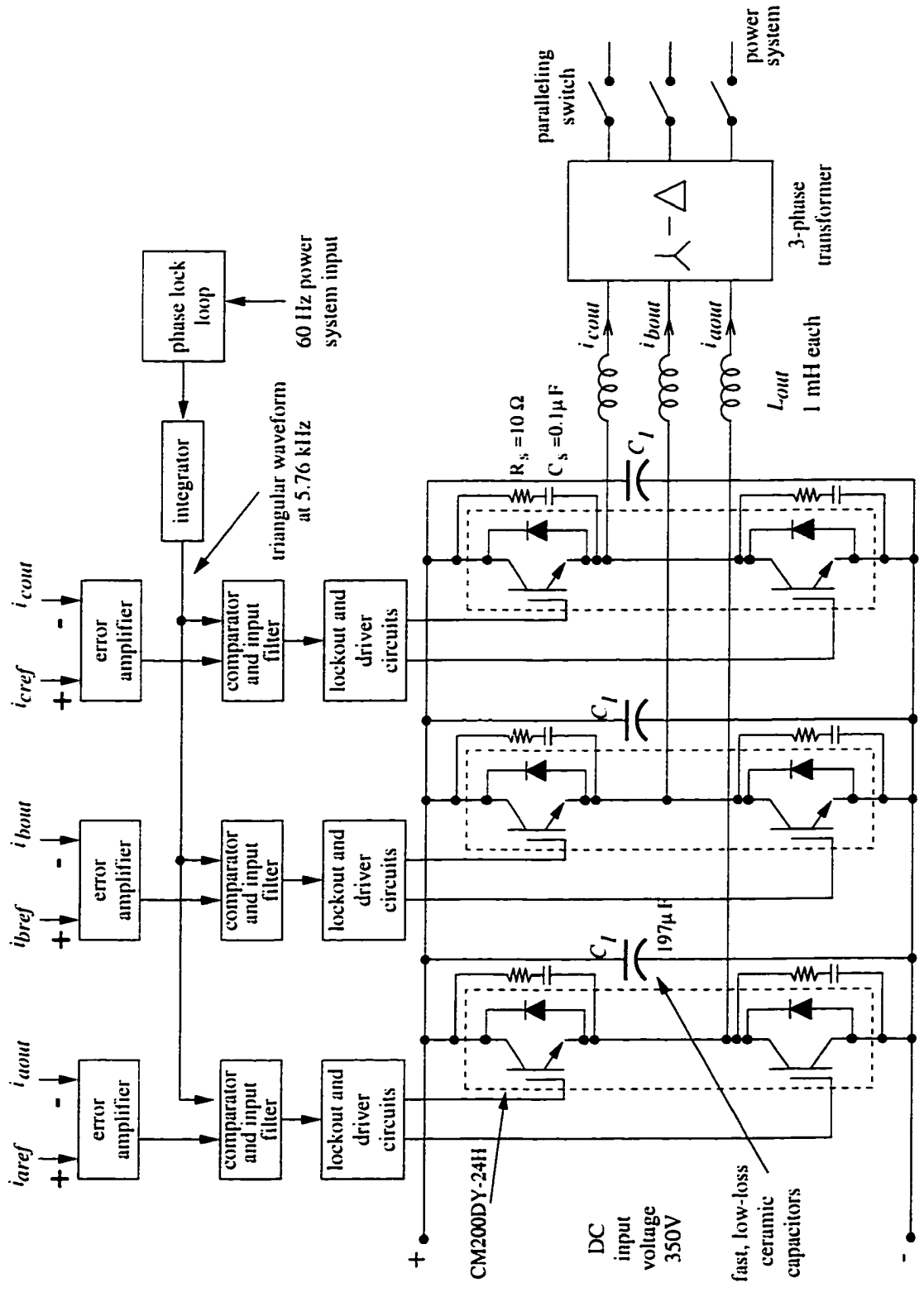

Figure 3.1: Three-phase, current-controlled PWM inverter.

- The gain of the error amplifier has been changed from 14.7 to 7.
- A capacitor is connected to the input of phase-lock loop (PLL) to reduce noise in the single-phase 60 Hz reference input: and the series connected capacitor at the output of the PLL, for removing the DC offset, has been increased from 0.4 μF to 4.4 μF.
- The 10 nF capacitor connected between gate and emitter of the lower IGBTs has been reduced to 3.5 nF, although a larger capacitor is desirable for reducing noise: it increases the value of the gate capacitance, and as a result increases the turn-on and turn-off times of the transistors (IGBTs).
- The lock-out time between turn-on (or turn-off) of upper IGBT and lower IGBT has been increased from 6 μsec to 10 μsec, because at 6 μsec lock-out time the upper and lower IGBTs sometimes conducted simultaneously during turn-on and turn-off, causing a short circuit of the DC input voltage (a so called shoot-through).
- The analog (error amplifier sections) and digital (PLL, lock-out and driver sections) ground terminals of the gating circuit have been separated from each other so that the noise at one of the grounds will not cause an EMI problem on the other one. These separate grounds are connected together at the grounding terminal of the power supply.
- Although there are decoupling capacitors connected to the main power supply inputs for the gating circuit, in order to achieve best noise immunity, decoupling capacitors of the ceramic (fast) type are also connected between power supplies of integrated circuits (IC) and ground (as closely as possible to the IC).
- For maximum noise immunity, the ground is applied to the C_{ext} nodes (pins 6 and 14 of 74LS123) of the monostable multivibrator used in the lock-out circuit

as described in [29], and unused pins 5 and 6 of the voltage comparator (LM311) are tied together as suggested by [30].

The modified gating circuit is shown in Appendix C. The layout of the gating circuit is also important to minimize the effects of unwanted noise signals. A copper sheet should be used as a ground plane because of its low resistance, and single point grounding should be used to avoid any ground loops, which may generate extra noise in the circuit. Noise in the circuit is mostly a result of a resonance between a parasitic capacitance and inductance; minimizing these two greatly reduces the effect of noise on the circuit. The value of parasitic inductance is proportional to the enclosed area of a current loop; therefore, this area should be minimized by twisting the signal wires, and the distance between the ground plane and the signal wire located above this ground plane should be minimized. Since the gating circuit is located within a very noisy environment, shielded cables should be used to carry the gating signals to the IGBTs thus decreasing parasitic capacitances; and the shield should be connected to ground on one end only, preferably at the source. Noise can sometimes be generated by the measurement of a signal (e.g., gating signal) in the circuit; therefore, common-mode toroids should be employed at the terminals of the scope and the scope's power leads. Last, but not least, the input capacitance of an oscilloscope may contribute to noise generation.

The inverter was first tested with a light load of three-phase Y-connected 100 Ω resistors, to achieve the specified line-to-line output voltage (e.g., 240 V) for the 370 V DC input voltage. A three-phase transformer, with a turns ratio of one, was connected between the output of the inverter and the resistor bank; the use of a transformer provides zero DC resistance at the output of the inverter and, therefore, any stability problems due to a faulty internal phase sequence associated with a DC offset in the output current of the inverter can easily be detected before making any connection to

the power system. As a next step, the load was increased to 15 kW by adjusting the value of the three-phase resistor bank such that, at a 40 A output phase current, the line-to-line voltage at the secondary of transformer was about 240 V_{L-L}. The output voltage of this type of inverter is not controlled, instead the inverter output currents are adjustable via reference currents.

Once the inverter was successfully operated at the desired input and output voltages and at the desired power level for resistive load operation, it was connected to the 240 V_{L-L} power system. Figure 3.2 shows the various wave forms of the inverter with and without an output filter in PWM operation mode; that is, the phase difference between the reference current (I_{ref}) and the actual output current (I_{out}) of the inverter is small (e.g., I_{out} lags I_{ref} by 35^o). The PWM operation can also be clearly seen in the voltage wave form across one of the lower IGBTs. The line-to-line output voltage of the drive system, e.g., 260V, should be higher than the power system voltage of $240V$ so that there is a positive power flow to the system right after paralleling. If there is no harmonic output filter, the rms value of line-to-line output voltage satisfies easily the required voltage value of $260V$. However, the voltage wave form contains a large amount of switching frequency ($5.76kHz$) harmonics. These high frequency voltages create audible noises and result in malfunctioning of the synchronization control circuit (explained in Chapter 4), which did not output the enable command for paralleling. Therefore, the operation without an output filter (tuned to $9kHz$) is not desirable.

When the output filter is connected, the audible noise decreases to acceptably low levels. In this case, the voltage wave form is very close to a sinusoidal signal. However, for the same DC input voltage as for the operation without a filter ($V_{DC} = 340V$), the rms value of the line-to-line output voltage of the drive system is $185V$, lower than the required voltage for paralleling. As a result, the inverter cannot successfully be paralleled to the power system in PWM operation mode for the given DC voltage of $V_{DC} = 340V$.

By operating the inverter near the PWM-Six step border, the rms value of the nearly sinusoidal output line-to-line voltage can be increased. This is achieved by introducing an additional lagging phase shift, for all operating conditions between the reference current and the actual output current of inverter as is illustrated in Figure 3.3. In this mode of operation, the peak value of the triangular carrier wave form is larger than the peak value of the error signal, i.e., the modulation index is $m > 1$. Modulation index is the ratio of the peak value of the sinusoidal error signal to that of the triangular signal, $m = V_{error}^{peak}/V_{triangular}^{peak}$. The voltage wave form across the lower IGBT implies that the device is not always switching, confirming the operation in PWM-Six Step mode. A line-to-line output voltage of $260VAC$ can be obtained with a DC input voltage $V_{DC} = 340V$ when the output filter is present. The DC voltage can be even lower than $340V$ if the output filter is removed; however, operation without an output filter is not advisable for the reasons explained previously. Similar wave forms are given in Figure 3.4 right after the inverter is paralleled to the power system (with output filter present). The operation near the border between PWM and six-step reduces the switching losses; however, it makes a harmonic compensation – as has been envisioned for this wind power plant - impossible. The manner how this operating-point-independent overmodulation is achieved is not discussed here, but it can be gathered from an invention disclosure.

After having successfully connected to the utility system, the output voltage of the inverter is fixed by the system at a nominal 240 V_{L-L}, with the same reference currents as before the paralleling. Now, the inverter is floating on the system as shown by the signal in Figure 3.5b. The DC input voltage is fixed at around 375 V ($350 - 400V$), and the output current of inverter is increased steadily by increasing the three-phase reference currents such that the output power is $20kW$. Figure 3.6 shows the DC input voltage wave form at $20kW$. If this wave form is compared with the DC voltage wave form plotted at the output of rectifier (Figure 2.21a), it is seen that the DC link voltage

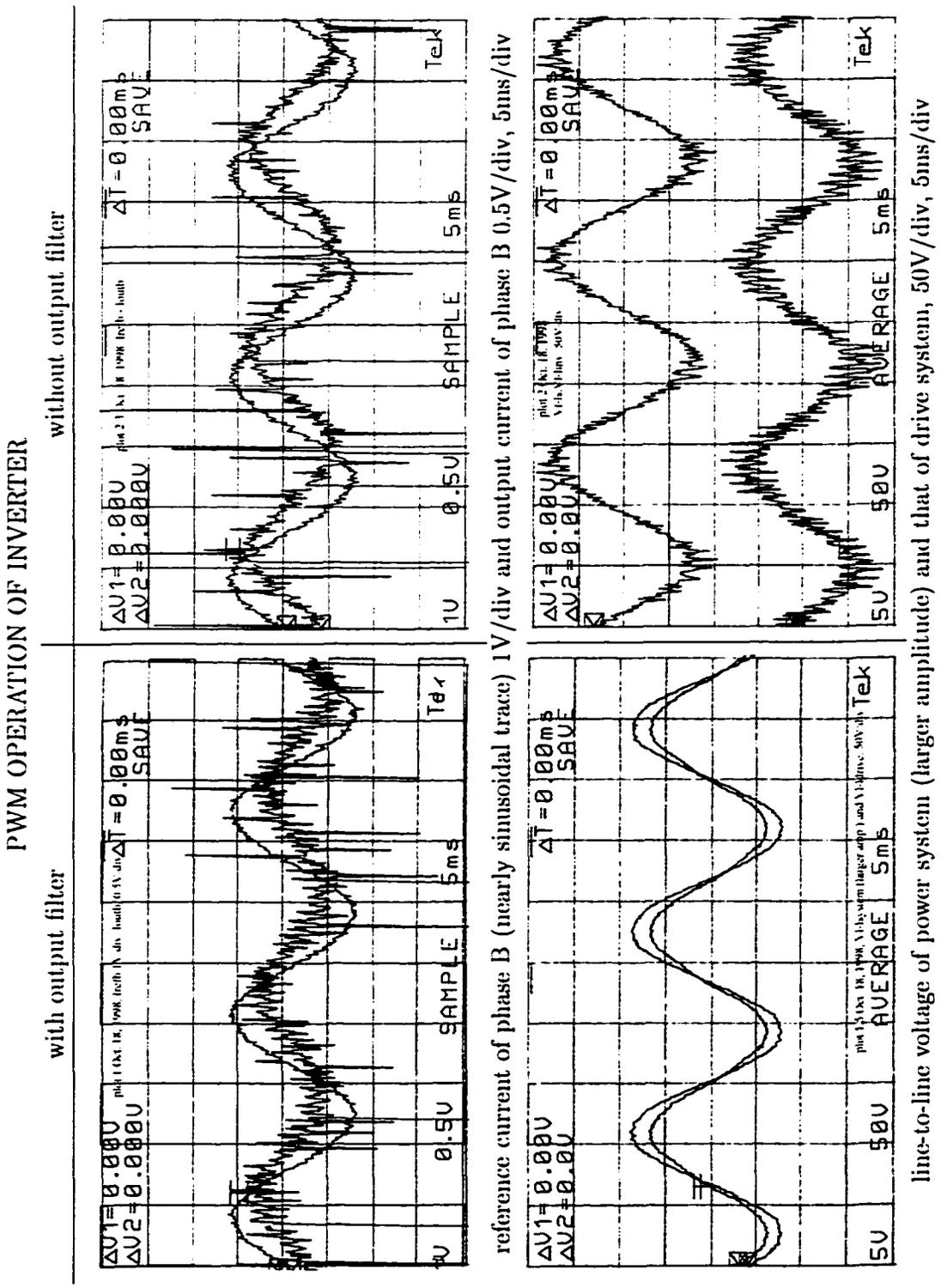

Figure 3.2: PWM inverter wave forms at $V_{DC} = 340V\ DC$, $I_{DC} = 1.9A\ DC$, $V_{L-L}^{drive} = 185V\ AC$ (with output filter); and at $V_{DC} = 340V\ DC$, $I_{DC} = 2A\ DC$, $V_{L-L}^{drive} = 260V\ AC$ (without output filter).

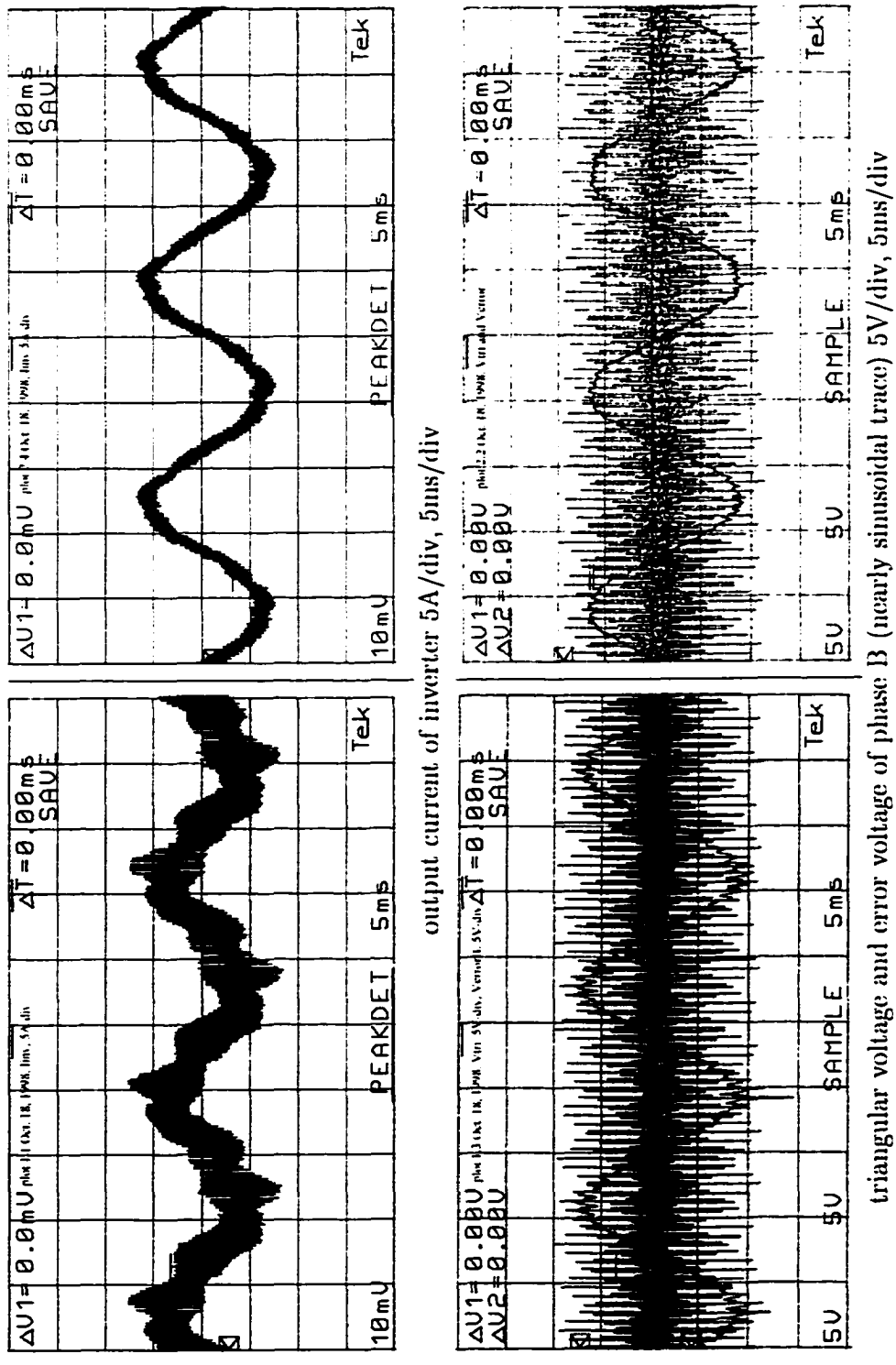

output current of inverter 5A/div, 5ms/div

triangular voltage and error voltage of phase B (nearly sinusoidal trace) 5V/div, 5ms/div

Figure 3.2: continued.

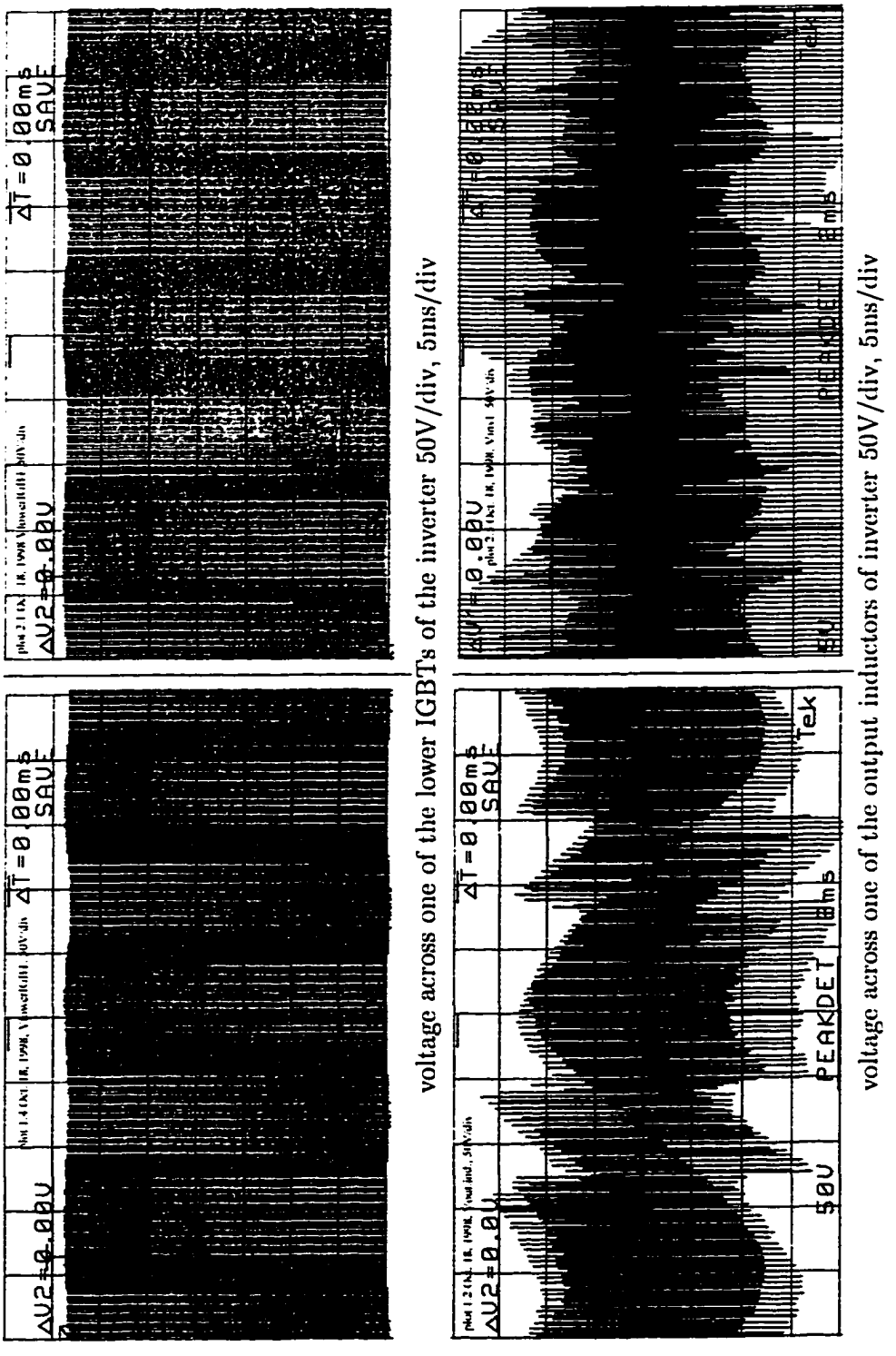

voltage across one of the lower IGBTs of the inverter 50V/div, 5ms/div

voltage across one of the output inductors of inverter 50V/div, 5ms/div

Figure 3.2: continued.

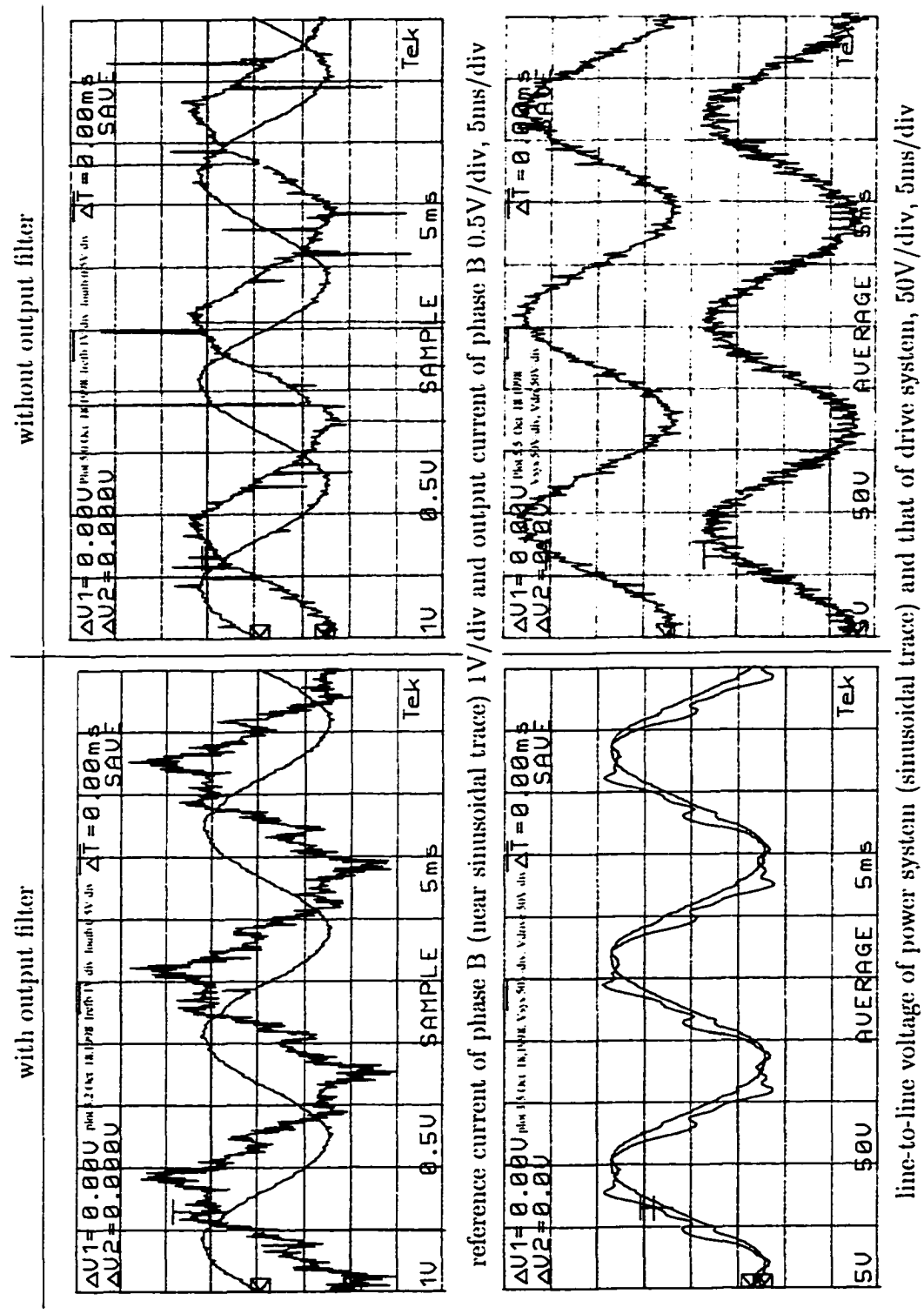

Figure 3.3: PWM inverter wave forms at $V_{DC} = 340VDC$, $I_{DC} = 3ADC$, $V_{L-L}^{drive} = 258VAC$ (with output filter); and at $V_{DC} = 299.5VDC$, $I_{DC} = 2.5ADC$, $V_{L-L}^{drive} = 260VAC$ (without output filter).

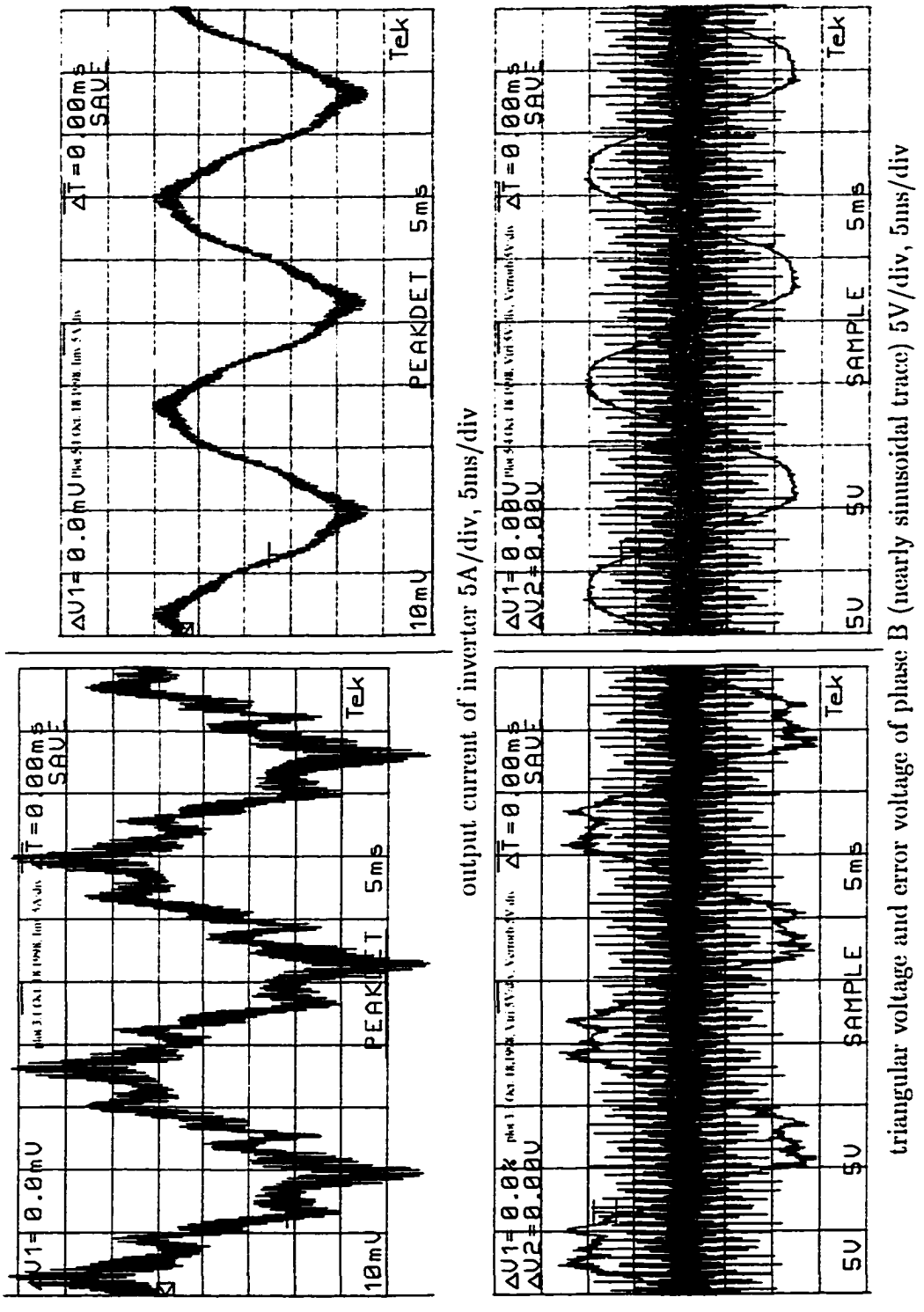

Figure 3.3: continued.

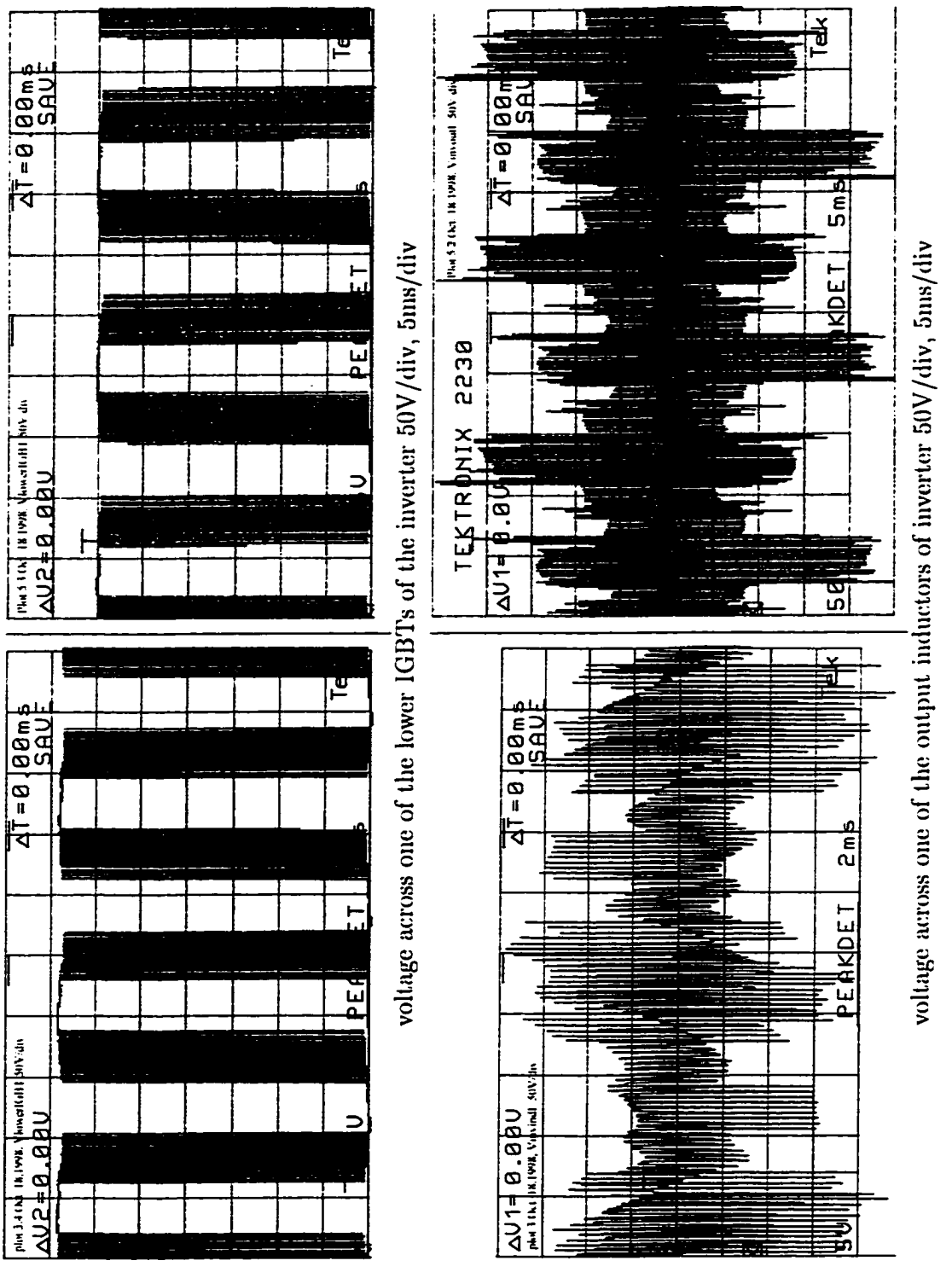

voltage across one of the lower IGBTs of the inverter 50V/div, 5ms/div

voltage across one of the output inductors of inverter 50V/div, 5ms/div

Figure 3.3: continued.

OPERATION OF THE INVERTER IN PWM-SIX STEP MODE CONNECTED TO POWER SYSTEM

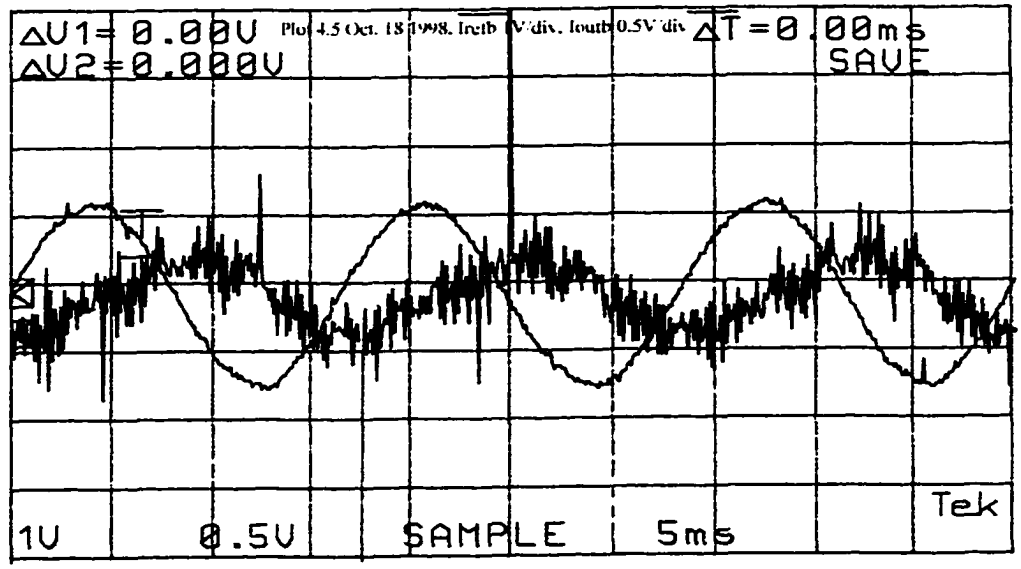

reference current of phase B (nearly sinusoidal trace), 1V/div and output current of phase B 0.5V/div, 5ms/div

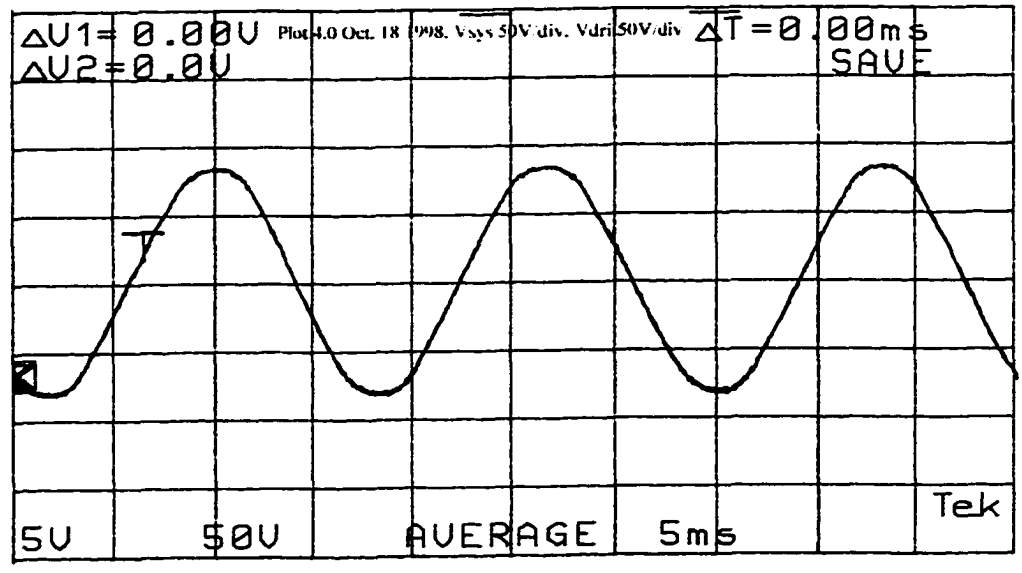

line-to-line voltage of power system (sinusoidal trace) and that of drive system, 50V/div, 5ms/div

Figure 3.4: PWM inverter wave forms at $V_{DC} = 346VDC$, $I_{DC} = 1.5ADC$, $V_{L-L}^{sys} = V_{L-L}^{drive} = 245VAC$, $I_{sys} = 4.5AAC$, $P_{sys} = 0kW$, (with output filter, connected to power system with the conditions of Figure 3.3).

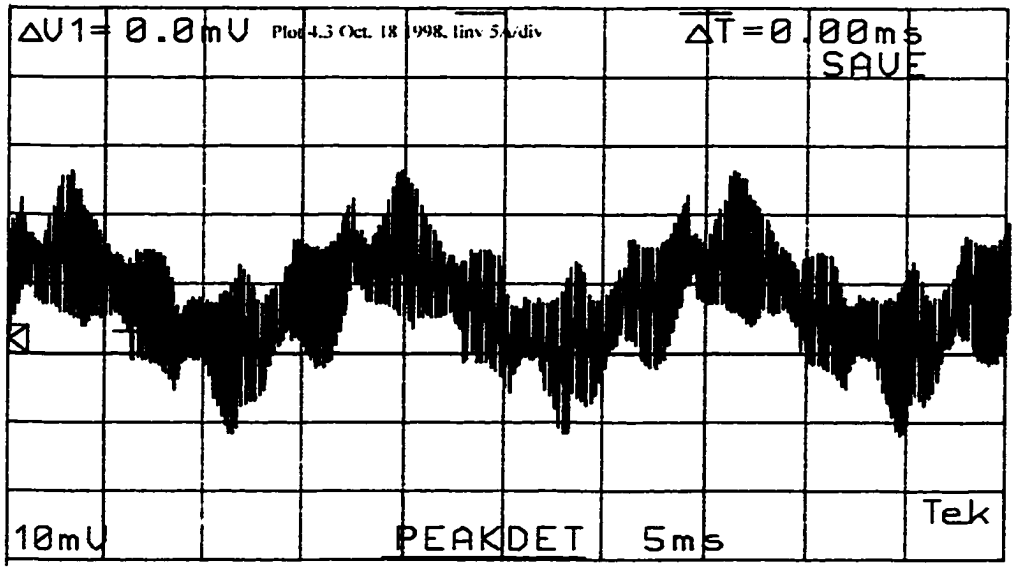

output current of inverter 5A/div, 5ms/div

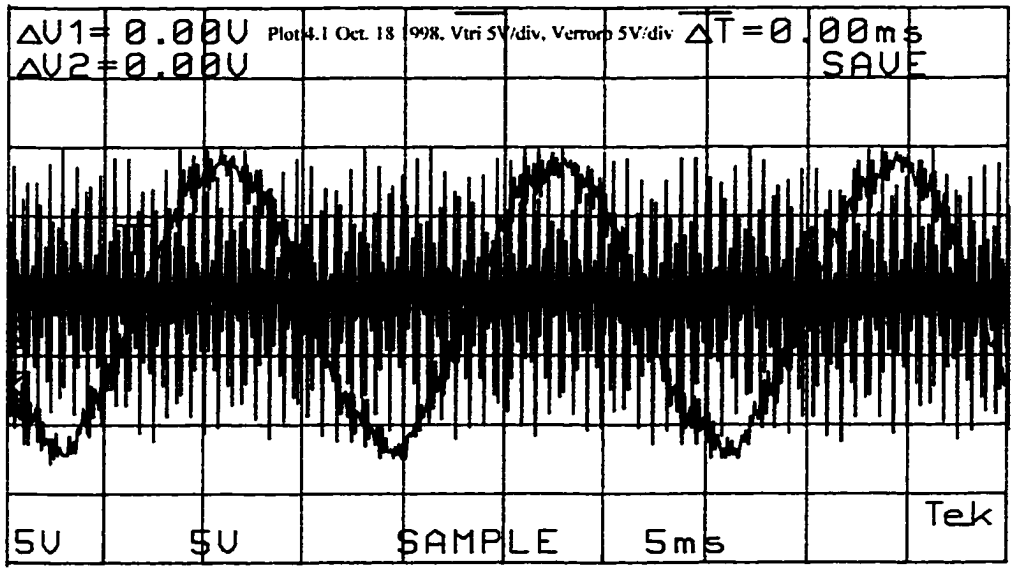

triangular voltage and error voltage of phase B
(nearly sinusoidal trace) 5V/div, 5ms/div

Figure 3.4: continued.

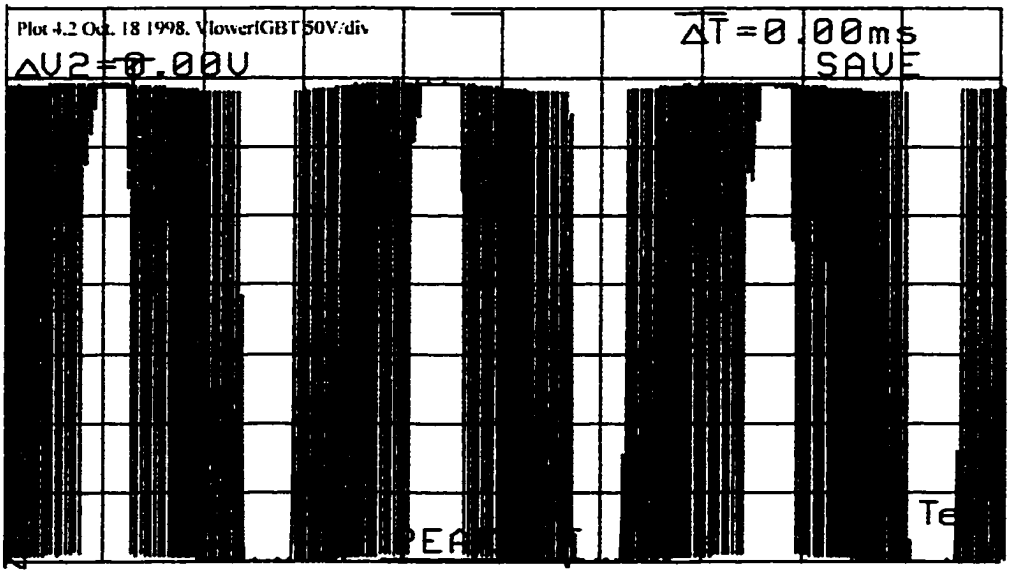

voltage across one of the lower IGBTs of the inverter 50V/div, 5ms/div

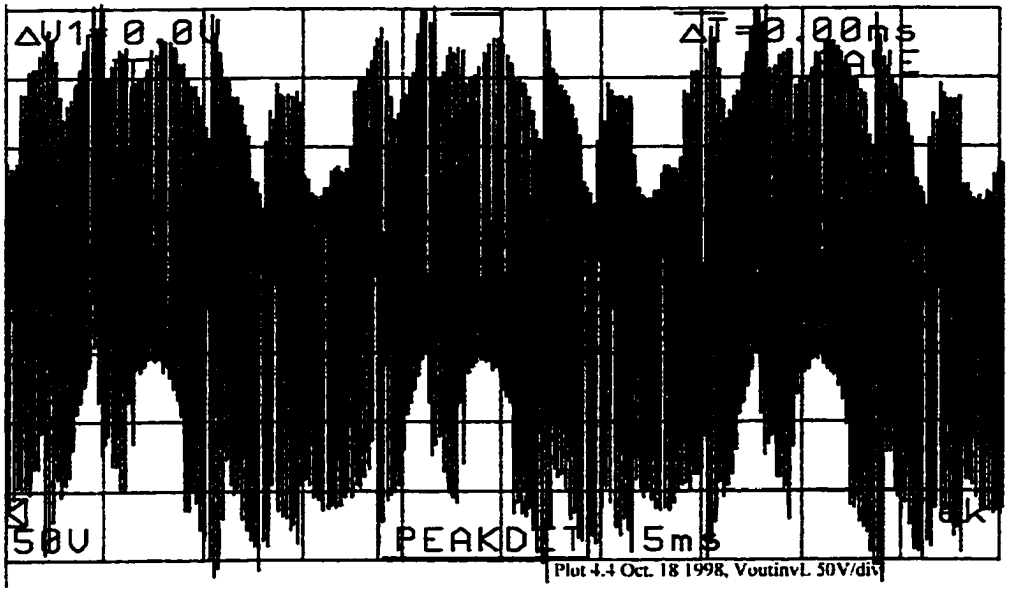

voltage across one of the output inductors of inverter 50V/div, 5ms/div

Figure 3.4: continued.

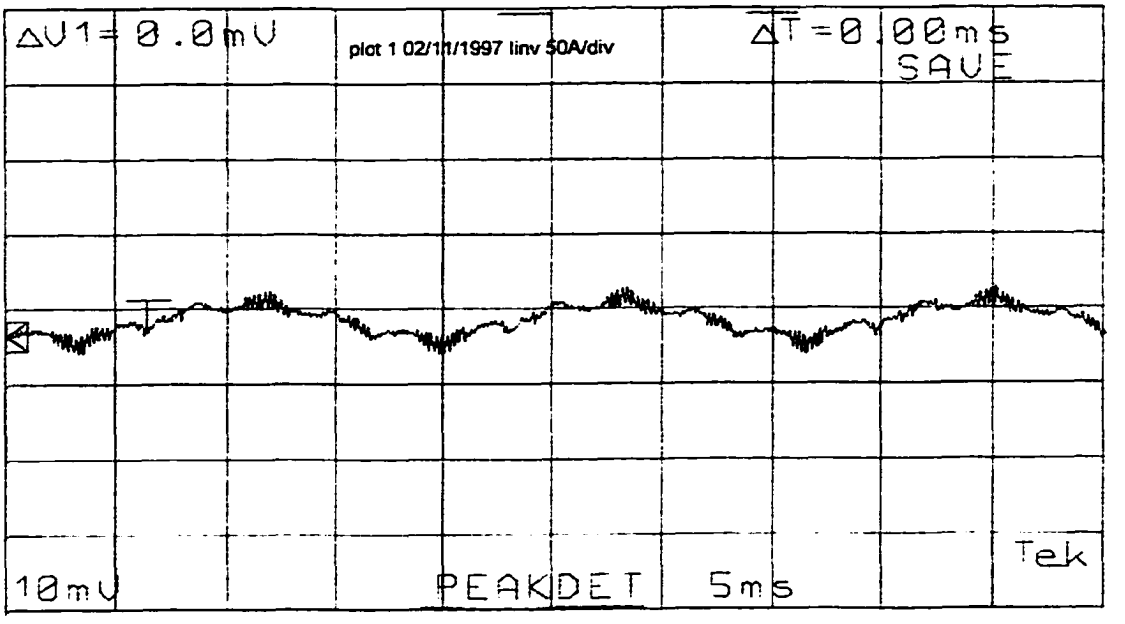

(a)

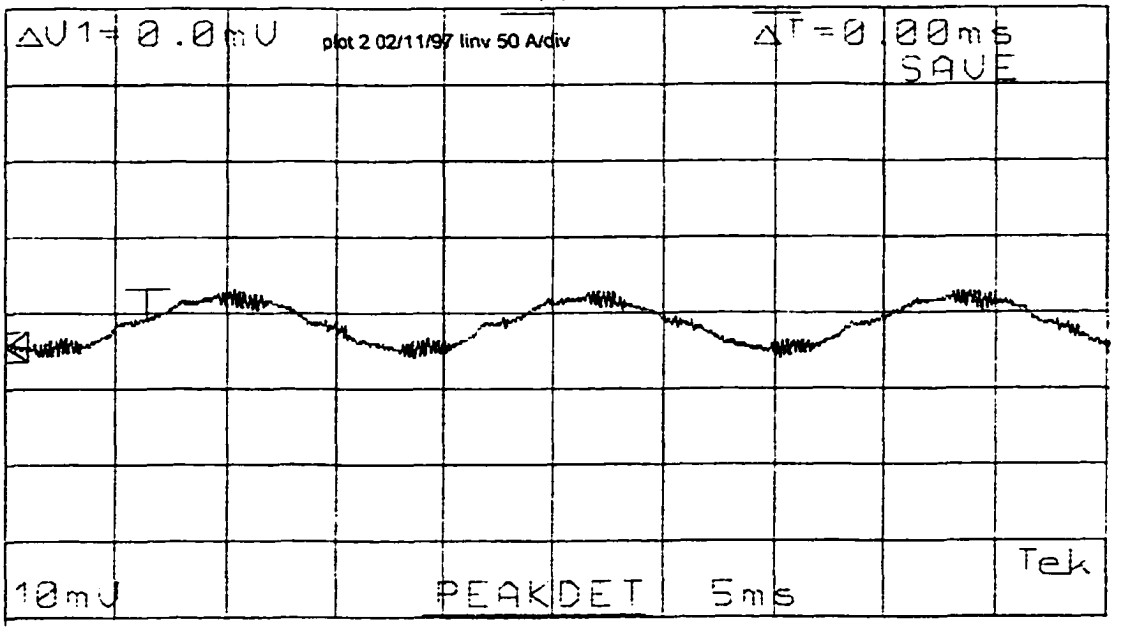

(b)

Figure 3.5: (a) Inverter output current (with filter); before connecting to power system, (b) right after connecting to power system, floating on system, 50 A/div, 5 ms/div.

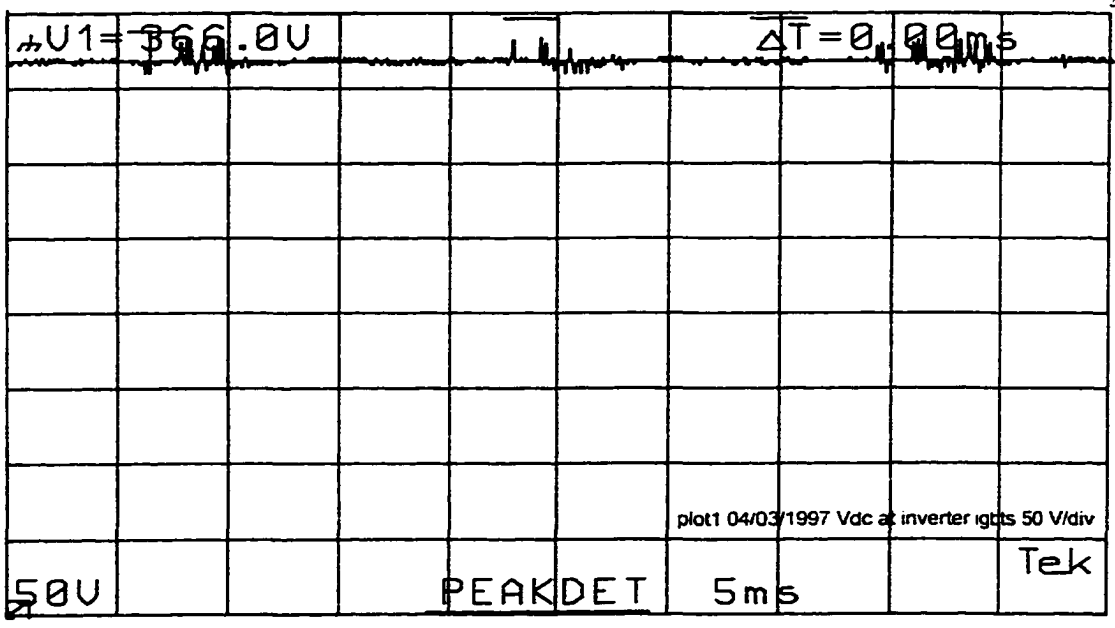

Figure 3.6: Input DC voltage of the inverter. 50 V/div. 5 ms/div.

contains much less switching harmonics ($6kHz$) at no load and $24kHz$ at full load. This can be explained by the fact that the high frequency, low-loss, ceramic capacitors short circuit the switching harmonic voltages at the input of the inverter. Figure 3.7 shows the adjustment of the phase of the reference current signal of one of the phases, by use of a phase shifting transformer. The signal in the center corresponds to unity displacement-factor operation; the one to the left of it is for lagging power[†] factor, and leading power factor is obtained with that on the right. Figure 3.8 shows the output line current of the inverter feeding $25kVA$ to the utility system at a somewhat leading power factor. The Fourier analysis of the output current wave form yields a THD of 5.5% ($I_{rms} = 64.38A$), with the amplitudes of higher order harmonics as a percentage of the fundamental illustrated in Figure 3.9.

A phase shifting transformer is used to change the power factor by changing the phases of the reference currents, so that leading, lagging and unity power could be adjusted for the currents fed into the utility system. Apparent power S, real power P and reactive power Q are illustrated in Figures 3.10 and 3.11 for different power factors.

[†] It is really the displacement factor, not the power factor.

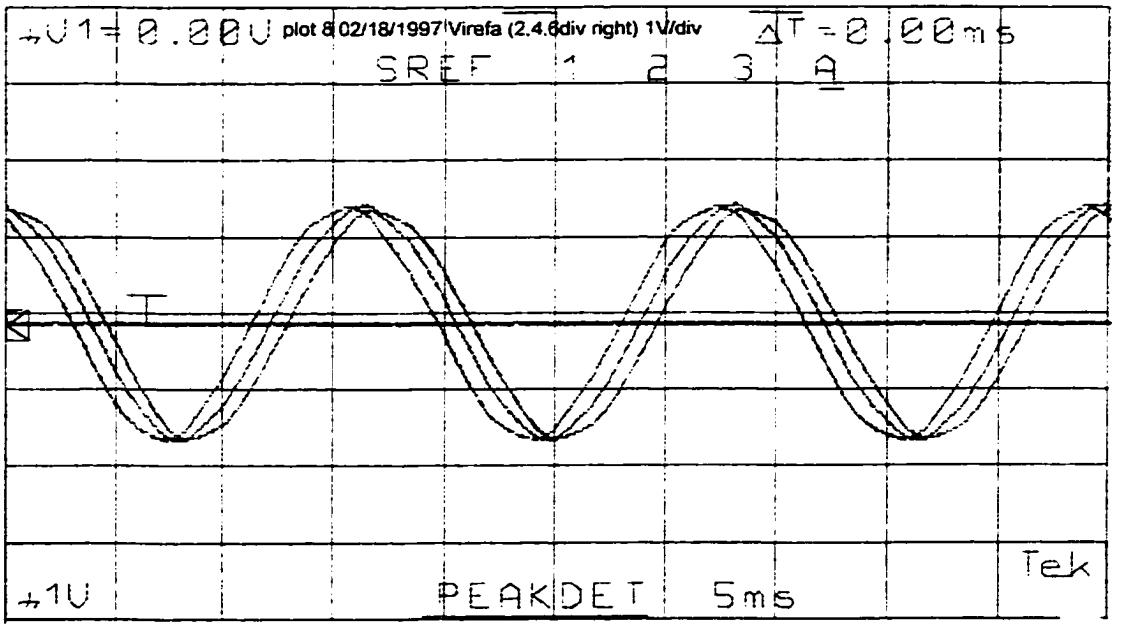

Figure 3.7: Reference current signal of phase A at different phase angles. 1 V/div, 5 ms/div.

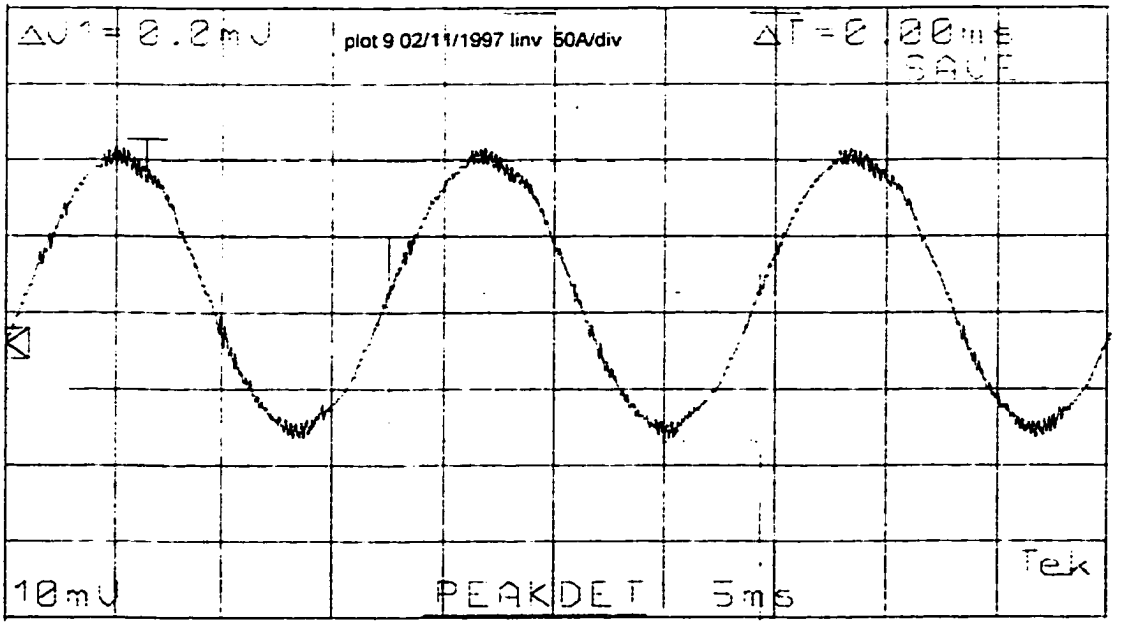

Figure 3.8: Inverter output current (with filter) at full load of 20 kW-25 kVA, 50 A/div, 5 ms/div.

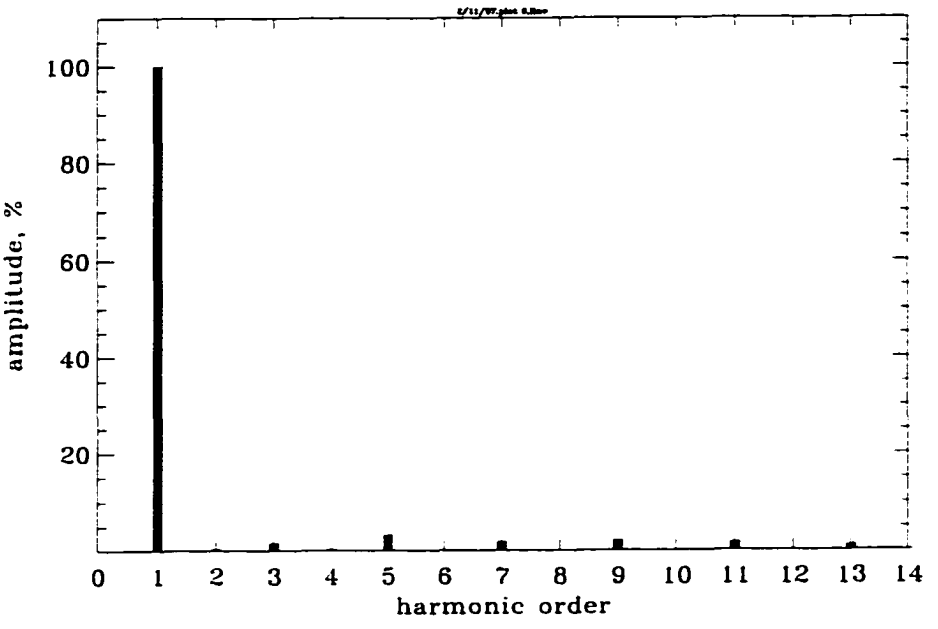

Figure 3.9: Harmonic content of output current of inverter of Figure 3.8.

Note that the leading power factor operation accepts reactive power from the utility system: that is the utility system acts like a resistance and capacitance. Lagging power factor operation delivers reactive power to the utility system; that is, the utility system behaves like a resistance and an inductance. Figure 3.12 shows the real and apparent powers as a function of the rms values of the three reference current (I_{ref}) signals.

3.3 Analysis of PWM-Inverter Operation

Figure 3.13 illustrates the inverter, coupling transformer, harmonic filter, paralleling switch and the utility system. It is well known that the coupling transformer is not really needed for paralleling the inverter with the utility. However, such a transformer increases the reliability of the interconnection because a transformer represents a very low resistance for DC current; and any asymmetry of the gating signals of the inverter can be detected before paralleling, since asymmetries will generate DC currents, even harmonic current components, or for certain conditions instabilities of inverter operation.

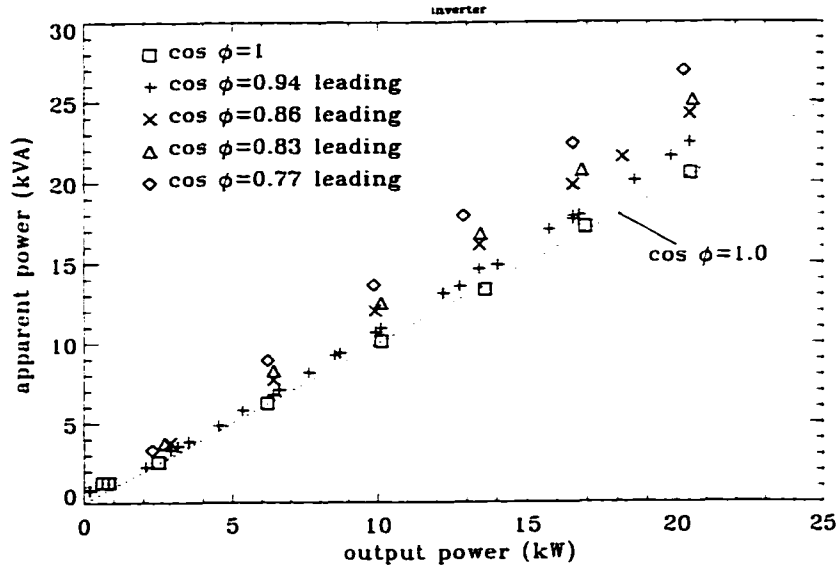

Figure 3.10: Feeding power to the system at different power factors.

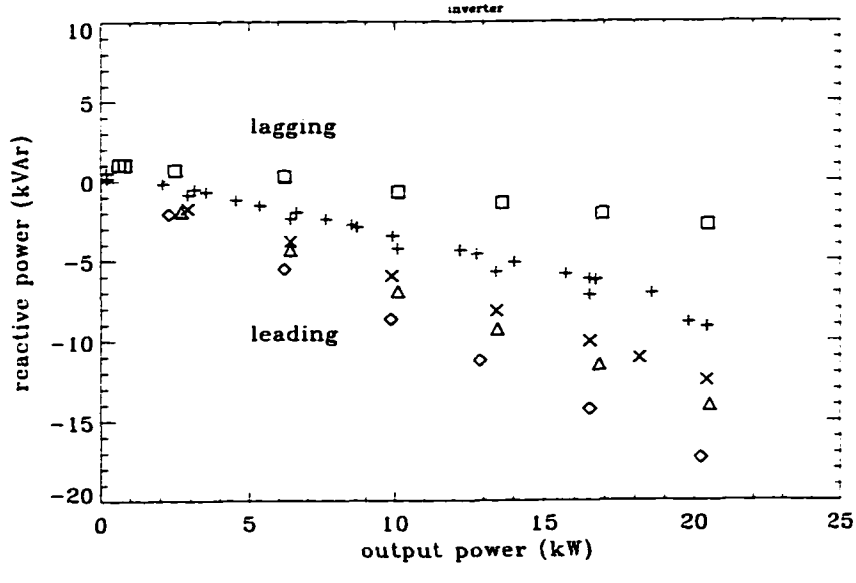

Figure 3.11: Feeding real and reactive power to the system at different power factors.

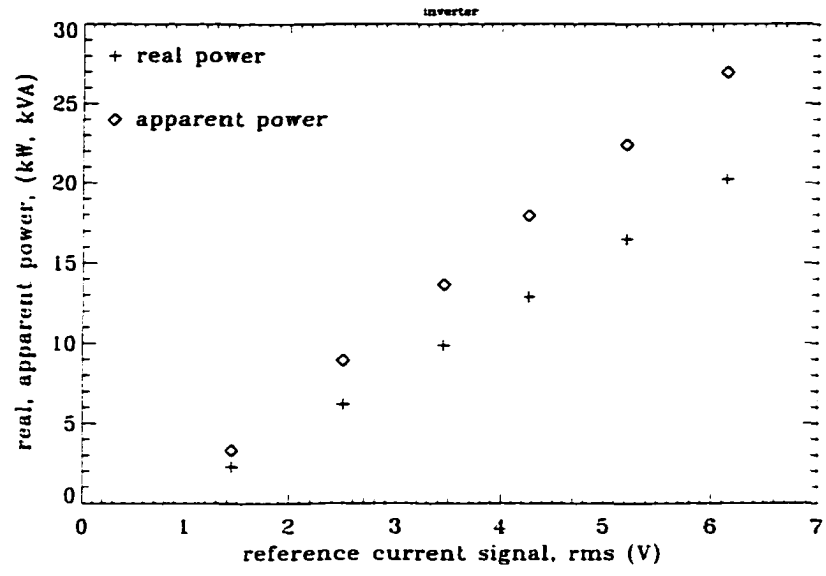

Figure 3.12: Control of apparent and real powers with the amplitude of three reference currents.

PWM inverters are controlled such that the actual current wave shape follows a given reference. This is achieved in this thesis by the turning on and off of the semiconductor switches at the high frequency of $f_s = 5.76kHz$. Therefore, the current of the inverter consists of a fundamental frequency component modulated with a harmonic current of switching frequency. The output current wave form of inverter is depicted in an ideal manner in Figure 3.14.

3.3.1 Analysis at Fundamental Frequency

Analysis at fundamental frequency can be performed, assuming balanced operation of this inverter-utility system, using the single-phase equivalent circuit of Figure 3.15, where R_{tr} and L_{tr} are the resistance and leakage inductance of the transformer, respectively, referred to the primary (inverter) side, and the "primed" quantities are the values referred to the primary side of the transformer; e.g., $R'_S = R_S/n^2$, $E'_{S-N} = E_{S-N}/n$, $I'_S = nI_S$ with the turns ratio $n = 240/208 = 1.15$. The voltage and

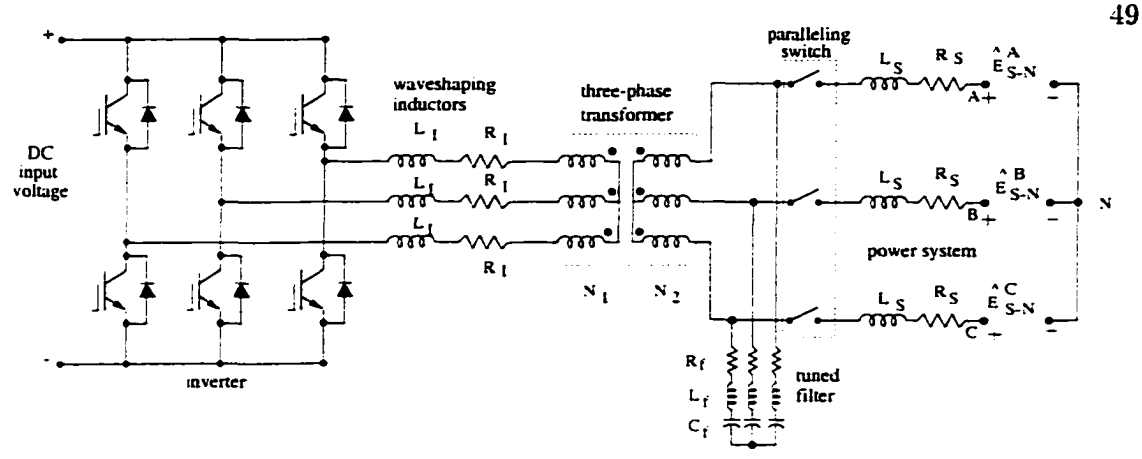

Figure 3.13: Current-controlled PWM inverter-utility system with output transformer and filter.

currents are defined as

$$\hat{E}_{S-N} = \sqrt{2}E_{S-N}\sin(\omega t) \quad , \quad \hat{V}_{PCC-N} = \sqrt{2}V_{PCC-N}\sin(\omega t + \delta)$$

$$\hat{E}_{I-N} = \sqrt{2}E_{I-N}\sin(\omega t + \varepsilon) \quad , \quad \hat{I}_S = \sqrt{2}I_S\sin(\omega t + \theta) \quad ,$$

and the parameter values at $f = 60Hz$ (from Chapter 7) are

$$R_l = 28.3\ m\Omega \quad , \quad L_l = 1.2\ mH$$

$$R_{tr} = 56.25\ m\Omega \quad , \quad L_{tr} = 131.06\ \mu H$$

$$R_S = 16.67\ m\Omega \quad , \quad L_S = 88\ \mu H$$

$$R_f = 4.2\ m\Omega \quad , \quad L_f = 12\ \mu H \quad , \quad C_f = 31\ \mu F \quad .$$

The phasor diagram at the fundamental frequency is shown in Figure 3.16, for the current delivered to the utility system ($\hat{I}_s$) leading the induced line-to-neutral voltage

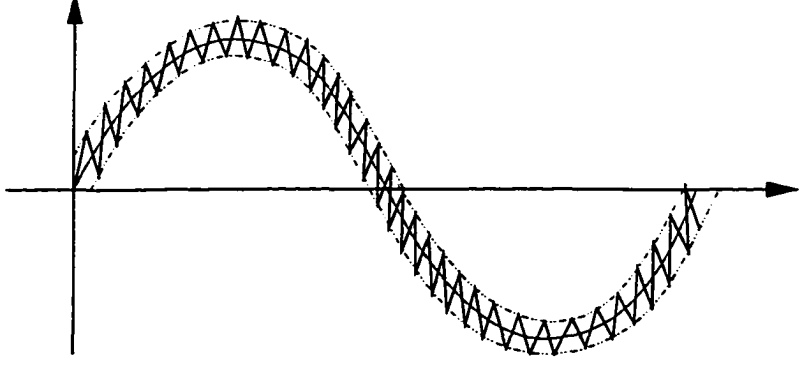

Figure 3.14: Typical output current of current-controlled PWM inverter.

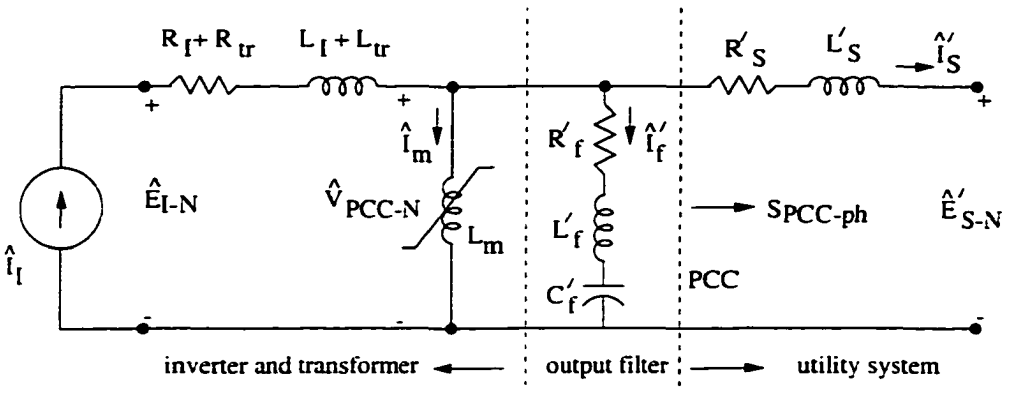

Figure 3.15: Single-phase representation of PWM inverter at fundamental frequency, connected to utility system.

of the utility system by $\theta > 0$ degrees. Note that $\hat{E}_{S-N}$ has been taken as the reference.

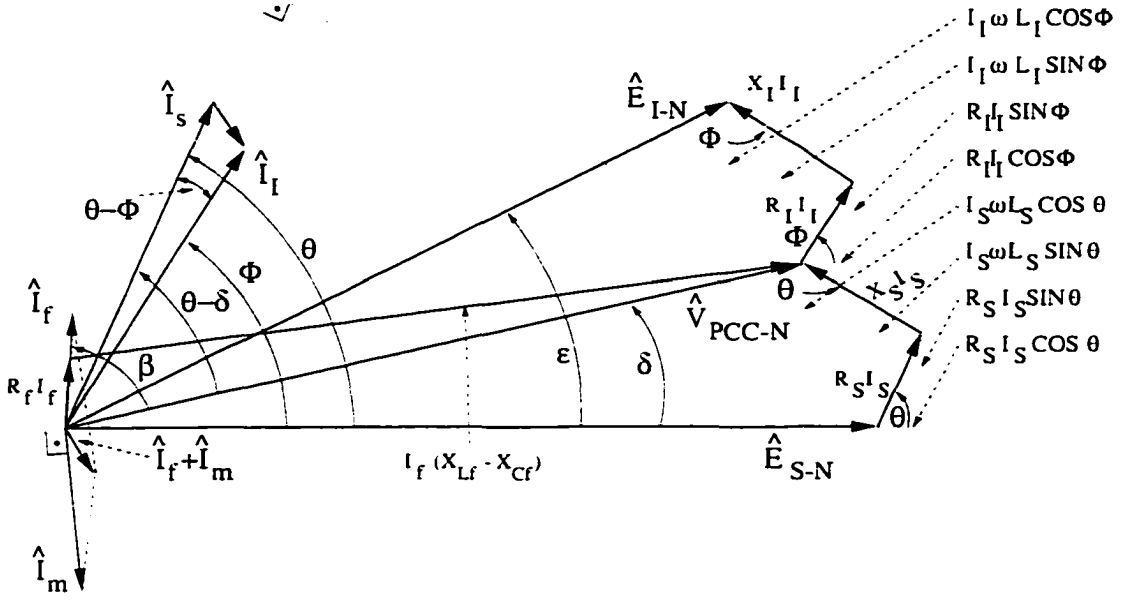

Figure 3.16: Phasor diagram of inverter-utility system including coupling transformer and harmonic filter, not drawn to scale.

From the phasor diagram of Figure 3.16 one gets

$$V_{PCC-N} = \sqrt{(E_{S-N} + I_S R_S \cos\theta - I_S X_S \sin\theta)^2 + (I_S R_S \sin\theta + I_S X_S \cos\theta)^2}\ , \quad (3.1)$$

and

$$V_{PCC-N}\cos\delta = E_{S-N} + I_S R_S \cos\theta - I_S X_S \sin\theta \ . \tag{3.2}$$

$$V_{PCC-N}\sin\delta = I_S R_S \sin\theta + I_S X_S \cos\theta \ , \tag{3.3}$$

where $X_S = \omega L_S$. The apparent power delivered to the utility at PCC is

$$\hat{S}_{PCC} = \hat{V}_{PCC-N}\hat{I}_S^* = P_{Sph} + jQ_{Sph} \ . \tag{3.4}$$

With

$$\hat{V}_{PCC-N} = V_{PCC-N}\ e^{j\delta} \ , \hat{I}_S = I_S\ e^{j\theta} \ .$$

Equation 3.4 becomes

$$P_{Sph} = V_{PCC-N} I_S \cos(\delta - \theta) \ . \tag{3.5}$$

$$Q_{Sph} = V_{PCC-N} I_S \sin(\delta - \theta) \ . \tag{3.6}$$

Use of trigonometric identities

$$\cos(a-b) = \cos a \cos b + \sin a \sin b \ .$$

$$\sin(a-b) = \sin a \cos b - \cos a \sin b \ .$$

gives

$$P_{Sph} = V_{PCC-N} I_S (\cos\delta\cos\theta + \sin\delta\sin\theta) \ , \tag{3.7}$$

$$Q_{Sph} = V_{PCC-N} I_S (\sin\delta\cos\theta - \cos\delta\sin\theta) \ . \tag{3.8}$$

Employing Equations 3.2 and 3.3, real and reactive powers at PCC can be written as

$$P_{Sph} = E_{S-N} I_S \cos\theta + I_S^2 R_S \ , \tag{3.9}$$

$$Q_{Sph} = -E_{S-N} I_S \sin\theta + I_S^2 X_S \ . \tag{3.10}$$

With this consumer definition [31] of real and reactive powers at the point of common coupling (PCC), the current leads if $\hat{I}_S = I_S\ e^{j(\theta-\delta)}$, where $(\theta - \delta) > 0$, and the utility

behaves like a capacitor and resistor combination, resulting in $Q_{Sph} < 0$. For lagging currents, $(\theta - \delta) < 0$ and $Q_{Sph} > 0$, the utility system behaves like an inductor and resistor combination. The total power for the three-phase network is then computed from

$$P_S = 3P_{Sph} \ , \quad Q_S = 3Q_{Sph} \ . \tag{3.11}$$

The output current of the inverter is (from Figure 3.15)

$$\hat{I}_I = \hat{I}_m + \hat{I}_f + \hat{I}_S \tag{3.12}$$

where $\hat{I}_m$ is the magnetizing current of the transformer; its value can be obtained from the voltage across the magnetizing inductance, as illustrated by the nonlinear characteristic of Figure 3.17.

$$I_m = f(V_{PCC-N}) \tag{3.13}$$

Figure 3.18 shows the current phasors of Figure 3.16 in more detailed form. Applying

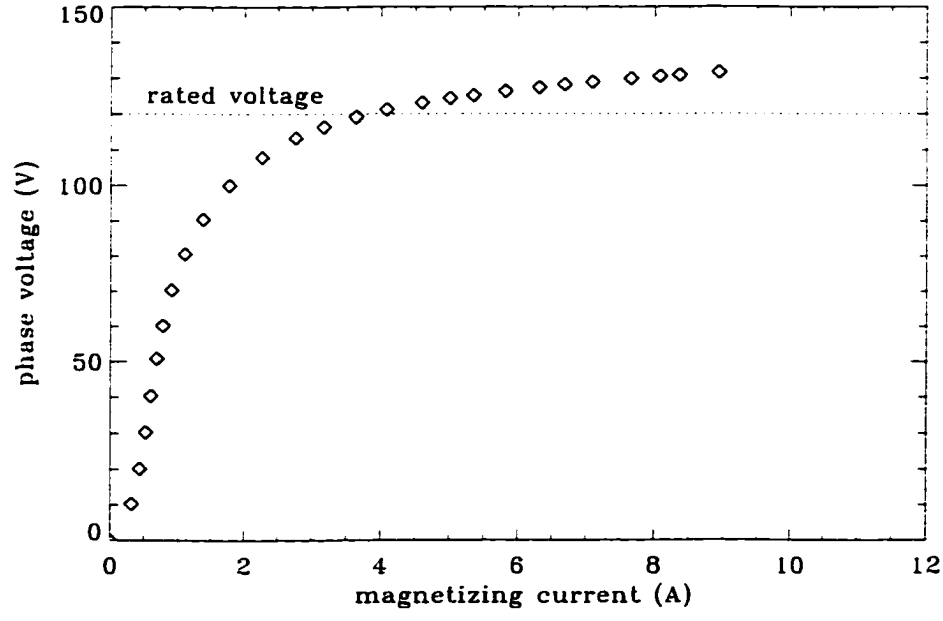

Figure 3.17: Magnetizing current of output transformer as a function of phase voltage.

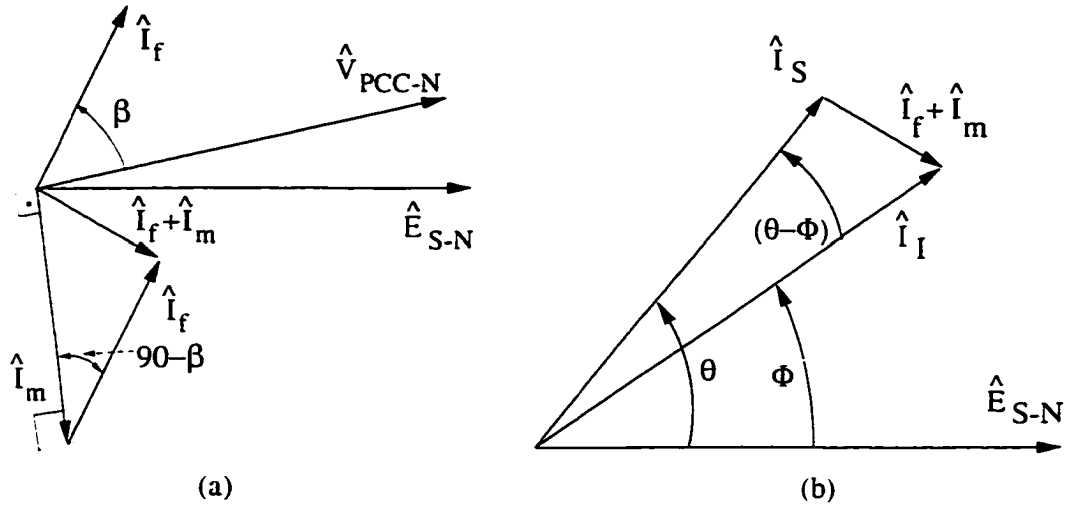

Figure 3.18: Detailed view of current phasors of Figure 3.16.

the "cosine law" to Figure 3.18a,b results in

$$(I_f + I_m)^2 = I_f^2 + I_m^2 - 2I_f I_m \cos(90 - \beta) \tag{3.14}$$

$$(I_f + I_m)^2 = I_S^2 + I_I^2 - 2I_S I_I \cos(\theta - \Phi) \tag{3.15}$$

where

$$I_f = \frac{V_{PCC-N}}{\sqrt{R_f^2 + (X_{Lf} - X_{Cf})^2}} . \qquad \cos\beta = \frac{R_f I_f}{V_{PCC-N}} .$$

Solution of I_I in Equation 3.15 yields

$$I_I^{(a)} = I_S \cos(\theta - \Phi) \pm \sqrt{I_S^2 \cos^2(\theta - \Phi) - (I_S^2 - I_f^2 - I_m^2)} . \tag{3.16}$$

Neglecting the losses (real) of the output transformer and those (real, reactive) of the output filter, the power delivered to the power system at PCC can also be written as

$$\hat{S}_{PCC} = \hat{V}_{PCC-N}\hat{I}_I^* = V_{PCC-N}\ I_I\ e^{j(\delta-\Phi)} , \tag{3.17}$$

and

$$P_{Sph} = V_{PCC-N} I_I \cos(\delta - \Phi) \tag{3.18}$$

$$= V_{PCC-N} I_I (\cos\delta\cos\Phi + \sin\delta\sin\Phi) . \tag{3.19}$$

Simplification of Equation 3.19 using Equations 3.2 and 3.3 yields for the inverter current

$$I_I^{(b)} = \frac{P_{Sph}}{\cos\Phi\,(E_{S-N} + I_S R_S \cos\theta - I_S X_S \sin\theta) + \sin\Phi\,(I_S R_S \sin\theta + I_S X_S \cos\theta)} \quad . \tag{3.20}$$

Equations 3.16 and 3.20 must be identical, due to the assumption of a lossless transformer and output filter. For a given angle, θ, and a current delivered to system, I_S, the transcendental equation

$$F = I_I^{(a)} - I_I^{(b)} = 0 \tag{3.21}$$

can be solved for Φ with the condition of $\theta > \Phi$. Note that $I_I^{(a)}$ of Equation 3.16 has two different solutions: therefore, each must be considered when solving Equation 3.21.

The inverter voltage E_{I-N} can be written from the phasor diagram of Figure 3.16

$$\begin{aligned} E_{I-N}^2 &= (E_{S-N} + I_S R_S \cos\theta - I_S X_S \sin\theta + I_I R_I \cos\Phi - I_I X_I \sin\Phi)^2 \\ &+ (I_S R_S \sin\theta + I_S X_S \cos\theta + I_I R_I \sin\Phi + I_I X_I \cos\Phi)^2 \quad . \end{aligned} \tag{3.22}$$

where $X_I = \omega L_I$ and the angle ε is given by

$$\sin\varepsilon = \frac{I_S R_S \sin\theta + I_S X_S \cos\theta + I_I R_I \sin\Phi + I_I X_I \cos\Phi}{E_{I-N}} \quad . \tag{3.23}$$

The (rms) component of the line-to-neutral inverter voltage is given by [32], [33], [34] as a function of the inverter DC voltage V_{DC}

$$E_{I-N}^{rms} = \frac{V_{DC}}{2\sqrt{2}} \cdot m \quad . \tag{3.24}$$

The rms values of higher-order harmonics can also be calculated with the procedure given in [35]. With modulation index $m = 1$, the DC input voltage of the inverter is then usually computed as

$$V_{DC} = 2\sqrt{2}\,E_{I-N} \quad . \tag{3.25}$$

Table 3.1 lists various quantities (voltage, current, power, and phase angles) at varying phase angles for a given utility-system fundamental current of $I_S = 70A$. Negative phase angles in Table 3.1 correspond to lagging power factors (positive Q_S), while the positive phase angles imply a leading power factor operation (negative Q_S). At lagging power factor, the required DC input voltage of the inverter must be much higher than that at leading power factor. Since the DC voltage of the inverter is maintained constant by the rectifier at about $V_{DC} = 360V$, operation at lagging power factors will not be possible.

3.3.2 Analysis at Switching Frequency

Switching harmonics must be taken into account in order to realistically estimate the minimum inverter input voltage required, so that the inverter currents can follow the given inverter reference currents. The single-phase equivalent circuit of the inverter at switching frequency ($f_S = 5.76kHz$) is shown in Figure 3.19. Since the voltage of the power system has only a fundamental frequency of $60Hz$, the switching-harmonic voltage of the power system is considered to be zero. The magnetizing impedance of transformer (ωL_m) at $f_h = 5.76kHz$ will be 96 times higher than that at $60Hz$: for this reason it can be neglected in Figure 3.19. The component values at $f = 5.76kHz$ (from

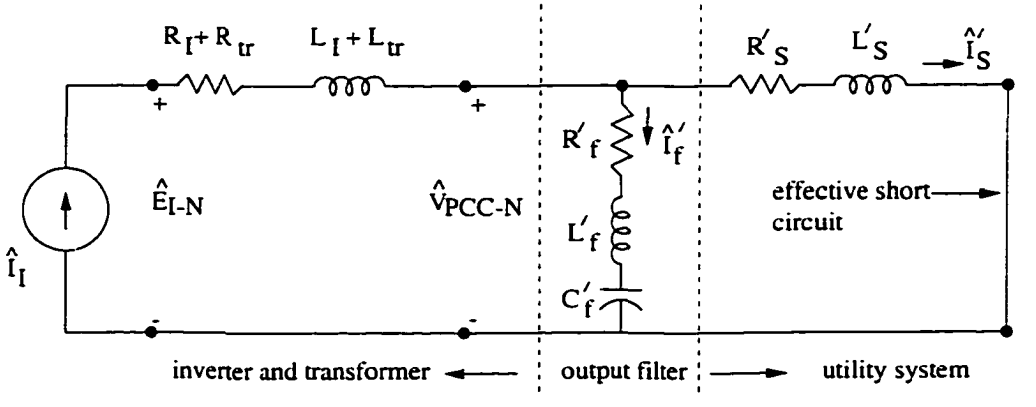

Figure 3.19: Single-phase representation of PWM inverter at switching frequency, connected to utility system.

Table 3.1: Required inverter DC voltage as a function of power factor for given system current of $I_S = 70A$ and rated line-to-line power system voltage of $240V$

θ (deg.)	P_S (kW)	Q_S (kVAr)	S_S (kVA)	V_{PCC-N} (V)	I_m (A)	I_f (A)	I_I (A)	Φ (deg.)	E_{I-N} (V)	δ (deg.)	V_{DC} (V)
-80	5.35	29.45	29.94	124.73	5.16	1.94	86.99	-80.8357	168.99	0.29	478.001
-60	14.95	25.96	29.9563	124.82	5.2	1.94	86.26	-62.37	167.11	0.059	472.67
-40	22.78	19.39	29.91	124.6	5.12	1.93	84.74	-43.63	161.40	0.40	456.51
-20	27.88	10.54	29.8136	124.22	4.96	1.93	82.69	-24.47	152.18	0.70	430.44
0	29.66	0.47	29.66	123.61	4.75	1.92	80.	-4.76	140.04	0.92	396.11
20	27.88	-9.58	29.48	122.87	4.52	1.91	78.14	15.52	125.85	1.03	355.96
40	22.77	-18.43	29.30	122.09	4.32	1.89	76.23	36.36	110.87	1.01	313.58
60	14.95	-25.00	29.13	121.37	4.12	1.88	74.89	57.63	96.94	0.88	274.19
80	5.34	-28.49	28.99	120.80	3.99	1.87	74.23	79.16	86.61	0.63	244.98

Chapter 7) are

$$R_I = 11.70\ \Omega\ .\ L_I = 0.69\ mH$$

$$R_{tr} = 1.43\ \Omega\ .\ L_{tr} = 100.95\ \mu H$$

$$R_S = 16.67\ m\Omega\ .\ L_S = 88\ \mu H$$

$$R_f = 46.7\ m\Omega\ .\ L_f = 10.94\ \mu H\ .\ C_f = 31\ \mu F\ .$$

Figure 3.20 illustrates the phasor diagram of Figure 3.19. Knowing the inverter

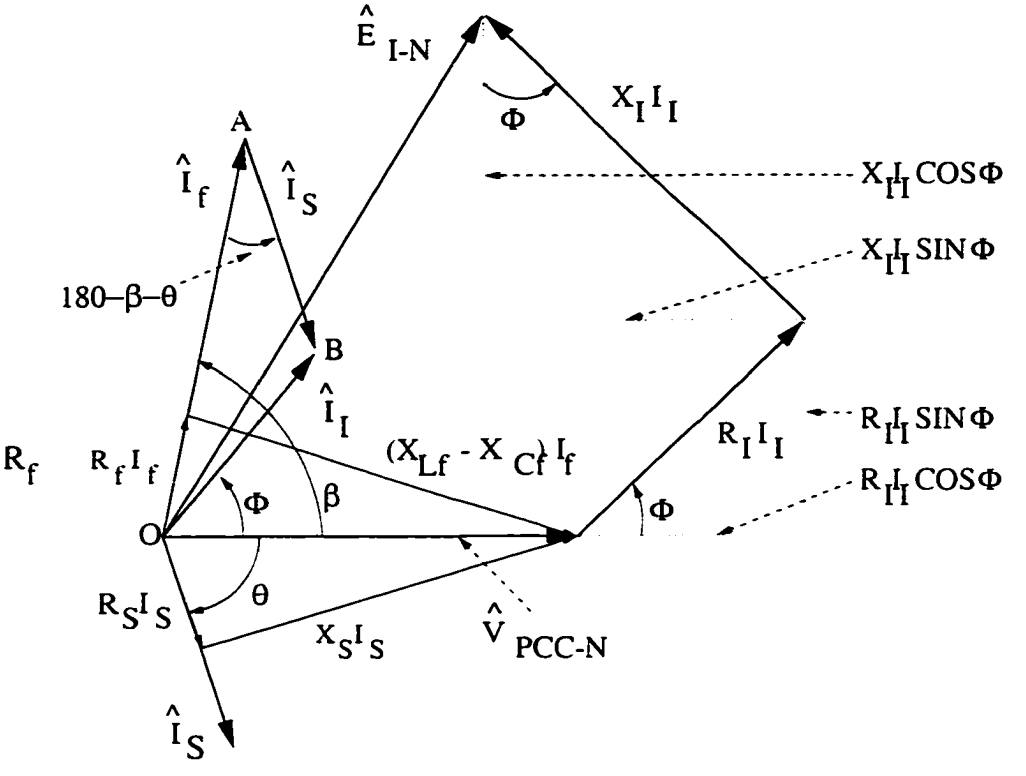

Figure 3.20: Phasor diagram of inverter-utility system of Figure 3.19. not drawn to scale.

current, the system ($\hat{I}_S$) and the filter ($\hat{I}_f$) currents can be calculated as

$$\hat{I}_f = \frac{Z_s}{Z_s + Z_f} \cdot \hat{I}_I \ , \quad \hat{I}_S = \frac{Z_f}{Z_s + Z_f} \cdot \hat{I}_I \ , \tag{3.26}$$

where $Z_s = \sqrt{R_S^2 + X_S^2}$ and $Z_s = \sqrt{R_S + X_S^2}$. The voltage at PCC, the phase angles θ and β are

$$V_{PCC-N} = Z_S I_S \ , \ \cos\theta = \frac{R_S I_S}{V_{PCC-N}} \ , \ \cos\beta = \frac{R_f I_f}{V_{PCC-N}} \ . \tag{3.27}$$

The inverter voltage is equal to

$$E_{I-N} = \sqrt{(V_{PCC-N} + I_I R_I \cos\Phi - I_I X_I \sin\Phi)^2 + (I_I R_I \sin\Phi + I_I X_I \cos\Phi)^2} \quad . \tag{3.28}$$

and

$$\sin\delta = \frac{I_I R_I \sin\Phi + I_I X_I \cos\Phi}{E_{I-N}} \quad . \tag{3.29}$$

The phase angle Φ of inverter current I_I can be determined by applying the "sine law" to the OAB triangle of Figure 3.20

$$\Phi = \beta - \arcsin\left[\frac{I_S}{I_I} \cdot \sin(180^o - \beta - \theta)\right] \tag{3.30}$$

Using the inverter current of $I_I = 3.24Arms$ at $f = 5.76kHz$, obtained from measurements (see Figure 3.8), the inverter voltage is $E_{I-N}^{5.76kHz} = 100.8Vrms$.

When the modulation index is larger than 1, i.e., $m > 1$, the fundamental line-to-neutral voltage of the inverter can be written as

$$E_{I-N}^{rms} = \frac{\sqrt{2}}{\pi} \cdot V_{DC} \quad . \tag{3.31}$$

and

$$V_{DC} = \frac{\pi}{\sqrt{2}} E_{I-N} \quad . \tag{3.32}$$

The DC voltage of the inverter must also supply the harmonic voltage drop across the output inductor. Then the DC voltage of the inverter becomes approximately neglecting any phase shifts

$$V_{DC}^{total} = V_{DC} + E_{I-N}^{5.76kHz}\ (rms) \quad . \tag{3.33}$$

Figure 3.21 illustrates the feasible operating region of the inverter in the $P_S - Q_S$ plane (see Appendix D for the Fortran program). The "◇" markers indicate the measured values and the ideal (with sufficiently high V_{DC} values) operating curve

is given with "+" markers. The "△" markers are plotted for the cases where the DC input voltage of the inverter, computed from Equation 3.25, is less than $360V$ ($V_{DC} \leq 360V$) while the ones with "□" symbols represent cases computed from Equation 3.33 (fundamental and harmonic) with the above limitation of the DC input voltage. Although the inverter can supply leading current (with respect to voltage) to the power system for a given maximum DC voltage of $360V$, larger DC voltages are required to deliver lagging currents, resulting in lagging power factors. The harmonic voltages increase the required DC voltage resulting in a decrease in the reactive power output of the inverter (supplied to the utility system), as is evident from Figure 3.21.

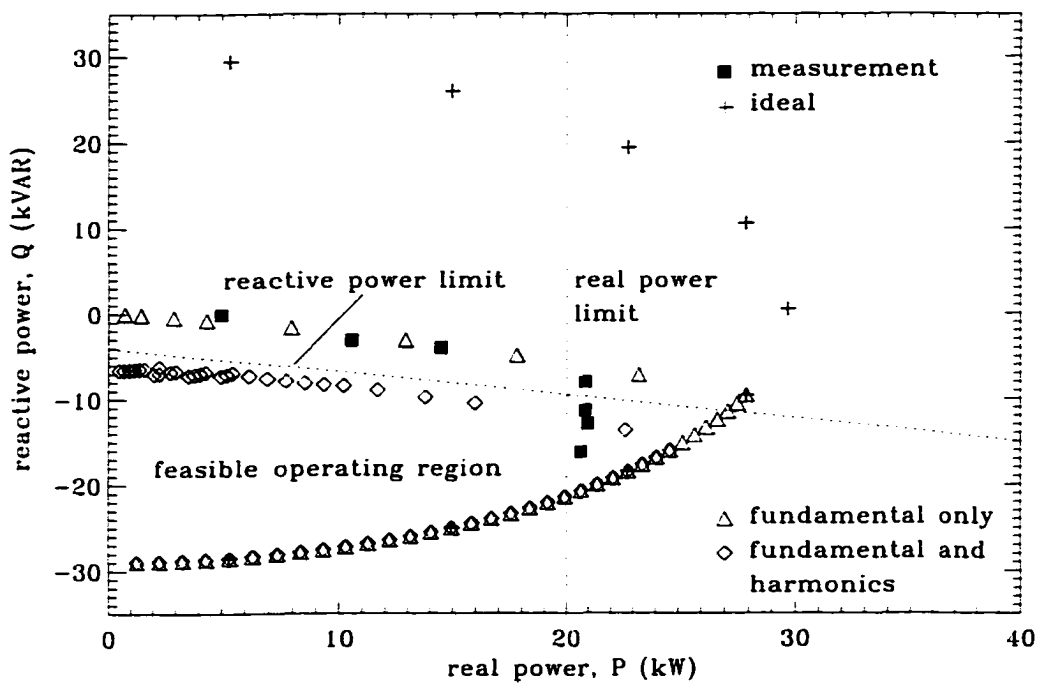

Figure 3.21: Operation in $P_S - Q_S$ plane of inverter as a function of I_S, E_{S-N} and power factor $\cos(\theta - \Phi)$ at a given maximum inverter voltage of $V_{DC} = 360V$.

3.4 Discussion of Results and Conclusions

The reactive-power controllability of a current-controlled PWM inverter depends to a great measure on the DC input voltage of the inverter. Leading power factors (e.g.,

$\cos\theta = 0.5$ leading) can be sustained with a low DC input voltage (e.g.. $V_{DC_{min}} = 360V$); while lagging power factors ($cos\theta = 0.5$ lagging) demand higher input voltages (e.g.. $V_{DC_{max}} = 473V$). Such a dependency penalizes inverters operating at lagging power factors. and therefore it might be best to operate such inverters at about unity power factor. and control the reactive power flow with well-known flexible AC transmission systems (FACTS) [36], [37] [38] devices. such as thyristor controlled reactors and capacitors. The analytically obtained results are confirmed by Pspice simulation [39], and measurements obtained at a 30kVA unit corroborate the theoretical analysis. The efficiency of the current-controlled PWM inverter (including two output transformers) is in the neighborhood of 93% at nominal operation. It has been found that the efficiency is largest at unity-power factor. If the two transformers (see Chapter 4) are excluded. then the inverter efficiency is close to 95%.

CHAPTER 4

JOINT OPERATION OF THE GENERATOR, RECTIFIER, INVERTER AND THE UTILITY SYSTEM

4.1 Introduction

Figure 4.1 illustrates the variable-speed wind power plant consisting of a low-speed permanent-magnet generator, a resonant rectifier and a pulse-width-modulated (PWM) inverter. The permanent-magnet generator operating at low speeds, e.g. $60 - 120rpm$, produces a three-phase variable AC voltage, 300 volts to 450 volts line-to-line [7], at a frequency of $6 - 12Hz$ at below rated output power or at rated power of $20kW$. Because of the low speed operation, the gear box between the wind turbine and the PM generator can be eliminated, resulting in less weight requirements of the tower. Three-phase AC voltage is then fed to the zero-current-switch (ZCS) resonant rectifier operating at a slightly leading input power factor, to produce a nearly constant DC voltage - independent of input voltage variations and load changes. A nominally constant AC voltage synchronized with the utility system 60 Hz, 240 V_{L-L} AC voltage is obtained by using a three-phase, current-controlled PWM inverter. inverter is connected to the 240 V_{L-L} utility a three phase transformer. The amplitude and the phase of the AC current delivered to the system are adjustable through the proper adjustment of the three-phase reference currents.

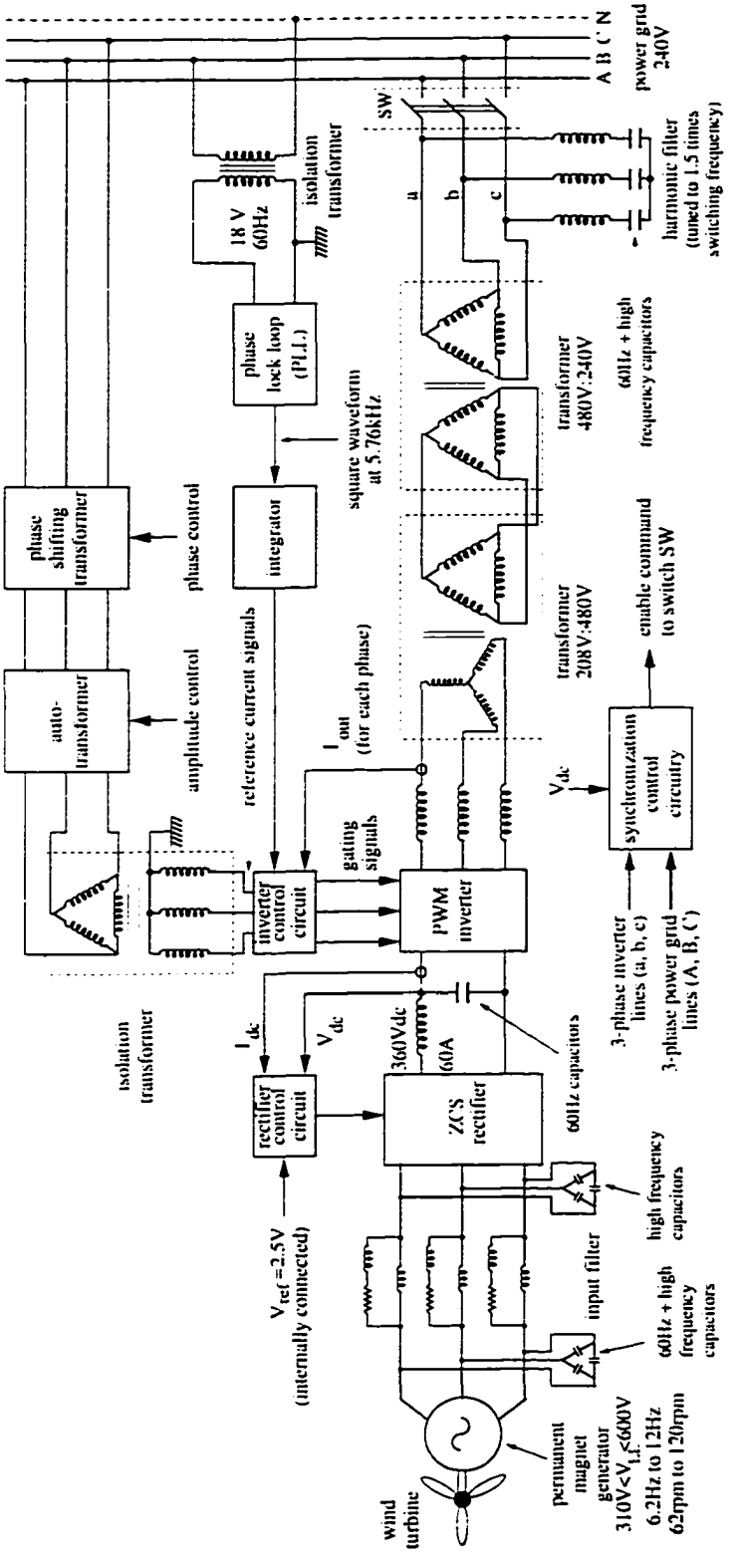

Figure 4.1: Variable-speed wind power plant.

4.2 Permanent Magnet Generator

The generator used in this drive system is a $20kW$ 12-pole longitudinal type PM generator with a speed range of 60 to 120 *rpm*. The permanent magnets (NdFeB) are mounted directly on the rotor. The no-load voltage of the generator is between $300V$ to $600V$ line-to-line. Figure 4.2 shows the field distribution at no load for 2 pole pitches [6]. This machine has been extensively tested in [7] and the efficiencies are between

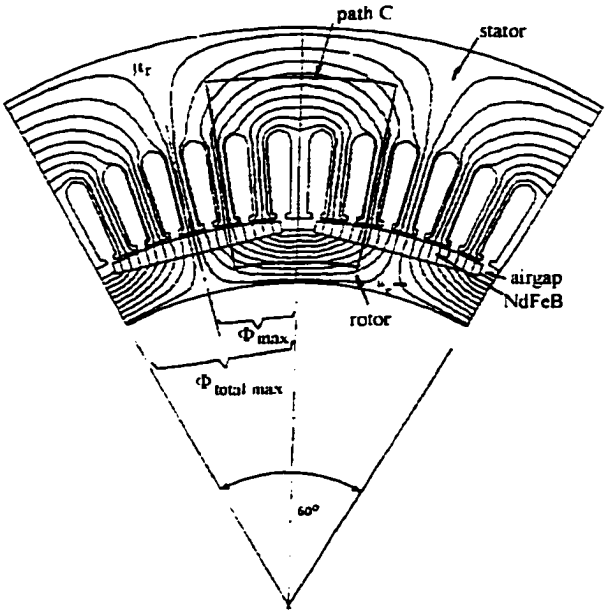

Figure 4.2: Two pole pitches of longitudinal PM machine showing the magnetic flux at no load ($B_{max} = 1T$).

80-95% depending on the load, and the speed of the generator is from 60 to 120 *rpm*. Figure 4.3 shows the feasible operating region of the PM generator corresponding to speeds from $60 - 120$ *rpm*. The measured data points are obtained from [7] and the remaining values are approximated by interpolation. The generator produces about 2.3 kW at a cut-in speed of $n = 70$ *rpm*. Note that the cut-in speed is larger than the minimum permissible operating speed of 62 *rpm*.

To present an alternative design, a transversal permanent-magnet machine is designed [39]. Unlike conventional (longitudinal) machines which have fields that are

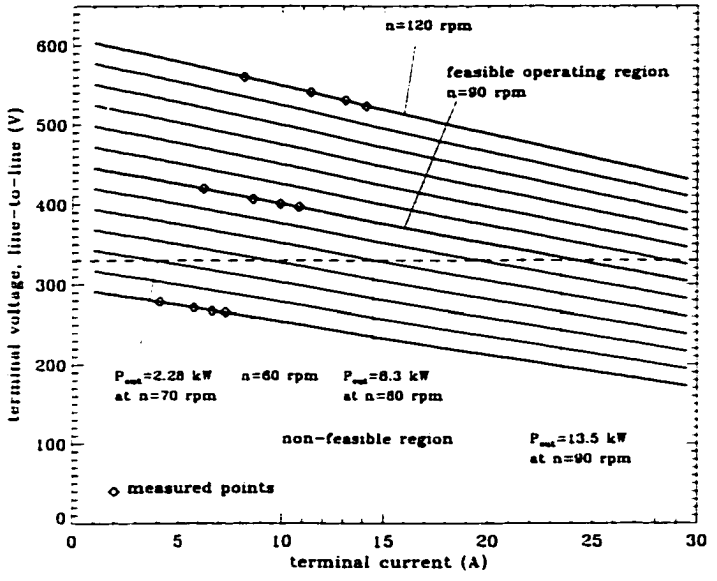

Figure 4.3: Output voltage-current characteristic of permanent-magnet generator at different speeds.

more or less uniform with respect to their axial lengths, with the flux in the same plane as the direction of rotation, in this new type of machine the flux lies in planes perpendicular to the direction of rotation [13]. The advantage of this machine is its ability to produce high torque at low speeds, and the weight-to-power ratio of this design is much lower (about by a factor of 10) than existing longitudinal designs for a rated speed of 120rpm. The field distributions at full load and for short-circuit condition, for one pole pitch, are illustrated in Figures 4.4a, b [40].

4.3 Paralleling of Inverter of the Drive Train with Power System

Before paralleling of the drive train with the power system, the following conditions should be satisfied:

1. The output line-to-line voltage of drive train should be slightly higher (e.g., 265V rms) than that of power grid (e.g., 240V rms), so that there is a positive power flow to the grid right after paralleling,

2. The difference voltage between the voltage of the drive train and that of the power system, that is the phase shift between V_{L-L}^{drive} and V_{L-L}^{system}, should be

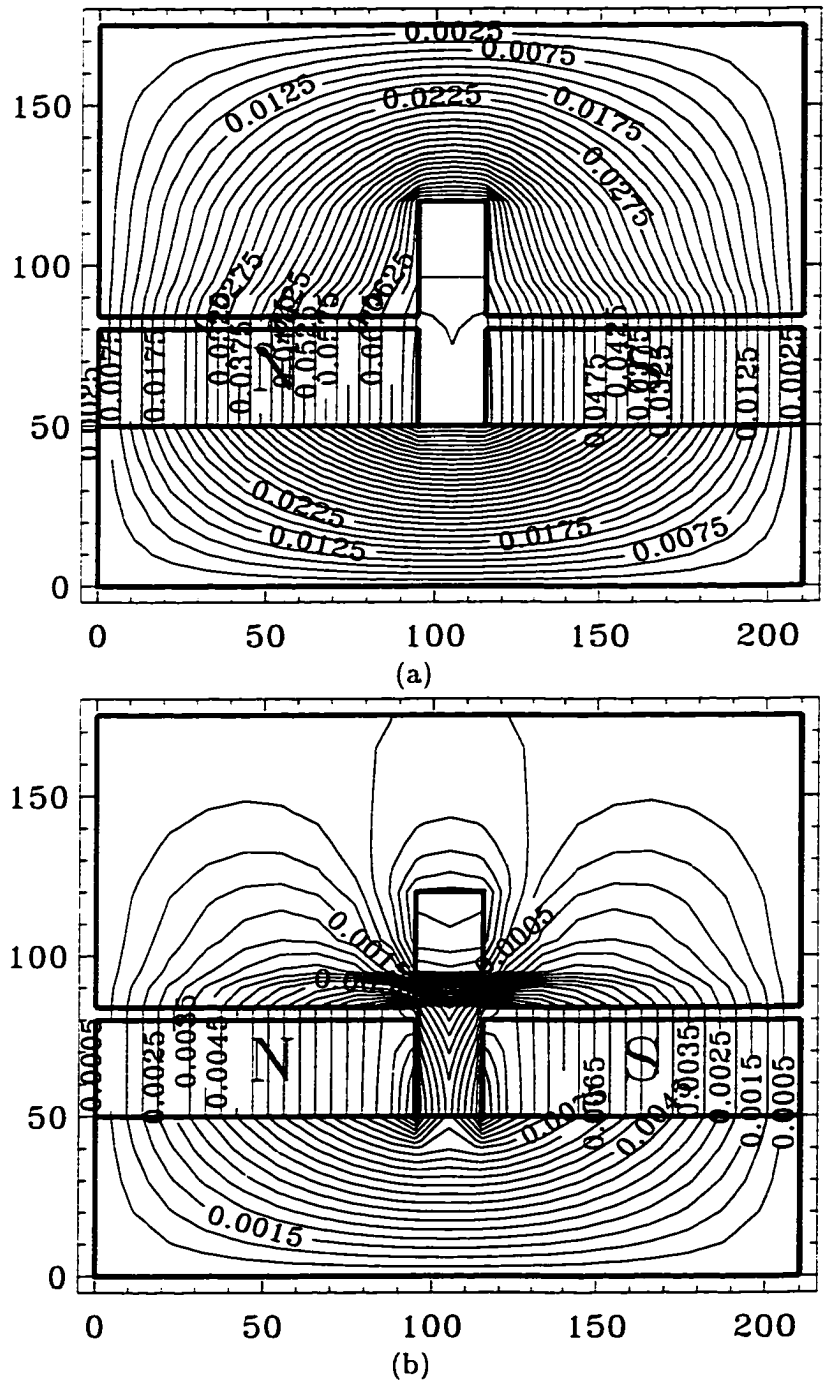

Figure 4.4: Field distribution within one pole pitch of transversal permanent-magnet machine at (a) full load (86A, 40 turns, $B_{max} = 1T$), and (b) short-circuit condition (325A). All dimensions are in mm.

sufficiently small (see Figure 4.5).

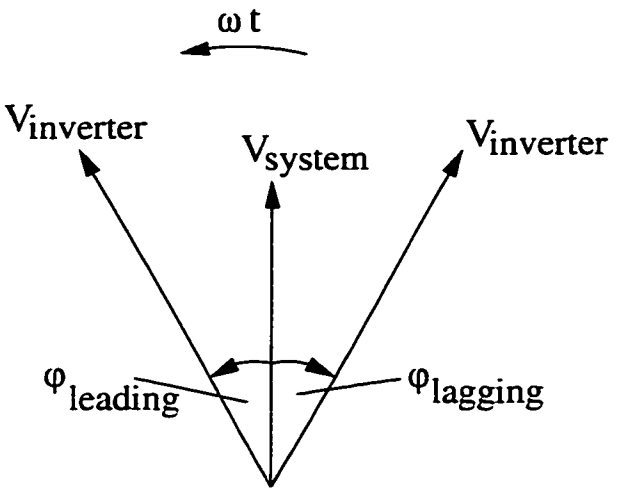

Figure 4.5: Phasor diagram showing the phase angle between inverter and power system voltages.

The above conditions can be achieved by adjusting the amplitudes and phase angles of the reference current signals, respectively. A synchronization control circuit, as shown in Figure 4.6, triggers the paralleling switch SW in Figure 4.1 when the above conditions are met. It also automatically disconnects the inverter from the grid if at least one phase of the power system voltage collapses, or if the DC link voltage drops below a certain value ($\approx 330V\ DC$).

The schematic diagram of this control circuit is given in Figure 4.6, where the individual subcircuits are given in Appendix C. Inputs to the synchronization control circuit are the rectifier DC voltage V_{DC}, 3-phase power grid voltages (A, B, C), and 3-phase drive train voltages (a, b, c, at the output of transformer). The function of each relay can be outlined as follows:

- **Relay R1**: Main connect/disconnect switch relay, (normally open, NO). Relay R1 can be energized after all the conditions are satisfied.
- **Relay R2**: Checks the voltage difference (i.e., phase angle) between power system and drive train (normally closed, NC). It is energized when the phase

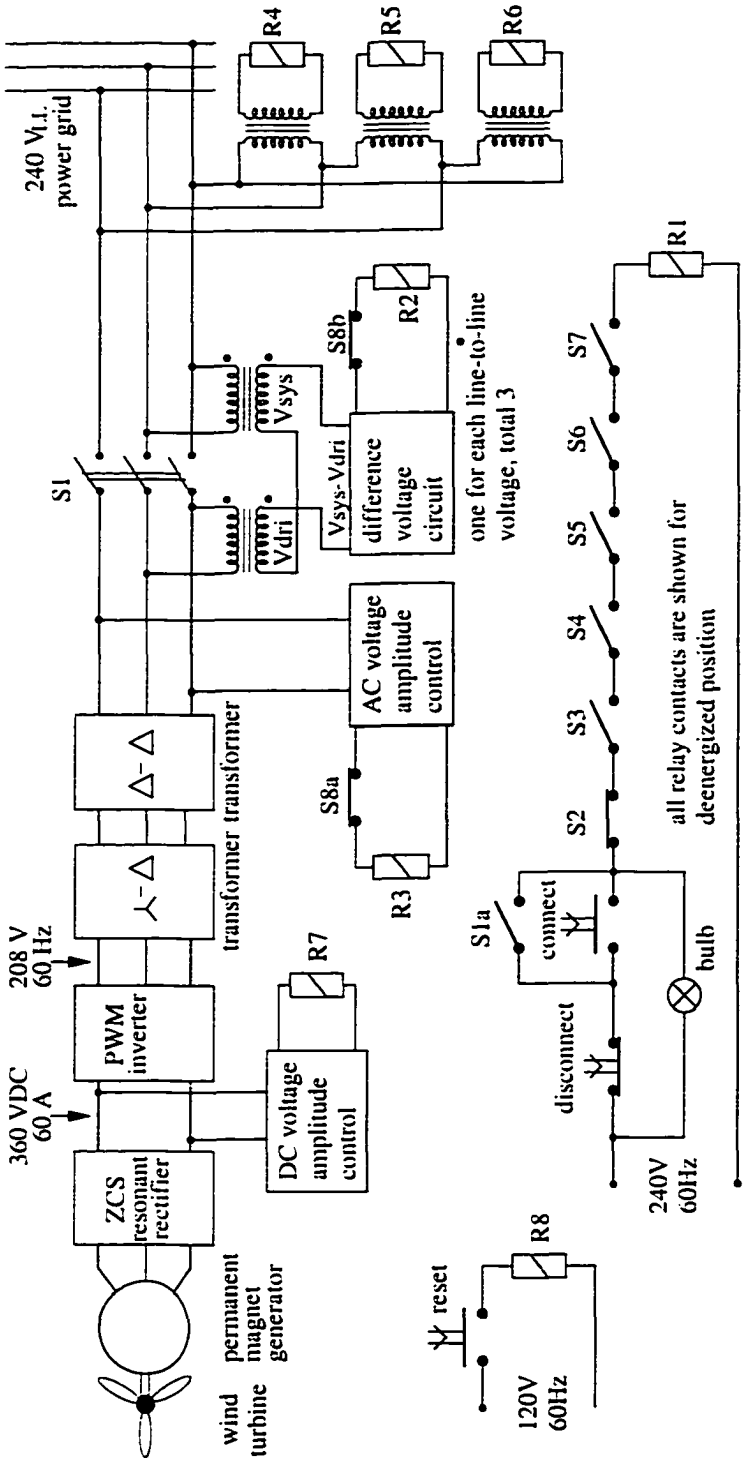

Figure 4.6: Synchronization control circuit.

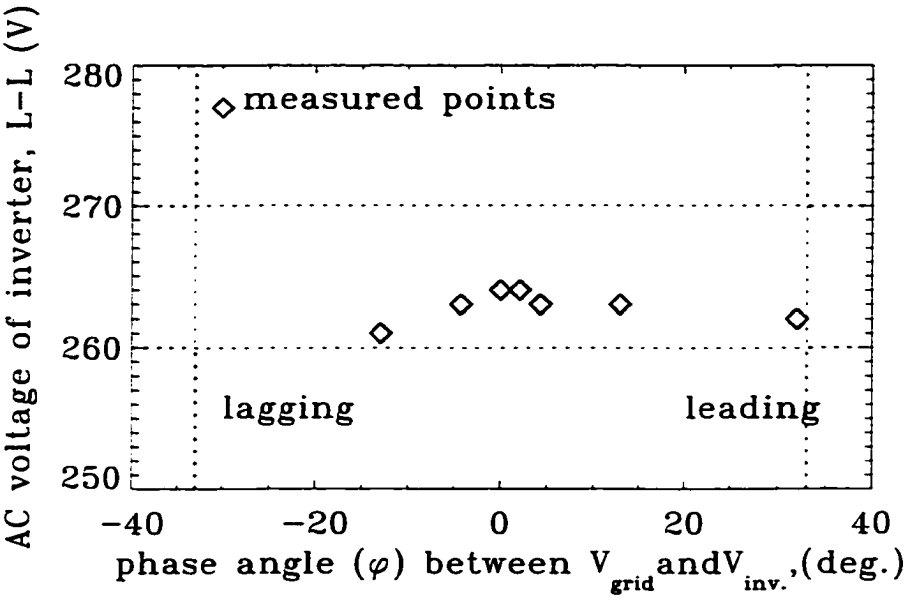

Figure 4.7: Feasible synchronization window for paralleling.

difference is greater than 34^o.

- **Relay R3**: AC output voltage amplitude control of drive train (NO). It is energized when $V_{L-L_{drive}} > 260V$ rms.

- **Relays R4, R5, R6**: Checks the power system voltage (NO). It is energized when line-to-line voltage is $240V$ rms.

- **Relay R7**: DC link voltage amplitude control (NO). It is energized when $V_{DC} > 330VDC$, and deenergized at $V_{DC} < 315VDC$.

- **Relay R8**: Reset relay. Denergizes relays R2 and R3 when activated.

When all the conditions for paralleling are satisfied, the light bulb in Figure 4.6 is on, indicating that the drive train can be paralleled to the power system.

A possible synchronization window is shown in Figure 4.7 as a function of the line-to-line voltage of the inverter before paralleling, and the difference voltage (due to phase angle difference), where the voltage amplitude and phase values as shown permit a successful paralleling to the grid. When the difference voltage is not small, i.e., the phase angle between the two systems is quite large, then there is a high transient current

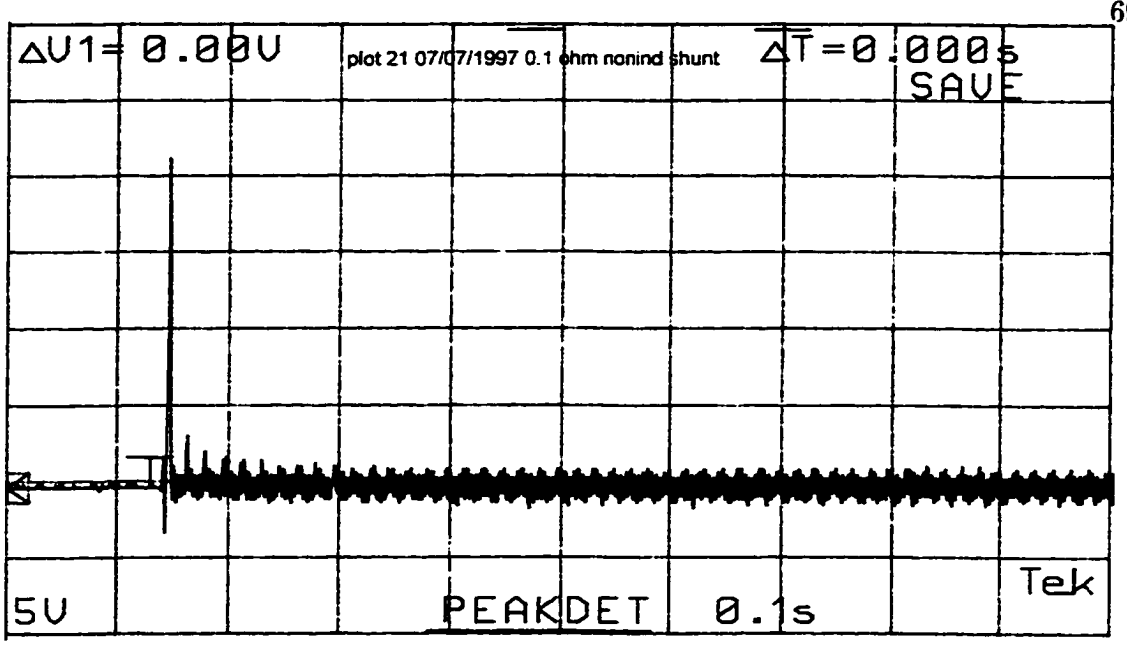

Figure 4.8: Measured transient current at the instant of paralleling to the power system, $\phi = 24^o$ (inverter voltage is leading), 0.1s/div, 50 A/div.

at the moment of paralleling as is depicted in Figure 4.8. The peak value of this transient current increases with the phase angle between the two systems as can be gathered from Figure 4.9. The voltage and current wave forms at PCC are depicted in Figure 4.10 when there is no power flow between the two systems (floating). Figure 4.11 shows the current delivered to the grid at 20 kW at a THD_i of 4.65% and the line-to-line voltage at this condition. The harmonic content of the full-load current is illustrated in Figure 4.12. The efficiency of the entire drive system is about 83%, where the individual component efficiencies are shown in Figure 4.13.

The equivalent circuit parameters of three-phase transformers are determined from open- and short-circuit tests as illustrated in Figure 4.14. Note that both tests are applied to two transformers connected in series. Table 4.1 shows the results of these tests.

The equivalent per-phase resistance is computed from a short-circuit test as $R_{eq} = 0.0799\Omega$ (referred to the voltage $V_1 = 240V$ side). The copper losses of the two transformers, when delivering rated real power of $20kW$ to the utility system at a

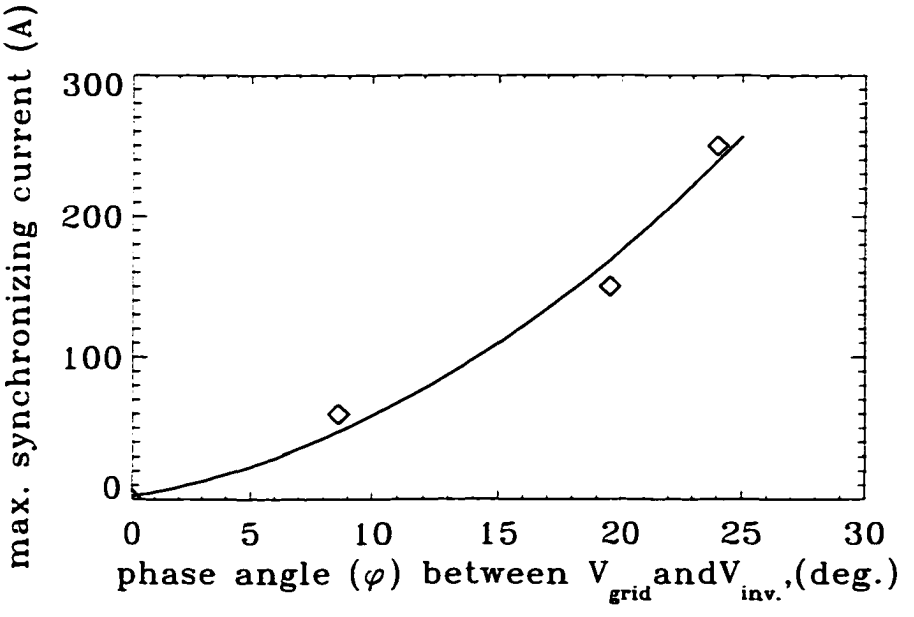

Figure 4.9: Measured maximum synchronizing currents (transient amplitude) as a function of the phase angle. $\varphi = \varphi_{drive} - \varphi_{system}$.

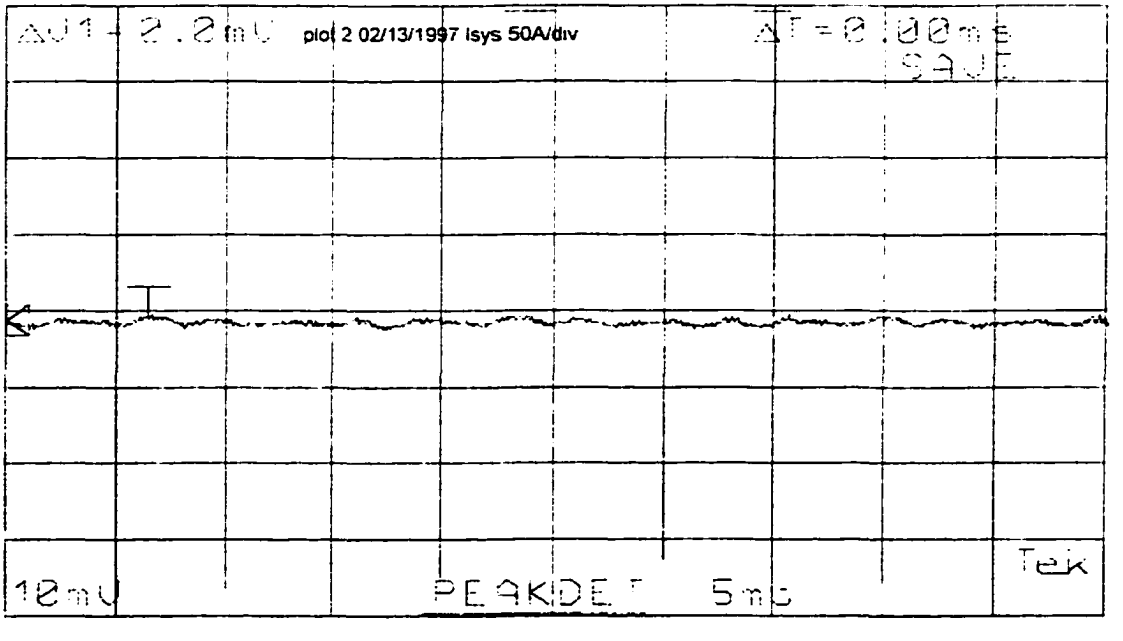

Figure 4.10: Line current at the PCC, floating on the system at $V_{DC} = 327.3V\ DC$, $I_{DC} = 2.5A\ DC$, $V_{L-L}^{sys} = 247V\ AC$, $I_{sys} = 2.0A\ AC$, $P_{sys} = 0kW$. 50 A/div, 5 ms/div.

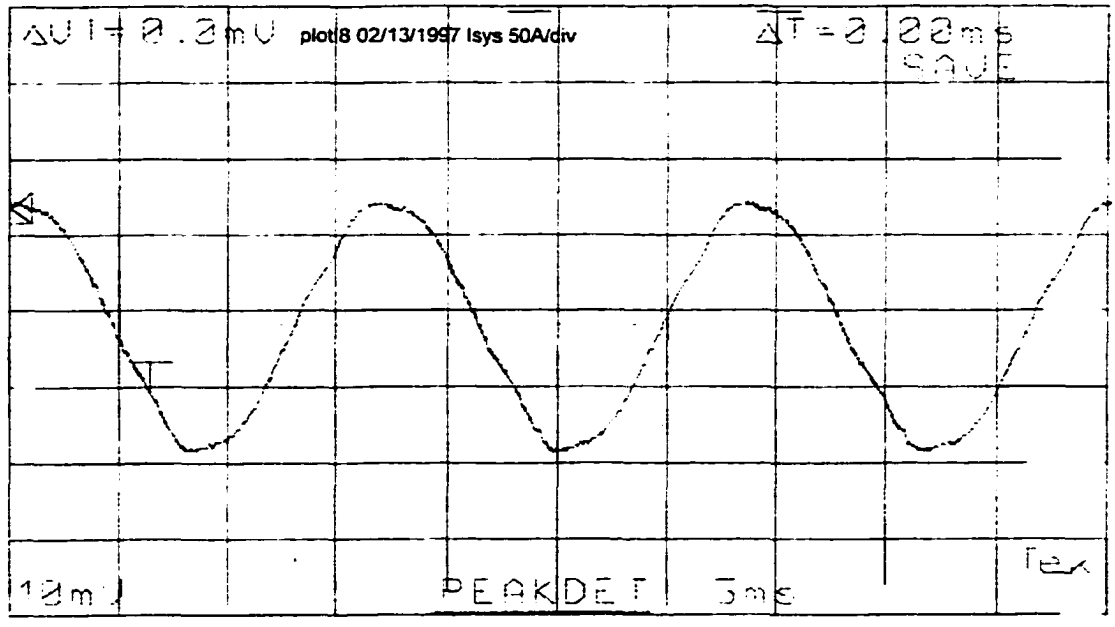

(a)

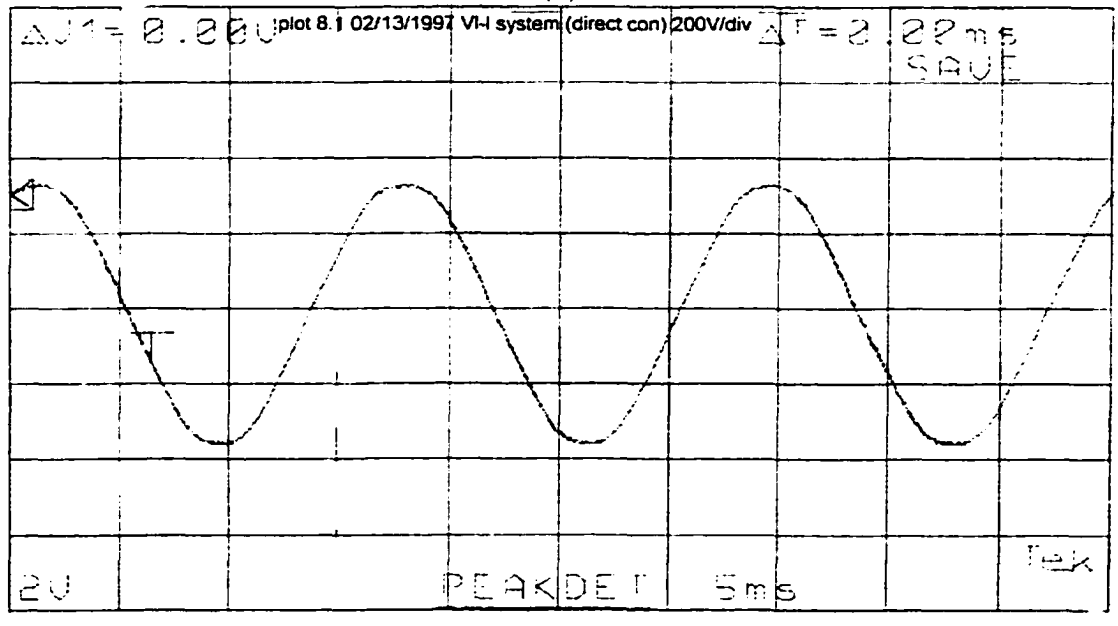

(b)

Figure 4.11: Current delivered to the system, 50 A/div, 5 ms/div (a) and line-to-line voltage, 200 V/div, 5 ms/div (b) at the PCC at $V_{DC} = 349.8V\ DC$, $I_{DC} = 62.5A\ DC$, $V_{L-L}^{sys} = 250V\ AC$, $I_{sys} = 58A\ AC$, $P_{sys} = 20kW$.

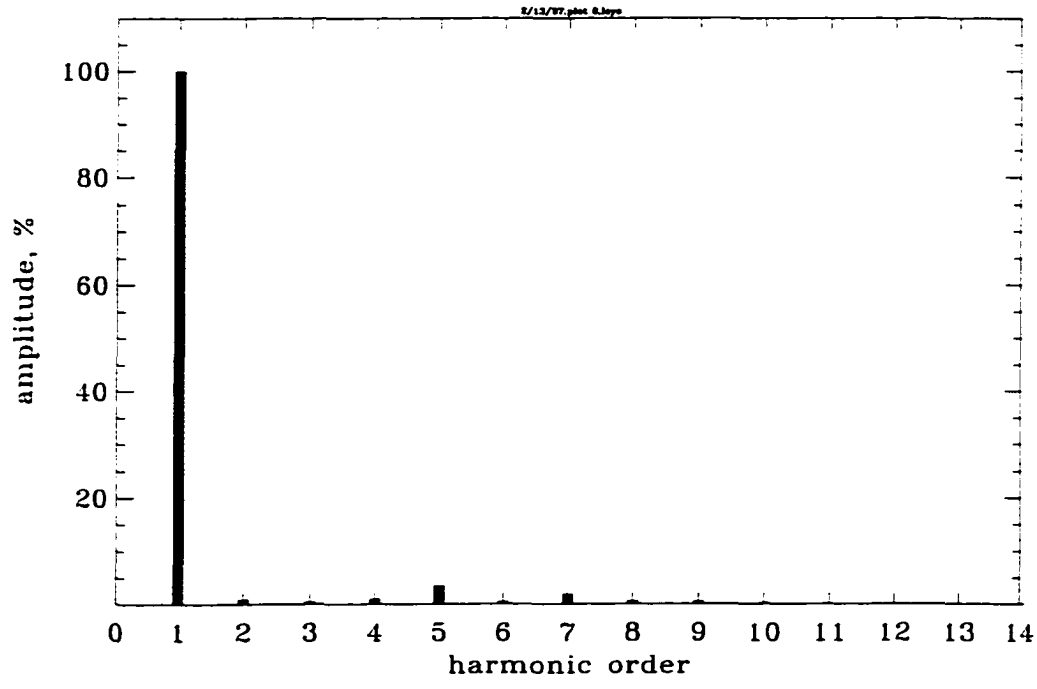

Figure 4.12: Harmonic amplitudes of current fed into the power system as presented in Figure 4.11a.

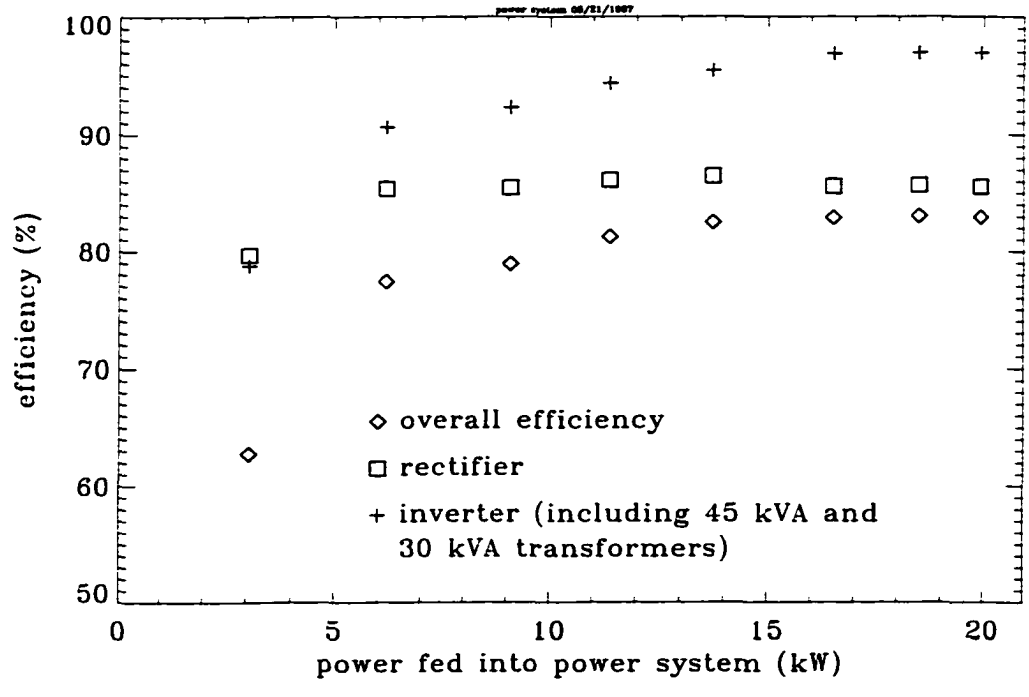

Figure 4.13: Efficiency of entire drive system connected to the utility system.

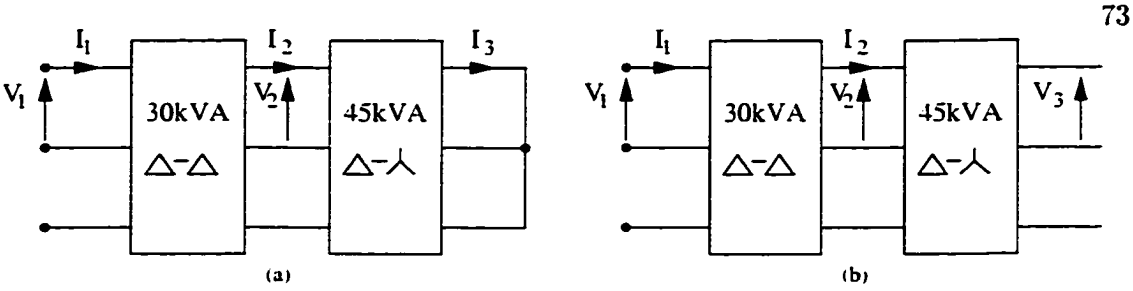

Figure 4.14: Measurement of losses from (a) short-circuit and (b) open-circuit tests of the transformers.

current of $I_1 = 52.95A$ are $P_{cu} = 672W$. The iron core losses of the two transformers will be equal to the losses obtained from the open-circuit test, since the applied voltage to the transformers is the same ($V_1 = 240V$). The total losses of the two transformers at rated power is then

$$P_{loss} = P_{cu} + P_{fe} = 672 + 440 = 1.11kW \quad .$$

The resistance of the output inductor of the inverter at $f = 60Hz$ is $R_{AC_1} = 28.3m\Omega$ and at $f = 5.76khz$ is $R_{AC_h} = 11.7\Omega$. Using the fundamental current ($I_{I_1} = 52.95A$) and harmonic current ($I_{I_h} = 3.24A$) of the inverter, the total loss of this inductor at rated real power of $20kW$ is

$$P^{one}_{loss_{ind}} = I^2_{I_1} R_{AC_1} + I^2_{I_h} R_{AC_h} = 202W \quad .$$

Since there are three inductors, the total losses of the inductors are

$$P^{total}_{loss_{ind}} = 3 \cdot P^{one}_{loss_{ind}} = 606W.$$

Switching losses of the inverter can be estimated to be around $P_{switching} = 300W$. Using the rated real power output ($20kW$) and the switching and inductor losses, the efficiency of the inverter (without the two transformers) is about $\eta = 95\%$.

Table 4.1: Open-circuit and short-circuit results of the two transformers connected in series

	V_1 (V)	V_2 (V)	V_3 (V)	I_1 (A)	I_2 (A)	I_3 (A)	P_{loss} (W)
short-circuit test	4.9	6.7	-	30.71	15.17	37.37	226
open-circuit test	240.83	482.90	196.5	4.33	-	-	440

In the efficiency curve of Figure 4.13. the inverter and including the two transformers have the efficiency

$$\eta = \frac{P_{ACout}}{P_{DCin}} = \frac{19.93kW}{20.55kW} = 96.98\% \quad .$$

The total losses of the inverter and two transformers are then 620W. This number does not make sense because the losses of two transformers are about $1.1kW$. The reason for the discrepancy can be attributed to the subtraction of two large numbers which are close to each other. Even if high accuracy power meters are used (0.5% in this experiment). the losses measured by use of $P_{ACout} - P_{DCin}$ will have a large error as discussed in [40]. The most likely losses of the rectifier. inverter and transformers are itemized in Table 4.2 at $20kW$ output power (last point of Figure 4.13).

Table 4.2: Losses of different components of drive system.

device	component	power loss (W)
Rectifier		
	damping resistor (R_d. total 3)	300
	damping inductor (L_d. total 3)	135
	filter inductor ($L_{f_{in}}$. total 3)	100
	input diodes (total 18)	1200
	IGBT losses	160
	output inductor ($L_{f_{out}}$)	100
	other (snubbers. freewheeling diode. filter capacitors)	87
Inverter		
	output inductors (total 3)	606
	IGBT losses (total 6)	300
Transformers		
	iron-core losses	440
	copper losses	672
Total losses		4100

CHAPTER 5

TRANSVERSAL-FLUX GENERATOR FOR HIGH TORQUES AT LOW SPEEDS

5.1 Introduction

In propulsion applications (e.g.. electric cars, submarines, locomotives) and wind power generating plants, direct-drive trains without mechanical gears are desirable, because mechanical gears are subject to wear and tear. are expensive, and add to the weight of the drive train. Recently, a $20kW$ permanent-magnet generator of conventional longitudinal design has been built and tested [7]. While this machine can indeed deliver the required torque at very low speed (e.g., 30 to $60rpm$), the total weight of this machine (active parts. frame. bearings) turned out to be $587kg$. Such a large specific weight ($29.4kg/kW$) is not acceptable for propulsion and wind power plant applications of wind farm size (MW range), since this excessive weight reduces the mileage in propulsion, and increases the cost of the tower in wind power applications.

To present an alternative design, a transversal flux machine [14, 15] has been investigated, and preliminary calculations confirm that this new transverse flux generator design has much less weight (by a factor of 10); that is, a $300kW$ permanent-magnet generator would weigh $600lbs$. However, such a machine is much more complicated in the mechanical design than a conventional longitudinal machine. The basic feature of such a machine is that the flux spirals around the circumference of the armature coils, meaning that three-dimensional analysis techniques must be employed for the magnetic-field

analysis of such a machine. Significant work with respect to machines with transverse flux has been recently published [13, 41, 42]. Such transverse flux machines are able to produce a high torque at very low speeds, and the overall weight is of one magnitude lower than that of conventional longitudinal machines. The only disadvantage of such machines is their complicated structure from a mechanical point of view and apparantly low power factor.

5.2 Conceptual Design of Permanent-Magnet Machines with Transverse Flux

Recently, work has been published on the design and operation of permanent-magnet machines with transverse flux [13, 41, 42, 43, 44, 45] and it is stated that such a novel machine also has been used as a part of a small wind power plant. The above-mentioned work discusses the design of one and two-phase machines with transverse flux. In order to extract higher powers and to improve the rectification process through the reduction of voltage ripple, transverse flux machines with more than 2 phases are desirable. Figures 5.1, 5.2, 5.3 illustrate the conceptual features of such a transverse flux machine, where Figure 5.1 presents a cross-sectional view within 4 planes, Figure 5.2 illustrates the top view and Figure 5.3 gives the side view of such a permanent-magnet generator.

Longitudinal machines have fields that are axially more or less uniform, making a two-dimensional field analysis sufficient. In contrast, the transverse flux machines have fields in three dimensions, with the magnetic field spiraling around the n (e.g., n=4) armature coils, making a three-dimensional field analysis necessary. There is no doubt that the armature coil cross sections can be made as large as required for a given current density (e.g., $3A/mm^2$ for air cooling) and the maximum flux densities within the air gap of the machine can be in the range of $B_{transversemax} = 1.4T$, as compared to that of a longitudinal machine with $B_{longitudinalmax} = 0.9T$. The only drawback of such

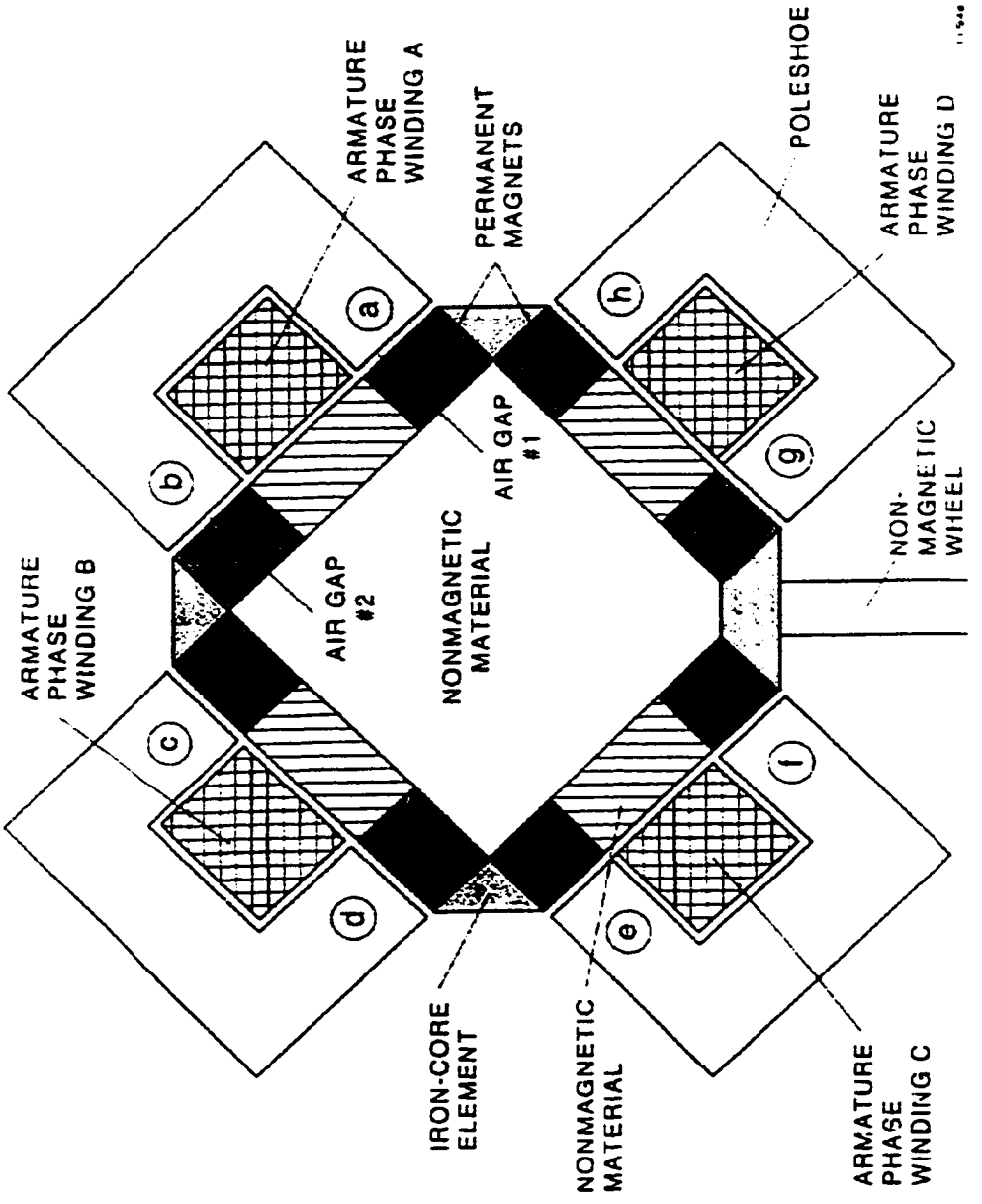

Figure 5.1: Cross-section of a transversal-flux generator.

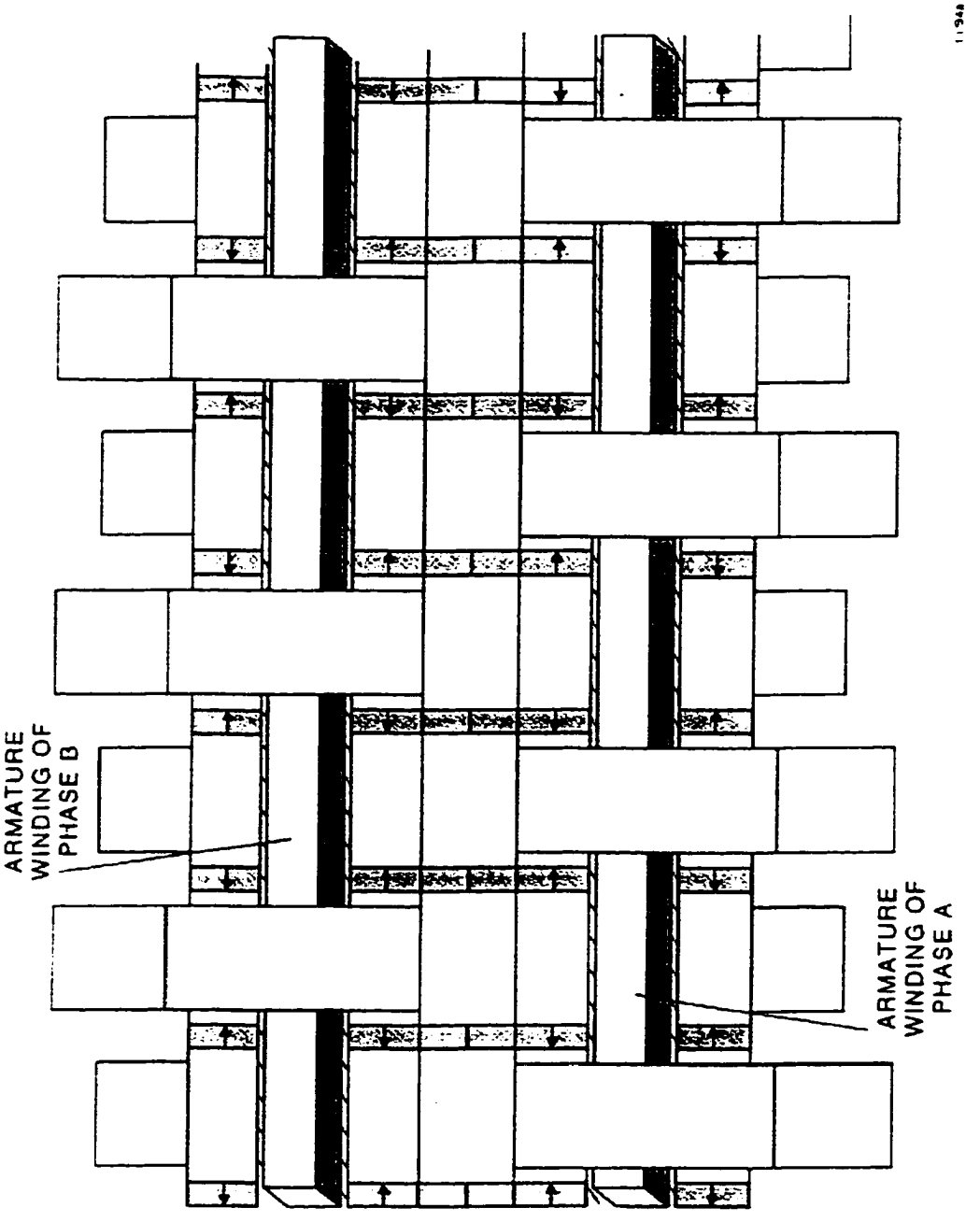

Figure 5.2: Top view of a transversal-flux generator.

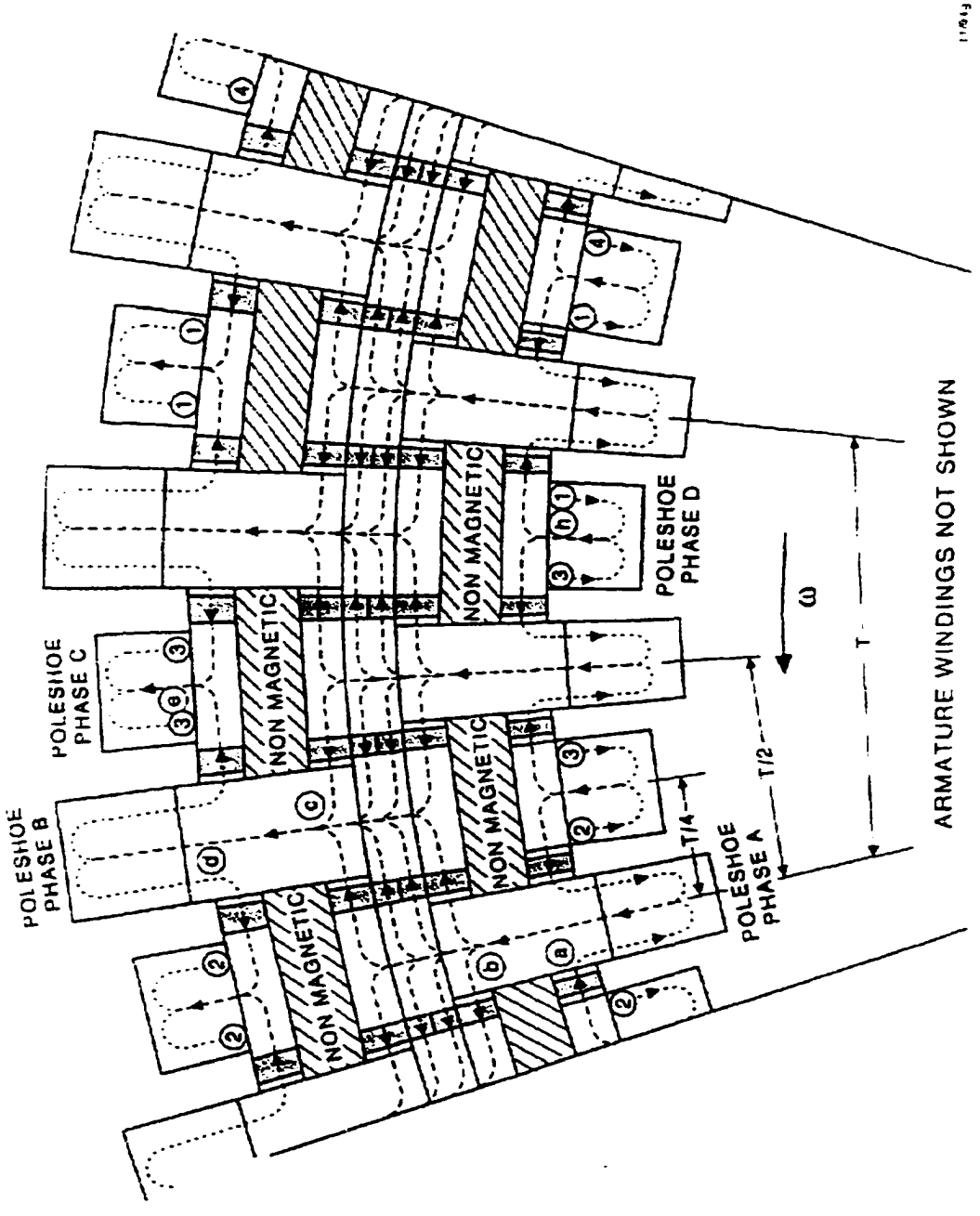

Figure 5.3: Side view of a transversal-flux generator.

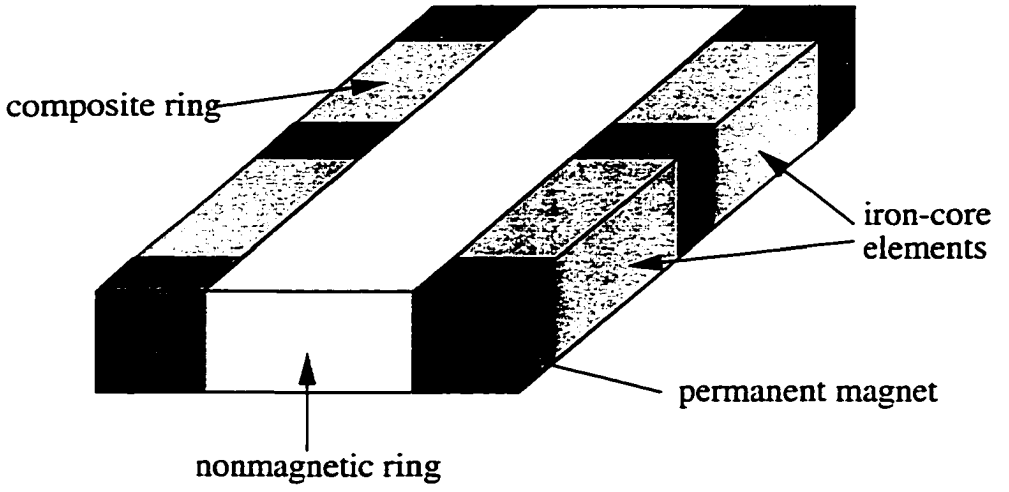

Figure 5.4: Structure of one phase of the rotor.

transverse flux machines is their complicated mechanical structure resulting in relatively high assembling and manufacturing costs. The material costs are lower as compared to the longitudinal design.

The rotor of Figure 5.1 consists of 8 composite rings of permanent magnets and iron-core elements arranged in a square. Permanent magnets are separated by iron elements in the direction of motion, and between the composite rings there is a nonmagnetic ring. One side (or phase) of the square rotor is shown in Figure 5.4, where the permanent magnets are magnetized in a tangential direction. Each phase is arranged as part of the rotor in such a way that no magnetic short circuits occur between neighboring magnets (Figure 5.5 a). The magnetization of magnets at each corner of the square rotor is in the same direction, precluding magnetic short circuits between magnets. At each corner of the square, a triangular-shaped, iron-core piece between neighboring iron parts is placed, to provide a continuing flux path from one phase to the neighboring one (Figure 5.5 b). The interior of the square rotor consists of nonmagnetic material so that magnets are not short-circuited. One corner of the square is mechanically connected to the shaft via a wheel as shown in Figure 5.1. This wheel should be of nonmagnetic material except those parts at the corner of the square, where it provides a connection between two iron pieces of adjacent rotor phases. The active part of the stator con-

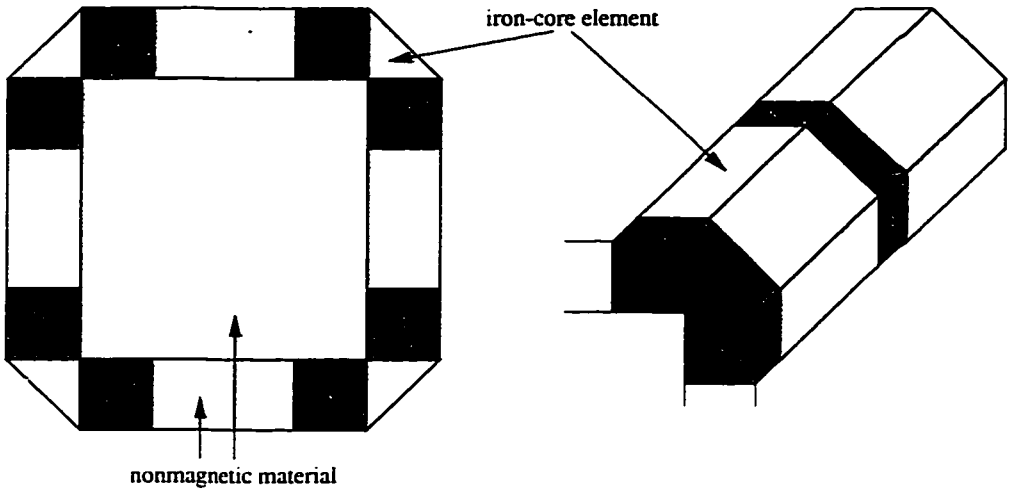

Figure 5.5: (a) Cross section of rotor of Figure 5.1 and (b) triangular iron piece at a corner.

sists of poleshoes placed above each phase of the square rotor separated by 90 electrical degrees from each other in space (Figure 5.1). Phase windings are placed inside the poleshoes, arranged in a circular manner. A side view of the machine showing how the flux lines travel is illustrated in Figure 5.3. The flux, directed by permanent magnets, crosses the first air gap (1) and flows across a stator poleshoe of phase a. The flux then emanates from the other side of that poleshoe and crosses the second air gap (2). There the flux divides into three paths, one part of the flux going directly to adjacent phase b via the triangularly-shaped iron-core element, the other two flux components passing through tangentially magnetized magnets, and then to the adjacent phase b via triangular iron-core elements. The flux follows similar paths for the other phases of the rotor. Flux travels in a spiral manner between rotor and stator.

CHAPTER 6

EXPERIMENTAL VALIDATION OF DISTORTION POWER D AND REVIEW OF EXISTING DEFINITIONS

6.1 Introduction

Power electronic equipment such as rectifiers, inverters,and adjustable-speed AC drives. can create nonsinusoidal current and voltage wave forms at the point of common coupling (PCC) with the utility system. These current and voltage harmonics contribute to reactive power. Q, producing an additional component called distortion power D such that the apparent power equation is satisfied [46].

$$S = \sqrt{P^2 + Q^2 + D^2} \tag{6.1}$$

Various definitions of distortion power are discussed in this chapter and accurate measurement results for the distortion power for different nonlinear loads are presented. From reference [46] it is known that the distortion power D can be expressed by current and voltage harmonics of unlike harmonic orders; that is. for example, V_m interacts with I_n, where $m \neq n$. A recent survey of engineers by North American Electric Utilities [47] states that only 20% found the definition of D in IEEE Standard 100-1992 useful, 62% state that the distortion power D is meaningless, and 18% have no opinion.

Existing formulations [46], [48], [49], [50], [51], [52] for the distortion power D as a function of the harmonic currents/voltages have been used for various nonlinear loads, and it has been found that different formulations generated different numerical results.

To validate computed results. an accurate computer-aided measurement circuit is used employing low-inductance shunts and voltage dividers instead of current and voltage transformers. which usually have. at high frequencies. larger amplitude and phase angle errors than shunts and voltage dividers. Such an accurate measurement method is essential because errors in the amplitudes add to the errors in the phase angles between voltage and current [53] components.

6.2 Measurement Approach

Experiments are performed to measure distortion power for a 25kVA. 7200/240V single-phase pole transformers with nonlinear loads (diode. thyristor. and combined diode-thyristor). The measurement circuit is shown in Figure 6.1. where two back-to-back connected transformers (see Appendix of [40]) supply power to rectifier loads.

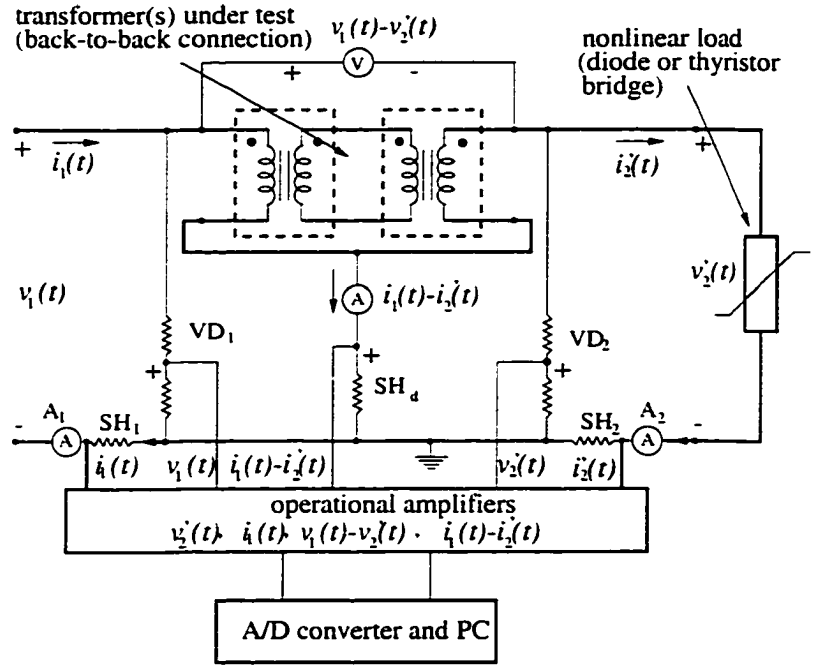

Figure 6.1: Experimental setup of the circuit.

Input current, $i_1(t)$, and input voltage, $v_1(t)$, are sampled by a 12 bit A/D converter, and Fourier coefficients (including DC components) up to the 49th harmonic are obtained

using a Fortran program based on Gaussian integration. Figures 6.2. 6.3, 6.4. and 6.5 show sampled wave forms of $i_l(t)$ and $v_l(t)$ for resistive, diode-bridge, thyristor-bridge, and diode-thyristor bridge loads, respectively.

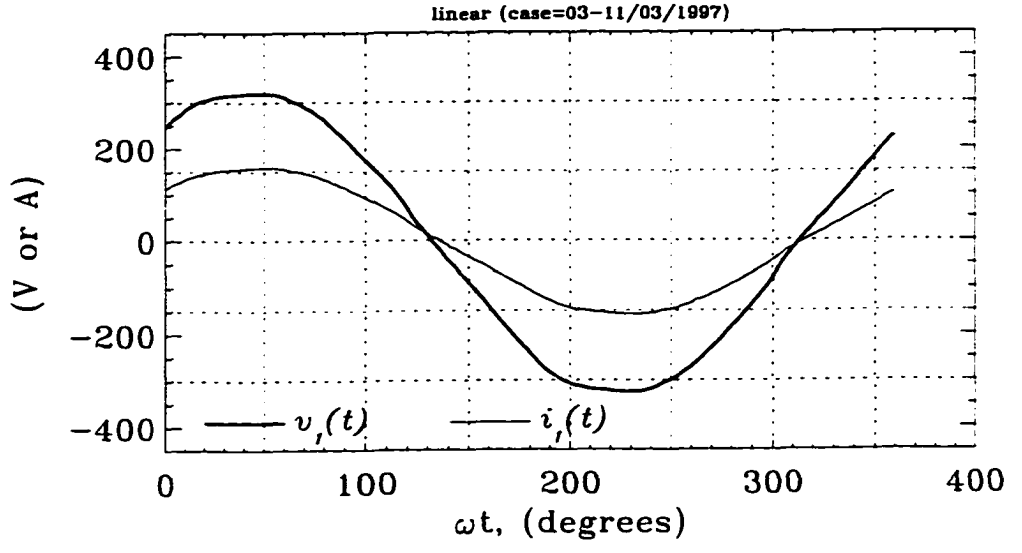

Figure 6.2: Voltage and current wave forms for resistive load.

Periodic nonsinusoidal voltages and currents can be written as

$$v_l(t) = V_0 + \sqrt{2}\sum_{h=1}^{\infty} V_h \sin(h\omega t + \alpha_h) \tag{6.2}$$

$$i_l(t) = I_0 + \sqrt{2}\sum_{h=1}^{\infty} I_h \sin(h\omega t + \beta_h) \tag{6.3}$$

where V_0 and I_0 are DC components, h is the harmonic number, V_h and I_h are the rms values of voltage and current harmonics, respectively, and α_h and β_h are harmonic phase angles of the harmonic voltages and currents, respectively. The total apparent power (S), real power (P), reactive power (Q), and distortion power (D) can be calculated

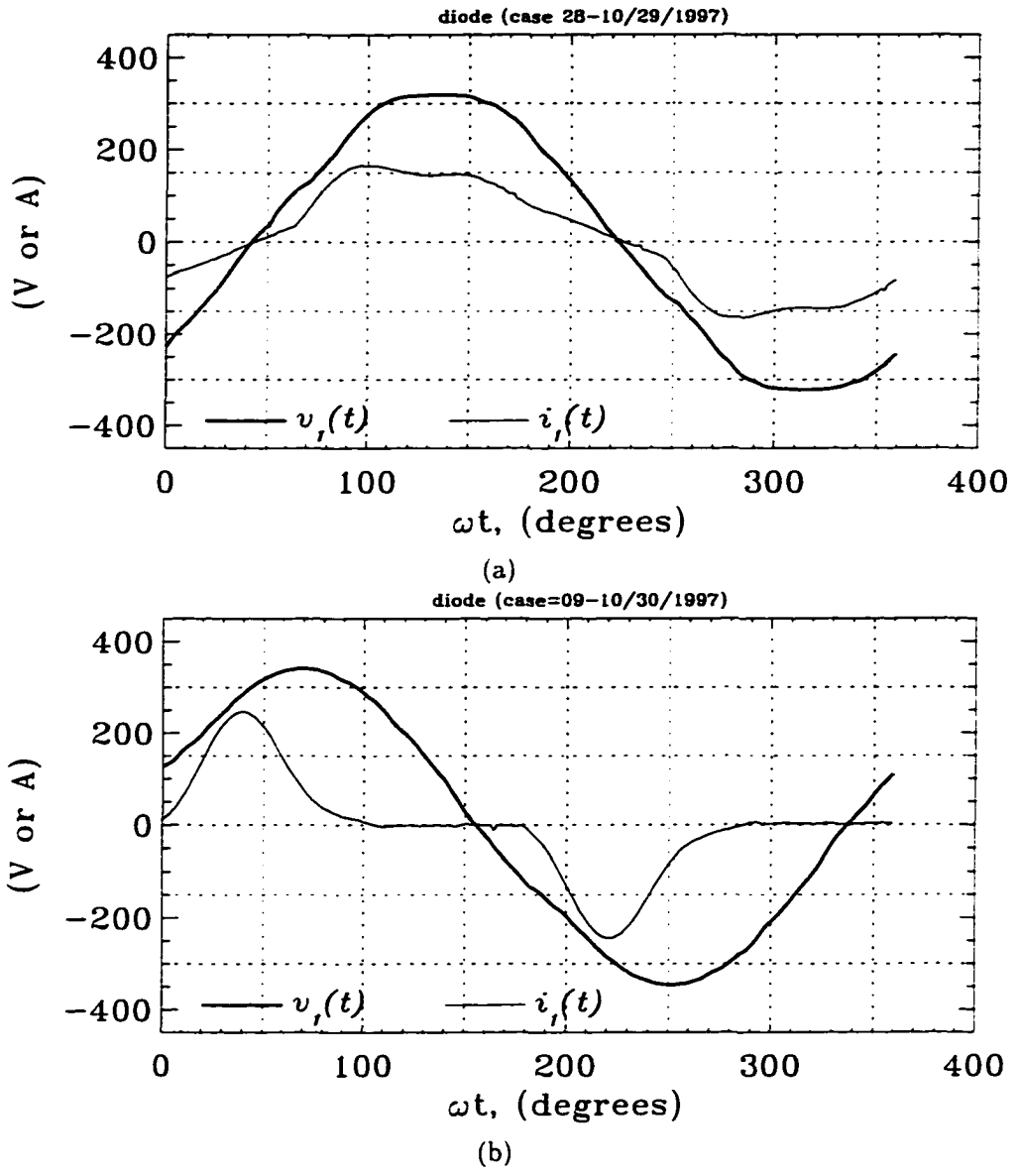

Figure 6.3: Voltage and current wave forms for diode-bridge rectifier with (a) C_{od} = 400 μF (b) C_{od} = 1200 μF capacitor across resistive load.

from the following

$$S = V_{rms} I_{rms} \tag{6.4}$$

$$P = V_0 I_0 + \sum_{h=1}^{\infty} V_h I_h \cos\theta_h \tag{6.5}$$

$$Q = \sum_{h=1}^{\infty} V_h I_h \sin\theta_h \tag{6.6}$$

$$D = \sqrt{S^2 - P^2 - Q^2} \tag{6.7}$$

where $V_{rms} = \sqrt{\sum_{h=0}^{49} V_h^2}$, $I_{rms} = \sqrt{\sum_{h=0}^{49} I_h^2}$, and $\theta_h = \alpha_h - \beta_h$. As an example, Table

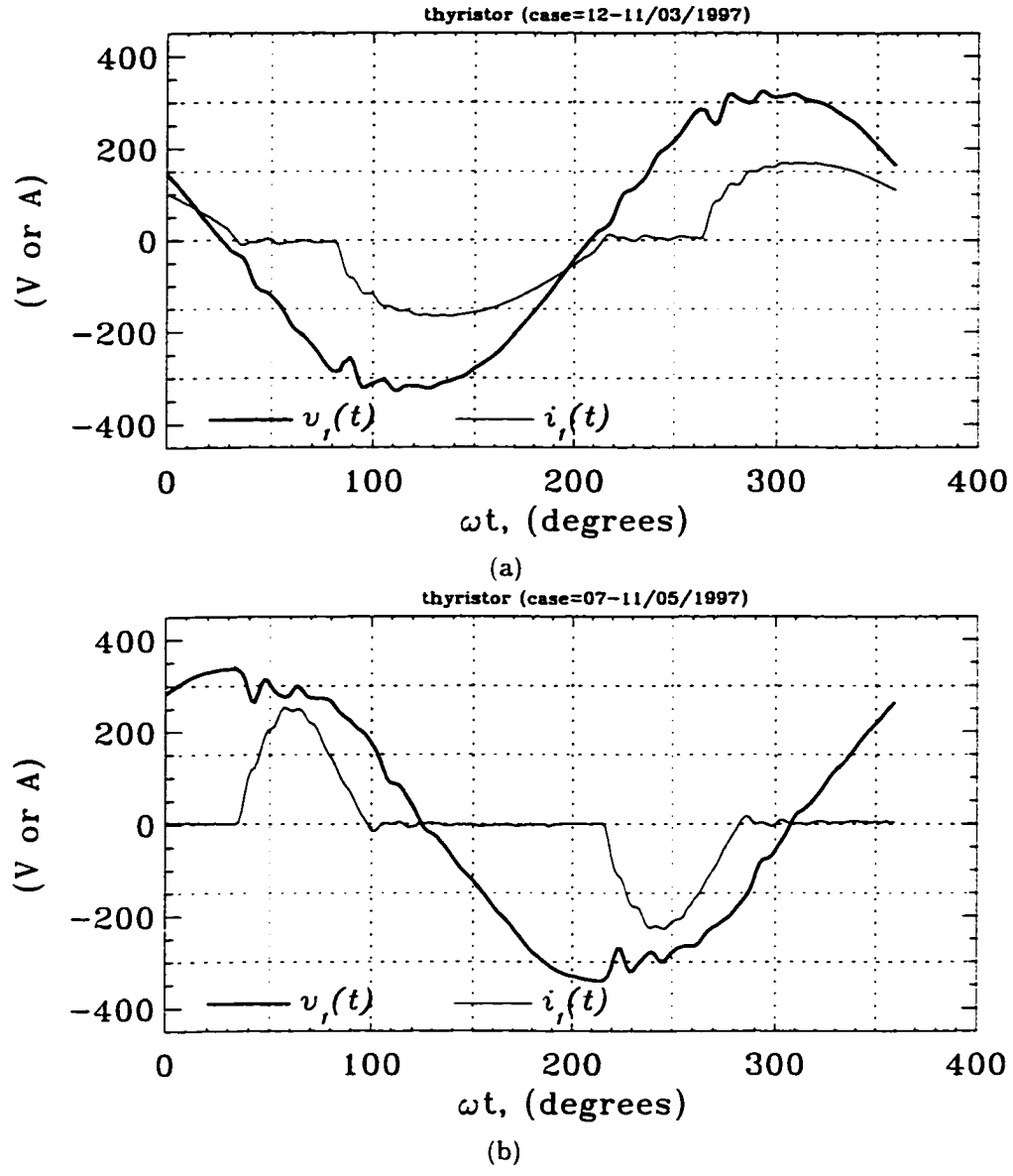

Figure 6.4: Voltage and current wave forms for half-controlled thyristor rectifier with (a) no capacitor (b) $C_{ot} = 800\ \mu F$ capacitor across resistive load.

6.1 lists the rms and THD values for the measured load conditions corresponding to Figures 6.2 to 6.5. The amplitudes of harmonic voltages and currents, along with the harmonic angles, are tabulated in Tables 6.2, 6.3, and 6.4 for diode-, thyristor-, and diode-thyristor bridge rectifier loads, respectively. The different power quantities for the wave shapes of Figures 6.2, 6.3, 6.4, 6.5 are computed using Equations 6.4 to 6.7, and the results are shown in Table 6.5.

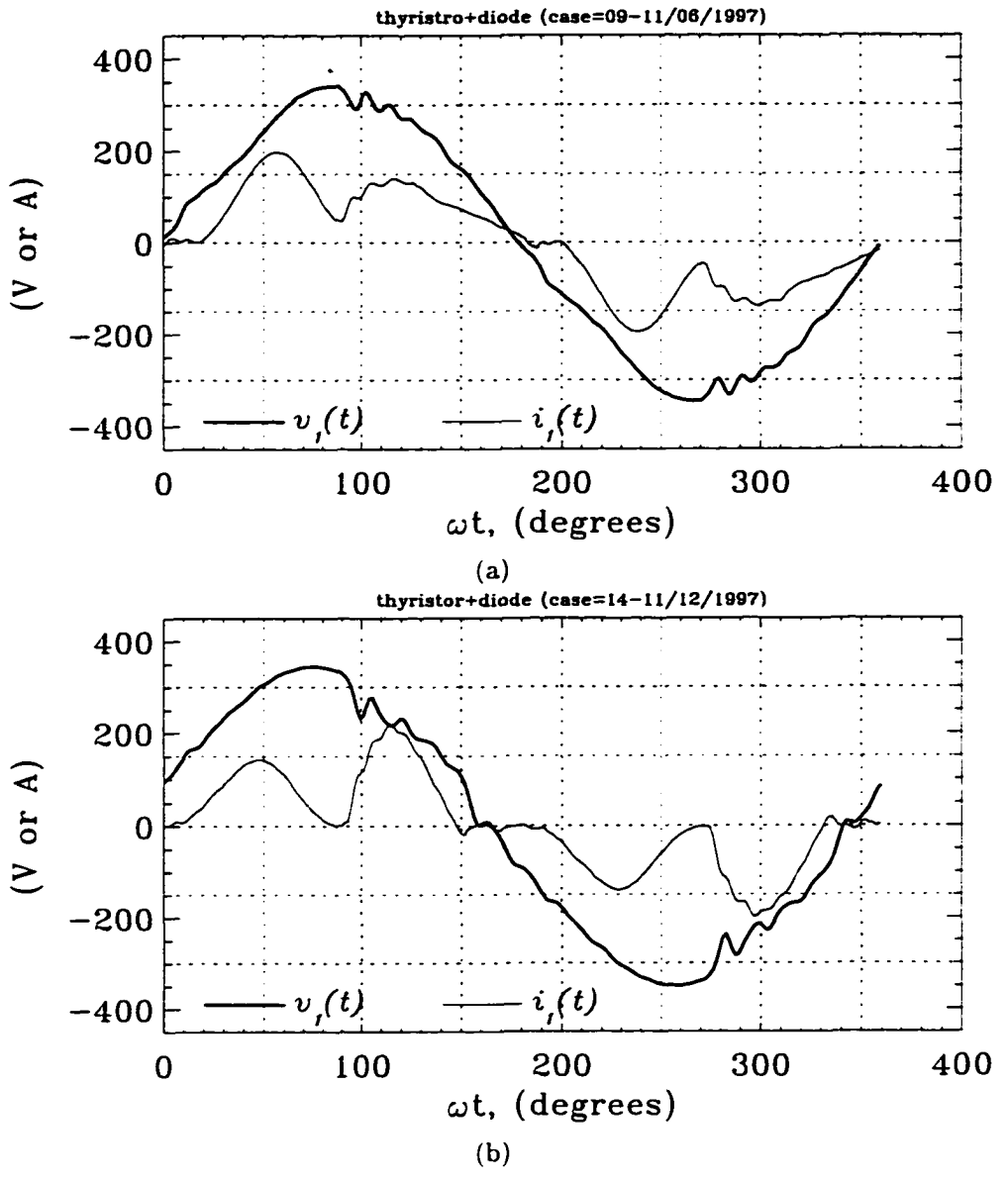

Figure 6.5: Voltage and current wave forms for half-controlled thyristor- and diode-bridge rectifiers with (a) $C_{od} = 900\ \mu F$ capacitor across resistive load of diode-bridge rectifier, no capacitor across resistive load of thyristor-bridge rectifier (b) $C_{od} = 900\ \mu F$ capacitor across resistive load of diode-bridge rectifier, and $C_{ot} = 800\ \mu F$ capacitor across resistive load of thyristor-bridge rectifier.

6.3 Formulations of Distortion Power

6.3.1 Formulation of D according to Budeanu [46], [48], Shepherd and Zand [49], and Emanuel [54], [55]

The distortion power, D, in terms of individual harmonic components for the voltages and currents described by Equations 6.2 and 6.3 is defined but not derived in

Table 6.1: RMS and THD values for voltage and current wave forms of Figures 6.2, 6.3, 6.4, and 6.5.

wave form	V_{rms} (V)	I_{rms} (A)	THD_v^{49} (%)	THD_i^{49} (%)
Fig. 6.2	231.03	111.96	2.49	2.69
Fig. 6.3a	230.53	110.52	3.49	15.69
Fig. 6.3b	235.81	106.5	4.46	70.54
Fig. 6.4a	230.55	108.34	4.10	25.41
Fig. 6.4b	236.07	99.48	7.34	92.20
Fig. 6.5a	232.73	105.88	4.93	39.19
Fig. 6.5b	235.26	97.88	6.81	70.03

the references above as (excluding the DC component),

$$D^2 = \sum_{\substack{m,n=1 \\ m \neq n}} V_m^2 I_n^2 + V_n^2 I_m^2 - 2V_m V_n I_m I_n \cos(\theta_m - \theta_n) \tag{6.8}$$

where $\theta_m = \alpha_m - \beta_m$ and $\theta_n = \alpha_n - \beta_n$. Computed values of distortion power for the above loads are given in Table 6.6, where Equation 6.8 is applied to 49 harmonics. Note that the distortion powers of Table 6.5 are not same as those of Table 6.6. The difference can be explained as follows: explicit terms of the summation of Equation 6.8 for the first two harmonics only (neglecting DC) are

$$\begin{aligned} D^2 &= V_1^2 I_2^2 + V_2^2 I_1^2 - 2V_1 V_2 I_1 I_2 \cos(\theta_1 - \theta_2) \\ &+ V_2^2 I_1^2 + V_1^2 I_2^2 - 2V_2 V_1 I_2 I_1 \cos(\theta_2 - \theta_1) \end{aligned} \tag{6.9}$$

This is the common mathematical interpretation of Equation 6.8 [56]. Examining Equation 6.9 closely, one notes that the ($m = 1$, $n = 2$) set of terms is the same as the ($m = 2$, $n = 1$) set, because $\cos(-\theta) = \cos(\theta)$. Therefore, the computed D^2 from Equation 6.8 will be twice as large as than the actual value, which explains the difference of a $\sqrt{2}$ factor between rows 3, 4, ... of Table 6.5 and columns 3, 4, ... of Table 6.6, respectively.

Table 6.2: Measured harmonic voltage and current amplitudes and phase angles for diode-bridge rectifier, using wave forms of Figures 6.3a and 6.3b.

harmonic	V_h (V RMS)	α_h (deg.)	I_h (A RMS)	β_h (deg.)
Figure 6.3a				
0	0.2	-	1.47	-
1	230.39	-44.48	109.18	-38.29
2	1.60	-33.89	1.15	-38.86
3	3.80	8.89	12.24	132.90
4	0.46	10.65	0.38	179.18
5	5.16	-76.68	10.50	-4.98
6	0.57	-44.68	0.92	-15.74
7	3.83	59.13	4.89	150.18
8	0.49	18.22	0.05	-58.90
9	1.04	-48.09	2.16	46.87
10	0.33	-7.76	0.34	38.07
11	1.03	46.67	0.98	-87.72
12	0.23	22.22	0.20	-53.79
13	1.28	-9.53	0.77	88.77
THD^{49} (%)	3.49	-	15.69	-
Figure 6.3b				
0	-2.6†	-	0.44†	-
1	235.57	21.30	87.02	48.05
2	2.38	15.80	1.96	95.96
3	9.47	-159.75	55.98	-35.66
4	0.81	-27.51	1.83	2.88
5	3.04	169.59	23.85	-107.54
6	0.47	-16.95	0.97	-57.29
7	1.06	138.45	7.43	-173.00
8	0.29	4.78	0.34	-101.81
9	0.46	6.51	0.02	-133.93
10	0.21	-16.83	0.10	18.02
11	1.24	38.06	0.84	-149.25
12	0.36	-3.03	0.08	83.08
13	0.70	111.71	0.65	-90.03
THD^{49} (%)	4.46	-	70.54	-

† Due to the nonlinear flux linkage-current (λ-i) characteristic of a transformer a negative DC voltage may result in a positive DC current, and vice versa.

6.3.2 Formulation of D according to Filipski [50]

Filipski gives the following formula for the distortion power D

$$D = \sqrt{\sum_m \sum_n [U_m^2 I_n^2 - U_m U_n I_m I_n \cos(\phi_m - \phi_n)]} \tag{6.10}$$

where U_n, I_n, and ϕ_n are the rms values and the phase angles of the n^{th} harmonic of voltage and current. Expanding the double summation of Equation 6.10 for the first

Table 6.3: Measured harmonic voltage and current amplitudes and phase angles for thyristor-bridge rectifier, using wave forms of Figures 6.4a and 6.4b.

harmonic	V_h (V RMS)	α_h (deg.)	I_h (A RMS)	β_h (deg.)
Figure 6.4a				
0	-3.02	-	-0.03	-
1	230.35	152.32	105.00	129.84
2	1.96	156.62	0.78	164.40
3	2.96	113.11	21.63	-138.86
4	0.99	155.38	1.09	-108.19
5	3.74	-132.53	12.84	82.44
6	0.48	-164.78	1.02	113.55
7	1.88	136.33	5.63	-68.78
8	0.60	170.03	0.51	-77.43
9	0.65	-20.24	2.09	95.11
10	0.08	105.21	0.53	100.34
11	1.51	157.24	3.24	-84.72
12	0.66	-178.66	0.63	-67.87
13	2.10	17.51	2.95	142.08
THD^{49} (%)	4.10	-	25.41	-
Figure 6.4b				
0	-4.09	-	0.75	-
1	235.43	51.88	73.12	26.68
2	2.00	18.72	3.77	44.31
3	8.86	118.26	56.68	-104.06
4	0.91	132.58	5.45	-98.25
5	11.65	15.23	32.75	130.24
6	1.87	-3.14	4.39	117.54
7	1.63	-81.11	10.46	15.68
8	0.30	-173.95	1.86	-41.84
9	1.96	-125.08	4.69	-7.34
10	0.57	-19.95	0.75	94.38
11	1.96	114.25	5.01	-106.12
12	0.31	82.72	0.79	-105.94
13	1.37	55.85	1.52	167.47
THD^{49} (%)	7.34	-	92.20	-

two voltage and current harmonics yields

$$\begin{aligned} D^2 &= U_1^2 I_1^2 - U_1 U_1 I_1 I_1 \cos(\phi_1 - \phi_1) \\ &+ U_1^2 I_2^2 - U_1 U_2 I_1 I_2 \cos(\phi_1 - \phi_2) \\ &+ U_2^2 I_1^2 - U_2 U_1 I_2 I_1 \cos(\phi_2 - \phi_1) \\ &+ U_2^2 I_2^2 - U_2 U_2 I_2 I_2 \cos(\phi_2 - \phi_2). \end{aligned} \tag{6.11}$$

Table 6.4: Measured harmonic voltage and current amplitudes and phase angles for diode-thyristor bridge rectifier, using wave forms of Figures 6.5a and 6.5b.

harmonic	V_h (V RMS)	α_h (deg.)	I_h (A RMS)	β_h (deg.)
Figure 6.5a				
0	-2.00	-	0.97	-
1	232.45	-0.21	98.57	0.05
2	2.62	8.13	0.95	8.48
3	3.22	-177.01	20.94	-50.36
4	0.49	-34.63	1.76	-16.24
5	7.87	78.04	28.09	-178.45
6	0.57	52.93	1.96	-154.77
7	4.07	-43.24	14.76	43.37
8	0.66	-20.18	0.89	34.88
9	0.82	25.01	1.16	173.64
10	0.67	16.40	0.43	-166.05
11	1.25	-100.66	3.84	37.34
12	0.48	-28.02	0.61	53.97
13	1.12	134.14	1.47	-109.33
THD^{49} (%)	4.93	-	39.19	-
Figure 6.5b				
0	-2.73	-	1.04	-
1	234.71	15.39	80.16	3.30
2	2.26	24.05	2.14	-57.70
3	5.23	-75.48	26.81	-48.50
4	1.58	-63.40	5.13	35.08
5	9.75	96.93	46.67	-144.19
6	1.68	-27.15	4.32	174.93
7	4.54	-142.55	11.50	5.16
8	0.30	141.44	2.12	-79.65
9	1.41	17.15	2.54	151.87
10	0.12	-35.28	0.57	-46.26
11	2.71	-87.19	3.48	14.43
12	0.70	-95.10	1.20	4.67
13	3.75	15.70	4.27	141.54
THD^{49} (%)	6.81	-	70.03	-

Note that the first and the last line of Equation 6.11 each are zero and the *cosine* terms of lines 2 and 3 are equal, yielding

$$D^2 = U_1^2 I_2^2 + U_2^2 I_1^2 - 2U_1 U_2 I_1 I_2 \cos(\phi_1 - \phi_2). \tag{6.12}$$

The numerical value of Equation 6.12 is two times as great as that of Equation 6.8, and thus Equation 6.10 is numerically correct, however, it involves voltage and current of like frequencies.

Table 6.5: Computed power quantities for the voltage and current wave forms of Figures 6.2 to 6.5 (results of Equations 6.4 to 6.7).

wave form	S (kVA)	P (kW)	Q† (kVAr)	D‡ (kVAd)
Fig. 6.2	25.87	25.83	1.3	≈ 0
Fig. 6.3a	25.48	25.00	-2.82	4.03
Fig. 6.3b	25.11	18.02	-9.75	14.52
Fig. 6.4a	24.98	22.26	9.19	6.64
Fig. 6.4b	23.48	15.00	6.59	16.82
Fig. 6.5a	24.64	22.81	-0.44	9.3
Fig. 6.5b	23.03	18.01	3.36	13.95

†kVAr means reactive power.
‡kVAd means distortion power.

6.3.3 Formulations of D according to Czarnecki [51], [57]

Czarnecki [51] computes the distortion power as

$$D_B = \sqrt{S^2 - (P^2 + Q_B^2)} = \sqrt{\sum_{r \in M} \sum_{s \in M} A_{rs}}$$
$$\text{with } A_{rs} = U_r^2 U_s^2 [Y_r^2 - 2 Y_r Y_s \cos(\phi_r - \phi_s) + Y_s^2] \tag{6.13}$$

where U is the voltage, P is the active power, Q_B is the reactive power, and $\hat{Y}_n = Y_n e^{-j\varphi_n}$ is the load admittance for harmonic frequencies. This definition is same as Equation 6.8 if $Y = \frac{I}{U}$ is substituted into Equation 6.13.

In a more recent paper [57], Czarnecki presents a similar definition for distortion power

$$D_B^2 = S^2 - (P^2 + Q_B^2) \tag{6.14}$$
$$\text{or } D_B^2 = \frac{1}{2} \sum_{r=0}^{\infty} \sum_{s=0}^{\infty} \{(U_r I_s - U_s I_r)^2 + 2 U_r I_s U_s I_r [1 - \cos(\theta_r - \theta_s)]\} \ . \tag{6.15}$$

This definition is similar to that described in [51]. For the first two harmonics (neglecting

DC component) Equation 6.15 becomes

$$\begin{aligned} D_B^2 = \frac{1}{2}\{&(U_1 I_1 - U_1 I_1)^2 + 2U_1 I_1 U_1 I_1[1 - \cos(\theta_1 - \theta_1)] \\ &+(U_1 I_2 - U_2 I_1)^2 + 2U_1 I_2 U_2 I_1[1 - \cos(\theta_1 - \theta_2)] \\ &+(U_2 I_1 - U_1 I_2)^2 + 2U_2 I_1 U_1 I_2[1 - \cos(\theta_2 - \theta_1)] \\ &+(U_2 I_2 - U_2 I_2)^2 + 2U_2 I_2 U_2 I_2[1 - \cos(\theta_2 - \theta_2)]\} \end{aligned} \tag{6.16}$$

A simplification of Equation 6.16 indicates that it is the same as that of Filipski (Equation 6.12).

6.3.4 Formulation of D according to IEEE Standard Dictionary [52]

IEEE Std 100-1996 [52] defines the distortion power in a single-phase two-wire circuit as

$$D = (U^2 - S^2)^{1/2} = (U^2 - P^2 - Q^2)^{1/2} \tag{6.17}$$

$$= \left(\sum_{r=1}^{r=\infty} \sum_{q=1}^{q=\infty} \{E_r^2 I_q^2 E_r E_q I_r I_q cos(\theta_r - \theta_q)\} \right)^{1/2} \tag{6.18}$$

where U is the apparent power defined by Equation 6.4; P and Q are the real and reactive powers defined by Equations 6.5 and 6.6, respectively; E_r, E_q and I_r, I_q are the rms values of the harmonic voltages and currents, respectively; and $\theta_r = \alpha_r - \beta_r$ and $\theta_q = \alpha_q - \beta_q$. It is apparent that there is somewhere a minus (-) sign missing, because the unit of D is not correct. The formulation in an older version of the dictionary (IEEE Std 100-1977) is similar to Equation 6.18, except that there is a minus sign after the term $E_r^2 I_q^2$, which makes it equal to the Equation 6.10 of Filipski.

6.3.5 Correct Interpretation of Budeanu's [46], [49], [54], [55], [50], [51] Definition of D

Using Equation 6.7 and considering only the first three harmonics of voltage and current (including DC components), the distortion power can be written as

$$\begin{aligned} D^2 &= S^2 - P^2 - Q^2 \qquad (6.19) \\ &= (V_0^2 + V_1^2 + V_2^2 + V_3^2)(I_0^2 + I_1^2 + I_2^2 + I_3^2) \\ &- (V_0 I_0 + V_1 I_1 \cos\theta_1 + V_2 I_2 \cos\theta_2 + V_3 I_3 \cos\theta_3)^2 \\ &- (V_1 I_1 \sin\theta_1 + V_2 I_2 \sin\theta_2 + V_3 I_3 \sin\theta_3)^2. \qquad (6.20) \end{aligned}$$

Expanding Equation 6.20 and using trigonometric identities yields

$$\begin{aligned} D^2 &= V_0^2 I_1^2 + V_1^2 I_0^2 - 2V_0 V_1 I_0 I_1 \cos\theta_1 \\ &+ V_0^2 I_2^2 + V_2^2 I_0^2 - 2V_0 V_2 I_0 I_2 \cos\theta_2 \\ &+ V_0^2 I_3^2 + V_3^2 I_0^2 - 2V_0 V_3 I_0 I_3 \cos\theta_3 \\ &+ V_1^2 I_2^2 + V_2^2 I_1^2 - 2V_1 V_2 I_1 I_2 \cos(\theta_1 - \theta_2) \\ &+ V_1^2 I_3^2 + V_3^2 I_1^2 - 2V_1 V_3 I_1 I_3 \cos(\theta_1 - \theta_3) \\ &+ V_2^2 I_3^2 + V_3^2 I_2^2 - 2V_2 V_3 I_2 I_3 \cos(\theta_2 - \theta_3). \qquad (6.21) \end{aligned}$$

Taking into account the components of h harmonic orders, Equation 6.21 becomes

$$D^2 = \sum_{m=0}^{h-1} \sum_{n=m+1}^{h} \{V_m^2 I_n^2 + V_n^2 I_m^2 - 2V_m V_n I_m I_n \cos(\theta_m - \theta_n)\} \qquad (6.22)$$

Knowing the Fourier coefficients of the wave forms, Equation 6.22 can be used to calculate the distortion power D without computing S, P, and Q.

6.4 Discussion of Results

In some of the referenced publications, the listed formulations do not generate correct numerical results for the definitions of D as a function of voltage and current

Table 6.6: Distortion power D in kVAd computed from different definitions.

figure #	6.2	6.3a	6.3b	6.4a	6.4b	6.5a	6.5b
Eq. 6.8	≈ 0	5.68	20.53	9.38	23.78	13.15	19.72
Eq. 6.10	≈ 0	4.02	14.52	6.63	16.81	9.30	13.94
Eq. 6.15	≈ 0	4.02	14.52	6.63	16.81	9.30	13.94
Eq. 6.22	≈ 0	4.02	14.52	6.63	16.81	9.30	13.94

harmonics. The formulations of Filipski [50], Czarnecki [57], and IEEE Std 100-1977 do produce correct numerical answers for D; however,they involve the products of current and voltage harmonics of the same order, as can be seen in Equations 6.11 and 6.16. The formulation for the distortion power D of Section 6.3.5 of this thesis is validated by measurements. The distortion power D as a function of THD_i for different types of nonlinear loads is shown in Figure 6.6, with very small errors of about 0.05%. The

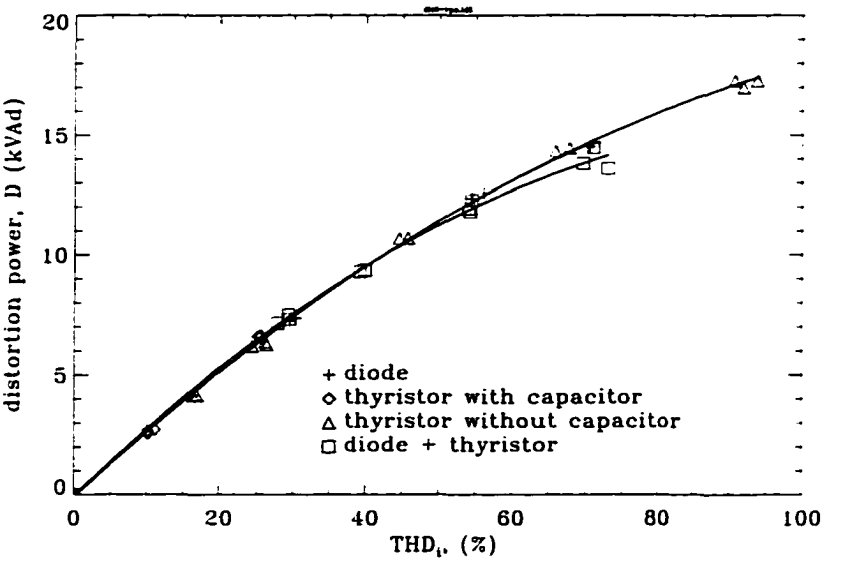

Figure 6.6: Measured values of distortion power as a function of THD_i for diode-, thyristor-, and combined diode-thyristor bridge rectifier loads.

independent determination of P, Q, D, and S leads to an excellent agreement with Equation 6.1, as defined in the 1930's by Budeanu.

CHAPTER 7

DETERMINATION OF HIGH-FREQUENCY LOSSES OF INDUCTORS

7.1 Introduction

There are three types of losses in an inductor: copper, iron-core, and stray power losses [58], [59]. Copper losses are caused by the resistivity of the wire material and they increase with frequency as $(f_h/f_1)^\epsilon$. This increase is due to the proximity, skin and the spirality effects [60]. At high frequencies, current tends to flow on the surface of a conductor, thus increasing the resistance of a wire. Spirality effects are caused by the twisting of the individual noninsulated strands of a conductor. Iron-core losses are the result of eddy currents generated inside the core material due to time-varying fluxes. Stray power losses can be defined as the losses originating in stray electromagnetic fluxes within windings, iron-cores, enclosures [61], clamps and nearby conductive regions [62], and from circulating currents due to asymmetries within the wire structure. Two methods for measuring losses of inductors at high frequencies from 0 to $6kHz$ are employed: the first involves the use of sampled inductor voltage and current wave forms obtained from an A/D converter and a computer. The second, called three-voltmeter method, consists of recording the rms values of three sinusoidal voltages.

7.2 Computer-Aided Testing (CAT)

To determine the losses of the inductors used in different parts of the drive system, e.g., rectifier, inverter and input and output filters, the measurement circuit of Figure 7.1 is proposed. A power amplifier along with a signal generator supplies sinu-

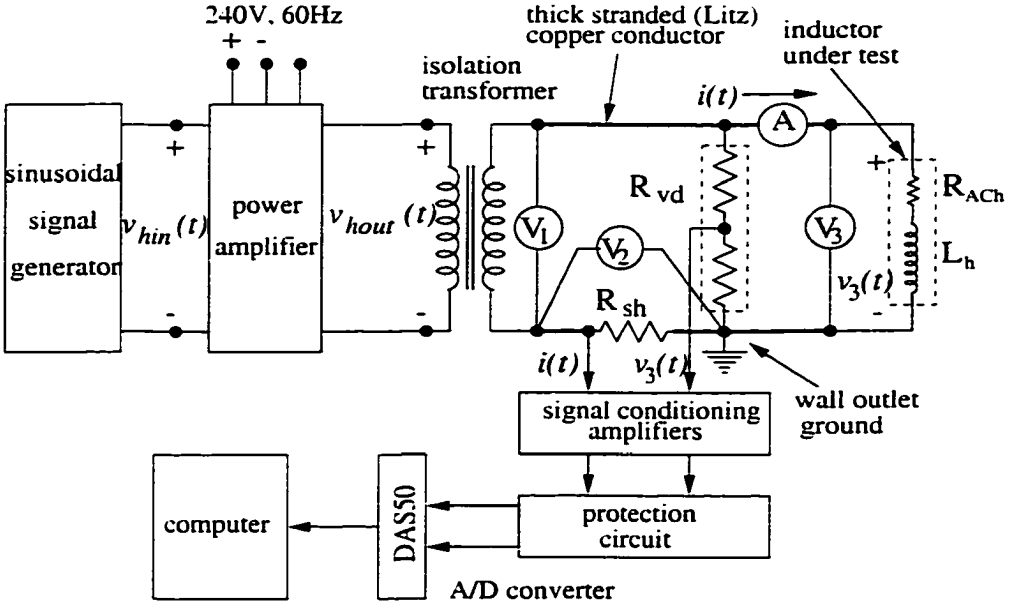

Figure 7.1: Measurement circuit to determine the losses of inductors.

soidal voltages at different frequencies to the inductor being tested. Voltage and current wave forms of an inductor are sensed by low-inductance resistor voltage dividers and shunts, respectively, and are sampled by a 12-bit A/D converter. The sampling program given in Appendix A sequentially samples 15,000 points for two channels at 900kHz for one 60Hz period (16.67ms), resulting in 7,500 points for each channel.

The average input power at any frequency is given by

$$P_{loss_h}^{CAT} = \frac{1}{T}\int_0^T v_3(t)i(t)dt \ , \tag{7.1}$$

where $v_3(t)$ and $i(t)$ are the voltage and current of the inductor, respectively. For sinusoidal voltage and current wave forms, Equation 7.1 becomes the familiar

$$P_{loss_h}^{CAT} = V_{3rms_h} I_{rms_h} \cos\theta_h \tag{7.2}$$

where θ is the phase angle between $v_3(t)$ and $i(t)$. The AC resistance (R_{ACh}) and inductance (L_h)of the inductor as a function of frequency ($f_h = h\ f_1$) are then computed as

$$R_{AC_h} = \frac{P_{loss_h}^{CAT}}{{I_{rms_h}}^2}\ ,\ L_h = \frac{\sqrt{Z_h^2 - {R_{AC_h}}^2}}{2\pi f_h}\ . \tag{7.3}$$

where $Z_h = V_{3rms_h}/I_{rms_h}$ and f_h is the frequency.

The data is sampled by a program provided by Keithley/MetraByte [63] and is written either in Quick Basic or C^{++}. The command file for sampling is shown in Appendix A; and for postprocessing, the sampled data are written on a floppy disk for evaluation on a workstation, where the loss, resistance, and inductance computations can be performed (for $h = 0, 1, 2, 3, \cdots 138$) within 2 minutes, employing a very exact Fourier analysis based on Gausssian integration [64]. A fast Fourier Transform (FFT) has not been chosen, in order not to compromise the accuracy of these measurements.

7.3 Three-Voltmeter Method (3VM)

The losses of some inductors are very small, e.g., 1 or 2 watts for a given current of $5Arms$: nevertheless, one has to raise the question of how accurate the measured results obtained from the circuit of Figure 7.1 are. For this reason, an alternative approach is used to check the results of the computer-aided method. This approach is based on three (sinusoidal) voltage measurements as shown in the circuit of Figure 7.2 [65]. From the phasor diagram of Figure 7.3, $\hat{V}_1 = \hat{V}_2 + \hat{V}_3$, one finds that the rms value of $\hat{V}_1$ is always greater than that of $\hat{V}_3$. The maximum value of the phase angle θ is 90^o, which corresponds to an ideal lossless inductor. The value of the resistor R_2 must be known in order to compute the power loss P_{loss}^{3VM} and AC resistance R_{AC_h} of the inductor. Depending on the value of the resistor R_{AC_h}, the voltage across the inductor is nearly equal to the input voltage, i.e., $V_{1_{rms}} \simeq V_{3_{rms}}$ when $V_{1_{rms}} \gg V_{2_{rms}}$. For such conditions the computed inductor loss measurement becomes inaccurate. To

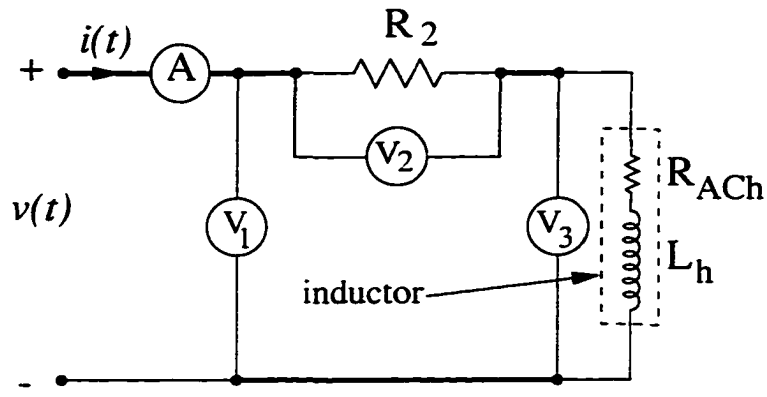

Figure 7.2: Three-voltmeter method for measuring the losses of an inductor.

remedy this problem. the resistance R_2 should be chosen such that the input voltage (V_1) applied to the circuit at a certain frequency and at a given current should satisfy the following condition: $V_1 < 8V_2$ where V_2 is the voltage across the resistor R_2. This condition stems from the laboratory experience gained. The three-voltmeter method can be combined with the computer-aided measurement circuit. if the shunt resistance R_{sh} of Figure 7.1 is used as resistance R_2 of Figure 7.2.

The rms values of the sinusoidal voltages V_1, V_2, and V_3 can be written as

$$V_1 = I\sqrt{(R_2 + R_{AC_h})^2 + X_h{}^2} \ . \tag{7.4}$$

$$V_2 = IR_2 \ . \tag{7.5}$$

$$V_3 = I\sqrt{R_{AC_h}{}^2 + X_h{}^2} \ . \tag{7.6}$$

where I is the rms value of the sinusoidal current $\hat{I}$ and $X_h = 2\pi f_h L_h$. Taking the squares of Equations 7.4 and 7.6 and subtracting Equation 7.6 from Equation 7.4 gives

$$R_2{}^2 + 2R_2R_{AC_h} = \frac{V_1{}^2 - V_3{}^2}{I^2} \ . \tag{7.7}$$

Substitution of R_2 from Equation 7.5 yields

$$P_{loss}^{3VM} = I^2R_{AC_h} = \frac{V_1{}^2 - V_2{}^2 - V_3{}^2}{2R_2} \ . \tag{7.8}$$

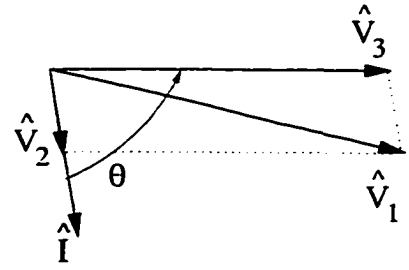

Figure 7.3: Phasor diagram of three-voltmeter method.

7.4 Error Analysis

Table 7.1 lists the errors of the sensors (low inductance voltage dividers and shunts) and digital meters used for both measurement circuits. Digital voltmeters have

Table 7.1: Sensors and instruments of Figures 7.1 and 7.2 and their full-scale errors.

instruments and sensors	full scale	full-scale error values	full-scale errors
R_{vd}	$300V/7V$	$\varepsilon_{R_{vd}} = 0.07V$	1%
R_{sh}	$12A$	$\varepsilon_{R_{sh}} = 0.12A$	1%
R_2	2Ω	$\varepsilon_{R_1} = 0.06\Omega$	3%
V_1, V_2, V_3	$300V$, $30V$, $3V$	$\varepsilon_{V_{1,2,3}} = 0.3V$, $0.03V$, $0.003V$	0.1%
I	$10A$	$\varepsilon_A = 0.01A$	0.1%

different voltage measurement ranges, e.g., $3V$, $30V$, $300V$, and they switch to a higher range if the measured voltage is greater than the maximum value of that range. Therefore, the maximum value of each range is used in error calculations, depending on the value of the measured voltage. If the input voltage is small for some inductors, in particular at low frequencies, the voltage divider (R_{vd}) is not used, therefore, $\varepsilon_{R_{vd}}$ does not enter the error calculations.

7.4.1 Computer-Aided Testing (CAT)

The computer-aided method relies on the rms values of voltage and current for the loss calculation. Therefore, the resulting error in the loss measurement can be computed by defining percentage errors in voltage amplitude, current amplitude, and the angle

between voltage and current. Rewriting Equation 7.2 including the error values gives at a given frequency f_h

$$P_{loss}^{CAT} + \Delta P_{loss}^{CAT} = (V_{3rms} + \Delta V)(I_{rms} + \Delta I)\cos(\theta + \Delta\theta) \ . \tag{7.9}$$

The error in the measurement of phase angle $\theta = \theta_2 - \theta_1$ depends on the sampling points for one period. As can be seen from Figure 7.4, the A/D converter samples signals at Δs

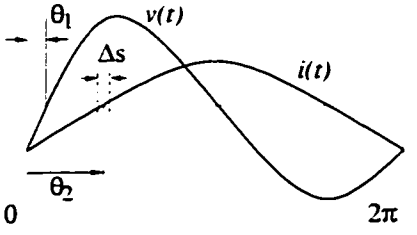

Figure 7.4: Measurement of phase angle $\theta = \theta_2 - \theta_1$.

intervals which results in a maximum error of $\Delta s/2$ for the zero crossing of the signal. Thus, the error in the measurement of this angle is $\Delta\theta = \Delta\theta_2 - \Delta\theta_1$.

From $\Delta\theta_1 = \Delta\theta_2 = \pm\Delta s/4\pi$ follows at a given frequency f_h:

$$\Delta\theta|_{max} = \pm\Delta s/2\pi \ , \tag{7.10}$$

where $\Delta s = \frac{f_h}{f_s/2}$, $f_s = 900\ kHz$ is the sampling frequency and f_h (from 0 to $6kHz$) is the frequency of the signal sampled.

Expanding Equation 7.9 results in

$$P_{loss} + \Delta P_{loss} = (V_{rms}I_{rms} + \Delta V I_{rms} + \Delta I V_{rms} + \Delta V\Delta I)(\cos\theta\cos\Delta\theta - \sin\theta\sin\Delta\theta) \tag{7.11}$$

where

$$\cos\Delta\theta = 1 - \frac{(\Delta\theta)^2}{2!} + \frac{(\Delta\theta)^4}{4!} - \cdots \ , \quad \sin\Delta\theta = \Delta\theta - \frac{(\Delta\theta)^3}{3!} + \frac{(\Delta\theta)^5}{5!} - \cdots \ .$$

Neglecting the second and higher order error terms, e.g., $(\Delta V)^2 \simeq 0$, the following result is obtained

$$\frac{\Delta P_{loss}}{P_{loss}} = \frac{\Delta V}{V_{3rms}} + \frac{\Delta I}{I_{rms}} - \tan\theta\Delta\theta|_{max} \ . \tag{7.12}$$

The voltage and current values are measured with the maximum error of

$$\frac{\Delta V}{V} = \frac{\pm\varepsilon_{R_{vd}} \pm \varepsilon_V}{V}, \quad \frac{\Delta I}{I} = \frac{\pm\varepsilon_{R_{sh}} \pm \varepsilon_I}{I}. \tag{7.13}$$

Consequently, the total loss is measured with the maximum error of

$$\frac{\Delta P_{loss}^{CAT}}{P_{loss}^{CAT}} = \frac{\pm\varepsilon_{R_{vd}} \pm \varepsilon_V}{V} + \frac{\pm\varepsilon_{R_{sh}} \pm \varepsilon_A}{I} - \tan\theta \frac{\pm\Delta s}{2\pi}. \tag{7.14}$$

Equation 7.14 reveals that for an ideal inductor ($\theta \rightarrow 90^0$) $\tan\theta$ will approach infinity. That means the maximum error of the computer-aided approach will become large as well. To reduce this error the sampling frequency (f_s) must be increased to a very high value, so that $\Delta s \approx 0$. In this case, $\tan\theta \cdot \Delta s$ yields an indeterminate expression of the form $\infty \cdot 0$. This can be solved by use of L'Hôspital's rule, whence

$$\lim_{\theta \rightarrow 90^0} \frac{\Delta s}{\cot\theta} = \lim_{\theta \rightarrow 90^0} \frac{0}{\frac{-1}{\sin^2\theta}} = 0\ . \tag{7.15}$$

Equation 7.15 suggests that the error of the measurement of angle approaches zero for an ideal inductor, if a sufficiently large (infinite) number of samples are used.

Table 7.2 presents, for selected frequencies, the phase angle θ and the maximum errors of the computer-aided measurement approach for inductor #1. The voltage divider is used for the frequency of $6000Hz$, but not at $900Hz$ for the values in Table 7.2. Errors at high frequencies can be reduced by limiting the sampling window to the frequency f_h of the signals (not fixed at $16.67ms$) and by increasing the maximum sampling frequency of the A/D converter, e.g., to $3MHz$.

Table 7.2: Errors of computer-aided method at selected frequencies.

f_h (Hz)	$\lvert\hat{V}_1\rvert$ (V)	$\lvert\hat{I}_1\rvert$ (A)	θ (degrees)	$\frac{\Delta P_{loss}^{CAT}}{P_{loss}^{CAT}}$
900	0.3737	5.02	69.81	3.95 %
6000	2.2647	5.016	79.74	13.21%

7.5 Three-Voltmeter Method (3VM)

Applying a similar error analysis to Equation 7.8 results in

$$P^{v}_{loss} + \Delta P^{v}_{loss} = \frac{(V_1 + \Delta V_1)^2 - (V_2 + \Delta V_2)^2 - (V_3 + \Delta V_3)^2}{2(R_1 + \Delta R_1)} \tag{7.16}$$

$$= \frac{({V_1}^2 + 2V_1\ \Delta V_1) - ({V_2}^2 + 2V_2\ \Delta V_2) - ({V_3}^2 + 2V_3\ \Delta V_3)}{2R_1(1 + \frac{\Delta R_1}{R_1})}. \tag{7.17}$$

Using the Taylor series expansion of $\frac{1}{1+x} = 1 - x + \frac{x^2}{2!} - \frac{x^3}{3!} + \cdots$. Equation 7.17 reduces to

$$= \left(\frac{{V_1}^2 - {V_2}^2 - {V_3}^2 + 2V_1\ \Delta V_1 - 2V_2\ \Delta V_2 - 2V_3\ \Delta V_3}{2R_1}\right)\left(1 - \frac{\Delta R_1}{R_1}\right). \tag{7.18}$$

Second-order error terms are neglected in Equations 7.17 and 7.18. Disregarding the products of error terms, e.g., $\Delta V_1\ \Delta R_2 \simeq 0$, we obtain

$$\begin{aligned} P^{3VM}_{loss} + \Delta P^{3VM}_{loss} &= \frac{{V_1}^2 - {V_2}^2 - {V_3}^2}{2R_1} + \frac{2V_1\ \Delta V_1 - 2V_2\ \Delta V_2 - 2V_3\ \Delta V_3}{2R_1} \\ &- \frac{{V_1}^2 - {V_2}^2 - {V_3}^2}{2R_1}\frac{\Delta R_2}{R_2}\ : \end{aligned} \tag{7.19}$$

then

$$\frac{\Delta P^{3VM}_{loss}}{P^{3VM}_{loss}} = \frac{2(V_1\ \Delta V_1 - V_2\ \Delta V_2 - V_3\ \Delta V_3)}{{V_1}^2 - {V_2}^2 - {V_3}^2} - \frac{\Delta R_2}{R_2}\ , \tag{7.20}$$

and

$$\frac{\Delta P^{3VM}_{loss}}{P^{3VM}_{loss}} = 2\ \frac{V_1\ (\pm\varepsilon_{V_1}) - V_2\ (\pm\varepsilon_{V_2}) - V_3\ (\pm\varepsilon_{V_3})}{{V_1}^2 - {V_2}^2 - {V_3}^2} - \frac{\pm\varepsilon_{R_2}}{R_2}\ . \tag{7.21}$$

where $\Delta R_2/R_2$ is the error in the measurement of resistor R_2. Its value is computed from $R_2 = V_2/I$ as defined in Figure 7.1. Then, the error in the measurement of R_2 is

$$R_2 + \Delta R_2 = \frac{V_2 + \Delta V_2}{I + \Delta I} = \frac{V_2}{I}\frac{1 + \frac{\Delta V_2}{V_2}}{1 + \frac{\Delta I}{I}}\ . \tag{7.22}$$

Applying a Taylor series expansion to $\frac{1}{1+\frac{\Delta I}{I}}$ in Equation 7.22 and eliminating higher order terms gives

$$\frac{\Delta R_2}{R_2} = \frac{\Delta V_2}{V_2} - \frac{\Delta I}{I} = \frac{\pm\varepsilon_{V_2}}{V_2} - \frac{\pm\varepsilon_A}{I}\ . \tag{7.23}$$

The three-voltmeter method generates errors which indirectly depend on the angle θ. For a large θ, $\hat{V}_2$ will be small as compared with $\hat{V}_1$ and $\hat{V}_3$. The smaller $\hat{V}_2$ is, the more difficult it becomes to measure it accurately. Table 7.3 presents some of the maximum errors as a function of $\hat{V}_2$ for inductor #1.

Table 7.3: Errors of Three-Voltmeter Method at selected frequencies.

f (Hz)	$\lvert\hat{V}_1\rvert$ (V)	$\lvert\hat{V}_2\rvert$ (V)	$\lvert\hat{V}_3\rvert$ (V)	$\left\lvert\frac{\Delta P_{loss}}{P_{loss}}\right\rvert_{3VM}$
900	0.776	0.540	0.370	6.57%
6000	2.413	0.542	2.260	8.21%

7.6 Experimental Results

7.6.1 Procedure

The inductors described in Appendix B are tested at frequencies from 60Hz to $6000Hz$ with $600Hz$ or less increments at a current of $5A$. As shown in Figure 7.1, the voltage signal is sampled through a voltage divider resistor network (R_{vd}) and there are signal conditioning amplifiers between the A/D converter and the actual signals. Some of the inductors have very small inductances and resistances ($m\Omega$-range). Thus, the voltages sampled are very small and an appropriate gain (e.g., 6) for the voltage amplifiers must be chosen. The AC resistances, for different gains of the amplifiers, are compared in Figure 7.5 for inductor inductor #5. The bandwidth of network used for amplification must be wide enough so that measurements at 6kHz are not impaired.

A signal generator supplies sinusoidal signals at various frequencies to the power amplifier, where the frequencies should be integer multiples of the power system frequency of 60Hz. Therefore, an exact measurement of the applied frequency of the sinusoidal voltage is required. One way to measure the frequency is to plot Lissajous curves on the oscilloscope as illustrated in Figure 7.6a, where the power system frequency is connected to the X input of oscilloscope, while the output of the power amplifier is attached to the Y input.

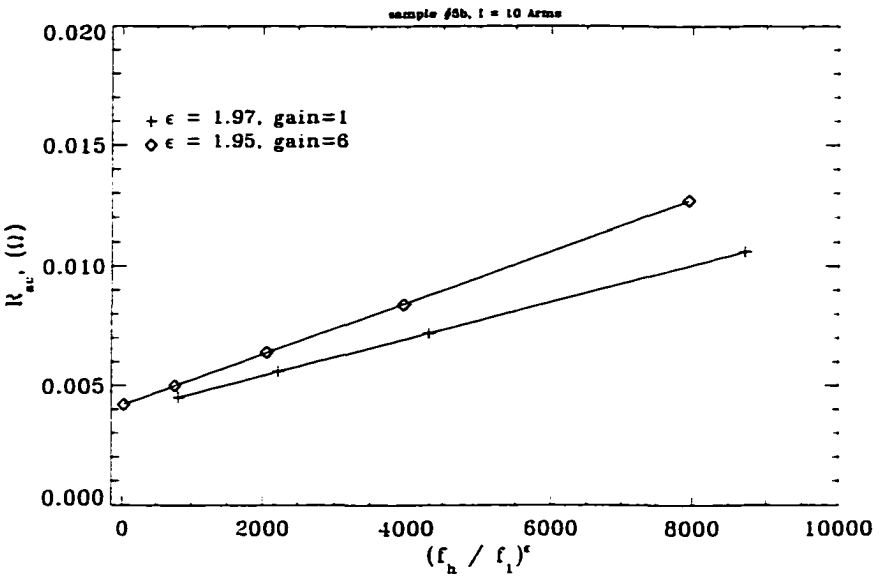

Figure 7.5: The effect of changing the gain of voltage amplifier on the R_{AC} of inductor #5 (without core).

The parametric plot of two sinusoidal functions given by the following equations

$$x(t) = A_1 \sin(\omega_1 t - \theta_1) \quad . \quad y(t) = A_2 \sin(\omega_2 t - \theta_2)$$

are called Lissajous curves [66]. The curves close if $\frac{\omega_2}{\omega_1}$ is rational, i.e., ω_2 is an integer multiple of ω_1. This is shown in Figure 7.6b, where the plot on the left-hand side is a closed curve since $f_h = 3 \cdot 60 = 180Hz$, while the one on the right-hand side is an open curve at $f_h = 3.1 \cdot 60 = 186Hz$. The curves will thus be stationary on the oscilloscope screen when the output frequency of the power amplifier is an integer multiple of $60Hz$, otherwise a movement of the trace will be observed on the screen.

Each inductor is connected to the measurement circuit through a thick, stranded (Litz) copper conductor. Since the AC resistances (R_{AC}) for some inductors are very small, this connecting wire may contribute to a somewhat higher measured resistance than the actual resistance of the inductor being tested because additional losses occur in this connecting wire. This difference is illustrated in Figure 7.7 for inductor #5 (with core), where the + sign denotes the R_{AC} with the use of a connecting wire and "◇" shows the R_{AC} with a direct connection to the measurement circuit. This connecting

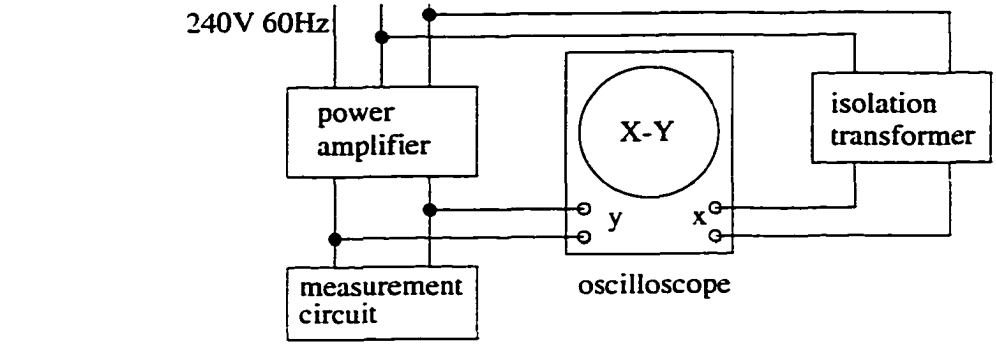

(a)

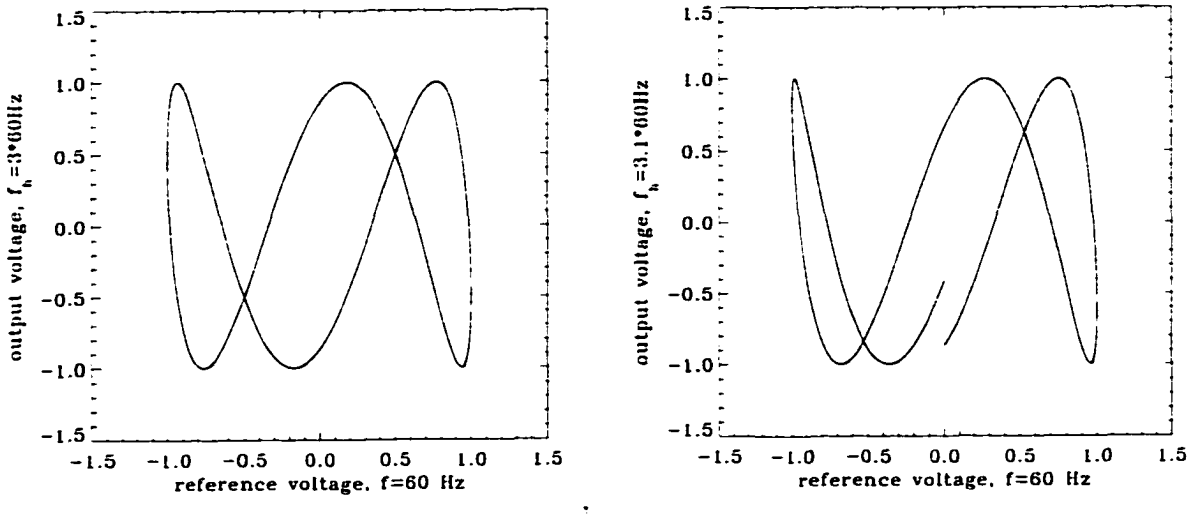

(b)

Figure 7.6: (a) Measurement circuit to determine the output frequency of power amplifier, and (b) Lissajous curves, $\theta_1 = 0^o$ and $\theta_2 = 60^o$.

wire will not affect the results of inductors with large AC resistances because of its small resistance. Note that, in this part of the experiment, inductor #5 has a core (Figure 7.7).

As shown in Figure 7.1, signals are referred to earth ground (wall outlet). In some applications it may be required to perform measurements on-line, i.e., measuring the losses of an inductor when the equipment is operating. Therefore, current and voltage signals need to be isolated from the measurement circuit to prevent ground conflicts, because the measurement circuit is tied to earth ground to protect personnel and equipment. A two-channel, optically isolated, data acquisition system has been developed [67] and tested in the laboratory. This system includes a dual instrumentation

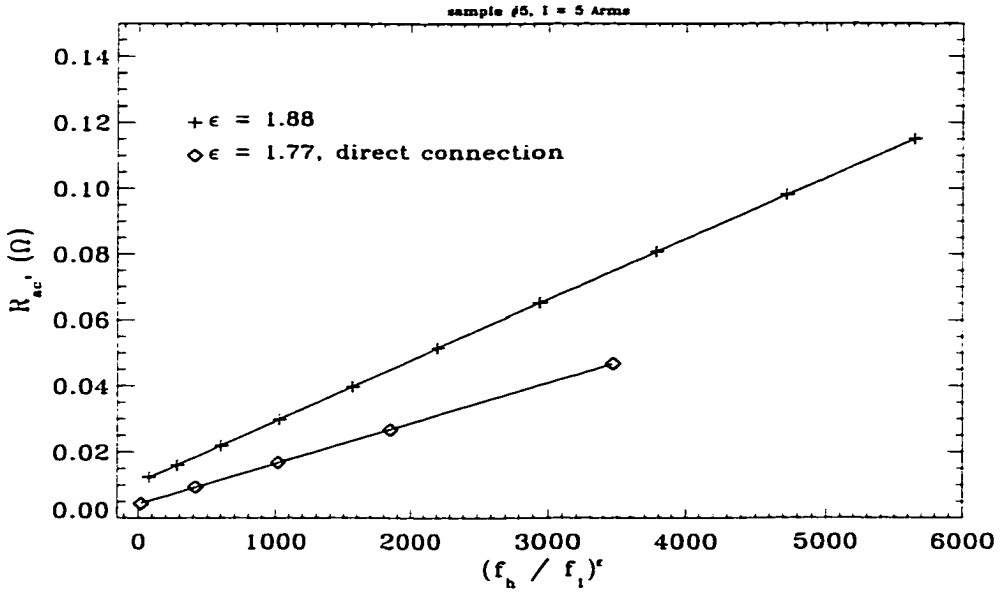

Figure 7.7: The effect of an external connecting wire on the R_{AC} of inductor #5 (with core).

amplifier, two isolated gain amplifiers, and two sample/hold amplifiers. The isolated-gain amplifier has a bandwidth of 6kHz, which limits the maximum operating frequency of this system. Inductor #8 is tested with this optically isolated circuit, and the results are compared in Figure 7.8 with non-isolated measurement results. At frequencies lower than the bandwidth of the amplifier, the results are very close, but at 6kHz the difference is large. The accuracy at high frequencies can be improved if an isolation amplifier with a higher bandwidth (e.g., 60 kHz) is used. Note that for each and every data set measured, a calibration with the participating voltage and current meters are performed; this will reduce the calculated maximum errors.

7.6.2 Comparison of Measurement Results with Theoretical Solutions

A solid circular wire fed by currents of high frequency can experience skin effects if the radius of the wire is larger than the penetration depth ($a > \delta$). This will result in an increase of the AC resistance of the wire because high frequency currents tend to flow on the surface of the wire. Two solid round "nonmagnetic"[†] steel rods are connected in

[†] No nonmagnetic material has $\mu_r = 1$, but $\mu_r \approx 1$.

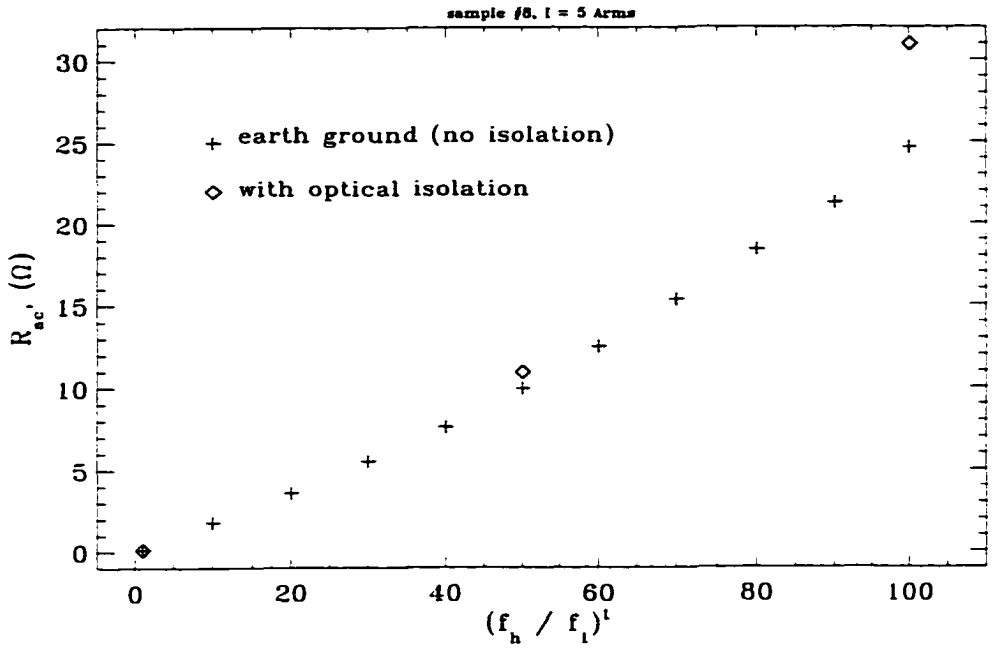

Figure 7.8: The AC resistance of inductor #8 measured with two different grounding methods.

series as shown in Figure 7.9. and the losses and AC resistances as a function of frequency are determined by using both the computer-aided measurement circuit of Figure 7.1 and that of the three-voltmeter method of Figure 7.2. Both approaches can be implemented

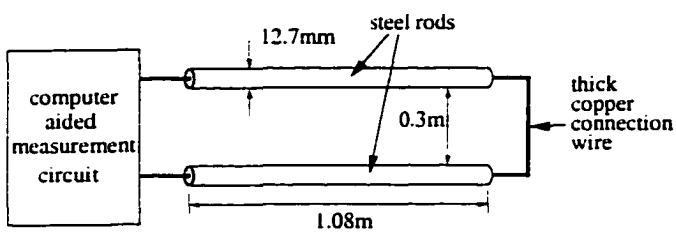

Figure 7.9: Loss measurement of two parallel steel rods.

together in one measurement circuit, if the shunt resistance R_{sh} of Figure 7.1 is used as the resistance R_2 of Figure 7.2. Since the applied voltage to the steel rods is less than one volt, the resistive voltage divider network R_{vd} is not used and the voltage signal is directly applied to the amplifier having a gain of six. Figure 7.10 illustrates the results of the two different measurement approaches which are in good agreement with each other. The errors for the results based on the computer-aided circuit of Figure 7.1 are

found from Equation 7.14. Because the voltage is directly applied to the steel rods, the error term $\varepsilon_{R_{vd}}$ of Equation 7.14 is zero. Using the voltage and current values (at 6kHz) of $I = 5.007A$, $V_1 = 0.905V$, $V_2 = 0.541V$, $V_3 = 0.557V$, $\tan\theta = 2.27$ and the values of Table 7.1, the maximum error for the computer-aided approach, where all the error values have same sign and therefore add up to each other, is

$$\left.\frac{\Delta P_{loss}}{P_{loss}}\right|_{CAT} = \frac{\pm 0.003}{0.5375} + \frac{\pm 0.12 \pm 0.01}{5.007} = \pm 3.15\%.$$

Using Equation 7.23 gives $\frac{\Delta R_2}{R_2} = \frac{0.003}{0.541} + \frac{0.01}{5.007} = \pm 0.0075$. The maximum error for the losses based on the three-voltmeter method is computed from Equation 7.21 and is $\Delta P_{loss}^{3VM} / P_{loss}^{3VM} = \pm 6.47\%$.

The reason for measuring the losses and AC resistances of the steel rod(s) of Figure 7.9, at varying frequencies with sinusoidal current and voltage, is to compare measured results with existing theoretical solutions [68]. If theoretical results corroborate those of the two measurement approaches, then one can use these two measurement methods for inductor configurations for which no theoretical solutions are known. The goal of such inductor loss measurements is the efficiency improvement of the rectifier and inverter of Chapters 2 and 3; only if the losses in these components are known can the efficiency of the entire drive train be improved.

For a solid round wire, the ratio of the AC resistance to the DC resistance can be written [68] as

$$\frac{R_{AC}}{R_{DC}} = \frac{1}{\sqrt{2}} \frac{a}{\delta} \frac{\text{ber } P \;\; \text{bei}' \; P - \text{bei } P \;\; \text{ber}' \; P}{(\text{ber}' \; P)^2 + (\text{bei}' \; P)^2} \;, \tag{7.24}$$

where $P = \sqrt{2}\left(\frac{a}{\delta}\right)$, a is the radius of the wire, $\delta = \sqrt{\frac{2}{\omega\mu\sigma}}$, μ and σ are the permeability and conductivity of the wire material respectively, $\omega = 2\pi f$ is the angular frequency, and $R_{DC} = \frac{1}{\pi a^2 \sigma}$. Equation 7.24 is obtained by solving the zero-order Bessel equation. The functions "ber" and "bei" are called "Bessel real" and "Bessel imaginary" and are

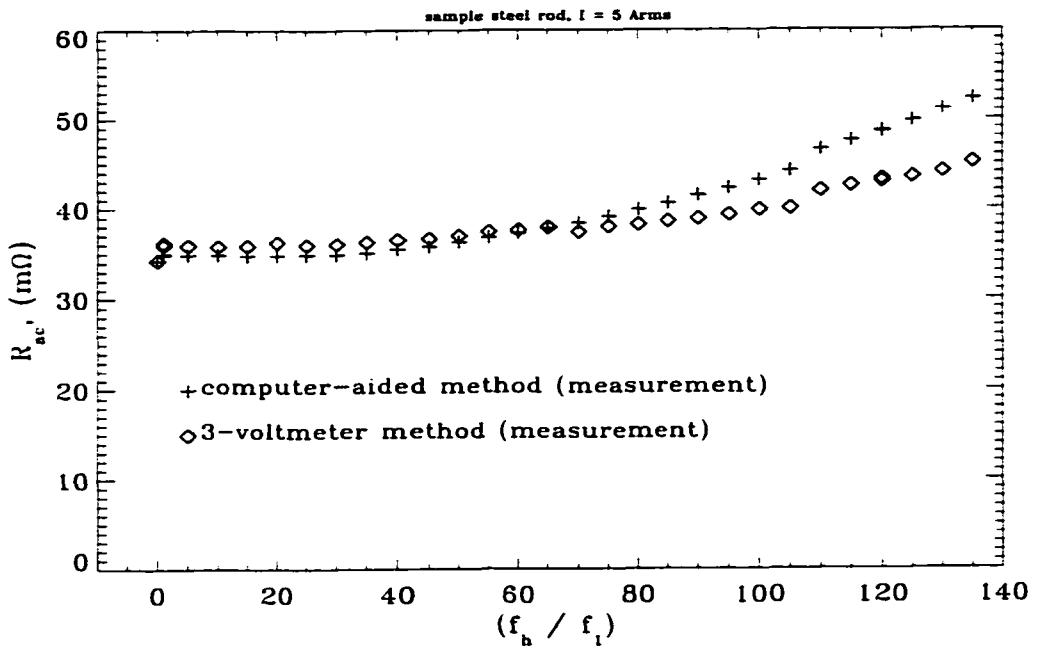

Figure 7.10: AC resistance, R_{AC} of steel rods, $f_1 = 60Hz$.

defined as

$$\text{ber } x = 1 - \frac{x^4}{(2!)^2 \cdot 2^4} + \frac{x^8}{(4!)^2 \cdot 2^8} - \frac{x^{12}}{(6!)^2 \cdot 2^{12}} + \cdots \tag{7.25}$$

$$\text{bei } x = \frac{x^2}{(1!)^2 \cdot 2^2} - \frac{x^6}{(3!)^2 \cdot 2^6} + \frac{x^{10}}{(5!)^2 \cdot 2^{10}} - \cdots \tag{7.26}$$

$$\text{ber}' x = \frac{d}{dx}(\text{ber } x) \tag{7.27}$$

$$\text{bei}' x = \frac{d}{dx}(\text{bei } x) \ . \tag{7.28}$$

At high frequencies, where the skin depth is much smaller than the radius of wire, i.e., $\delta \ll a$, then the current flows essentially only within a ring of outer radius a and a skin-thickness δ [69]. The resistance of the wire at high frequencies can be reasonably approximated as being equal to the resistance of the ring, becoming for a unit length (ohm/m):

$$R_{AC} = \frac{1}{\sigma A_{ring}} = \frac{1}{\sigma\pi(2a\delta - \delta^2)} \ . \tag{7.29}$$

Dividing by R_{DC}, obtains the approximation

$$\frac{R_{AC}}{R_{DC}} = \frac{a^2}{2a\delta - \delta^2} = \left(\frac{a}{\delta}\right)^2 \frac{1}{(2\frac{a}{\delta} - 1)} \ . \tag{7.30}$$

Equations 7.24 and 7.30 are plotted together in Figure 7.11 as a function of (a/δ). The x-axis can be converted to frequency with the following transformation

$$f = \left(\frac{a}{\delta}\right)^2 \frac{1}{a^2 \mu \sigma \pi} \tag{7.31}$$

where a and δ are in meters.

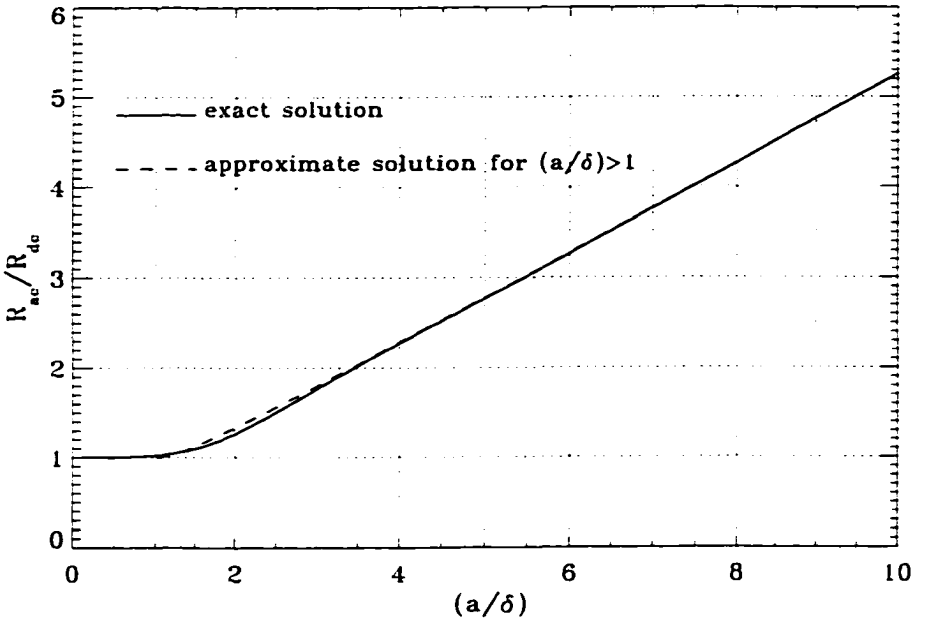

Figure 7.11: Analytical solution of skin effect resistance ratio for a solid round wire.

Equation 7.24 is plotted, together with the results of the two different measurement approaches, as a function of the a/δ in Figure 7.12. Permeability and conductivity of the "nonmagnetic" steel rods must be known in order to compute skin depth (δ). Using the DC voltage-drop method, the resistance can be determined, and then the conductivity is computed from the length of the steel rods. Conductivity of the connecting wires are also included in this measurement. Since the permeability of the "nonmagnetic" steel rod is not exactly known and the value of conductivity (σ_s) obtained from DC voltage drop method is only an approximation, a value of $\sigma\mu = \sigma_s \mu_r \mu_0$ (where μ_r=9) is used when determining penetration depth.

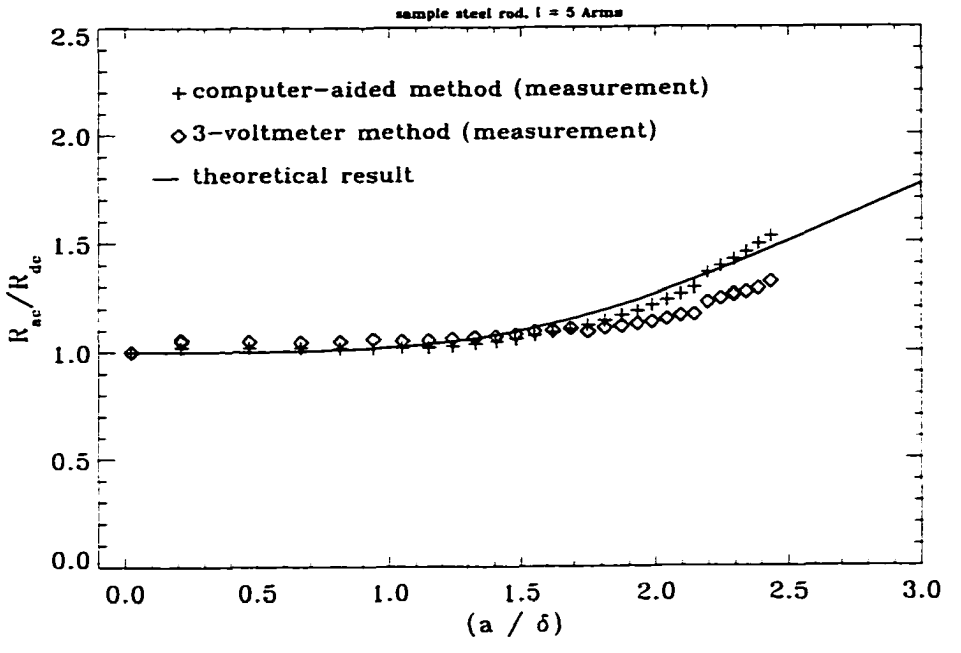

Figure 7.12: Skin effect resistance ratio of round steel rods.

7.6.3 Results for Inductors with Stranded Conductors

The measured AC resistance-frequency functions for inductor #1 (see Appendix A), based on the two methods, are compared in Figure 7.13 up to 6 kHz. The results of the two methods are in good agreement. Figures 7.14, 7.15 and 7.16 compare the losses of inductors #5 and #1 with and without an iron core. Such a comparison could be used for optimizing inductors, for a given inductance L_h and resistance R_{AC_h} at a certain frequency f_h (e.g., 6kHz), with respect to cost.

Losses of three different stranded wires (uninsulated from each other), where the properties are outlined in Table 7.4 are measured to compare the effects of different stranding methods. In these measurements the lengths of the wires are approximately equal, and they consist of only a single turn, where each conductor side is placed far apart to reduce the influence of the proximity effect, because at separating distances of $20cm$ or more, the proximity losses are negligible [60]. Inductors #1 and #13 have approximately same effective copper cross-section, whereas inductor #12 has about 3 times the cross-section than those of inductors #1 and #13. For each conductor, the

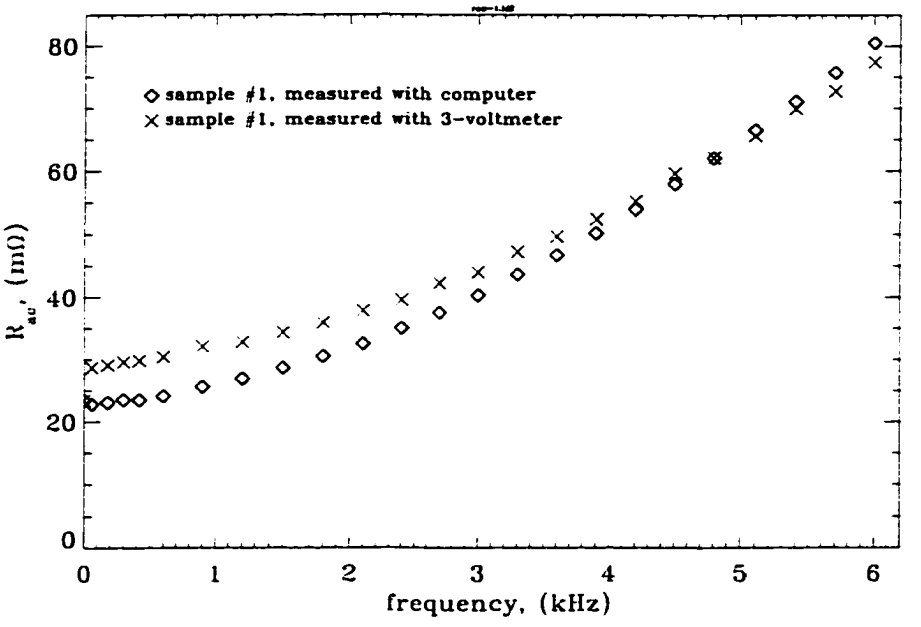

Figure 7.13: Comparison of AC resistance measured with computer-aided, and three-voltmeter methods (inductor #1, single turn).

equivalent radius of a solid wire is computed by multiplying the cross-sectional area of one strand with the number of strands.

Table 7.4: Dimensions of stranded wires.

inductor #	# of strands	# of wires in each strand	diameter of one wire in a strand (mm)	total cross sectional area (mm^2)	equivalent radius of a solid conductor (mm)
1	19	7	0.254	6.739	1.4646
12	7	1	1.9558	21.0299	2.5873
13	7	1	1.2192	8.1722	1.6128

Figure 7.17 illustrates that the strand size or the number of strands does not really affect the losses, provided the total cross-sectional areas are the same. The losses are reduced if a wire with a larger cross-sectional area is used. However, the increase in the AC resistance (due to frequency) of a conductor with a larger cross-section is greater than that of a smaller sized conductor. One reason for the significant resistance increase of conductors with strands versus those with a solid cross-section is the asymmetry in

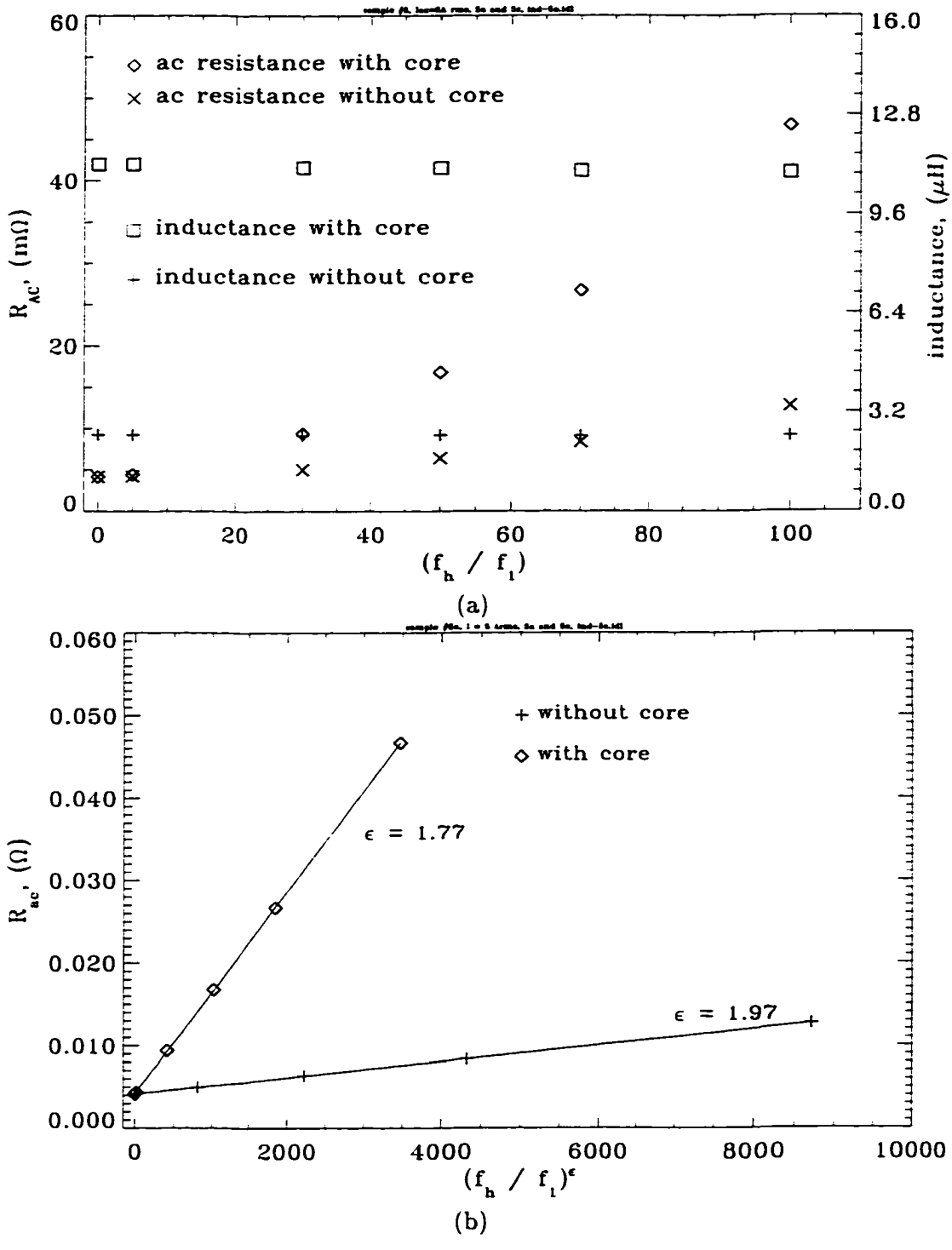

Figure 7.14: (a) The AC resistance and inductance of inductor #5, and (b) change of AC resistance as a function of frequency, $R_{DC} = 4.14m\Omega$, $R_{6kHz}/R_{DC} = 11.28$.

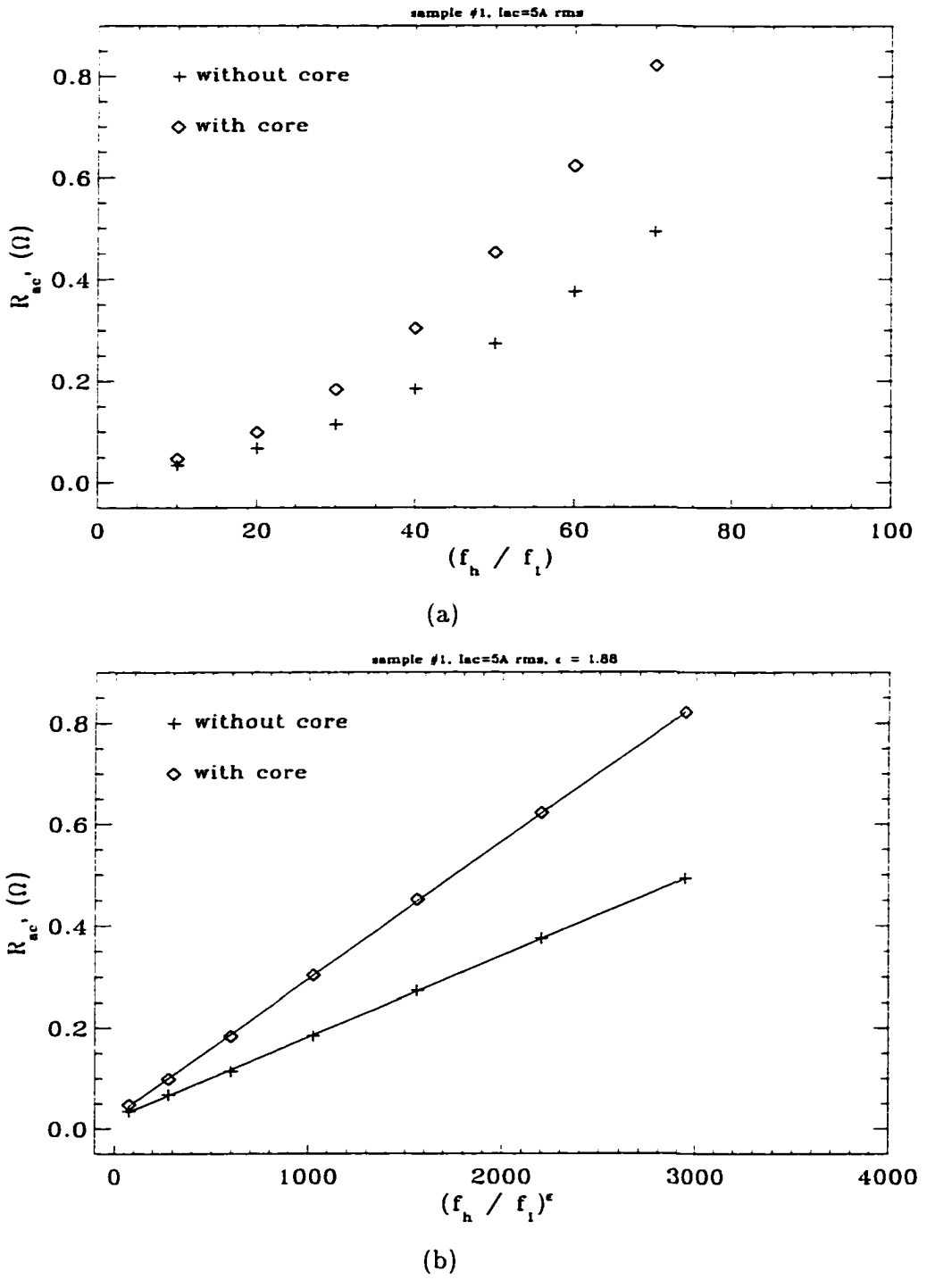

Figure 7.15: (a) The AC resistance of inductor #1, and (b) change of AC resistance as a function of frequency.

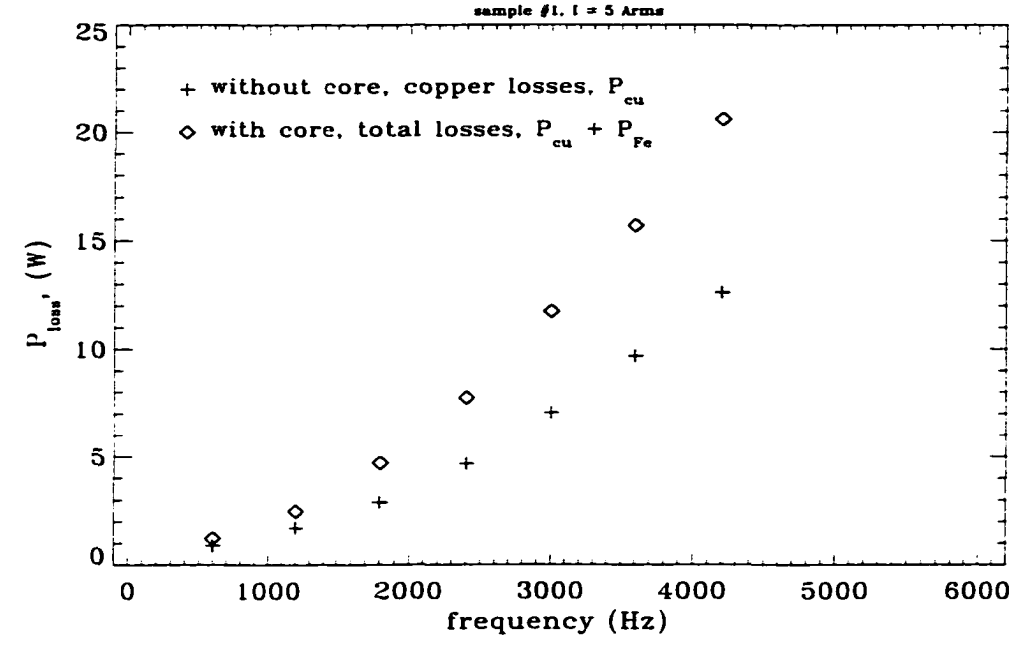

(a)

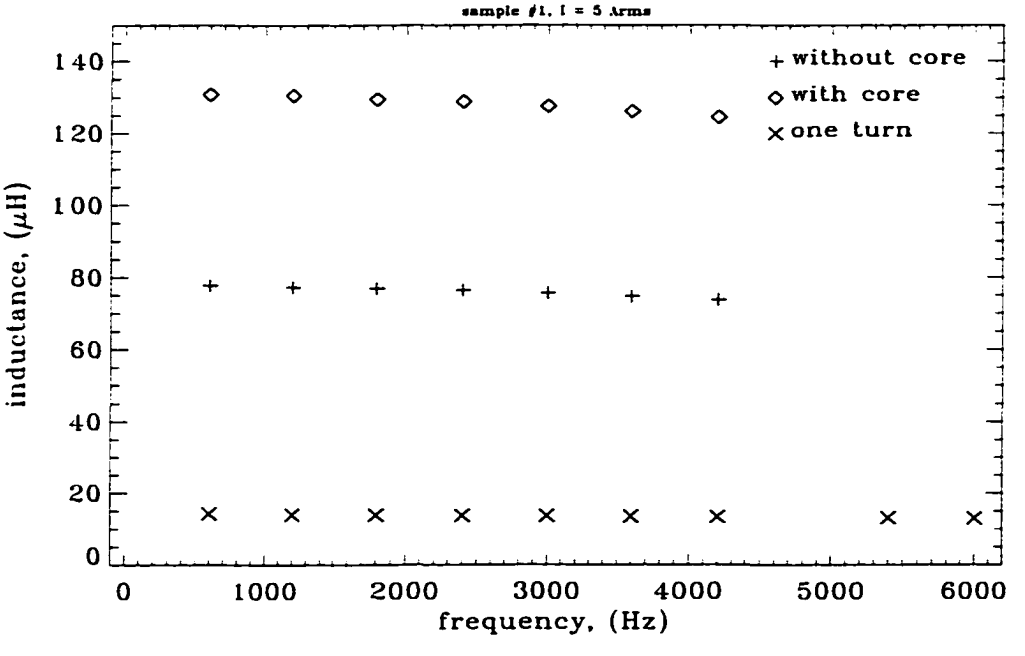

(b)

Figure 7.16: (a) Copper loss (P_{cu}) and iron core loss (P_{fe}) and (b) inductance of inductor #1.

the conductor structure introduced by uninsulated strands (spirality effect), resulting in additional eddy currents [60]. Figures 7.18 to 7.21 show the AC resistance increase as a

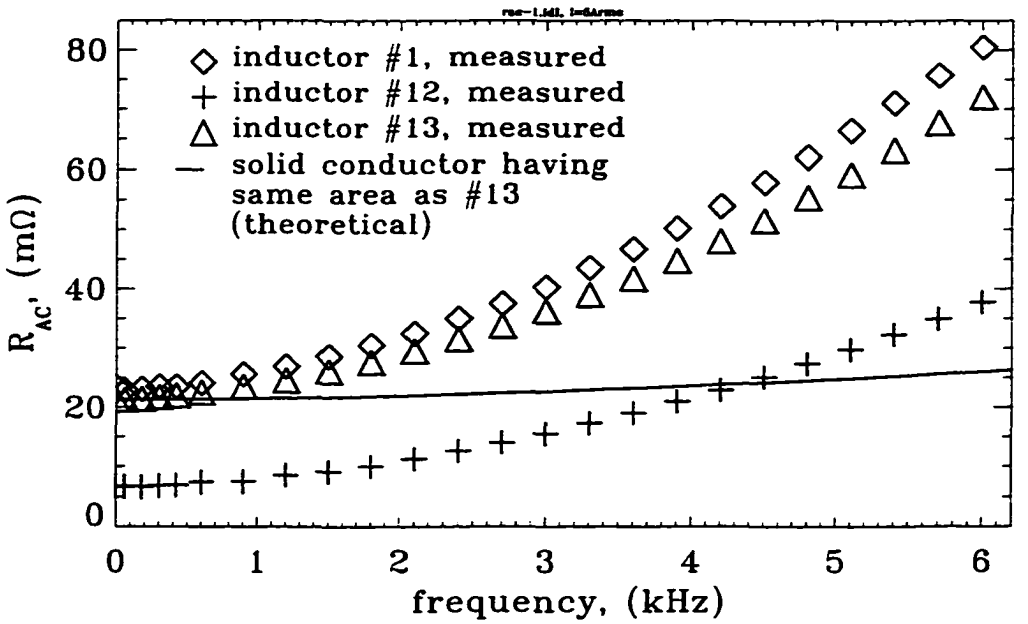

Figure 7.17: AC resistances of inductors #1, 12, and 13 at $I_{rms} = 5A$ (all inductors have single turns).

function of frequency for inductors #2, #6, #7, and #10. The measured AC resistances for inductors using solid wires are given in Figures 7.22 to 7.26.

7.7 Conclusions

Two different measurement approaches (computer-aided and three-voltmeter) have been applied to determine how the losses of inductors vary with frequency. Both methods can measure losses of a few watts with an error of less than 10% (see Figures 7.10, 7.12, and 7.13).

The resistance increase of inductor #2 (see Figure 7.18a) is much larger than that of inductor #5 (see Figure 7.14) where Litz wires are used. Figure 7.24 represents the resistance increase for a DC filter inductor #8. In this case a large increase of the resistance from DC to 6kHz is desirable, to reduce switching harmonics in the DC output

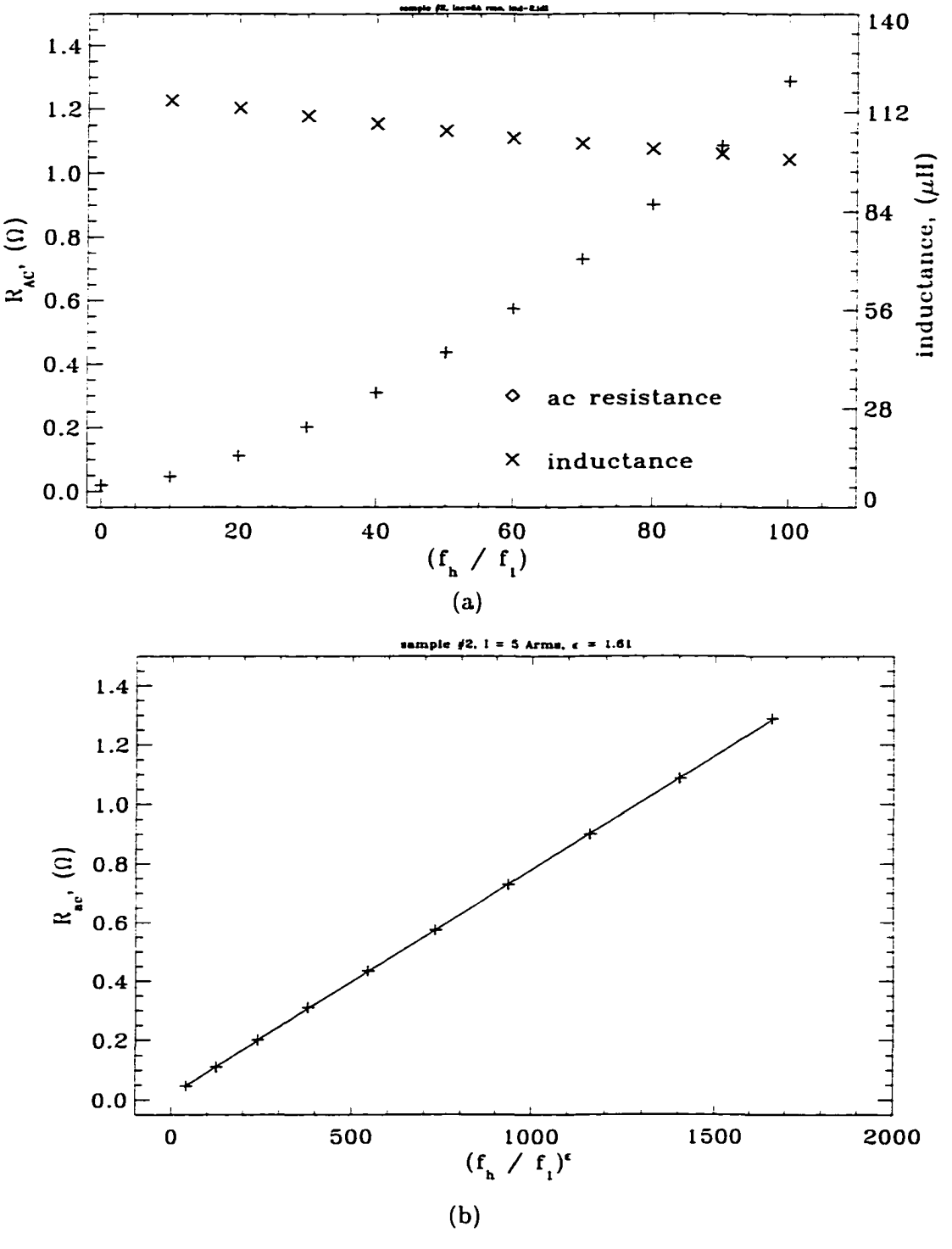

Figure 7.18: (a) The AC resistance and inductance of inductor #2, and (b) change of AC resistance as a function of frequency, $R_{DC} = 18.5m\Omega$, $R_{6kHz}/R_{DC} = 64.4$.

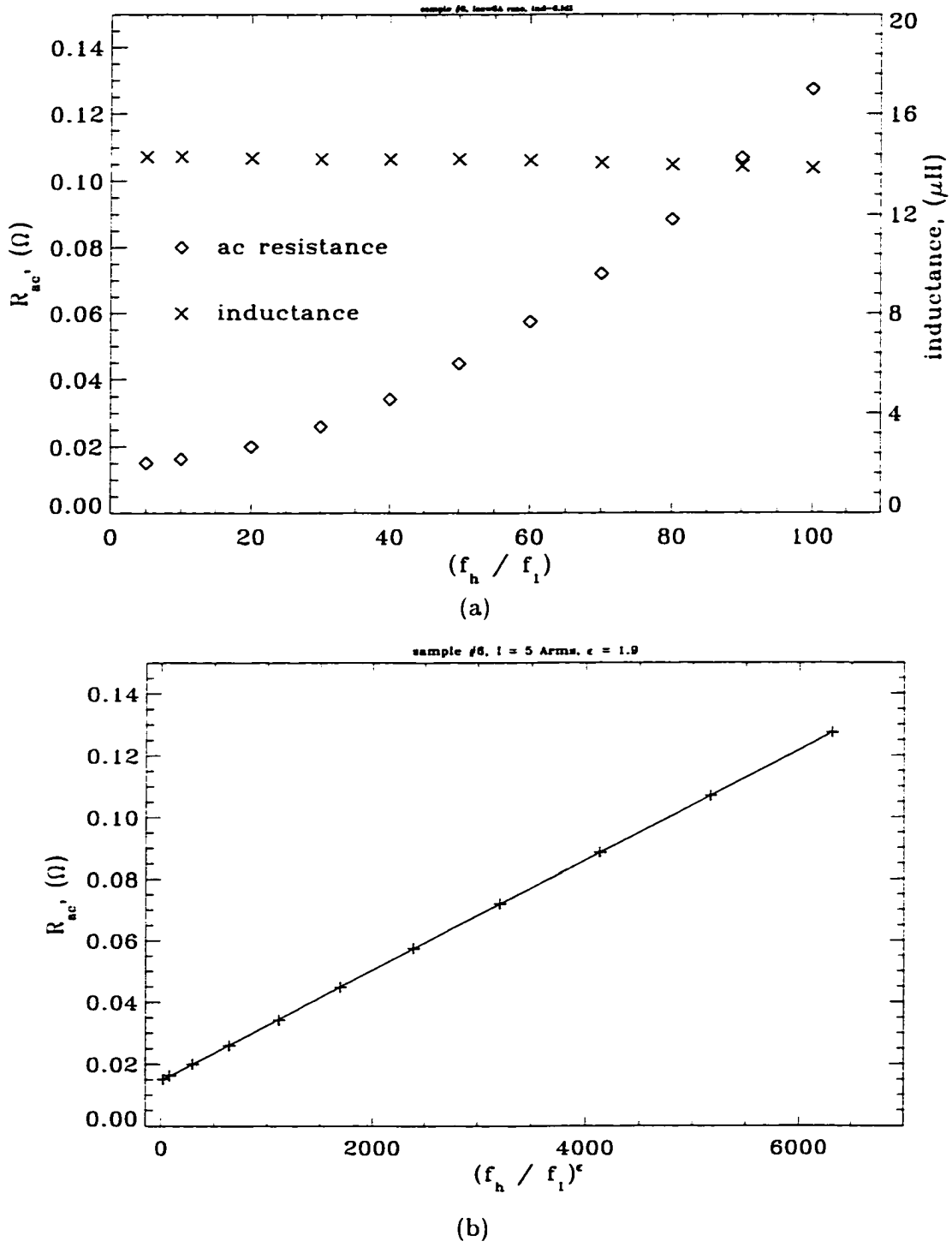

Figure 7.19: (a) The AC resistance and inductance of inductor #6, and (b) change of AC resistance as a function of frequency.

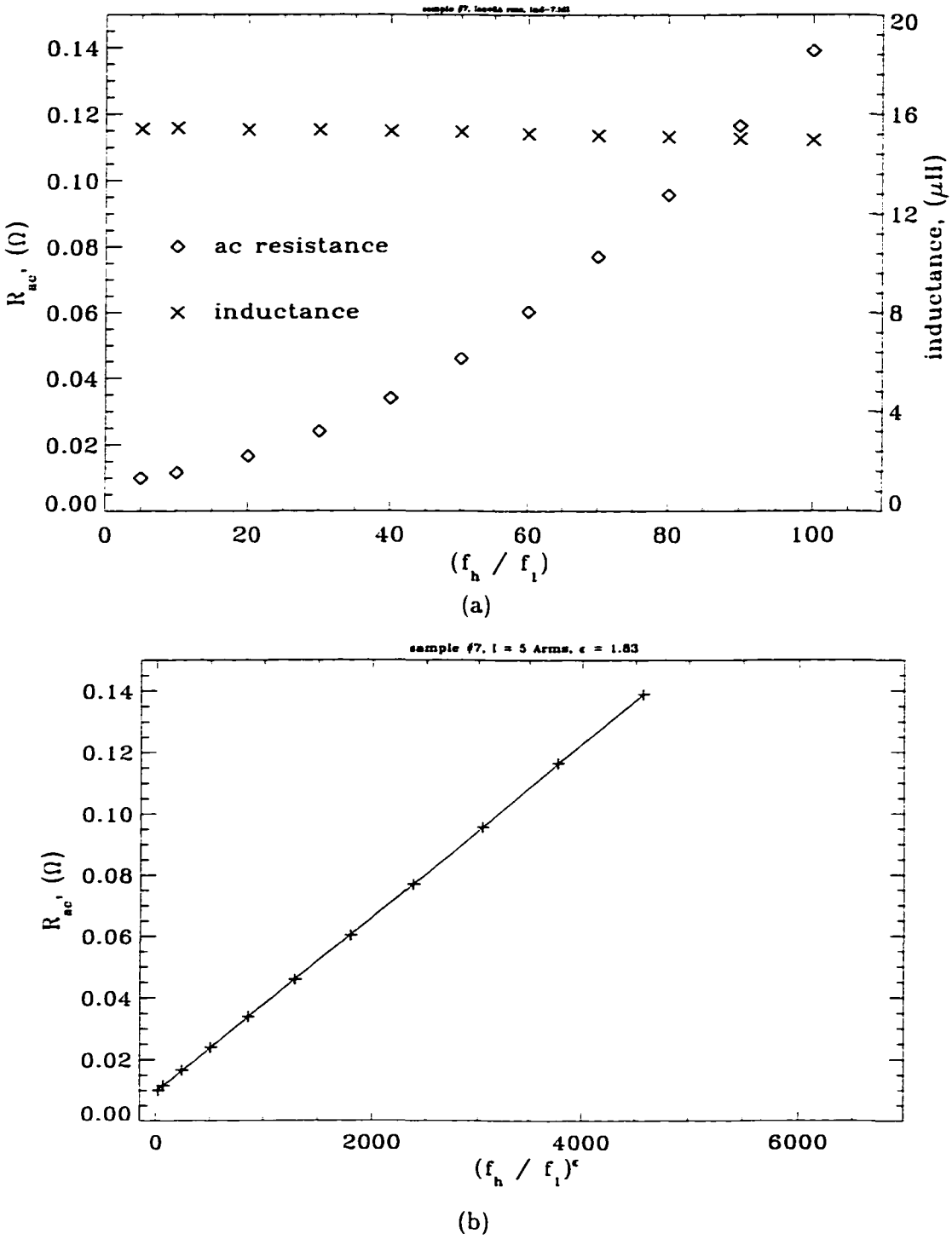

Figure 7.20: (a) The AC resistance and inductance of inductor #7, and (b) change of AC resistance as a function of frequency.

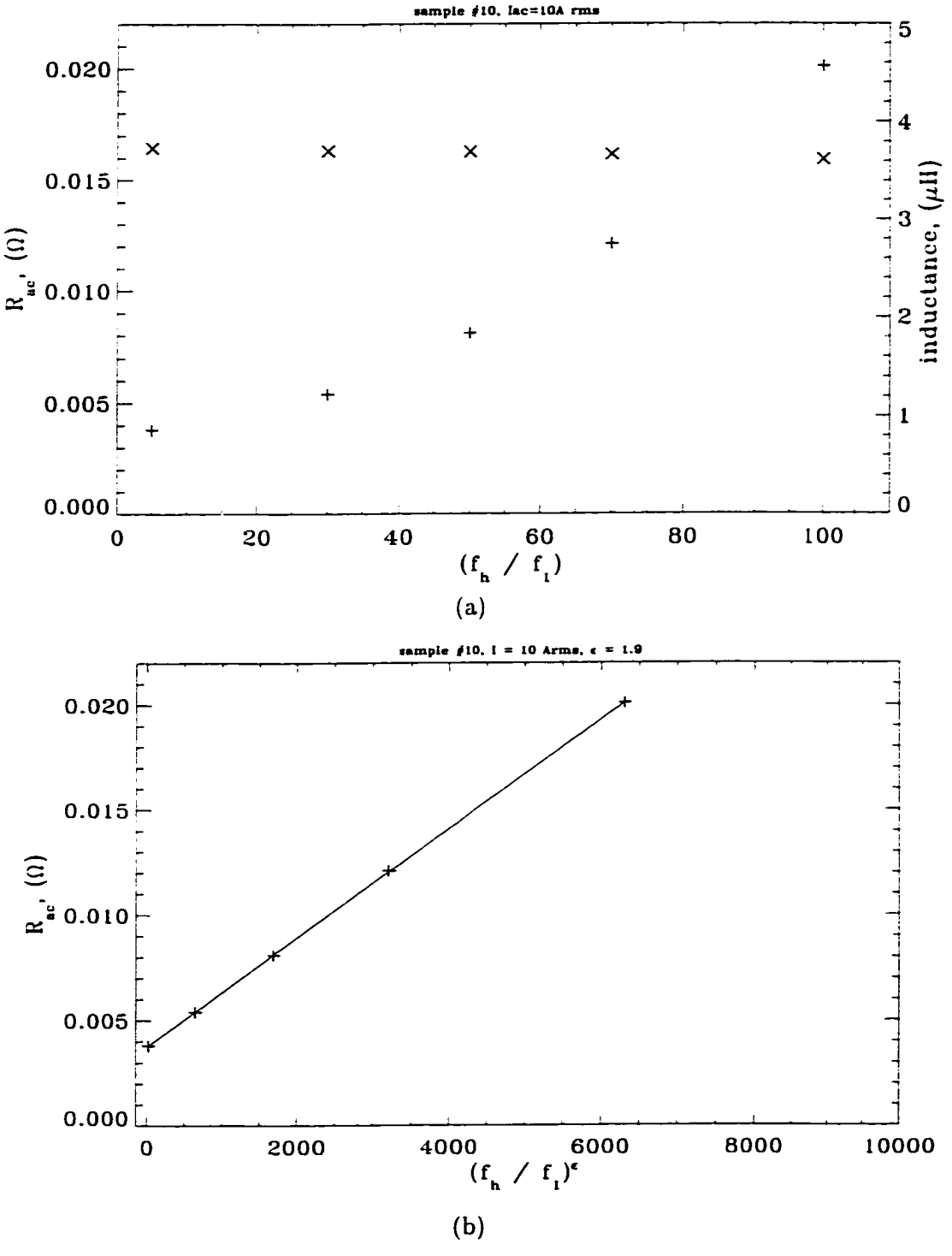

Figure 7.21: (a) The AC resistance and inductance of inductor #10, and (b) change of AC resistance as a function of frequency.

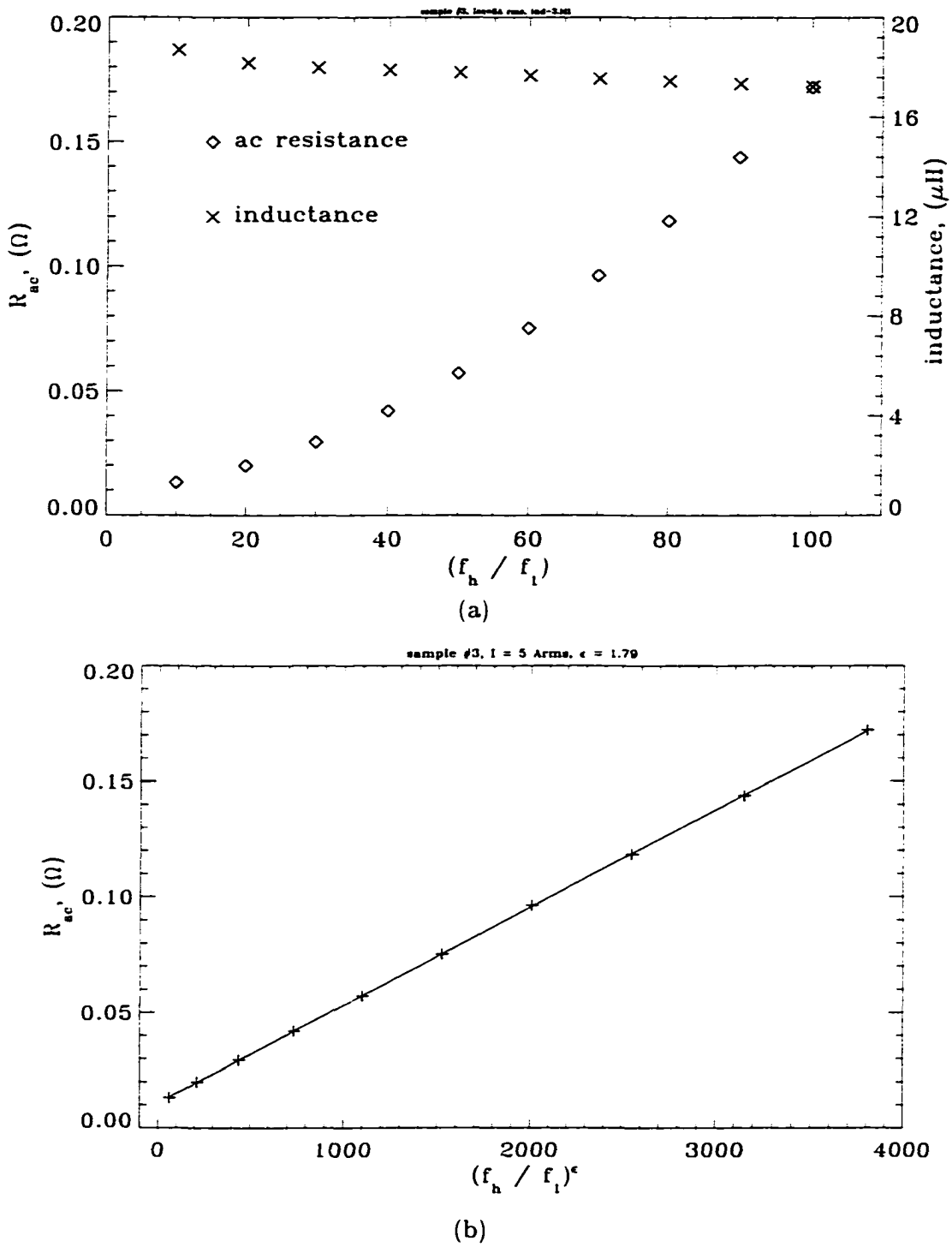

Figure 7.22: (a) The AC resistance and inductance of inductor #3, and (b) change of AC resistance as a function of frequency.

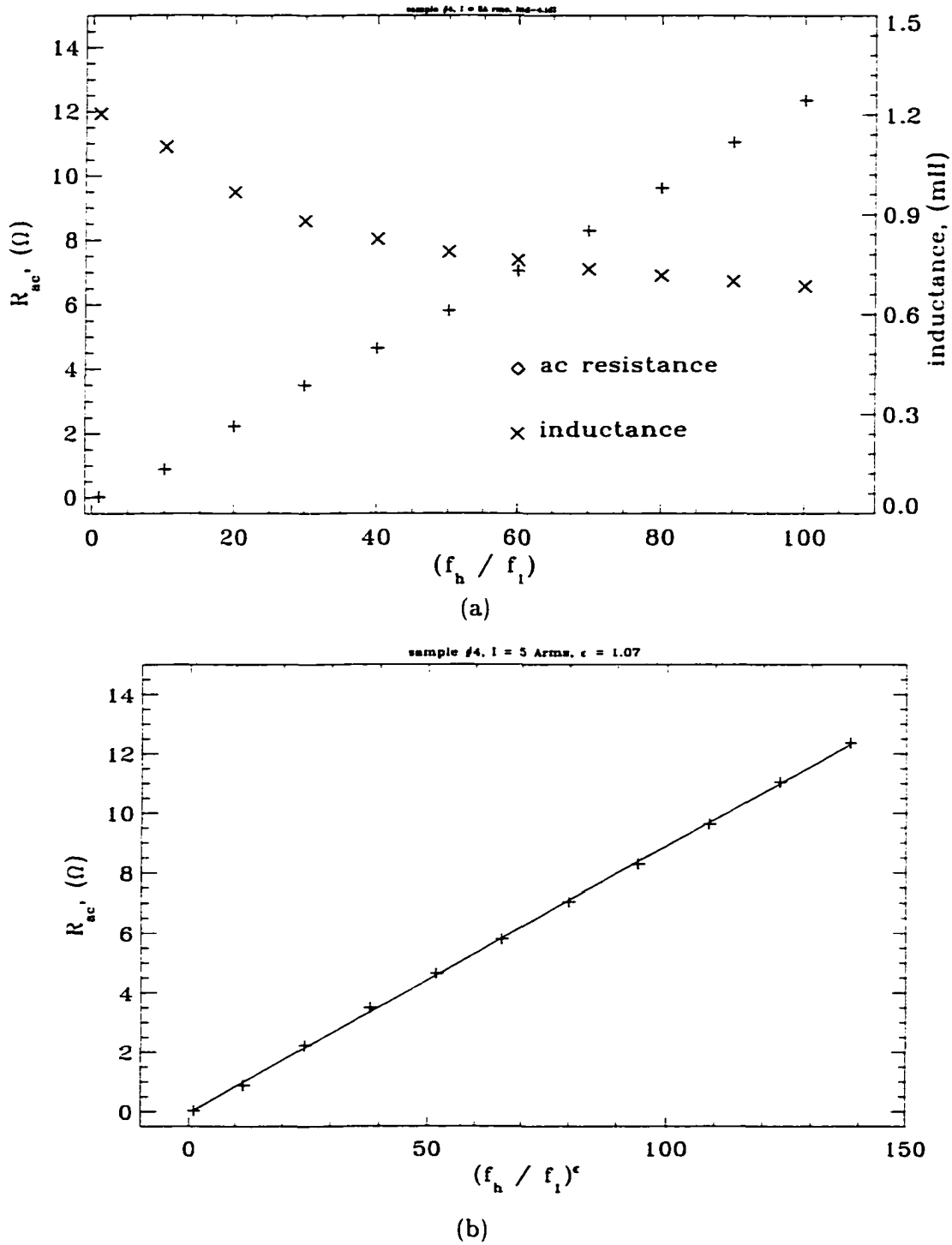

Figure 7.23: (a) The AC resistance and inductance of inductor #4, and (b) change of AC resistance as a function of frequency.

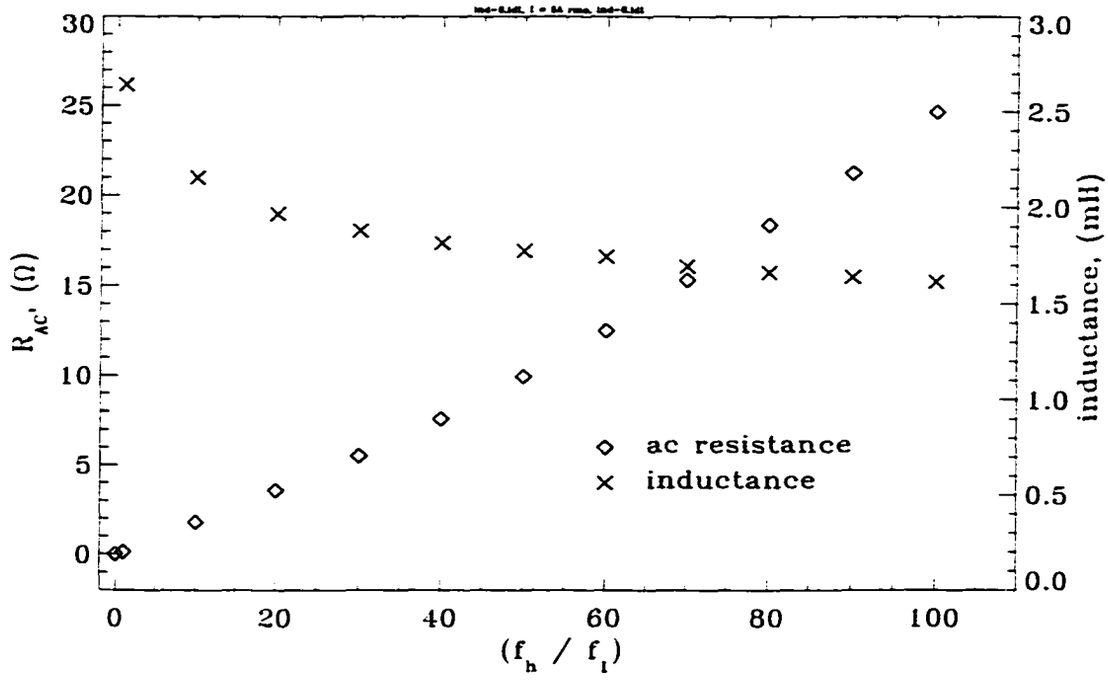

(a)

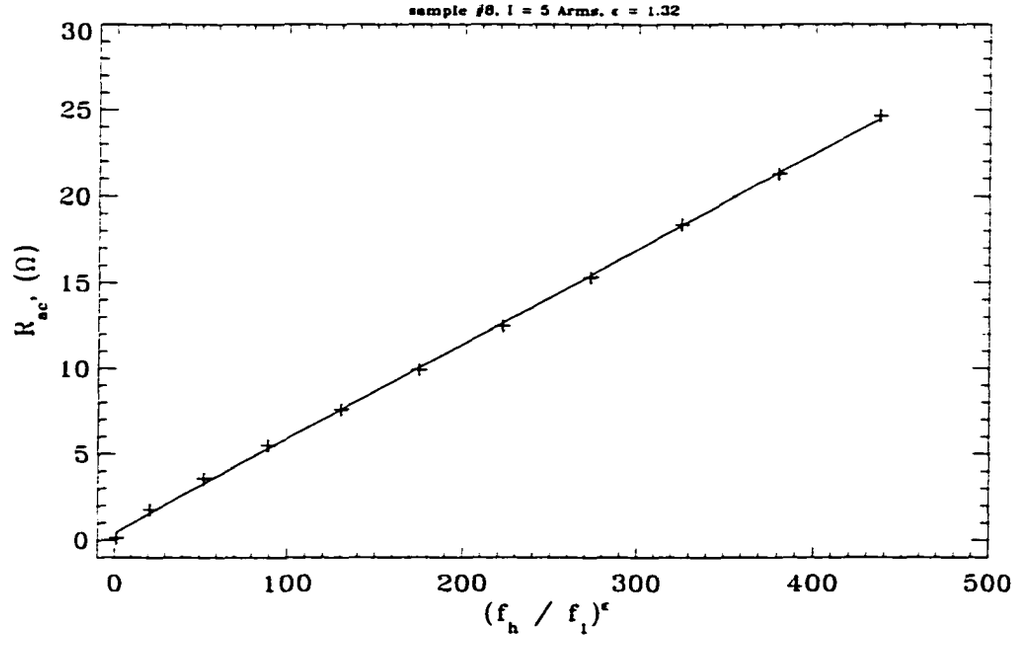

(b)

Figure 7.24: (a) The AC resistance and inductance of inductor #8, and (b) change of AC resistance as a function of frequency, $R_{DC} = 10.7m\Omega$, $R_{6kHz}/R_{DC} = 2303$.

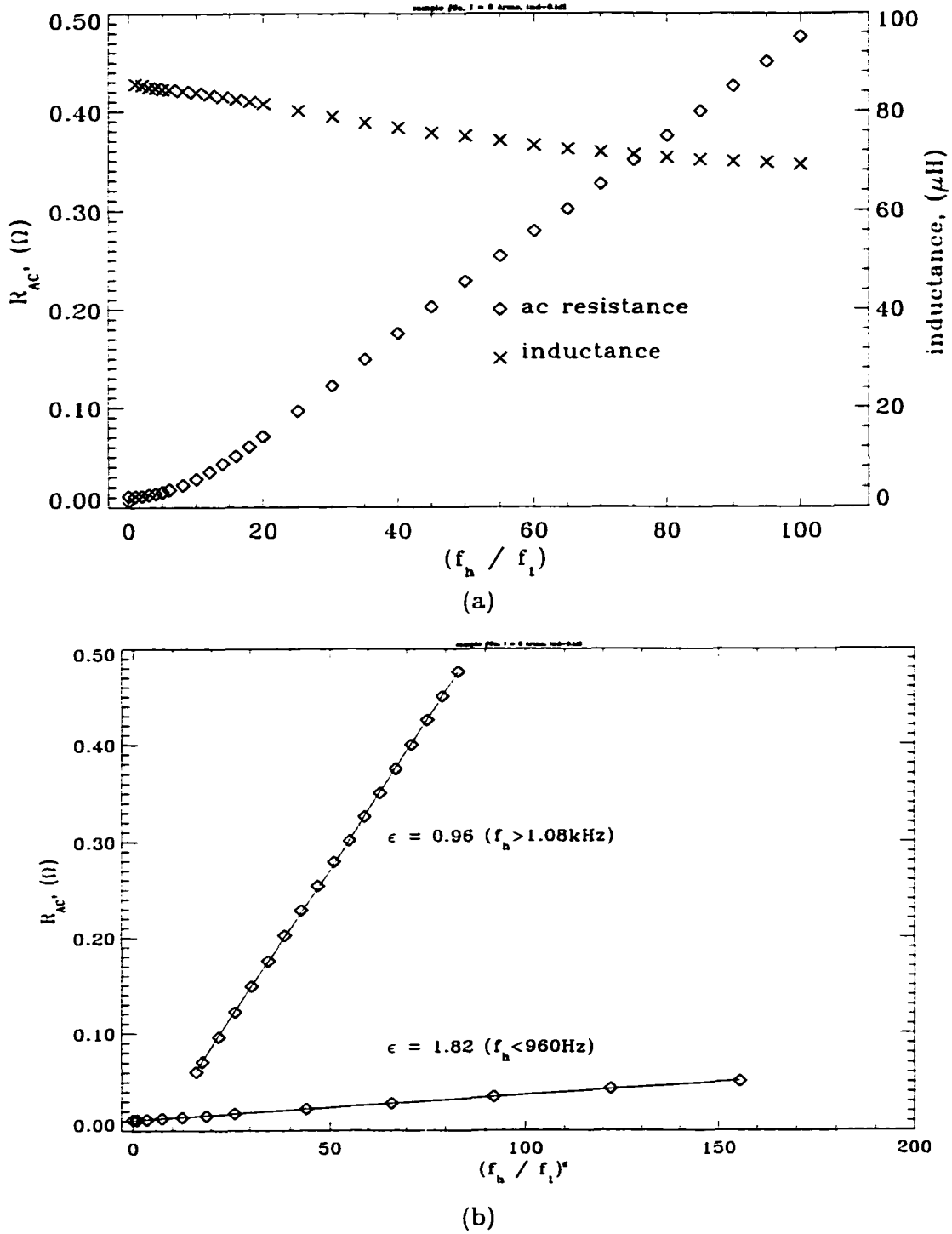

Figure 7.25: (a) The AC resistance and inductance of inductor #9, and (b) change of AC resistance as a function of frequency, $R_{DC} = 11.2m\Omega$, $R_{6kHz}/R_{DC} = 43$.

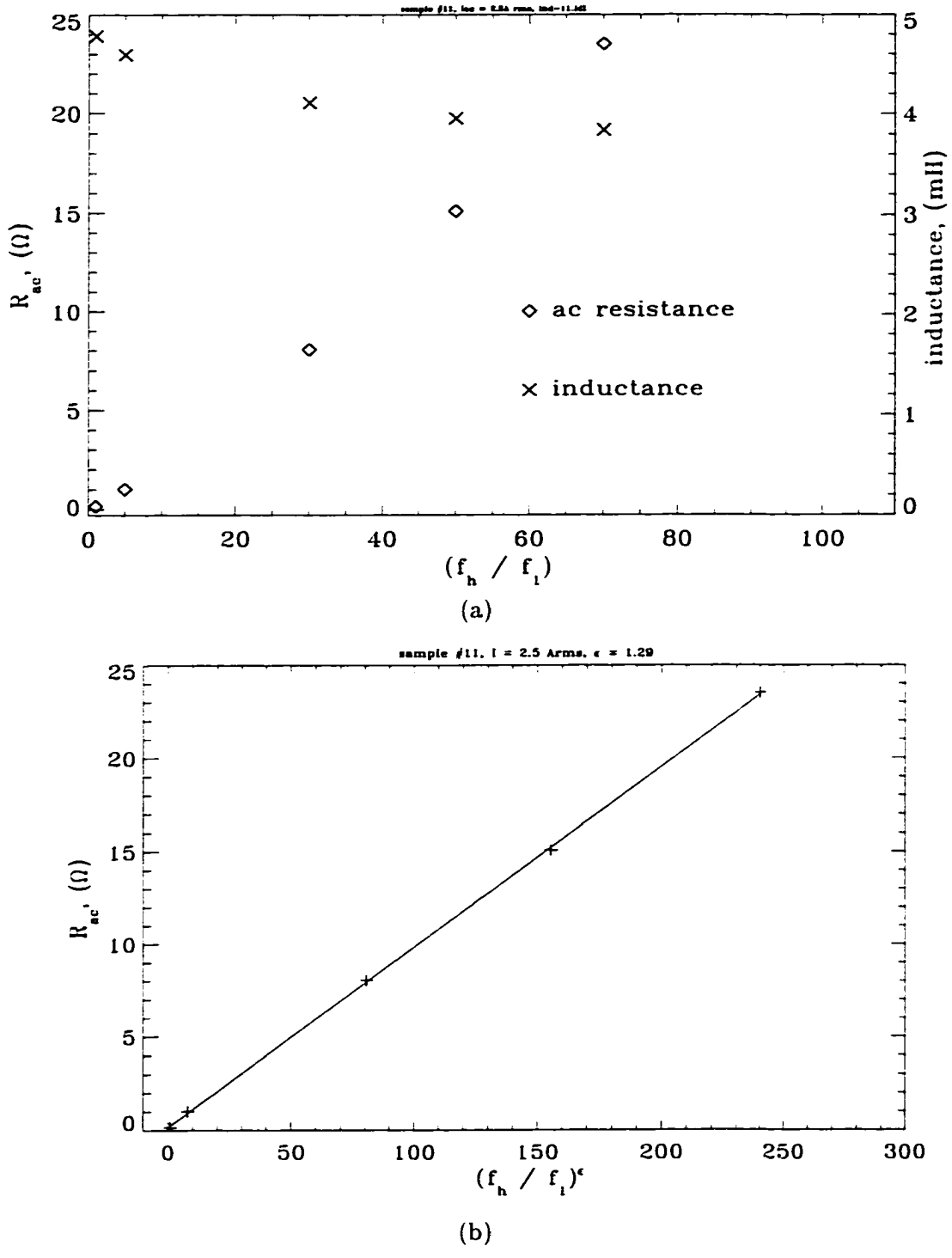

Figure 7.26: (a) The AC resistance and inductance of inductor #11, and (b) change of AC resistance as a function of frequency.

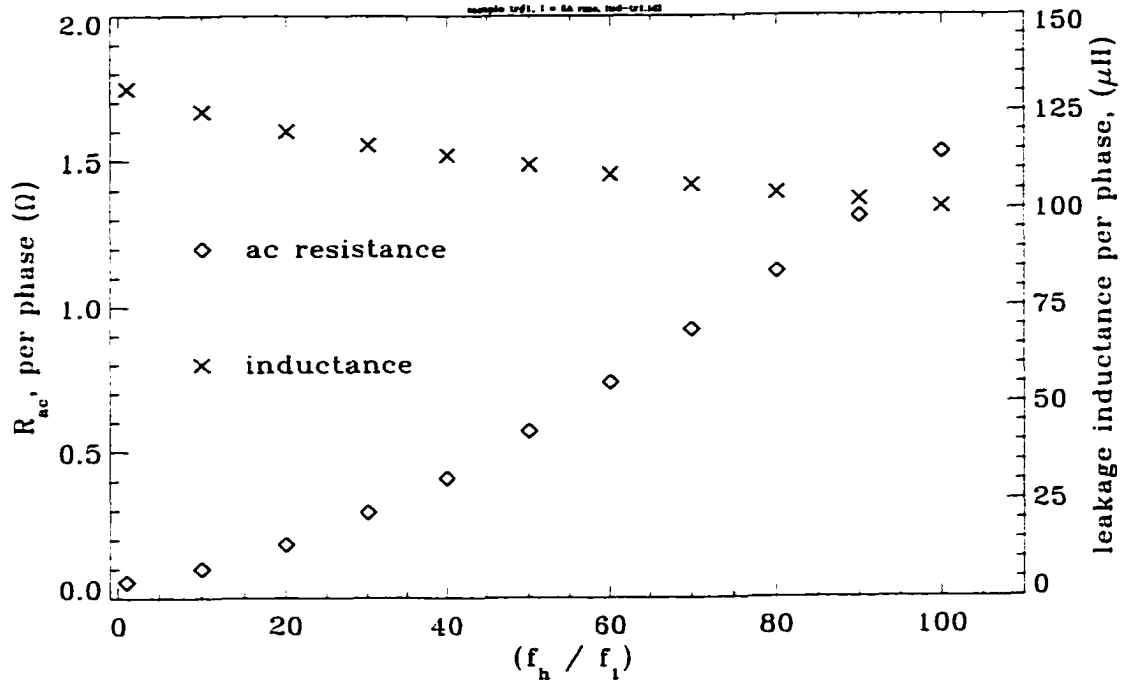

(a)

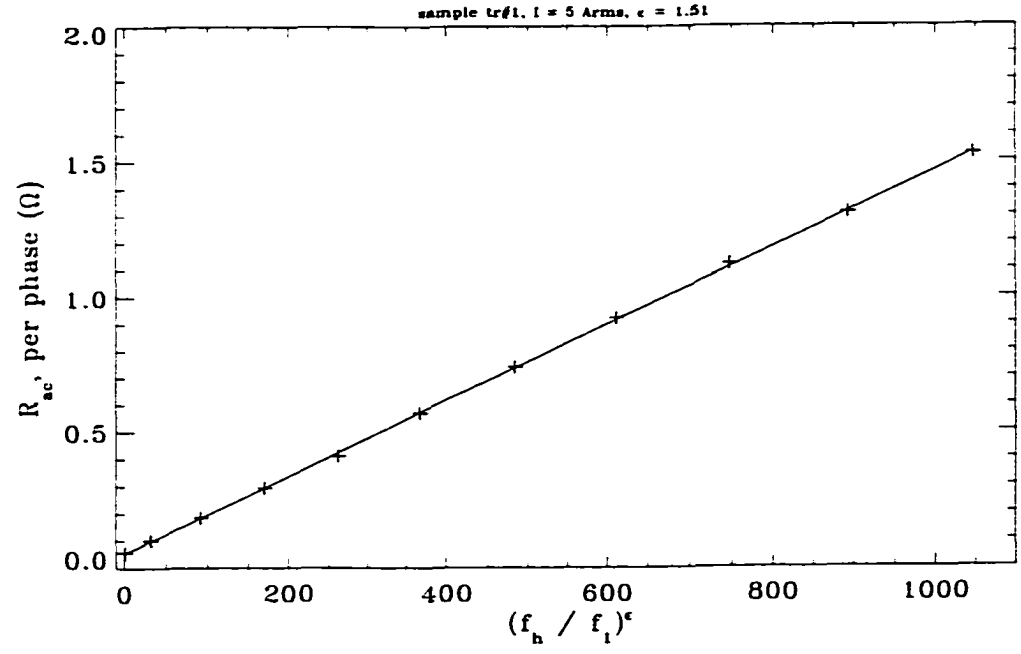

(b)

Figure 7.27: (a) The AC resistance and inductance of transformer #1, and (b) change of AC resistance as a function of frequency.

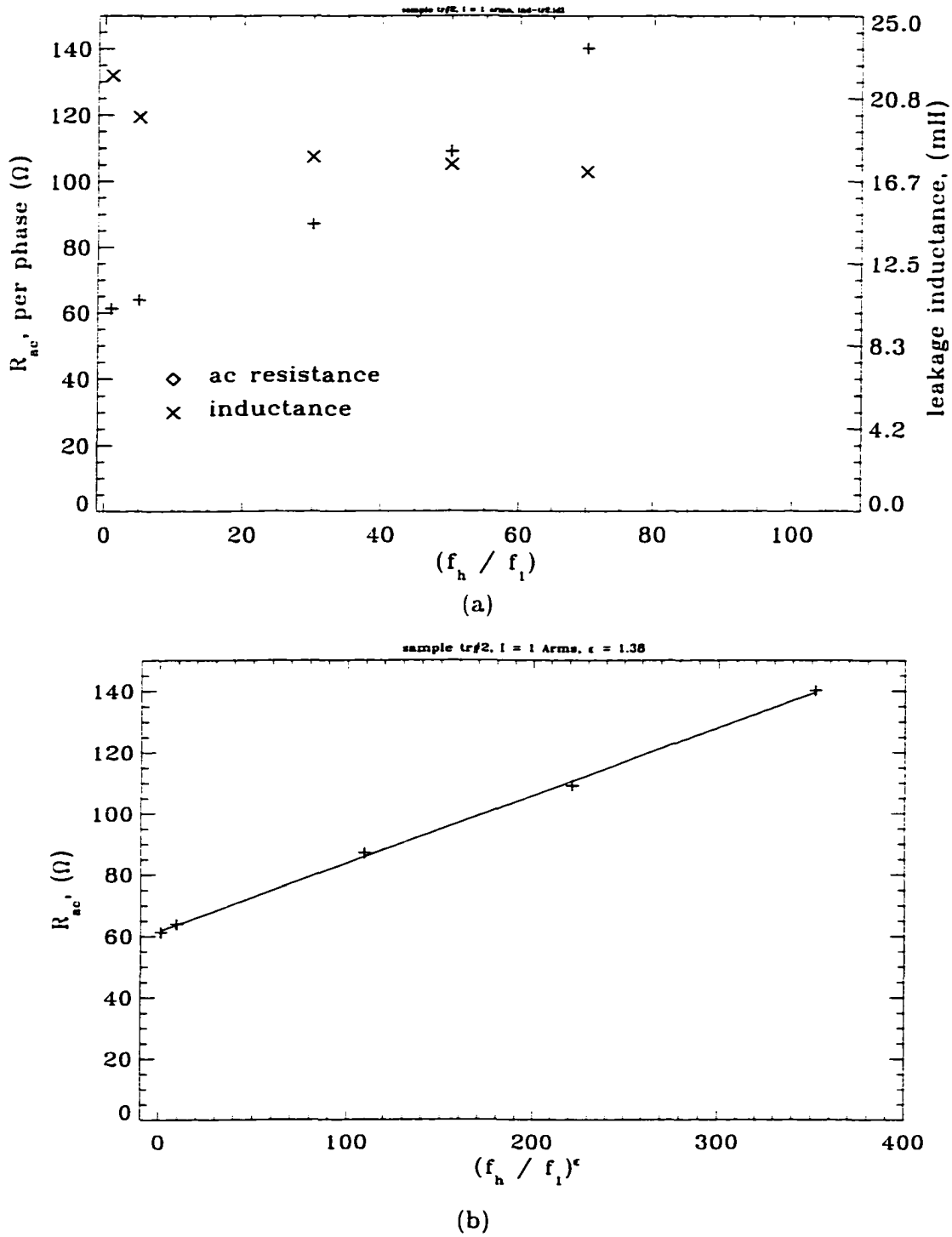

Figure 7.28: (a) The AC resistance and inductance of transformer #2, and (b) change of AC resistance as a function of frequency.

of a rectifier, however this increase reduces the efficiency if the harmonic currents are impressed. Inductor #9 contains an iron-core, therefore, the measured losses include copper, iron-core and stray-power losses. Examination of Figure 7.25a shows that at lower frequencies ($< 1kHz$) the losses increase as a quadratic function of frequency; while at high frequencies, a linear relationship is observed. This is illustrated in Figure 7.25b, where two different curves (for high and low frequencies) for R_{AC} are plotted. Note that the same type of core shown in Appendix B (type I) is used in inductors #5, 9, and 2, while inductor #8 has an EI type core. The AC resistance of inductor #8 is more than 2000 times its DC resistance value. This can be explained by the fact that since a large volume of core material is employed: the core losses are larger than the copper and stray-power losses.

Inductor #9 was also tested at 30 different frequencies, up to 6kHz. It can be seen from Figure 7.25a that at low frequencies, e.g., $f_h/f_1 < 12$, the AC resistance increases with the square of the frequency, but at high frequencies a linear relationship can be observed. This is illustrated in Figure 7.25b where the data are split into two portions at the 12th harmonic of 60Hz. By changing the value of x-axis, i.e., adjusting ε in $(f_h/f_1)^{\varepsilon}$, a linear relationship which best fits the measured data can be obtained. Table 7.5 summarizes the ratio of AC resistances at $6kHz$ to the DC resistance of wire for different inductors.

The following conclusions can be drawn from the measurement results:

1. This chapter demonstrates accurate loss measurement techniques for inductors operating at high frequency (e.g., $6kHz$) with low power dissipation. The upper limit of the frequency can be significantly (e.g., $30kHz$) increased if A/D converters, with a higher sampling frequency, e.g., $5MHz$, are employed.

2. The computer-aided measurement technique applies to any (non)sinusoidal wave form, while the three-voltmeter method is limited to sinusoidal signals.

Table 7.5: Ratio of the AC resistance values to the DC resistance values of the inductors (m indicates 10^{-3}).

inductor #	R_{DC} (Ω)	R_{AC}^{6kHz} (Ω)	$\frac{R_{AC}^{6kHz}}{R_{DC}}$	comments
1	$23.4m$	0.821	35.08	with core
1	$23.4m$	0.493	21.07	without core
1	$23.4m$	$80.5m$	3.44	single loop, one turn
2	$20.0m$	1.288	64.4	
3	$13.2m$	$172.1m$	13.04	
4	$28.3m$	12.36	436.75	
5	$4.14m$	$46.7m$	11.28	with core
5	$4.14m$	$10.5m$	2.54	wound as 7 turns in 2 layers, no core
6	$15.1m$	$127.4m$	8.44	
7	$10.0m$	$139.0m$	13.9	
8	$10.7m$	24.65	2303.7	
9	$11.1m$	$476.0m$	42.88	
10	$3.9m$	$19.9m$	5.1	
11	0.15	23.5	156.67	R_{AC} at $f_h = 4.2kHz$
12	$6.76m$	$37.76m$	5.59	single loop, one turn
12	$6.76m$	$170.57m$	25.23	wound as 8 turns in 4 layers, no core
13	$21.3m$	$72.08m$	3.38	single loop, one turn
steel rods	$34.26m$	$52.3m$	1.53	two in series
transformer 1	$56.3m$	1.526	27.1	
transformer 2	61.29	140.17	2.29	R_{AC} at $f_h = 4.2kHz$

3. A stranded wire (uninsulated strands, no core, proximity effects absent) has larger losses than a solid wire having the same cross-sectional area (see Fig. 7.17). This agrees with the results obtained in [60].

4. If a stranded conductor (uninsulated strands, no core, proximity effects absent) is used, losses are similar for different strand sizes if the conductors have the same total cross-sectional area.

5. For the same number of strands (uninsulated strands, no core, proximity effects absent) but different cross-sectional areas of conductors, the increase with fre-

quency of the AC resistance of a conductor with thicker strands is larger than those having thinner strands (Fig. 7.17).

6. For example, for a $10\mu H$ Litz-wire inductor with iron core, the resistance ratio is $R_{6kHz}/R_{DC} = 11.28$; for a $100\mu H$ stranded-wire inductor with iron core one measures $R_{6kHz}/R_{DC} = 64.4$; for a $17\mu H$ inductor wound with copper sheets $R_{6kHz}/R_{DC} = 13.04$; for a $100\mu H$ (uninsulated) solid-wire inductor with iron core $R_{6kHz}/R_{DC} = 43$; and for a $2mH$ solid-wire inductor with iron core, one measures $R_{6kHz}/R_{DC} = 2303$.

7. Total losses of an inductor with solid wire (copper winding and iron core), at high frequencies, increase linearly with frequency; however, the increase is quadratic at low frequencies (see Figure 7.25).

8. The other stray losses P_{OSL} increase up to a certain frequency with an exponent of ϵ=0.8, and then decrease with an exponent of ϵ=0.9. The frequency where maximum losses occur depends, at a given frequency ,on the type of conductor material used.

As can be expected, Litz wire has much lower AC resistance at high frequencies (e.g., 6kHz), as compared with solid and stranded conductors (uninsulated and no symmetric transposition of individual strands). Comparing Figures 7.14, 7.18,and 7.25 shows that the value of inductance does not change much with the frequency if Litz wires are used. Unfortunately, Litz wires are more expensive than solid-wire and stranded-conductor inductors. Hollow (tube shaped) conductors have also less skin effect than the solid and stranded wires [60]. However, they require a relatively large space for the winding.

CHAPTER 8

MEASUREMENT OF EDDY-CURRENT LOSS COEFFICIENT P_{EC-R}, DERATING OF SINGLE-PHASE TRANSFORMERS, AND COMPARISON WITH K-FACTOR APPROACH

8.1 Introduction

A power amplifier is now used to supply sinusoidal currents of different frequencies for measuring eddy-current losses of a 25kVA single-phase transformer under short-circuit conditions. Measured data show that eddy-current loss increases with the square of frequency. The linear eddy-current loss coefficient ($P_{EC-R_{linear}}$) is also computed from the measured data. New measurement techniques are applied to determine the derating of single-phase transformers with full-wave diode and thyristor rectifier loads. The derating of transformers has been defined such that for the (apparent, real) power transfer of a transformer, the total losses are identical to the rated losses at rated temperature neglecting hot spot phenomena. A relation between apparent power, derating and K-factor is given, taking into account iron-core and stray-power losses. Measured derating values are compared with computed results, based on the eddy-current losses, iron-core losses, stray-power losses and K-factors. The non-linear eddy-current loss coefficient ($P_{EC-R_{nonlinear}}$) is computed from the harmonics caused by diode/thyristor bridge loads.

Recent publications [64, 70] detail the separate measurement of the iron-core losses and copper losses of single-phase transformers under (non)sinusoidal load condi-

tions. In order to make a contribution to the recommended practice for establishing transformer capability when supplying nonsinusoidal load currents, the K-factor approach [71, 72, 73] is here modified to improve the prediction of the derating [52] of single-phase transformers. In reference [74] the harmonic loss factor F_{HL} is employed - not the K-factor as defined in [71]. An objective of this chapter is to establish a relationship between derating, K-factor and iron-core losses, and to measure P_{EC-R}. An attempt is being made to define derating with respect to apparent power, nonsinusoidal current capability and real power output. The total, copper and iron-core losses will be separately measured, and the derating is determined from measurements for given THDi (total harmonic distortion of current) values, where the individual current harmonics can be adjusted within certain limits.

Prior work includes the measurement of the temperature due to current harmonics [75] for the same type of pole transformer as tested: the temperatures were monitored in [75] for THD_i values (at the point of common coupling, PCC, between transformer and system) of less than 90%. It concludes that one has to derate the transformer tested, for a total harmonic distortion current of 40%, by about 3 to 12%. The associated voltage harmonic distortions have not been reported, and the individual current harmonic components could not be independently adjusted. The work in [76] measures temperatures of the same type of pole transformer for a THD_i of 110% based on two different measuring methods [74], and the paper arrives at derating values of 13% to 39% depending upon the method used; no voltage distortions have been reported.

8.2 Measurement of Linear Eddy-current Loss Coefficient

Eddy-current loss occurring in a transformer winding for sinusoidal currents is approximately proportional to the square of the frequency. Stray losses in components other than windings are proportional to less than the square [74] of the frequency. The

total copper loss in a transformer winding is commonly given by [74], [75], and [76] as

$$P_{cu} = P_{\Omega} + P_{EC} = I^2 R_{DC} + I^2 R_{EC} \left(\frac{f_h}{f_1}\right)^2 . \tag{8.1}$$

where P_{Ω} is the ohmic loss due to the DC resistance $R_{DC} = R_{DC7200V} + R'_{DC240V}$, P_{EC} represents the eddy-current losses at frequency f_h, I is the rms current. R_{EC} is an additional resistance due to the eddy-currents at rated frequency f_1. Defining

$$R_{AC} = \frac{P_{cu}}{I^2} = R_{DC} + R_{EC}\left(\frac{f_h}{f_1}\right)^2 = R_{DC}\left[1 + P_{EC-R}(pu)\left(\frac{f_h}{f_1}\right)^2\right] . \tag{8.2}$$

one can measure the AC winding resistance R_{AC} as a function of the frequency f_h by measuring the copper loss and the rms current, where $P_{EC-R}(pu)$ is the per-unit winding eddy-current loss at rated (R) load and frequency, and is given by

$$P_{EC-R}(pu) = \frac{R_{EC}}{R_{DC}} . \tag{8.3}$$

The circuit for measuring the AC winding resistance at different frequencies is shown in Figure 8.1, where a signal generator provides sinusoidal signals of different

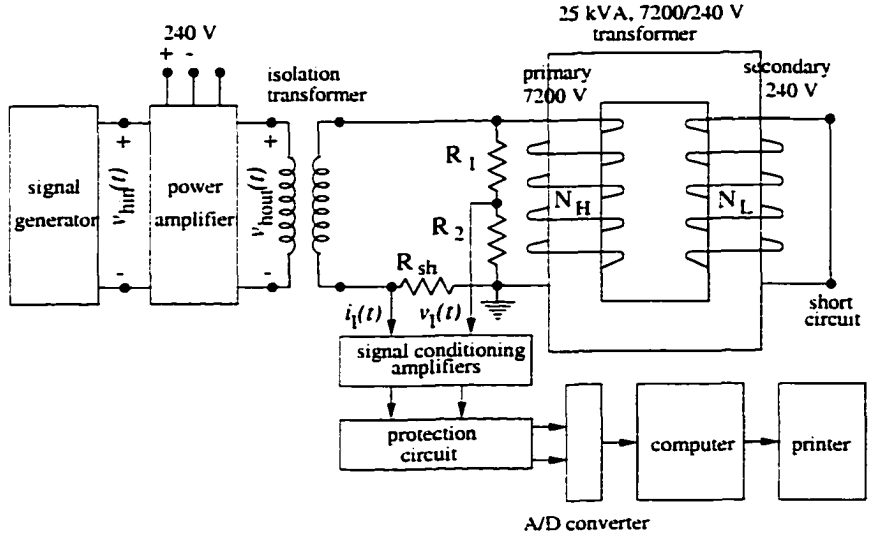

Figure 8.1: Circuit for measuring eddy-current losses of single-phase transformers at different frequencies with power amplifier.

frequencies to a power amplifier, which in turn supplies power to the transformer under test.

A 25kVA single-phase transformer (see [40]) is excited at the high-voltage winding with the low-voltage winding short-circuited. Sensors and instruments are shown in Figures 8.1 and 6.1. The copper loss and the rms current are recorded 2 times. The AC winding resistance is derived via the linear regression, and is computed from

$$R_{AC_h} = \frac{P_{avg_h}}{I^2_{rmsavg_h}} \tag{8.4}$$

where

$$P_{avg_h} = \frac{1}{n}\sum_{k=1}^{n} P_{hk} \quad . \quad I_{rmsavg_h} = \sqrt{\frac{1}{n}\sum_{k=1}^{n} I^2_{rmsh_k}}$$

with n=2.

The AC winding resistance values R_{AC}, measured at average winding temperature of $\theta_{wind.avg.rat.} = 69^oC$ and ambient temperature of $\theta_{amb.} = 25^oC$ at different harmonic frequencies, are extrapolated to the rated average winding temperature of 82.37^oC. They are listed in Table 8.1, and are graphed in Figure 8.2 as a function of the frequency for the range 0 to $780Hz$.

The average winding temperature was measured with the DC voltage drop method, and resistance values were extrapolated to the rated average winding temperature of 82.37^oC. One of the chromel-alumel thermocouples measured the frame temperature of the transformer, and the other one the ambient temperature. Unfortunately, no hot-spot measurements could be obtained because off-the-shelf-pole transformers were tested without any thermocouples inside the transformer structure.

The DC winding resistance has been measured in [40], and is $R_{DC} = R_{DC7200V} + R'_{DC240V} = 27.9\Omega$ at rated average winding temperature of $\theta_{wind.avg.rat.} = 82.37^oC$. The per-unit winding eddy-current loss at rated load and frequency $P_{EC-R}(pu)$ can be derived from the measured data as shown in Figure 8.2 by use of linear regression. From Figure 8.2 (+ symbols) one obtains

$$R_{AC_h} = 34.54 + 0.15\left(\frac{f_h}{f_1}\right)^2 , \tag{8.5}$$

Table 8.1: Measured AC winding resistances at different frequencies with power amplifier

$h = f_h/f_1$	P_{cu} (W) †	I_{hrms} (A)	$R_{AC(h)}$ (Ω) ‡
1	423.99	3.59	34.35
2	413.03	3.50	35.20
3	411.27	3.46	35.86
4	331.49	3.04	37.45
5	253.84	2.61	38.90
6	198.00	2.27	40.11
7	147.82	1.92	41.86
8	100.19	1.54	44.11
9	90.04	1.43	45.97
10	97.28	1.43	49.66
11	87.32	1.32	52.31
13	73.07	1.12	60.81

† $P_{avg_h} \approx P_{cu_h}$.
‡ referred to high-voltage side.

in which $R_{EC} = 0.15\Omega = 0.005 R_{DC}$ and $P_{EC-R_{linear}}(pu) = 0.00537$. In Figure 8.2, at the frequency $f = 0$ (i.e., DC), the R_{AC_h} should be equal to R_{DC}. During the measurements for R_{AC} as a function of frequency, it has been found that at lower frequencies the exponent of $(f_h/f_1)^\varepsilon$ is about $\varepsilon = 2$, and at higher frequencies this exponent is less than 2. In order not to complicate matters, however, in Figure 8.2 a value of $\varepsilon = 2$ has been assumed; this assumption is partly responsible for $R_{DC} = 27.9\Omega$ being less than $R_{AC}(f = 0) = 34.54\Omega$ as obtained from Equation 8.5, and less than the 30Ω found from Equation 8.6. This variation of the value of exponent ε may be responsible for the assumption of ANSI/IEEE C57.110/D7-February 1998, that the stray losses vary with $\varepsilon = 0.8$.

8.3 Simplified Measurement of Nonlinear, Eddy-current Loss Coefficient

The experimental determination of R_{AC} as a function of the factor $h = f_h/f_1$ with a variable frequency source (phase-lock circuit and power amplifier) is not convenient for measurements in the field. For this reason, the circuit of Figure 6.1 is proposed,

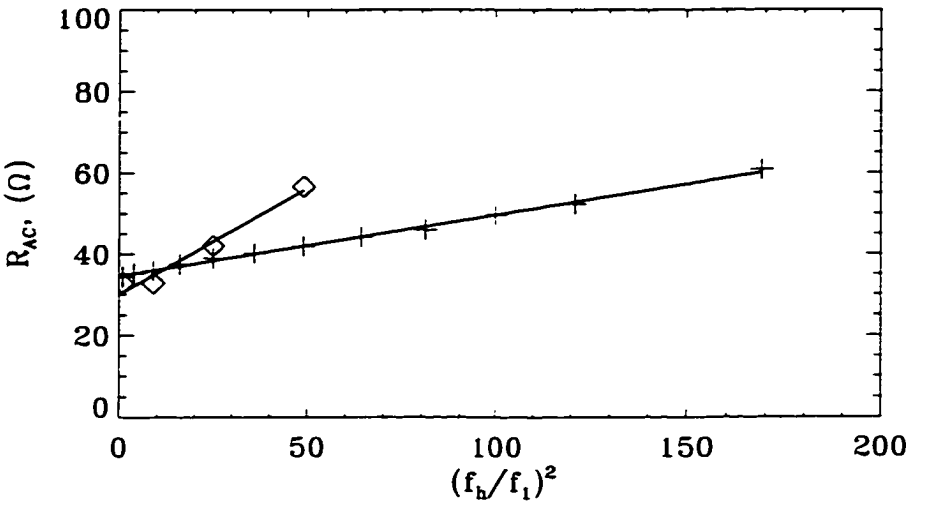

Figure 8.2: AC winding resistance as a function of square of frequencies from DC to $780Hz$ ("◇" symbols: method of Section 8.2 and "+" symbols: method of Section 8.3).

consisting of a voltage source $V_{1rms} = 240V$, two back-to-back connected transformers and a nonlinear load, and where the frequency spectrum of the transformer current i_1 can be adjusted. Such a nonlinear load can consist of a few parallel connected diode/thyristor bridge-rectifiers, where the conduction angle of each individual bridge can be adjusted via the output capacitance C_0 and the output resistance R_0 of the rectifier. As compared to the power amplifier measurement of Section 8.2, transformers operate at rated voltage in this present method. If a half-controlled thyristor bridge is employed, the firing angle α can be selected between 5^o and 175^o. Sensors and instruments are given in Figure 6.1. Table 8.2 lists measured AC winding resistance values R_{AC_h} at different frequencies and Figure 8.2 ("◇" symbols) illustrates the values of R_{EC} and $P_{EC-R}(pu)$ for the 25 kVA single-phase transformer based on the simplified approach employing the average resistance values of Table 8.3. From Figure 8.2 ("◇" symbols) one obtains

$$R_{AC_h} = 30.0 + 0.52\left(\frac{f_h}{f_1}\right)^2 , \tag{8.6}$$

wherein $R_{EC} = 0.52\Omega = 0.02R_{DC}$ and $P_{EC-R_{nonlinear}}(pu) = 0.0186$. These values approximately confirm those obtained from measurements employing a power amplifier.

Table 8.2: Measured AC winding resistance at different frequencies with constant voltage source and nonlinear load and at about rated average winding temperature.

$h = \frac{f_h}{f_1}$	P_{cu}† (W)	I_{hrms} (A)	$R_{AC(h)}$‡ (Ω)	$h = \frac{f_h}{f_1}$	P_{cu} (W)	I_{hrms} (A)	$R_{AC(h)}$ (Ω)
diode bridge				diode bridge and thyristor bridge			
1	318.94	94.27	32.29	3	30.38	28.77	33.03
1	319.89	94.4	32.31	3	26.41	27.62	31.16
1	305.41	92.2	32.33	3	32.12	28.42	35.78
1	304.73	92.11	32.33	3	27.76	26.98	34.33
1	275.8	87.6	32.34	3	30.37	28.02	34.82
1	270.29	87	32.14	3	36.74	30.26	36.12
1	266.6	87.02	31.69	3	19.02	24.19	29.27
diode bridge and thyristor bridge				diode bridge			
1	314.52	91.26	33.99	5	22.39	23.07	37.87
1	303.68	89.39	34.20	5	22.46	22.99	38.25
1	288.26	87.67	33.75	5	16.84	19.78	38.73
1	264.04	85.26	32.69	5	17.29	20.01	38.87
1	240.59	79.61	34.16	5	25.26	24.38	38.25
diode bridge				5	24.23	23.48	39.56
3	71.76	45.17	31.66	5	25.8	23.85	40.82
3	71.55	45.36	31.30	diode bridge and thyristor bridge			
3	92.20	51.14	31.73	5	45.47	29.48	47.09
3	93.89	51.43	31.94	5	40.01	28.34	44.83
3	114.70	56.86	31.93	5	32.82	26.08	43.42
3	114.26	55.98	32.8	5	32.86	25.59	45.16
3	114.26	55.98	32.82	5	106.79	47.06	43.40
3	112.96	56.09	32.32	7	35.63	24.89	51.73
				7	34.02	24.32	51.76
				7	37.82	24.04	58.90
				7	34.34	22.79	59.50
				7	10.73	12.58	61.00

†one transformer only.
‡referred to high-voltage side.

8.3.1 Comparison of $P_{EC-R_{linear}}$ with $P_{EC-R_{nonlinear}}$

The method of Section 8.2, where a power amplifier is used, gives $P_{EC-R_{linear}} = 0.537\%$, and the method of Section 8.3 yields $P_{EC-R_{nonlinear}} = 1.86\%$. Both methods cannot produce the same results, because in Section 8.2, low voltages ($\approx 7\%$ of rated voltage) are applied (harmonic voltages and zero fundamental), while in Section 8.3 close rated voltages are applied (harmonic voltage and rated fundamental voltage). In

the method of Section 8.2 the operating point on the BH characteristic is at the origin, and in the method of Section 8.3 the operating point on the BH characteristic is above or near the knee where saturation sets in. Therefore, the magnetizing and leakage inductances are different for both cases; this means also the eddy-current distribution due to increased leakage fluxes under saturated operating conditions are increased, resulting in a different harmonic eddy-current loss coefficient P_{EC-R}: $P_{EC-R_{nonlinear}}$, which reflects more accurately the actual harmonic load of a transformer and is, therefore, considered to be more accurate than $P_{EC-Rlinear}$.

8.4 Derating Measurements

According to [52], derating is defined as the intentional reduction of stress (e.g., temperature, mechanical core vibration) in the application of (nonlinear transformer) loads, usually for the purpose of reducing the occurrence of temperature-stress related failures, such as burnout or premature aging. It is well known [77] that voltage and current harmonics generate additional temperature rises which may lead to premature failures, and the rated lifetime of the apparatus may not be reached [78]. To prevent such a failure, the derating of a transformer is defined such that the rated temperature rise is not being exceeded – even when supplying nonsinusoidal load currents. Provided the cooling conditions are not altered, the rated temperature rise calls for a limitation of the losses under nonsinusoidal load identical to the rated losses occurring at linear load. Therefore, the derating with respect to apparent powers is defined as

$$derating_S = \frac{S_{out}}{S_{out}^{rated}} = \frac{V_{2rms} I_{2rms}}{V_{2rms}^{rated} I_{2rms}^{rated}} \tag{8.7}$$

where V_{2rms} and I_{2rms} are output rms voltage and current, which result in the generation of the rated total loss (iron-core and copper losses) within the apparatus.

Two identical 25kVA single-phase transformers are connected back-to-back with full-wave diode and thyristor rectifier loads, as shown in Figure 6.1. The back-to-back

connection is employed so that transformer losses can be measured more accurately (with error < 5%) [40]. A computer-aided testing (CAT) program [64], [70] is used, and all four signals (output voltage, current difference, voltage difference and input current) are calibrated under either linear resistive or nonlinear load conditions. First, rated loss is recorded when transformers supply rated output power to a linear resistive load at about rated average winding temperature. Then, the transformers are reconnected to supply power to full-wave diode and/or thyristor rectifier loads, as shown in [40]. All four signals are sampled at rated (total) loss, and measured data are listed in Tables of [40]. Additional data are presented in Tables 8.3, 8.4, and 8.5. In these the voltage

Table 8.3: Measured harmonic currents and voltages of two 25 kVA transformers connected back-to-back with diode-bridge load at rated losses, and at about rated average winding temperature

h	V_{1h} (V)	I_{1h} (A)	V_{1h} (V)	I_{1h} (A)
0	0.20	1.47	0.90	2.11
1	231.4	109.5†	232.8	103.5
2	1.61	1.16	0.86	0.4
3	3.81	12.28	6.03	27.26
4	0.46	0.38	0.58	1.01
5	5.18	10.53	4.56	14.11
6	0.57	0.92	0.27	0.57
7	3.84	4.90	1.72	5.47
8	0.49	0.05	0.17	0.45
9	1.04	2.17	1.10	2.72
11	1.04	0.98	0.40	1.05
13	1.28	0.77	1.00	0.80
THD (%)‡	3.5	15.7	3.5	30.3
$K^{(49)}$ (pu)	–	1.70	–	2.37

†$x(t) = \sum_{h=0,1,2,3,\ldots} \sqrt{2} X_h \sin(h\omega t + \phi_X)$.
‡At point of common coupling (PCC) of pole transformer with distribution system.

and current harmonics of the input port of the two transformers are listed, including the THD_v, THD_i and K-factor values up to $h_{max} = 49$ (see Equation 8.16).

Table 8.4: Measured harmonic currents and voltages of two 25 kVA transformers connected back-to-back with thyristor-bridge load at rated losses, and at about rated average winding temperature

h	V_{1h} (V)	I_{1h} (A)	V_{1h} (V)	I_{1h} (A)
0	-2.88	0.67	-3.79	-0.34
1	230.0	109.9	229.7	103.4
2	2.03	1.78	1.54	0.66
3	0.32	6.34	2.0	21.48
4	0.85	0.15	0.38	1.34
5	2.58	5.71	3.85	12.48
6	0.68	0.09	0.67	0.71
7	2.05	4.56	1.12	5.80
8	0.44	0.08	0.12	0.67
9	1.26	3.31	1.32	2.20
11	1.38	2.54	1.06	3.15
13	1.48	1.83	2.45	2.85
THD (%)	2.9	10.2	3.9	25.5
$K^{(49)}$ (pu)	-	2.10	-	3.56

8.5 Relationship Between Derating, Iron-core Losses, Stray-power Losses, and K-factor

An accurate transformer derating calculation hinges on the knowledge of the eddy-current loss P_{EC} within the transformer windings, and the knowledge of the iron-core losses at nonlinear loads. In most cases these quantities are not known and must be estimated, which questions the validity of any derating calculation.

The total transformer losses are

$$P_{loss} = P_{cu} + P_{fe} + P_{OSL} \ , \tag{8.8}$$

where P_{OSL} stands for the other stray losses, P_{cu} is given by Equation 8.1 as

$$P_{cu} = I^2 R_{DC} + I^2 R_{EC} \left(\frac{f_h}{f_1} \right)^2 \tag{8.9}$$

and the iron-core losses can be obtained from the analysis as described by Stensland [79], [80]

$$P_{fe} = \sum_h P_{feh} = P_{fe1} + P_{fe2} + P_{fe3} + P_{fe4} + \cdots \ . \tag{8.10}$$

Table 8.5: Measured harmonic currents and voltages of two 25 kVA transformers connected back-to-back with diode-bridge and thyristor-bridge load at rated losses, and at about rated average winding temperature

h	V_{1h} (V)	I_{1h} (A)	V_{1h} (V)	I_{1h} (A)
0	-3.51	-0.10	-2.22	0.74
1	231.7	106.7	233.7	97.02
2	1.89	0.67	2.51	0.93
3	1.98	19.95	3.41	20.71
4	0.42	0.79	0.80	1.73
5	4.5	5.58	7.34	28.52
6	0.70	0.55	0.26	1.98
7	2.17	5.79	4.11	14.75
8	0.53	0.37	0.58	0.62
9	1.05	2.02	0.52	0.99
11	0.72	2.84	1.42	3.32
13	1.33	1.48	1.25	1.60
THD (%)	3.0	20.7	4.8	39.9
$K^{(49)}$ (pu)	-	2.28	-	5.32

At rated sinusoidal load $I = I_R$, $f_h = f_1$, $V = V_R$ and

$$P_{lossR} = I_R^2 R_{DC} + I_R^2 R_{EC-R} + P_{feR} + P_{OSLR} \,. \tag{8.11}$$

where the last term in this equation represents the other stray losses. At nonsinusoidal loads ($h = 1, 2, 3, 4, 5, \cdots$)

$$P_{loss} = \sum_h I_h^2 R_{DC} + \sum_h I_h^2 R_{EC-R} \left(\frac{f_h}{f_1}\right)^2 + \sum_h P_{feh} + \sum_h P_{OSLh}. \tag{8.12}$$

Note that asymmetric rectifiers generate also even harmonics. Losses under any (non)sinusoidal load (see Equation 8.12) must not exceed the rated losses (see Equation 8.11); therefore, with $h = (f_h/f_1)$ and

$$\sum_h I_h^2 = I_1^2 + I_2^2 + I_3^2 + I_4^2 + \cdots \tag{8.13}$$

$$\sum_h I_h^2 h^2 = I_1^2 1^2 + I_2^2 2^2 + I_3^2 3^2 + I_4^2 4^2 + \cdots \tag{8.14}$$

follows

$$\begin{aligned} I_R^2 R_{DC} + I_R^2 R_{EC-R} + P_{feR} + P_{OSLR} &= \sum_h I_h^2 R_{DC} + \sum_h I_h^2 h^2 R_{EC-R} \\ &+ \sum_h P_{feh} + \sum_h P_{OSLh}. \end{aligned} \tag{8.15}$$

At the present time it appears that ANSI/IEEE C57.110-1986 has been updated to ANSI/IEEE C57.110/D7-February 1998, and a new term, the harmonic loss factor F_{HL}, has been defined. According to standards of the Underwriters Laboratory Inc., the K-factor is defined as [71], [72], and [73]

$$K = \frac{\sum_h I_h^2 h^2}{I_R^2}. \tag{8.16}$$

Now, one obtains from Equation 8.15

$$I_R^2(R_{DC} + R_{EC-R}) + P_{feR} + P_{OSL-R} = \sum_h I_h^2 R_{DC} + K I_R^2 R_{EC-R} + \sum_h P_{feh} + \sum_h P_{OSLh} \tag{8.17}$$

or

$$\sum_h I_h^2 R_{DC} = I_R^2 \left(R_{DC} + R_{EC-R}(1-K) - \frac{\Delta P_{fe}}{I_R^2} - \frac{\Delta P_{OSLR}}{I_R^2} \right), \tag{8.18}$$

where $\Delta P_{fe} = \sum_h P_{feh} - P_{feR}$ and $\Delta P_{OSL} = \sum_h P_{OSLh} - P_{OSL-R}$. The maximum amount of rms harmonic load current that the transformer can deliver is

$$I_{max}^{pu} = \frac{\sqrt{I_1^2 + I_2^2 + I_3^2 + \cdots}}{I_R} = \sqrt{\frac{R_{DC} + R_{EC-R}(1-K) - \frac{\Delta P_{fe} + \Delta P_{OSL}}{I_R^2}}{R_{DC}}}, \tag{8.19}$$

In Equation 8.19, the rated current I_R of the pole transformer is 3.472 A on the high-voltage side and 104.17 A on the low-voltage side. Equation 8.19 also indirectly reflects the dependency of the derating on the phase shift of the harmonic currents; these phase shifts can be such that the terminal voltage becomes either "peaky" (peak-to-peak is maximum) or "flat" (peak-to-peak is minimum), which results (if the third harmonic is considered only) in either a "flat" or "peaky" flux density within the transformer core, respectively [80]. Note that, for the measurement technique applied, the other stray-power losses $\sum_{h=1,2,3,\ldots} P_{OSLh}$ and P_{OSLR} are included in the measured iron-core losses $\sum_{h=1,2,3,\ldots} P_{feh}$ and P_{feR}, respectively. Updated ANSI/IEEE standards [74] and

[81] are using a relatively new term. the harmonic loss factor F_{HL}. This treatment of harmonics is somewhat different mathematically than the K-factor term which is used by Underwriters Laboratory. Inc. This new approach harmonizes the term with IEC and with the HVDC converter transformer standard of IEEE as well.

8.6 Reduction in Apparent Power Rating (RAPR)

The derating with respect to apparent power is defined by Equation 8.7. The reduction in apparent power rating can be defined by

$$RAPR = \frac{S_{out}^{rated} - S_{out}^{nonlinear}}{S_{out}^{rated}} 100\% \tag{8.20}$$

where

$$S_{out}^{rated} = V_{2rms}^{rated} I_{2rms}^{rated} \text{ at } P_{loss}^{rated} \quad . \tag{8.21}$$

$$S_{out}^{nonlinear} = V_{2rms}^{nonlinear} I_{2rms}^{nonlinear} \text{ at } P_{loss}^{rated} \quad . \tag{8.22}$$

For $V_{2rms}^{nonlinear} > V_{2rms}^{rated}$ follows $I_{2rms}^{nonlinear} < I_{2rms}^{rated}$, and with

$$I_{max}^{pu} = \frac{I_{2rms}^{nonlinear}}{I_{2rms}^{rated}} \tag{8.23}$$

one obtains from Equation 8.20

$$RAPR = 1 - \frac{V_{2rms}^{nonlinear}}{V_{2rms}^{rated}} \cdot I_{max}^{pu} \tag{8.24}$$

Table 8.6 presents the data required for the computation of I_{max}^{pu} and the reduction in apparent power rating (RAPR). In general, the measurement of P_{feR} occurs at the voltage $V_{P_{feR}}$ while that of $\sum_{h=1,2,3,\ldots} P_{feh}$ takes place at voltage $V_{\sum_{h=1,2,3,\ldots}}$. These voltages are not identical, and therefore, the iron-core losses P_{feR} and $\sum_{h=1,2,3,\ldots} P_{feh}$ must be referred to the same induced voltage within the transformer through interpolation; the iron-core losses of Tables listed in [40] can be used. The stray-power losses originating in the steel frame are included in these measured iron-core losses. Figure 8.3 illustrates the

Table 8.6: Calculated derating (I_{max}^{pu}) and reduction in apparent power rating of one 25 kVA transformer with diode-bridge load at rated losses and at about rated average winding temperature

	diode-bridge load			thyristor-bridge load			combined diode- and thyristor-bridge load		
THD_{vl} (%)	3.5	3.5	5.4	2.9	3.9	7.3	3.0	4.8	6.8
THD_{il} (%)	15.7	30.3	70.9	10.2	25.5	92.2	20.7	39.9	70.0
$K^{(49)}$ (pu)	1.70	2.37	4.95	2.10	3.56	9.11	2.28	5.32	9.68
$\sum_{h=1}^{49} P_{feh}$ (W)	46.75	49.4	55.4	46.6	47.3	57.0	47.2	50.4	55.6
P_{feR} (W)	45.5	46.5	49.5	44.5	44	49	46.1	46.5	48
ΔP_{fe} (W)	1.25	2.85	5.91	2.05	3.25	7.94	1.2	3.90	7.55
I_R (A)	3.47	3.47	3.47	3.47	3.47	3.47	3.47	3.47	3.47
$R_{DCrat}{}^{\dagger}$ (Ω)	27.9	27.9	27.9	27.9	27.9	27.9	27.9	27.9	27.9
$R_{EC-R}{}^{\dagger}$ (Ω)	0.52	0.52	0.52	0.52	0.52	0.52	0.52	0.52	0.52
$\Delta P_{OSL}{}^{\ddagger}$ (W)	0	0	0	0	0	0	0	0	0
I_{max}^{pu} (Eq. 8.19)	0.99	0.98	0.95	0.99	0.97	0.91	0.98	0.95	0.90
$RAPR$ (Eq. 8.24)	0.03	0.04	0.07	0.03	0.05	0.11	0.04	0.07	0.12

†at rated average winding temperature $\theta_{wind.avg.rat} = 82.37°C$.
‡included in ΔP_{fe}.

derating measurements as obtained in [40] and the values as calculated from Equation 8.19 via the K-factor. The latter approach represents the worst case because it neglects the increase of the apparent power due to voltage harmonics and the resulting decrease of the required rms terminal current $I_{2rmsnonlinear} < I_{2rmslinear}$ for maintaining rated output apparent power. However, one can state that, for $THD_i < 90\%$, the derating is surprisingly small, and Equation 8.19 can be considered a worst case approximation. Figure 8.3 illustrates that for the same THD_{i_1} but different harmonic current spectra (see Tables 8.3, 8.4, and 8.5), the derating may be different. From these tables one can obtain per-unit voltage and current values if one divides all voltages (harmonics and fundamental) by 240 V, and all currents (harmonics and fundamental) by 104.17 A.

8.7 Discussion and Conclusions

Measurements show that eddy-current losses of a 25 kVA single-phase transformer with a wound core and an aluminum secondary winding (consisting of sheets) are proportional to the frequency with a power of 2. From a linear regression analysis, the per

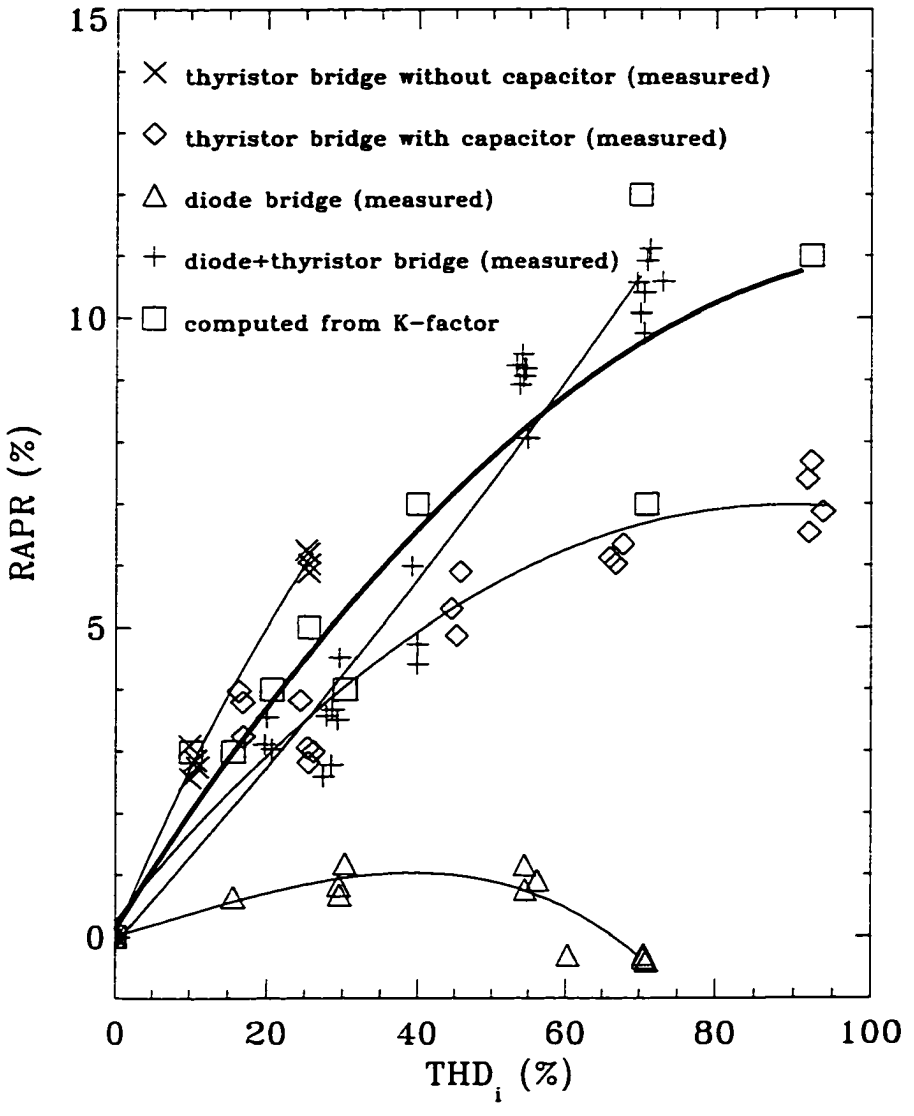

Figure 8.3: Reduction in apparent power rating ($RAPR$) of 25kVA transformer as a function of total harmonic current distortion (THD_{i_1}) where 3^{rd} and 5^{th} current harmonics are dominant.

unit eddy-current loss P_{EC-R}(pu) has been identified. This measuring method takes into account skin and proximity effects within the transformer windings. A simplified measurement of eddy-current losses within transformer windings, and the identification of $P_{EC-R_{nonlinear}}[pu] = R_{EC}/R_{DC}$ has been described and used. The derating of transformers in terms of apparent power is defined, and a relationship between derating, reduction in apparent power rating ($RAPR$), K-factor, and measured iron-core losses $\sum_h P_{feh}$ (which include the stray-power losses $\sum_h P_{OSLh}$) is formulated. Exam-

ples demonstrate the usefulness of this derating calculation. and is confirmed in [40] by measurements. For example. one concludes that for THD_i and THD_v values of 20% and 3%, respectively, the reduction in apparent power rating of a 25kVA single-phase transformer is small and in the range of 2.5%. The findings approximately agree with those of [75] and [76]. The difference is that in this paper the total losses are measured with an error of less than $\pm 5\%$, while in the above mentioned two papers temperature was monitored. It is fair to say that the results based on measured losses are more accurate than those of [75] and [76].

The derating of transformers depends on the following conditions:

1. phase shift of current and voltage harmonics.
2. output DC filter capacitance (C_0) of rectifiers,
3. temperature of transformer, and
4. rms value of terminal voltage.

CHAPTER 9

MEASURED TRANSFORMER DERATING AND COMPARISON WITH HARMONIC LOSS FACTOR (F_{HL}) APPROACH

9.1 Introduction

The eddy-current loss coefficient of a transformer can be determined by using the harmonic amplitudes of input current and the corresponding harmonic copper losses, when the transformer supplies nonlinear loads. Measured data show that eddy-current loss is a linear function of frequency, with a power of 2. Apparent power (kVA) derating of single-phase transformers, operating with nonsinusoidal currents and voltages, is measured by adjusting the total losses to the rated losses at rated temperature. Computed results of derating using the harmonic loss factor (F_{HL}), eddy-current loss coefficient $P_{EC-Rnonlinear}$, and iron-core losses match well with measured data. However, the real power derating of a transformer is much greater than the apparent power derating for a given THD_i value, and it is independent of the frequency spectra of the harmonics. Experiments show that the other stray power losses (P_{OSL}) in nearby conductive elements are proportional to the power of 0.8 at low frequencies, and inversely proportional to the power of 0.9 at high frequencies.

A computer aided measurement circuit of Chapter 8 is used to separately measure the copper and iron-core losses under any (non)linear load conditions. A 25kVA 7200V/240V transformer is operated at different THD_i values of input current ranging from 10% to 95% at rated temperature. Rated losses are determined by switching

to a linear load before or after a nonlinear load operation. In this way the effect of temperature variations is eliminated.

9.2 Definition of F_{HL}

Harmonic loss factor (F_{HL}) is defined in IEEE C57.110/D7-February 1998 [74] as

$$F_{HL} = \frac{P_{EC}}{P_{EC-O}} = \frac{\sum_{h=1}^{h=h_{max}} I_h^2 h^2}{\sum_{h=1}^{h=h_{max}} I_h^2} \,. \tag{9.1}$$

where:

P_{EC} = total eddy-current losses due to harmonics,

P_{EC-O} = eddy-current losses at power frequency
as if no harmonic currents existed,

I_h = actual rms values of harmonic currents

h = harmonic order.

Per-unit current values can also be used in Eq. 9.1 by dividing the numerator and denominator by the total rms current. The harmonic loss factor is different from the K-factor definition of UL 1561 [71], and the relationship between these two definitions is given by

$$\text{K-factor} = \left[\frac{\sum_{h=1}^{h=h_{max}} I_h^2}{I_R^2}\right] F_{HL} \,. \tag{9.2}$$

where I_R is the rated rms load current. The numerical value of the K-factor is equal to the numerical value of F_{HL} when the rms value of the load current is equal to the rated load current of a transformer.

9.3 Relationship Between Derating, Iron-Core Losses, Stray-Power Losses, and F_{HL}

When a transformer is operated under nonsinusoidal voltages and currents, the nameplate value of the output power must be reduced so that the rated temperature

of the transformer is not exceeded (neglecting hot-spot temperatures). This can be achieved by limiting the total losses of the transformer at any nonlinear load to the rated losses at sinusoidal currents and voltages.

Table 9.1 and 9.2 list the per-unit quantities of harmonic input voltage and current values at the low-voltage side for various nonlinear loads. Even though only harmonic values up to 13^{th} are given. a total of 49 harmonics are used when computing THD_i and F_{HL}. Following the procedure in Chapter 8 and using harmonic loss factor (F_{HL}) of Eq. 9.1, one obtains from Equation 8.15

$$I_R^2 R_{DC} + I_R^2 R_{EC-R} + P_{feR} + P_{OSL-R} = \sum_h I_h^2 R_{DC}$$
$$+ F_{HL} \sum_h I_h^2 R_{EC-R} + \sum_h P_{feh} + \sum_h P_{OSLh} \; . \tag{9.3}$$

where subscript R represents the rated linear load operation, and P_{feR} and P_{OSL-R} are the rated iron-core and stray power losses, respectively. Then

$$\sum_h I_h^2 (R_{DC} + F_{HL} R_{EC-R}) =$$
$$I_R^2 \left(R_{DC} + R_{EC-R} - \frac{\Delta P_{fe} + \Delta P_{OSL}}{I_R^2} \right) \; . \tag{9.4}$$

where $\Delta P_{fe} = \sum_h P_{feh} - P_{feR}$ and $\Delta P_{OSL} = \sum_h P_{OSLh} - P_{OSL-R}$. It follows that the maximum output current of the transformer is

$$I_{max}^{pu} = \frac{\sqrt{I_1^2 + I_2^2 + I_3^2 + \cdots}}{I_R}$$
$$= \sqrt{\frac{R_{DC} + R_{EC-R} - \frac{\Delta P_{fe} + \Delta P_{OSL}}{I_R^2}}{R_{DC} + F_{HL} R_{EC-R}}} \; , \tag{9.5}$$

where I_R is the rated current of the transformer and all quantities are referred to high-voltage side (current and resistance values), and $R_{EC-R} = R_{EC-Rnonlinear}$ is the slope of the line in Figure 8.2.

9.4 Reduction in Apparent Power Rating ($RAPR$) and Real Power Capability (RPC)

Table 9.3 presents the data for computing $RAPR$. Three different THD_i values

Table 9.1: Measured harmonic currents and voltages (per unit of rms values) of two 25 kVA transformers connected back-to-back at rated losses.

diode-bridge load				
h	V_{1h} [pu]	I_{1h} [pu]	V_{1h} [pu]	I_{1h} [pu]
0	0.0023	0.0115	-0.0034	0.0044
1	0.9990	0.8779†	0.9985	0.8171
2	0.0057	0.0143	0.0104	0.0182
3	0.0401	0.4218	0.0476	0.5276
4	0.0021	0.0170	0.0038	0.0188
5	0.0119	0.2138	0.0189	0.2205
6	0.0023	0.0101	0.0036	0.0088
7	0.0021	0.0666	0.0048	0.0656
8	0.0017	0.0039	0.0021	0.0019
9	0.0052	0.0159	0.0026	0.0022
11	0.0048	0.0076	0.0058	0.0085
13	0.0017	0.0057	0.0042	0.0044
RMS values	233.70 V	107.52 A	236.12 V	106.48 A
$THD^{(49)}$ [%]	4.34	54.52	5.38	70.54
$F_{HL}^{(49)}$ [pu]	-	3.82	-	4.66
thyristor-bridge load				
h	V_{1h} [pu]	I_{1h} [pu]	V_{1h} [pu]	I_{1h} [pu]
0	-0.0088	0.0049	-0.0175	-0.0124
1	0.9976	0.8349	0.9975	0.7294
2	0.0110	0.0048	0.0097	0.0267
3	0.0398	0.4948	0.0346	0.5702
4	0.0071	0.0108	0.0042	0.0310
5	0.0342	0.1803	0.0459	0.3392
6	0.0025	0.0229	0.0051	0.0423
7	0.0166	0.1244	0.0073	0.1192
8	0.0039	0.0201	0.0045	0.0369
9	0.0126	0.0531	0.0092	0.0423
11	0.0079	0.0459	0.0097	0.0500
13	0.0090	0.0236	0.0055	0.0159
RMS values	232.64 V	103.94 A	235.42 V	101.94 A
$THD^{(49)}$ [%]	6.91	65.89	7.01	93.74
$F_{HL}^{(49)}$ [pu]	-	7.38	-	10.36

† $x(t) = \sum_{h=0,1,2,\ldots} \sqrt{2} X_h \sin(h\omega t + \phi_x)$.

Table 9.2: Measured harmonic currents and voltages (per unit of rms values) of two 25 kVA transformers connected back-to-back with diode-bridge and thyristor-bridge load at rated losses.

h	V_{1h} [pu]	I_{1h} [pu]	V_{1h} [pu]	I_{1h} [pu]
0	-0.0118	0.0076	-0.0174	-0.0042
1	0.9981	0.8807	0.9977	0.8151
2	0.0092	0.0301	0.0054	0.0271
3	0.0190	0.2824	0.0223	0.2719
4	0.0059	0.0304	0.0009	0.0241
5	0.0269	0.2688	0.0412	0.4816
6	0.0023	0.0464	0.0038	0.0401
7	0.0245	0.2319	0.0228	0.1297
8	0.0058	0.0242	0.0041	0.0316
9	0.0128	0.0695	0.0068	0.0380
11	0.0059	0.0488	0.0098	0.0337
13	0.0121	0.0472	0.0150	0.0477
RMS values	236.21 V	99.20 A	235.16 V	100.28 A
$THD^{(49)}$ [%]	6.06	53.72	6.73	71.03
$F_{HL}^{(49)}$ [pu]	-	9.93	-	11.46

are chosen for each of three different loads. Although the THD_i values are similar, the frequency spectrum is different for each type of load, e.g., $I_3 > I_5$ or $I_5 > I_3$.

Today's transformers are highly efficient and they operate at or above the knee point of the magnetization curve. Therefore, any variations in the input voltage will directly affect the iron-core losses of the transformer and, indirectly, the copper losses. The rms values of the input voltages given in Table 9.3 are voltages at particular load conditions, (i.e., THD_i value): the rated iron-core losses (P_{feR}) are measured at similar input voltage rms values with linear loads. The other stray power losses are included in the iron-core losses; therefore, their values are taken as zero in Equation 9.5.

Computed values of $RAPR$ are compared with the measured values in Figure 9.1. Measured data reflect three different frequency spectra: $I_3 > I_5$ relates to symbols "×" and "◇", while $I_5 > I_3$ pertains to diode- and thyristor-bridge operation ("+" symbols). $RAPR$ is larger when the 5^{th} harmonic is dominant. The "×" symbols represent thyristor-bridge operation without an output capacitor across the load, as

Table 9.3: Calculated derating $I_{max}(pu)$ and reduction in apparent power rating ($RAPR$) of one $25kVA$ transformer at rated losses.

	diode-bridge load			thyristor-bridge load			combined diode- and thyristor-bridge load		
$THD_v^{(49)}$ (%)	3.22	4.34	5.38	3.94	6.91	7.01	2.94	6.06	6.73
$THD_i^{(49)}$ (%)	16.17	54.52	70.54	25.54	65.89	93.74	20.01	53.72	71.03
$F_{\mu h}^{(49)}$ (pu)	1.51	3.82	4.66	3.39	7.38	10.36	2.04	9.93	11.46
$\sum_{h=1}^{49} P_{feh}$ (W)	46.61	51.31	55.77	46.40	55.09	56.70	47.71	53.40	56.03
P_{feR} (W)	45.71	47.23	48.72	44.65	45.75	48.27	45.93	49.78	48.88
ΔP_{fe} (W)	0.90	4.08	7.05	1.75	9.34	8.43	1.78	3.62	7.15
I_{1R} (A)	3.47	3.47	3.47	3.47	3.47	3.47	3.47	3.47	3.47
V_{rms} (V)	232.11	233.70	236.12	230.73	232.64	235.42	231.81	236.21	235.16
R_{DCrat} (Ω)†	27.9	27.9	27.9	27.9	27.9	27.9	27.9	27.9	27.9
R_{EC-R} (Ω)†	0.52	0.52	0.52	0.52	0.52	0.52	0.52	0.52	0.52
$I_{max}(pu)$ (Eq. 9.5)	0.994	0.969	0.958	0.976	0.932	0.911	0.988	0.921	0.905
$RAPR$ (Eq. 8.24)	0.039	0.057	0.058	0.062	0.096	0.106	0.046	0.094	0.113

†at rated average winding temperature $\theta_{wind.avg.rat} = 82.37°C$.

compared to "o" symbols where a capacitor is present. The effect of this capacitor on the RAPR is clearly seen in Figure 9.1: the apparent power reduction is larger without a capacitor. This can be explained by the fact that output capacitors increase the input voltage because of supplied reactive power; this requires a reduced load current for producing rated output apparent power of the transformer, and therefore, results in

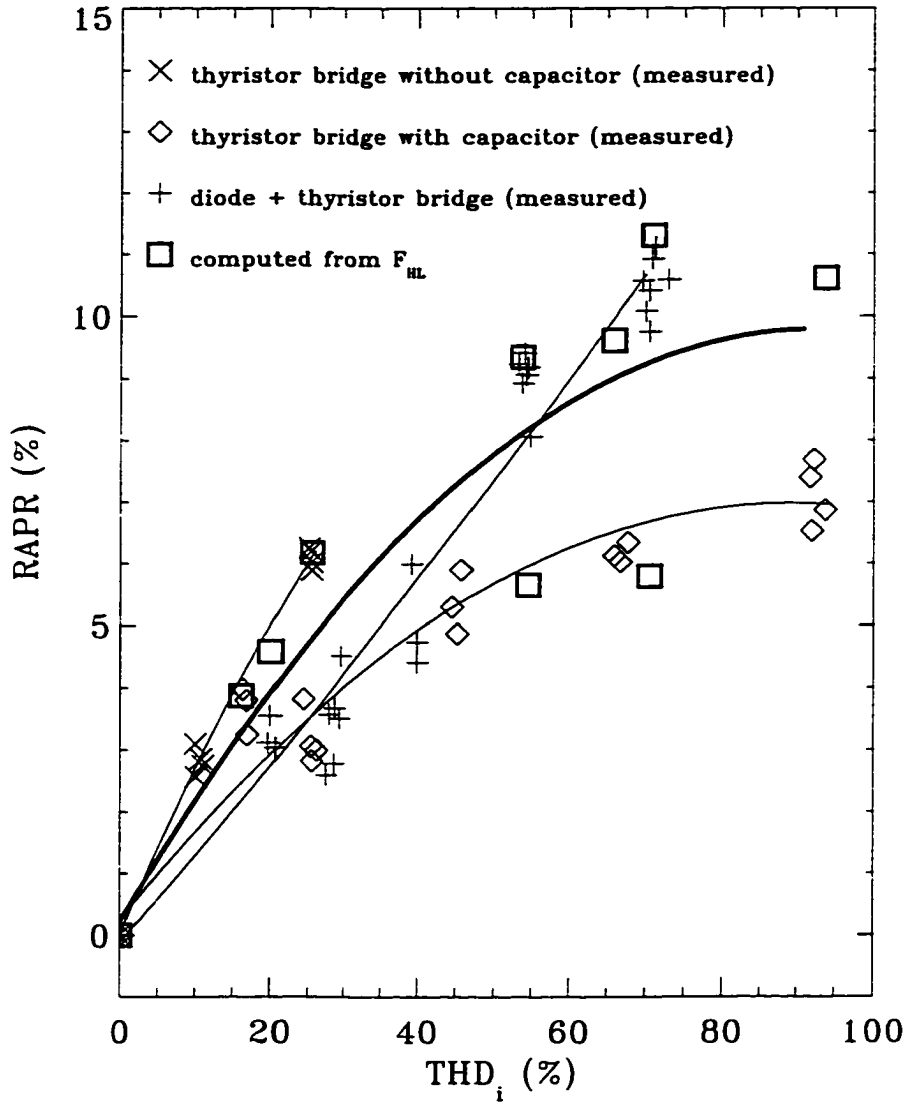

Figure 9.1: Reduction of apparent power rating of 25kVA transformer as a function of total harmonic current distortion (THD_i).

reduced copper losses.

The capacitors at the output of the rectifiers introduce a leading phase shift of the primary current of the transformer, thus reducing the real power capability of the $25kVA$ transformer. RPC is defined as

$$RPC = \frac{P_{out}}{S_{out}^{rated}} , \tag{9.6}$$

where

$$P_{out} = \sum_{h=0,1,2,\cdots}^{49} V_h I_h \cos\phi_h ,$$

$$S_{out}^{rated} = (V_{rms} I_{rms})_{rated} = 25kVA \ .$$

Figure 9.2 illustrates the RPC as a function of THD_i values for different types of loads where the operating points are similar to those of Table 9.3. It is evident from Figure 9.2

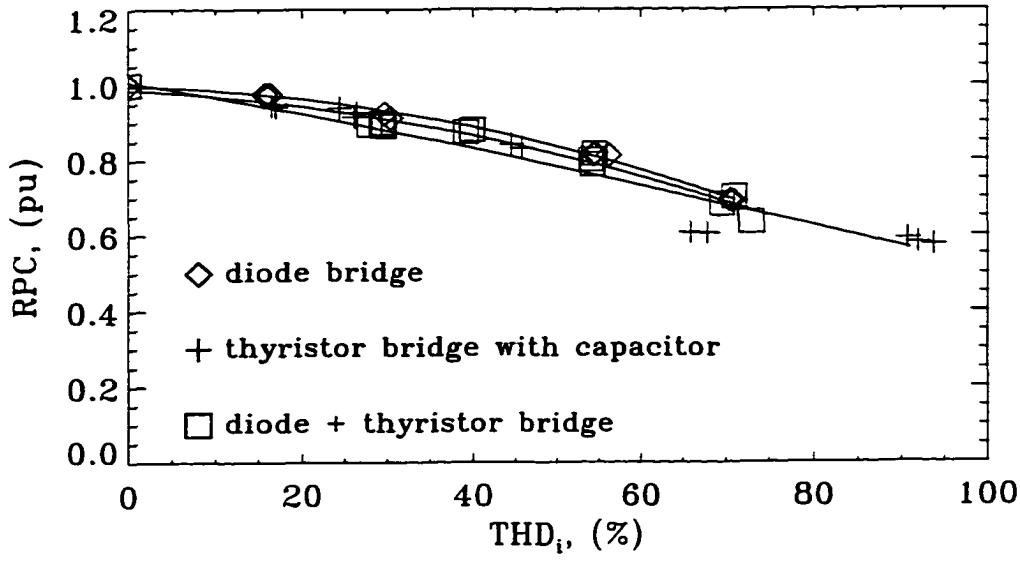

Figure 9.2: Real power capability (RPC) as a function of total harmonic current distortion (THD_i).

that the RPC is independent of the frequency spectrum of the harmonics but changes with the total harmonic distortion of the current.

9.5 Other Stray Power Losses (P_{OSL})

Time-varying fluxes in transformers and inductors induce eddy currents in nearby conductive parts, e.g., enclosures and clamps. These currents produce other stray losses because of the finite resistivity of the conductive parts.

The losses of an air-core inductor, P_{loss}, (inductor #9 of Appendix B), where there are no metallic parts in the close proximity, are measured using a computer-aided measurement circuit similar to the one described in Chapter 7. Sinusoidal voltages of different frequencies are applied to the inductor, and the total power losses at each frequency is computed from the sampled voltage and current wave forms of the inductor.

Then, total losses of the same inductor with a U-shaped nonmagnetic steel member adjacent to it, P_{loss}^{enc}, are measured. Note that the measurement circuits used for both above experiments are the same. Even though the absolute error of the total losses may be large ($\pm 10\%$), the relative error of the difference $P_{OSL} = P_{loss}^{enc} - P_{loss}$ is small ($\pm 1\%$).

Figure 9.3 shows the power losses of the inductor in two different configurations. As the frequency increases, the difference between these two loss components becomes

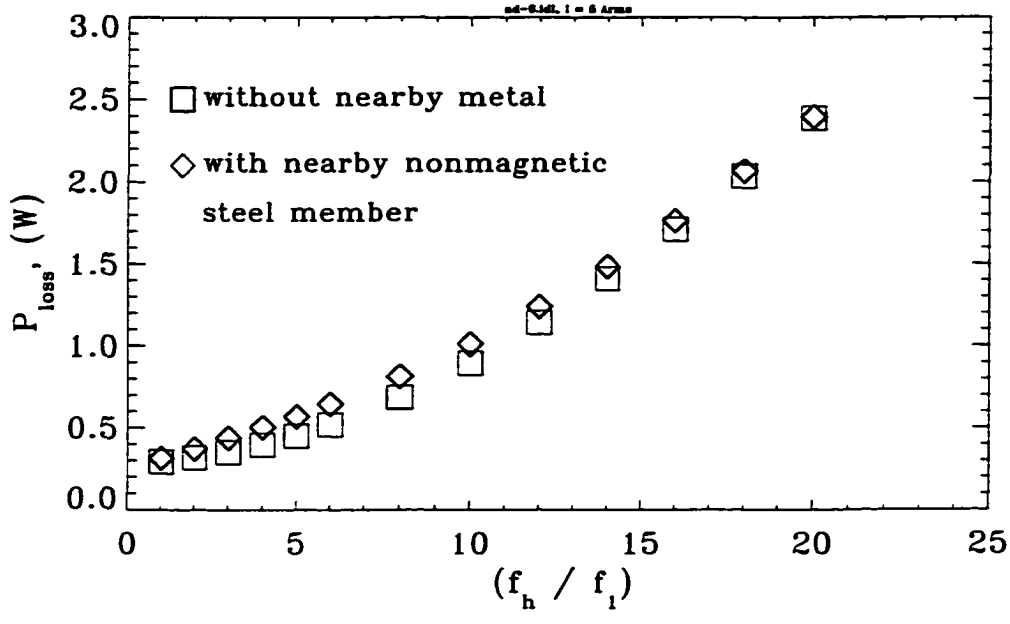

Figure 9.3: Total power losses of an inductor with and without a metallic part nearby at a current of $5A$.

small. Any conductive material in proximity of the inductor, even if it is nonmagnetic ($\mu_r \approx 1$), will affect the value of the inductance. This is due to the reduction of the field of the inductor by an opposing field created by the eddy currents flowing in nearby conductive parts. Ideally, the inductance values should remain the same with and without an enclosure for comparing the power losses. In reality, they do not. The AC resistance of the nonmagnetic steel member is given in Figure 9.4, along with the inductance values. At low frequencies, the induced eddy currents are low, and therefore the change in the inductance is small, while the difference in the inductance is increasing at higher frequencies. The AC resistance reaches a maximum value at around $420Hz$,

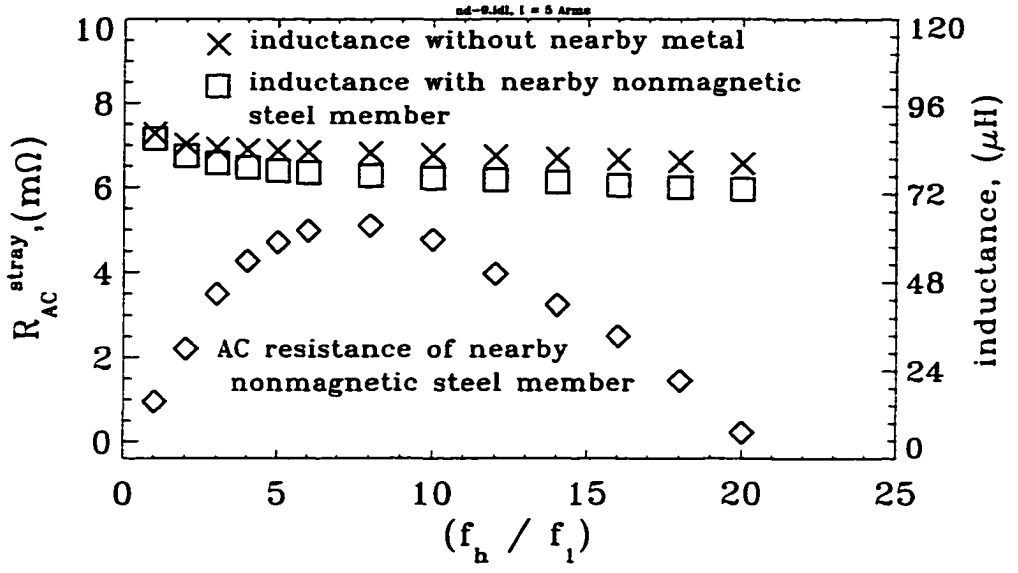

Figure 9.4: AC resistance of nonmagnetic steel and inductance values.

and then decreases with increased frequency because the electromagnetic fields penetrate less into the non-magnetic steel at high frequencies.

To find the change of the other stray losses with frequency, a linear regression analysis is applied to the data of Fig. 9.4. The results are shown in Fig. 9.5. where the formula for the two different linear approximations - one at low frequency (0 to $360Hz$)

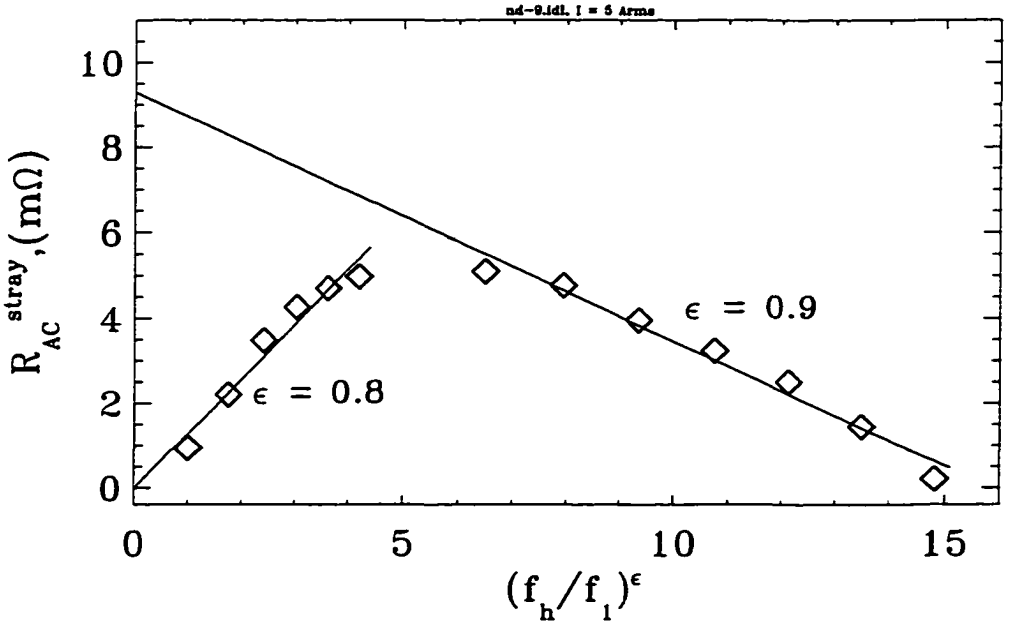

Figure 9.5: Change of AC resistance with frequency.

and one for the high frequency ($420Hz$ to $1200Hz$) - are given as

$$R_{AC}^{lf} = 1.29\left(\frac{f_h}{f_1}\right)^{0.8} \quad [m\Omega] \tag{9.7}$$

$$R_{AC}^{hf} = 9.29 - 0.58\left(\frac{f_h}{f_1}\right)^{0.9} \quad [m\Omega] \tag{9.8}$$

where superscripts "lf" and "hf" represent low and high frequency, respectively. One concludes from Figure 9.5 that the stray power losses increase with the power of 0.8 (at low frequency), and decrease with power of 0.9 at high frequency. These results confirm the data given in [74].

9.6 Discussion and Conclusions

The eddy-current loss coefficient of a single-phase transformer can be determined from real-time measurement data, and it has been shown that eddy-current losses increase with the square of frequency. The apparent power derating of transformers in terms of the harmonic loss factor (F_{HL}), iron-core losses, and other stray losses (P_{OSL}) is computed, and the results are compared with measured data. Figure 9.1 shows that the apparent power derating is about 7% for a THD_i of about 90%. The apparent power derating depends on the type of load connected to the transformer, because certain loads increase the input voltage resulting in a current which is less than its rated value. Since the copper losses are the major part of the total losses of a transformer, the derating will be smaller for increased input voltages. Comparing Figure 9.1 with the Figure 8.3, where the K-Factor approach is used, gives

$$RAPR_{K-factor} > RAPR_{F_{HL}}.$$

The K-Factor approach is a somewhat more conservative approximation to the apparent power derating than the harmonic loss factor (F_{HL}) approach, considering the fact that derating values are computed for the worst case, because the variation of input voltage is neglected.

Unlike the apparent power derating, the real power capability (R_{PC}) of the transformer is more severe: for example, RPC equals to about 0.5 pu at a THD_i of about 90%: that is, transformer can only supply 50% of its rated real power output (12.5kW). This reduction is due to a phase shift between the voltage and current created by the output capacitors of rectifiers. Since this phase shift is positive (leading), the power factor cannot be improved by adding power factor correction capacitors at the transformer terminals. Moreover, the $RAPR$ is affected by the frequency spectra of the harmonics, while RPC is practically independent of the frequency spectra.

The other stray losses change with a power of frequency less than 1. Reference [74] comes to a similar conclusion where it reads "$\cdots$ eddy current losses in bus bars, connections and structural parts increase by a harmonic exponent factor of 0.8 or less". This may imply that the P_{OSL} always increases with frequency with a power of 0.8. However, Figure 9.4 shows that P_{OSL} increases up to a certain frequency with an exponent of 0.8, and then decreases with an exponent of 0.9 as frequency increases. The frequency where maximum losses occur depends on the type of material is used [82] at a given frequency. It has been shown in [82] that for a given frequency nonmagnetic steel has the highest losses.

CHAPTER 10

CONCLUSIONS

A direct drive train for a wind power plant without any mechanical gear, operating at variable speeds (60-120rpm) can extract more power from wind than a constant speed drive. Any voltage fluctuations (300-600V_{L-L}) on the generator side as the wind velocity changes will permit the drive train to remain on-line, because the rectifier maintains a constant DC link voltage (360V_{DC}). The real and reactive powers delivered to the utility system are adjustable by changing the amplitude and phase angle of the reference current signals of the inverter. Therefore, leading, lagging, and unity currents (with respect to voltage) can be supplied. However, higher DC voltages (about $V_{DC} = 450VDC$) are required to supply lagging currents as compared to the operation with leading currents ($V_{DC} = 350VDC$). Since the input voltage to the inverter is fixed by the rectifier at around $V_{DC} = 360VDC$, this drive train can deliver power to the utility system at unity or leading power factors only.

The losses of inductors as a function of frequency (0 to 6kHz) have been measured using two different approaches (computer-aided and three-voltmeter methods). Errors of both methods are less than 10% when measuring a fraction of one watt. It has been found that inductors wound with Litz wires have the lowest losses and the value of the inductance reduces slightly with the frequency. A stranded straight wire, where the individual strands are not insulated and proximity effects due to a wound coil do not exist, has larger losses than a solid straight wire if both wires have the same cross-

sectional area. This is due to an effect called "spirality effect" caused by the stranding.

Existing formulations of the distortion power D have been reviewed as a function of voltage and current harmonic amplitudes and phase angles. The correct double trigonometric sum for the definition of D , given by Equation 6.22, is not similar to (with respect to the indices of the double sum) existing formulations which are not quite correct, neither from a numerical nor a physical point of view, due to the involvement of like voltage and current components in D. Experimental results agree well with the results obtained by using individual voltage and current harmonics. If distortion power exists in a system, it increases the rms current and as a result additional losses are produced: usual compensation techniques cannot be applied to reduce the distortion power in a system. Any compensation must be based either on filtering of harmonics or injecting harmonics to the power system.

The derating of a single-phase transformer in the presence of nonsinusoidal voltages and currents is measured using a computer-aided testing circuit. Measured results are compared with results obtained by using K-factor and F_{HL}-factor approaches. It has been found that the K-factor (favored by UL) derating is somewhat larger than that of F_{HL}-factor (favored by IEEE) derating as applied to a $25kVA$ transformer. Capacitors connected across the DC side of rectifiers have an influence on the derating of transformers since they increase the input voltage and decrease the required input current of an apparent power rated transformer resulting in less severe derating values. The other stray losses in enclosures, clamps and nearby conductive regions due to changing fluxes have a maximum value at a certain frequency, depending on the type of material used. Up to this frequency, losses increase with a power of 0.8 of frequency $(f_h/f_1)^{0.8}$, and further increase of the frequency results in a decrease of the losses with a power of 0.9 of frequency $(f_h/f_1)^{0.9}$.

10.1 Contribution of this Thesis

- The experimental testing of the rectifier and the PWM inverter which are components of a 30 kVA variable-speed, direct-drive wind power plant and the operation of the entire drive system, that is synchronous generator, rectifier and inverter connected to the utility system, are presented.

- The $20kW$ zero-current-switch (ZCS) rectifier employs one switching transistor to control the output voltage to be nearly constant for variable input voltage and variable frequency. Such a large rating ZCS rectifier has not yet been designed and built.

- Reactive-power controllability of the inverter was studied. It has been found that for a given DC input voltage, leading and unity-power factor operations are easily obtained, but for lagging power factor operations the DC input voltage must be increased substantially.

- For a given DC input voltage, the AC output voltage of the inverter can be increased by operating the inverter in overmodulation mode ($m > 1.0$). This overmodulation is achieved by introducing, for all operating conditions, an additional lagging phase shift between the reference currents and the (actual) output currents of the inverter.

- An accurate measurement of frequency-dependent losses of inductors by use of two different methods are presented. The results obtained from the two measurements agree well with each other, and each method can measure a fraction of a watt with a maximum error of less than 10% over a large frequency range (0-$6kHz$).

- A transverse-flux type permanent magnet machine is investigated for applications to high-power wind generation because of its light weight compared to

those of conventional longitudinal-type generators.

10.2 Further Work

Generation of electricity from wind has been increasing steadily (about 10%) with the installation of new wind farms each year. However, installed capacity of wind farms is still low ($7GW$) compared to the total installed ($700GW$) power capacity in the United States. Wind farms consist of a great number (typically hundreds) of small ($100kW$ to $1MW$) wind turbines operating at constant speed ($30rpm$). Use of variable speed enables the wind turbine to operate more energy-efficient at different wind speeds; therefore, somewhat more energy can be extracted from the wind. It is desirable to increase the power rating of an individual wind turbine so that larger amounts of power can be generated by one unit. One of the problems associated with increasing power of one unit is the increase of weight (generator and gear box) on the tower.

- This problem may partially be solved by employing a transverse-flux type generator which offers a light weight for high torques at low speeds, therefore, more work should be done to completely study the transversal-flux type machines for such an application.

- Since the variable-speed type system employs expensive power semiconductor devices, a cost analysis should be performed to determine the effectiveness of this type of drive system and rectifier; inverter and machine efficiencies should be in the range from 98 to 96%.

- High-efficiency converter (rectifier/inverter) losses should be measured with small maximum errors (3%).

BIBLIOGRAPHY

[1] E. F. Fuchs. "Electromagnetically Commutated Variable-Speed, Permanent-Magnet Drive Train for Wind Power Plants." *Power Engineering Review*, December 1992, Vol. 12, No. 12, pp. 7-8.

[2] E. F. Fuchs and P. W. Carlin. "An Electronically Commutated Permanent-Magnet Generator with Flux Weakening Voltage Control." *Proceedings of the 11th ASME ETCE Wind Energy Symposium*, Houston, Texas, January 26-30, 1992.

[3] E. F. Fuchs, A. A. Fardoun, P. W. Carlin , and R. W. Erickson. "Permanent-Magnet Machines for Operation with Large Speed Variations." *Proceedings of Windpower 1992*, Seattle, WA, October 19-23, 1992.

[4] A. A. Fardoun, E. F. Fuchs, and P. W. Carlin,"Variable-Speed Generators with Flux Weakening," *Proceedings of Technology 2002*, Baltimore, MD, December 1-3, 1992.

[5] A. A. Fardoun, E. F. Fuchs, and P. W. Carlin. "Variable-Speed, Direct-Drive Power Train for a Wind Power Plant." *Proceedings of Windpower 1993*, San Francisco, CA, July 12-16, 1993.

[6] A. A. Fardoun, "A Novel Wind-Power Train: Permanent-Magnet Generator with Flux Weakening Feeding a Controlled Real/Reactive Power Inverter," *Ph.D. Thesis*, University of Colorado at Boulder, May 1994.

[7] L. J. Fingersh, "The Testing of a Low-Speed, Permanent-Magnet Generator for Wind Power Applications." *M.S. Thesis*, University of Colorado at Boulder, July 1995.

[8] E. F. Fuchs, "Architecture of a Variable-Speed, Direct-Drive Wind Power Plant," *Proceedings of 26th Annual Frontiers of Power Conference*, Oklahoma State University, Stillwater, Oklahoma, October 25-26, 1993.

[9] E.F. Fuchs, P.W. Carlin, E.B. Muljadi, and L.J. Fingersh,"Dynamometer Test Results from the Colorado University Low-Speed, Permanent-Magnet Electric Generator," *Fourteenth ASME Wind Energy Symposium*, Houston, TX, January 29-February 1, 1995 (Abstract).

[10] P. W. Carlin, L. J. Fingersh, and E. F. Fuchs, " Preliminary Results from the Variable-Speed, Direct-Drive Generating System," *Presentation at the 15th ASME ETCE Wind Energy Symposium*, Houston, Texas, January 1996 (Abstract).

[11] E. F. Fuchs and A. A. Fardoun, "Architecture of a Variable-Speed Direct-Transmission Wind Power Plant of Wind Farm Size," *Invention Disclosure*, University of Colorado, Boulder, February 1994.

[12] E. F. Fuchs and B. Gregory, "Control of a Wind Power Plant with Variable Displacement (or Power Factor) Angle and Waveshape of AC current Fed into the Power System." *Invention Disclosure*, University of Colorado, Boulder, February 1994.

[13] H. Weh, and J. Jiang, "Berechnungsgrundlagen für Transversalflußmaschinen," *Archiv für Elektrotechnik* 71 (1988), pp. 187-198.

[14] E. F. Fuchs and D. Yildirim, "Transverse Flux Machines with Phase Numbers Higher than Two," *Invention Disclosure*, University of Colorado, Boulder, CO, January 19, 1995.

[15] E. F. Fuchs and D. Yildirim, "Permanent-Magnet Reluctance Machine for High Torques at Low Rated Speeds and Low Weight Based on Alternating Magnetic Field Theory," *Provisional Patent Application*, University of Colorado, Boulder, CO, April 6, 1997.

[16] B. Gregory, "Current Control of Inverter via Computer-Controlled Arbitrary Function Generator," *M.S. Thesis*, University of Colorado at Boulder, May 1993.

[17] J. Jayadev, "Harnessing the Wind," *IEEE Spectrum*, November 1995, pp. 78-83.

[18] E. Muljadi, K. Pierce, P. Migliore, "Control Strategy for Variable-Speed, Stall-Regulated Wind Turbines," *American Controls Conference*, Philadelphia, PA, June 24-26, 1998.

[19] P. Gipe, *Wind Energy Comes of Age*, John Wiley & Sons Inc., 1995.

[20] E. Ismail, "Three-Phase High Quality Rectification," *Ph.D. Thesis*, University of Colorado at Boulder, 1993.

[21] L. Golcher, "Theoretical Study of Three-Phase Buck-Type Zero-Current-Switching Resonant Rectifier," *M.S. Thesis*, University of Colorado at Boulder, 1994.

[22] M. H. Rashid, *Power Electronics: Circuits, Devices, and Applications*, 2nd edition, Prentice Hall, 1993.

[23] C. W. Lander, *Power Electronics*, 2nd Ed., McGraw-Hill, 1987.

[24] A. Consoli, S. Musumeci, G. Oriti and A. Testa, "Active Voltage Balancement of Series Connected IGBTs," *IEEE Industry Applications Conference*, Vol. 3, October 8-12, 1995.

[25] C. Gerster, "Fast High-power/High-voltage Switch Using Series-connected IGBT with Active Gate-controlled Voltage-balancing," *IEEE APEC*, 1994.

[26] P. R. Palmer, A. N. Githiari, and R. J. Leedham, "A Comparison of IGBT Technologies for Use in the Series Connection" *IEE Power Electronics and Variable Speed Drives*, 23-25 September 1996, Conf. Publ. No. 429.

[27] W. McMurray, "Optimum Snubbers for Power Semiconductors" *IEEE Trans. on Ind. Appl.*, Vol. IA-8. no. 5. September/October 1972.

[28] R. W. Erickson. Power Electronics II. *Course Notes*, University of Colorado. 1993.

[29] Motorola FAST and LS TTL Data Book. DL121/D, 5th edition. 1992.

[30] Analog and Interface Integrated Circuits Data Book. Motorola Inc.. 1996.

[31] CEI/IEC *Standard 555*. Bureau Central de la Commission Electrotechnique Internationale 3. rue de Varembè. Genéve, Switzerland.

[32] N. Mohan. T. M. Undeland. and W. P. Robbins. *Power Electronics. Converters. Applications and Design*. 2nd Ed.. John Wiley & Sons. 1995.

[33] W. Shephard. L. N. Hulley and D. T. W. Liang, *Power Electronics and Motor Control*. 2nd Ed.. Cambridge University Press. 1995.

[34] G. K. Dubey. *Power Semiconductor Controlled Drives*. Prentice Hall. 1989.

[35] K. S. Rajashekara and J. Vithayathil. "Harmonics in Voltage Source Inverters." *International Journal of Electronics*. Vol. 50. No. 5. 1981. pp. 325-337.

[36] K. K. Sen. "SSSC-Static Synchronous Series Compensator: Theory, Modeling, and Application." *IEEE Trans. on Power Delivery*. Vol. 13, No. 1, 1998, pp. 241-246.

[37] I. Papic, P. Zunko. D. Povh, M. Weinhold. "Basic Control of Unified Power Flow Controller." *IEEE Trans. on Power Systems*, Vol. 12. No. 4. 1996. pp. 1999-2004.

[38] L.A.C. Lopes. G. Joos. O. Boon-Teck. "A PWM Quadrature Booster Phase-Shifter for FACTS." *IEEE Trans. on Power Delivery*, Vol. 11. No. 4. 1998. pp. 241-246.

[39] M. Teltsch. "Adjustable-Speed Drive for an Electric Car with Large Rated Torque at Low Rated Speed." *M.S. Thesis*, University of Colorado at Boulder. August 1997.

[40] T. Batan. "Real-Time Monitoring and Calculation of the Derating of Single-Phase Transformers under (Non)Sinusoidal Operations." *Ph.D. Thesis*, University of Colorado at Boulder. 1998.

[41] H. Weh. H. May. and M. Shalaby. "Highly Effective Magnetic Circuits for Permanent Magnet Excited Synchronous Machines" *Proceedings of the International Conference on Electrical Machines*, Cambridge, MA, August 12-15, 1990.

[42] H. Weh, H. Mosebach, W. Niemann, and A. Tareilus,"Field Control in Synchronous Machines with Permanent Magnet Excitations in Flux Concentration Mode" *Proceedings of the International Conference on Electrical Machines*, Cambridge, MA, August 12-15, 1990.

[43] H. Weh, H. Hoffmann, J. Landrath, H. Mosebach, J.Poschadel, "Directly-Driven Permanent-Magnet Excited Synchronous Generator for Variable Speed Operation" *European Community Wind Energy Conference*, Herning, Denmark, 1988.

[44] H. Weh, B. Degele, J. Poschadel, R. Sundermeier, S. Tareilus, "Inverter Concept with Fast Commutation for Feeding Synchronous Machines with High Frequency Stator Currents," *International Conference on Electrical Machines ICEM 1988*, Pisa, Italy, September 12-14 1988, pp. 425-430.

[45] H. Weh, H. Hoffmann and J. Landrath, "New Permanent Magnet Excited Synchronous Machine with High Efficiency at Low Speeds," *International Conference on Electrical Machines ICEM 1988*, Pisa, Italy, September 12-14 1988, pp. 35-40.

[46] C. I. Budeanu, "Puissances Réactives et Fictives," *Inst. Romain de l'Energie*, Bucharest, 1927.

[47] IEEE Working Group on Nonsinusoidal Situations, "A Survey of North American Electric Utility Concerns Regarding Nonsinusoidal Waveforms," IEEE Trans. on Power Delivery, Vol.11, No. 1, January 1996, pp.73 -78.

[48] C. Budeanu, "Kapazitäten und Induktivitäten als verzerrende Elemente," *Archiv für Elektrotechnik*, XXXII. Band, 4. Heft, 1938, pp. 251-259

[49] W. Shepherd and P. Zand, *Energy Flow and Power Factor in Nonsinusoidal Circuits*, Cambridge University Press, 1979, p. 185.

[50] P. Filipski, "The Measurement of Distortion Current and Distortion Power," *IEEE Trans. on Instr. and Meas.*, Vol. IM-33, No. 1, March 1984, pp. 36-40.

[51] L. S. Czarnecki, "Methods of Describing the Power Properties of Linear Nonsinusoidal Systems," *Second International Conference On Harmonics in Power Systems*, Oct. 6-8 1986, Winnipeg, Canada, pp. 142-147.

[52] *The IEEE Standard Dictionary of Electrical and Electronics Terms*, IEEE Std 100-1996, 6th ed., Institute of Electrical and Electronics Engineers, 1996, p. 306.

[53] D. Yildirim and E.F. Fuchs, "Computer-Aided Measurement of Inductor Losses at High Frequencies (0 to 6kHz)," 14th Applied Power Electronis Conference and Exhibition, Dallas, TX, March 14-18, 1999.

[54] A. E. Emanuel, "Powers in Nonsinusoidal Situations A Review of Definitions and Physical Meaning," *IEEE Trans. on Power Delivery*, Vol. 5, No. 3, July 1990, pp. 1377-1389.

[55] A. E. Emanuel, "Power Components in a System with Sinusoidal and Nonsinusoidal Voltages and/or Currents," *IEE Proceedings*, Vol. 137, Pt. B, No. 3, May 1990, pp. 194-196.

[56] Private communication with Prof. R. Roth, University of Colorado, Dept. of Mathematics, Boulder, CO, October 1997.

[57] L. S. Czarnecki, "Distortion Power in Systems with Nonsinusoidal Voltage," *IEE Proceedings*, Vol. 139, Pt. B, No. 3, May 1992, pp. 276-280.

[58] M. P. Perry, *Low Frequency Electromagnetic Design*, Marcel Dekker Inc., New York, 1985.

[59] J. A. Ferreira and J. D. van Wyk, "Experimental Evaluation of Losses in Magnetic Components for Power Converters," *IEEE Industry Applications Society Annual Meeting*, October 2-7, 1988, Pittsburgh, PA, pp. 668-673.

[60] A. E. Kennelly, F. A. Laws, and P. H. Pierce, "Experimental Researches on Skin Effect in Conductors," *AIEE Proceedings*, Vol. 34, No. 8, Sep. 16, 1915, pp. 1749-1814.

[61] P. F. Ryff, T. H. Fawzi, and A. M. Hussein, "Enclosure Losses in High Power Systems," *IEEE Trans. on Magnetics*, Vol. 30, No. 6, Nov. 1994, pp. 4338-4340.

[62] K. V. Namjoshi, J. D. Lavers, and P. P. Biringer, "Eddy Current Power Loss in Structural Steel Due to Cables Carrying Ceuurent in a Perpendicular Direction," *IEEE Trans. on Magnetics*, Vol. 30, No. 1, Jan. 1994, pp. 85-91.

[63] DAS-50 User's Guide, Part # 24851, Revision Level C, Keithley/MetraByte Corporation, Taunton, MA, July 1990.

[64] E. F. Fuchs and R. Fei, "A New Computer-Aided Method for the Efficiency Measurement of Low-Loss Transformers and Inductors under Nonsinusoidal Operation," *IEEE Trans. on Power Delivery*, January 1996, Vol. PWRD-11, No. 1, pp. 292-304.

[65] M. Stöckl, *Elektrische Meßtechnik*, B. G. Teubner Verlagsgesellschaft, Stuttgart, 1961.

[66] H. Cundy and A. Rollett, *Mathematical Models*, 3rd ed., Tarquin Publishing, Stradbroke, England, 1989, pp. 242-244.

[67] S. Rieman, "An Optically Isolated Data Acquisition System," *Independent Study*, University of Colorado at Boulder, December 1997.

[68] W. Thomson, *Mathematical and Physical Papers*, Vol. 3, Cambridge University Press Warehouse, 1890, p. 492.

[69] J. B. Walsh, *Electromagnetic Theory and Engineering Applications*, The Ronald Press Company, New York, 1960.

[70] D. Lin, E. F. Fuchs, and M. Doyle, "Computer-Aided Testing of Electrical Apparatus Supplying Nonlinear Loads," *IEEE Trans. on Power Systems*, Vol. 12, No. 1, February 1997, pp. 11- 21.

[71] Standard UL 1561, *Dry-Type General Purpose and Power Transformers*, Underwriters Laboratory Inc., April 22, 1994.

[72] L. W. Pierce, "Transformer Design and Application Considerations for Nonsinusoidal Load Currents," *IEEE Trans. on Industry Applications*, Vol. 32, No.3, May/June 1996, pp. 633- 645.

[73] Standard UL 1562, *Transformers, Distribution Dry Type Over 600 Volts*, Underwriters Laboratory Inc., January 28, 1994.

[74] *ANSI/IEEE Recommended Practice for Establishing Transformer Capability when Supplying Nonsinusoidal Load Currents*, ANSI/IEEE C57.110/D7-February 1998, Institute of Electrical and Electronics Engineers, Inc., New York, NY, 1998.

[75] A. W. Galli and M. D. Cox, "Temperature Rise of Small Oil-Filled Distribution Transformers Supplying Nonsinusoidal Load Currents," *IEEE Trans. on Power Delivery*, Vol. 11, No. 1, January 1996, pp. 283-291.

[76] M. T. Bishop, J. F. Baranowski, D. Heath, and S. J. Benna, "Evaluating Harmonic-Induced Transformer Heating," *IEEE Trans. on Power Delivery*, Vol. 11, No. 1, January 1996, pp. 305-311.

[77] C. K. Duffey and R. P. Stratford, "Update of Harmonic Standard IEEE-519: IEEE Recommended Practices and Requirements for Harmonic Control in Electric Power Systems", *IEEE Trans. on Industry Applications*, Vol. 25, No. 6, November/December 1989.

[78] E. F. Fuchs, D. J. Roesler and K. P. Kovacs, "Aging of Electrical Appliances Due to Harmonics of the Power System's Voltage", *IEEE Trans. on Power Delivery*, July 1986, Vol. PWRD-1, No. 3, pp. 301-307.

[79] T. D. Stensland, E. F. Fuchs, W. M. Grady, and M. T. Doyle, "Modeling of Magnetizing and Core-Loss Currents in Single-Phase Transformers with Voltage Harmonics for Use in Power Flow," *IEEE Trans. on Power Delivery*, Vol. 12, No. 2, April 1997, pp. 768- 774.

[80] E. F. Fuchs, T. D. Stensland, W. M. Grady, and M. T. Doyle, "Measurement of Harmonic Losses of Pole Transformers and Single-Phase Induction Motors," *Proceedings of the IEEE-IAS Industry Applications Society Annual Meeting*, Denver, CO, October 2-7, 1994, paper No. EM-03-162, pp. 128- 134.

[81] *ANSI/IEEE Standard Practices and Requirements for Semiconductor Rectifier Transformers*, ANSI/IEEE C57.18.10-1998, Institute of Electrical and Electronics Engineers, Inc., New York, NY, 1998.

[82] K. Sasaki, Magnetic Field Analysis of a Linear Motion Electromagnetic Pile Driver, *M.S. Thesis*, University of Colorado at Boulder, 1980.

[83] Unitrode Integrated Circuits, Products and Application Handbook, 1995-96, pp. 6-323 to 6-328.

APPENDIX A

SAMPLING AND DATA ACQUISITION/ANALYSIS OF INDUCTOR LOSS MEASUREMENTS

A.1 Procedure

The two channels CH0 and CH1 of the A/D converter (DAS50/4) are used to sample the current and voltage wave forms, respectively. CH0 is also triggering the A/D converter. DAS50/4 will start collecting data when the wave form in CH0 has a negative zero crossing. In this measurement the voltage wave form is used for triggering.

Before starting sampling, the driver file for the DAS50/4 must be loaded by typing *LDD* at the DOS prompt. The content of the batch file *LDD.BAT* is given below. This should be done only once after the computer is turned on the first time. The BASIC sampling program listed in Section A.2 can be run by typing *gwbasic twochb.bas* at the DOS prompt. It plots the sampled wave forms on the screen and then writes the values to a file called *ch2.dat*.

After determining the calibration constants for each channel, the FORTRAN program (*2chd.f*) in Section A.3 can be executed to determine the Fourier coefficients of each wave form. The calibration file *ch2cal.dat* and the output file of the FORTRAN program for one case are given in Section A.4. The total computing time of the program up to the 102nd harmonic (6,120Hz) on a Sun/Sparc workstation is about 50 seconds.

LDD.BAT

```
cd \sys
ls c:\sys\vi.sys
ls c:\sys\vi.sys
ls c:\sys\das50drv.sys
cd \das50
```

A.2 Sampling Program for Two-Channel A/D Converter

twochb.bas

```
10 ' -- Name of the program : twochb.bas
20 '*******************************************************
30 'This program will read 15,008 samples at 900kHz to get one
40 'fundamental period of a 60 Hz wave. It is for two channel.
50 'This program also can send data to a file called CH2.DAT.
60 '*******************************************************
70 KEY OFF : CLS : COLOR 7,0
80 NS = 15002 ' Number of samples
90 DIM A%(20000)
100 '-----Step 1 -- This sets up the DAS50 and reads in Data ---
110 OPEN "$DAS50" FOR OUTPUT AS #1
120 PRINT #1,"CLEAR" ' Just clearing for setup
130 OPEN "$DAS50" FOR INPUT AS #2
140 '
150 PRINT "Ready to Aquire Data. Strike any Key to Continue."
160 IF INKEY$="" GOTO 160
170 PRINT #1,"SAmples 15008 RATE INT 9E5 ch 1&2 +-10v tm 8 ACquire"
175 PRINT "Continue?"
177 IF INKEY$="" GOTO 177
180 PRINT #1,"Set ADdress 0"
185 ' ---- Get NS points to variable A%
190 PRINT #1,"transfer ";-1;VARPTR(A%(0));NS
200 '-----Step 2 -- This will plot the data ---------
210 SCREEN 2
220 ' Plot data in array A%(). Normalize data +-2048 and +-85
225 GOSUB 300  'Print reference lines on screen
230 FOR I% = 0 TO NS-1 STEP 2
235 PSET((I%+1)/23.4375!,85!-((A%(I%+1)*85!)/2048!))
240 PSET(I%/23.4375!,85!-((A%(I%)*85!)/2048!))
250 NEXT I%
254 '-----Step 3 -- Subroutine at 400 will send data to file -
255 GOSUB 400 'Interpolate data and send to datafile.
260 LOCATE 23,1:PRINT "          Strike any key to continue";
270 IF INKEY$="" GOTO 270
280 SCREEN 0 : CLS : LOCATE 10,1
281 '-----Step 4 -- Ask user if measurements are to be repeated-
282 INPUT "End Program";A$
283 IF (A$="Y" OR A$="y") THEN END
290 GOTO 150
300 LINE (0,170)-(0,0)    '----This subroutine will put reference
310 LINE (0,0)-(640,0)    '--- Lines on the screen.
320 LINE (0,170)-(640,170)
330 LINE (639,0)-(639,170)
```

```
340 FOR I% = 0 TO 640 STEP 10
350 LINE (I%,85)-(I%+3,85)
360 LINE (I%,127.5)-(I%+2,127.5)
370 LINE (I%,42.5)-(I%+2,42.5)
380 NEXT I%
390 RETURN
400 LOCATE 23,1                              'Beginning of subroutine
405 INPUT "Send data to an output file";A$ 'that will
410 IF (A$<>"Y" AND A$<>"y") GOTO 860        'send data to a file
420 FOR I% = 0 TO NS-2 STEP 2                'if desired after it
430 A%(I%) = (A%(I%)+A%(I%+2))/2.0!          'interpolates the data.
450 NEXT I%
460 'Write data to data file
470 OPEN "CH2.DAT" FOR OUTPUT AS #3
480 FOR I% = 0 TO 14999 STEP 10
490 PRINT #3,USING"##.######^^^^  ";A%(I%),A%(I%+2),A%(I%+4),
                                     A%(I%+6),A%(I%+8)
500 NEXT I%
510 FOR I% = 1 TO 14999 STEP 10
520 PRINT #3,USING"##.######^^^^  ";A%(I%),A%(I%+2),A%(I%+4),
                                     A%(I%+6),A%(I%+8)
530 NEXT I%
800 CLOSE #3
810 'OPEN "CH2.QPR" FOR OUTPUT AS #4
820 'FOR I% = 0 TO 14999 STEP 14
830 'PRINT #4,USING"##.####^^^^  ";A%(I%)*0.1942705!,
                                    A%(I%+1)*0.012159097!*50!
840 'NEXT I%
850 'CLOSE #4
860 RETURN
```

A.3 Data Analysis Program

2chd.f

```
c       last modified: Wed Mar 25 14:52:45 MST 1998
c       name of the program : 2chd.f
c
c       this program is used for analyzing full-
c       wave curves with 7500 points of full period.
c       odd and even harmonics are both included up to
c       a harmonic of 100.
c
        parameter(tnh=102,set=2,pt=7500)

        common nw,deg(pt),rad(pt)
        common npts,nps,int,inc,nh,ga,pi,ww,om,nc,rf,er,el,err,itmax

        dimension y(set,pt),scale(set),ymax(set),x(pt),yvalue(pt)
        dimension curvt(tnh),curvc(tnh),curvs(tnh),curvp(tnh)
        dimension amp(set,tnh),ang(set,tnh),work(pt),rms(set,tnh)
        real tpin(pt)
        dimension rac(tnh),pinh(tnh)
        real dccomp(set)
        real fc(pt), fcang(set,pt),th21(tnh)

        real dcoff,tpinav,pinsum,harmno,zind,xlind,lind
c
c       read data from data file. (for non-linear load)
c
        open(5,file='ch2cal.dat',status='unknown',
     &   access='sequential')
c
c       ch1 i1 , ch2 v1
c       set nsets and npts here
c       read scaling constants set v and i constants here
c
        read(5,*) nsets,npts
        do 43 j = 1, nsets
 43     read(5,*) scale(j)
        close(unit=5)
c
        open(3,file='ch2.dat',status='unknown',access='sequential')

        open(10,file='d2chout.txt',status='unknown')
        open(80,file='d2chorig.txt',status='unknown')
        open(81,file='d2chcons.txt',status='unknown')
        open(83,file='d2chrms.txt',status='unknown')
```

```
c       open(84,file='d2chrac.txt',status='unknown')

        rewind 3
        print*, '-----------------------------------------------'
        print*, '|  last compiled Wed Mar 25 14:52:45 MST 1998  |'
        print*, '-----------------------------------------------'
        do 5 j=1,nsets
        read(3,132) (y(j,i),i=1,npts)
c
c       multiply scaling factors
c
        do 899 ii=1,npts
        y(j,ii)= scale(j)*y(j,ii)
899     continue
5       continue
132     format(e13.6,2x,e13.6,2x,e13.6,2x,e13.6,2x,e13.6)
c
c       invert primary current
c
        do 160 i=1,npts
160     y(1,i) = -1.0 * y(1,i)
c
c       set some constants
c
        om = 314.1592654
        ga = 0.017453292
        pi = 3.141592654
        intf = pt
        int  = pt
        inc  = 5
        nw   = 1
        nh   = tnh
c
c       setting up the time-axis in radians, rad(i)
c
        radin =( 2*pi) /(npts-1)
        t1 = -radin
        do 22 i=1,int
        t1 = t1+radin
        rad(i) = t1
22      continue
c
c       setting up the time-axis in degrees, x(j)
c
        do 50 i=1,npts
50      x(i)=float(i-1)
        nspace=npts-1
```

```
        degmult = 360.0/float(nspace)
        do 19 j=1,npts
        x(j) = x(j)*degmult
        if (j.eq.npts) x(j) = x(j)+0.001
19      continue
c
c       writing scaled row data to a file called forig.txt
c
        do 88 k=1,npts
        write(80,89) x(k),y(1,k),y(2,k)
88      continue
89      format(7(1x,f10.4))
c
c       compute d.c. component
c
        do 30 j=1,nsets
        ymax(j)=0.
        dcoff = 0.0
        do 231 k=1,npts
231     work(k)=y(j,k)
c
c       subroutine mean computes average value
c
        call mean(work,dcoff,npts)
c
c       computing dc in another way
c
        do 37 k=1,npts-1
37      dc=dc+y(j,k)
        dc=dc/float(npts-1)
c
        write(0,*) 'ch',j,' dc ......... : ',dcoff
        write(10,*)'ch',j,' dc ......... : ',dc
        dccomp(j)=dcoff
        do 20 i=1,npts
        y(j,i)=(y(j,i)-dcoff)
20      if (abs(y(j,i)).gt.ymax(j)) ymax(j)=abs(y(j,i))
30      continue
c
c       computing Pin
c
        do 165 i=1,npts
165     tpin(i) = y(1,i)*y(2,i)

        pinsum=0.0
        do 104 i=1,npts-1
104     pinsum  = pinsum + tpin(i)
```

```
        pinsum = pinsum/float(npts-1)

        call mean(tpin,tpinav,npts)

        write (10,*)
        write (10,*) 'THE NUMBER OF KNOWN POINT (NPTS) IS  ',NPTS
        write (10,*) 'THE NUMBER OF DATA SETS (NSETS) IS',NSETS
        write (10,*)
c
c       this part is based on the algorithms in page 119
c       of vandergraft.
c
        do 1 j=1,nh
        curvc(j) =0.0
        curvs(j) =0.0
        curvt(j) =0.0
        curvp(j) =0.0
 1      continue
        write(0,*)
c ---------------------------------------
        do 12 j=1,nsets
        nc=j
        do 13 i=1,npts
        yvalue(i) = y(j,i)
13      continue
c
c       computing rms value from subroutine trap
c
        call trap (yvalue,rmsval,npts)
c
c       calling sub harm to get the harmonics
c
        call harm (yvalue,curvc,curvs,curvt,curvp)
c
c       constructing original waveform from the harmonics
c       writing it to fconst.txt
c
c----------------------------------------
        do 57 i=1,npts
          fc(i)=0.0
          fcang(j,i)=0.0
c
c       constructing original waveforms from fourier coefficients
c       f(wt) = sigma (Ch sin(hwt + fih))
c
            do 58 k=1,nh
```

```
              har=float(k)
c              fc(i)=fc(i) + curvc(har)*cos(har*rad(i)) +
c     &              curvs(har)*sin(har*rad(i))
              fcang(j,i)=fcang(j,i) + curvt(har)*sin(har*rad(i)
     &                  + curvp(har))
58          continue
c
c       writing the constructed waveforms to fconst.txt
c
        if (j.eq.2) then
           write(81,89) x(i),
     &      fcang(1,i)+dccomp(1),fcang(2,i)+dccomp(2)
        endif
57      continue
c -------------------------------
c
c       amp: amplitude of harmonic h
c       ang: angle of harmonic h (radians)
c

        do 133 i=1,nh
        amp(j,i)=curvt(i)
        ang(j,i)=curvp(i)
        curvp(i) = curvp(i)/ga
133     continue
c
c       calculating THD
c
        toplam=0.0
          do 343  i=1, nh
        if (i . gt. 1) then
          toplam = toplam + amp(j,i)*amp(j,i)
        end if
 343    continue
          thd = (sqrt(toplam)/amp(j,1))*100.
C
C      compute rms from harmonics
C
        fsq=0.0
        do 35 i=1,nh
        fsq = fsq + curvt(i)**2
35      continue
        frms = sqrt (fsq/2.)

        write(83,*) rmsval

        if (j.eq.1) write(0,*)'CH',J,' (I1)', '.... RMS : ',
```

```
     &  rmsval,' - THD.:',thd, '  %'
        if (j.eq.1) rmsi1 =rmsval
        if (j.eq.2) write(0,*)'CH',J,' (V1)', '.... RMS : ',
     &  rmsval,' - THD.:',thd, '  %'
        if (j.eq.2)  rmsv1 =rmsval

        write (10,*) '-----------------------------------------'
        write (10,*) 'CHANNEL NUMBER', J
        write(10,*)'RMS VALUE FROM  HARMONICS .... :', rmsval,frms
        write(10,*)'RMS VALUE OF FUNDAMENTAL ..... :',
     &             curvt(1)/sqrt(2.)
        write(10,*)'Total Harmonic Distortion .... : ',thd
        write (10,*)
        write(10,*)' THE MAGNITUDE OF THE HARMONICS (RMS values)'
c       *' PERCENTAGE OF THE FUNDAMENTAL:'
        if (curvt(1).eq.0.00000) then
        write(10,100) (0.0,k=1,nh)
        else
c       write(10,100)(100.*curvt(k)/curvt(1),k=1,nh)
        write(10,100)(curvt(k)/sqrt(2.), k=1,nh)
        end if
        write (10,*)
        write(10,*)' THE PHASOR ANGLES, SINE BASED (in degrees):'
c       write(10,100)(-CURVP(K)-90.,K=1,NH)
        write(10,100)(CURVP(K),K=1,NH)
        write (10,*)
12      CONTINUE
c ------------------------------------
100     format(6(1X,f11.4))

        endfile(3)
        rewind 3
        close(3)
c
c       computing losses of each harmonic
c
        do 155 i=1,nh
c
c       computing fundamental and harmonic input power
c       rms(1,i)=i1, rms(2,i)=v1
c
           rms(1,i)=amp(1,i)/sqrt(2.)
           rms(2,i)=amp(2,i)/sqrt(2.)

           th21(i)=ang(2,i) - ang(1,i)

           pinh(i)=rms(1,i)*rms(2,i)*cos(th21(i))
```

```
155     continue
c
        pinht=0.0

        do 166 i=1,nh
           pinht=pinht + pinh(i)
166     continue
ccccccccccccccccccccccccccccccccccccccccccccccccccccccccccccccccc
c
c       computing ac resistance Rac-h=Pinh/I1h-rms^2
c
        do 177 i=1,nh
177     rac(i)=pinh(i)/rms(1,i)**2

        write(0,*)
        WRITE(0,*) 'REAL POWER - ,Pin (from integ, harm).. :',
     &   tpinav,pinsum,pinht, '  W'
        WRITE(0,*) 'APPARENT POWER - Sin (Vrms*Irms) ..... :',
     &   rmsv1*rmsi1, '  VA'
        write(0,*)
       write(0,*) '------------------------------'
        write(0,*)' h','       Pin','            Ih', '       Rac '
        do 178 i=1,nh
        if (pinh(i) .ge. 0.1 .and. rms(1,i) .gt. 2) then
          racind=rac(i)
          harmno=i
          write(0,777) i,pinh(i),rms(1,i),rac(i)
        endif
178     continue
ccccccccccccccccccccccccccccccccccccccccccccccccccccccccccccccccc
c
c       computing inductance from Xl=sqrt(Z^2 - Rac^2)
c
        zind=rmsv1/rmsi1
        xlind=sqrt(zind**2 - racind**2)
        wlind=2*pi*harmno*60
        lind=xlind/wlind
cccc
        write(0,*)
        write(0,*) '      h','          Z','           Xl',
     &  '        L (microHenry) '
        write(0,*) '   ----------------------------------------'
        write(0,*) harmno,zind,xlind,lind*1e6

        write(10,*)
        WRITE(10,*) 'INPUT REAL POWER (from integration) ....... :',
     & tpinav,pinsum, '  W'
```

```
      WRITE(10,*) 'INPUT REAL POWER (from harmonics) ..... :',
     & pinht, '  W'
      write(10,*)
      WRITE(10,*) 'INPUT APPARENT POWER (using V1 and I1)..... :',
     & rmsv1*rmsi1, '  VA'

      write(10,*)
      WRITE(10,*) 'POWERS OF EACH HARMONIC'
      write(10,*) '-----------------------'
      write(10,*)' h','       Pin'
      write(10,*)
      do 82 i=1,nh
82    if (pinh(i) .ge. 0.4) write(10,770) i, pinh(i)
770   format(i3,2x,f11.4)

      write(10,*)
      WRITE(10,*) 'LOSSES OF HARMONICS (Method A)'
      write(10,*) '------------------------------'
      write(10,*)' h','       Pcu','             Ih', '       Rac'
      do 83 i=1,nh
      if (pinh(i) .ge. 0.1) write(10,777) i,pinh(i),rms(1,i),rac(i)
c     write(84,*) i**2,rac(i)
83    continue

      write(10,*)
      write(10,*) '      h','          Z','           Xl',
     &  '        L (microHenry) '
      write(10,*) '-----------------------------------------'
      write(10,*) harmno,zind,xlind,lind*1e6

777   format(i3,2x,f11.4,2x,f11.4,2x,f11.4)

      endfile(10)
      rewind 10
      close(10)
      stop
     end
c
      subroutine harm (value,compc,comps,compt,compp)
c     this subroutine performs fourier analysis for period from
c     1 to 361,361 points, nh harmonics, using three points
c     gauss integration formula.
      common nw,deg(7500),rad(7500)
      common npts,nps,int,inc,nh,ga,pi,ww,om,nc,rf,er,el,err,itmax
C
      parameter(tnh=102,set=2,pt=7500)
      dimension value(pt),compc(tnh),comps(tnh),compt(tnh)
```

```
      dimension compp(tnh),valuec(pt)
      check = 2.0
      p=sqrt(0.6)
      a1=5./9.
      a2=8./9.
      fk1=0.5*p*(1.+p)
      fk2=(1.+p)*(1.-p)
      fk3=0.5*p*(p-1.)
      do 44 j=1,nh
       dl1=0.0
       dl2=0.0
       h=float(j)
                do 33 i=1,int-2,2
                  t1=h*(rad(i))
                  t2=h*(rad(i+1))
                  t3=h*(rad(i+2))
                  x1=fk1*t1+fk2*t2+fk3*t3
                  x2=t2
                  x3=fk3*t1+fk2*t2+fk1*t3
                  c1=value(i)
                  c2=value(i+1)
                  c3=value(i+2)
                  c4=fk1*c1+fk2*c2+fk3*c3
                  c6=fk3*c1+fk2*c2+fk1*c3
                  d1=c4*cos(x1)
                  d2=c2*cos(x2)
                  d3=c6*cos(x3)
                  d4=c4*sin(x1)
                  d5=c2*sin(x2)
                  d6=c6*sin(x3)
                  dl1=dl1+a1*(d1+d3)+a2*d2
                  dl2=dl2+a1*(d4+d6)+a2*d5
33              continue
       xpt1 = 2./float(npts-1)
       compc(j)=dl1*xpt1
       comps(j)=dl2*xpt1
c
c     computing amplitude(compt) and fi(compp) in cv sin(vt+fi)
c
       compt(j) = sqrt(compc(j)**2+comps(j)**2)
c       if (comps(j).eq.0.00000) then
c            compp(j)=0.0
c       else
c            compp(j) = -atan(compc(j)/comps(j))
c       end if
c       if (comps(j).lt.0.0) compp(j) =compp(j)+pi
c
```

```
      ac=compc(j)
      bs=comps(j)
      if (bs.eq.0. .and. ac.eq.0.) then
      f=0.0
      elseif (bs.eq.0. .and. ac.lt.0.) then
      f=-pi/2
      elseif (bs.eq.0. .and. ac.gt.0.) then
      f=pi/2
      elseif (bs.lt.0. .and. ac.ge.0.) then
      f=pi+atan(ac/bs)
      elseif (bs.lt.0. .and. ac.lt.0.) then
      f=-pi+atan(ac/bs)
      else
      f=atan(ac/bs)
      endif
      compp(j)=f
44    continue
c
c     the above data is to be plotted and checked
c     if the fourier analysis give the same curve
c     data are given in amplitude and radius in sine wave
c     this section is used for
c     checking fourier analysis************
      nww = 5*nw
      if ((check.eq.1.).and.(nc.eq.nww)) then
      emdif = 0.
      do 51 i=1,int
      valuec(i) = 0.
      do 52 j=1,nh,2
      h = float(j)
      valuec(i)=valuec(i)+compc(j)*cos(h*rad(i))+
     &          comps(j)*sin(h*rad(i))
 52   continue
      dif=abs(value(i)-valuec(i))
      if (dif.gt.emdif) then
          emdif = dif
          difn = float(i)
      endif
 51   continue
c
      write (10,*) '*********checking fourier
     &             $analysis*****************'
      write (10,*)
      write (10,*) 'value(457) at nc = ',nc
      write (10,1001) (value(i),i=1,457)
      write (10,*)
      write (10,*) 'valuec(457) at nc = ',nc
```

```
      write (10,1001) (valuec(i),i=1,457)
      write (10,*) 'the maximun difference is :',emdif,'at i=',difn
      endif

1001  format (10(1x,1pe11.4))

      return
      end

      subroutine trap (fin,rmsval,nn)
      real rmsval,f(7500),fin(7500),sum,inte
      integer nn
      do 19 i=1,nn
19     f(i)=fin(i)*fin(i)
       sum = 0.0
       do 29 i=2,nn-1
        sum = sum + f(i)
29     continue
      inte =(1./float(nn-1))*0.5*((f(1)+f(nn))+2.*sum)
      rmsval = sqrt (inte)
      return
      end
c
      subroutine mean (fin,meanvl,nn)
      real meanvl,fin(7500),sum
      integer nn
c     nn is number of sampling points
c
c                      t
c     Imean =  (1/t)* S i dt)
c                      o
c
      sum = 0.0
      do 129 i=2,nn-1
       sum = sum + fin(i)
129   continue
      meanvl =( 1./float(nn-1))*0.5*((fin(1)+fin(nn))+2.*sum)
      return
      end
```

A.4 Sample Input and Output Files of the Fortran Program

There are two input files to the FORTRAN program: 1) *ch2cal.dat*: calibration information of channels. the first line contains number of data sets and number of points per channel, respectively, on the second and third lines are the calibration numbers of channels 1 and 2, respectively. 2) *ch2.dat*: sampled 15.000 points of channels 1 and 2. This file is generated by the BASIC sampling program (*twochb.bas*). It has 3.000 lines in 5 columns.

The output file (*d2chout.txt*) of the FORTRAN program contains the harmonic magnitude and phase angles of voltage and current wave forms along with RMS values.

ch2cal.dat

```
  2  7500
    1.00417E-02
    4.88530E-03
```

d2chout.txt

```
 ch  1 dc ......... :     5.15195E-02
 ch  2 dc ......... :    -1.31058E-02

 THE NUMBER OF KNOWN POINT (NPTS) IS    7500
 THE NUMBER OF DATA SETS (NSETS) IS  2

 ------------------------------------------
 CHANNEL NUMBER  1
 RMS VALUE FROM  HARMONICS .... :   10.06098   10.05753
 RMS VALUE OF FUNDAMENTAL ..... :    1.26211E-03
 Total Harmonic Distortion .... :     796880.

  THE MAGNITUDE OF THE HARMONICS (RMS values)
0.0013      0.0004      0.0020      0.0009      0.0007      0.0020
0.0007      0.0013      0.0026      0.0007      0.0010      0.0011
0.0004      0.0007      0.0009      0.0008      0.0014      0.0010
0.0007      0.0004      0.0007      0.0008      0.0003      0.0013
0.0007      0.0015      0.0011      0.0009      0.0007      0.0016
0.0015      0.0016      0.0012      0.0012      0.0010      0.0012
0.0025      0.0016      0.0011      0.0016      0.0014      0.0018
0.0014      0.0017      0.0020      0.0017      0.0024      0.0022
0.0022      0.0026      0.0028      0.0027      0.0027      0.0027
```

0.0034	0.0033	0.0036	0.0034	0.0039	0.0038
0.0042	0.0044	0.0049	0.0054	0.0055	0.0058
0.0063	0.0066	0.0074	0.0082	0.0098	0.0147
0.0051	0.0076	0.0089	0.0096	0.0111	0.0130
0.0145	0.0165	0.0175	0.0215	0.0241	0.0300
0.0356	0.0482	0.0621	0.0884	0.2022	10.0509
0.2172	0.0972	0.0705	0.0569	0.0447	0.0369
0.0330	0.0302	0.0289	0.0261	0.0234	0.0239

THE PHASOR ANGLES, SINE BASED (in degrees):

-22.7559	80.2591	86.1727	38.6769	97.5891	113.4677
112.3141	160.8428	15.4956	40.1406	41.6437	83.7186
17.0222	90.3065	131.3456	96.4791	147.1464	40.0829
83.8979	120.3654	141.4417	98.7514	19.7848	122.1131
123.8212	163.4427	96.7690	142.2037	134.8140	98.6200
103.5485	124.9866	103.3057	114.1712	133.6590	103.9091
117.4050	122.2604	134.9693	120.2171	80.7872	117.0144
116.2441	109.6489	115.5169	97.9016	106.5252	112.9081
111.4322	117.6583	116.0953	112.5800	103.7468	115.7933
152.3804	117.4649	118.5104	128.1004	117.2229	110.9189
115.6149	111.4294	114.0136	112.4236	111.7616	113.9911
114.8536	111.2458	115.0822	117.8363	117.1569	124.8563
70.0014	101.7730	105.0073	108.2006	107.6501	108.1093
113.3542	108.3764	106.9531	110.8264	110.1257	110.4579
112.2263	111.1620	110.4198	112.8370	116.3860	109.6904
-76.5920	-72.0684	-71.1048	-69.0135	-70.8694	-72.4334
-69.5994	-71.3618	-66.8538	-67.0534	-65.3124	-71.5075

CHANNEL NUMBER 2

RMS VALUE FROM HARMONICS .... : 4.42100 4.41992

RMS VALUE OF FUNDAMENTAL ..... : 3.50557E-04

Total Harmonic Distortion .... : 1.26083E+06

THE MAGNITUDE OF THE HARMONICS (RMS values)

0.0004	0.0005	0.0001	0.0003	0.0002	0.0004
0.0005	0.0002	0.0004	0.0004	0.0004	0.0002
0.0003	0.0004	0.0004	0.0005	0.0002	0.0007
0.0006	0.0006	0.0005	0.0010	0.0003	0.0006
0.0007	0.0004	0.0007	0.0003	0.0006	0.0008
0.0005	0.0010	0.0006	0.0010	0.0008	0.0009
0.0012	0.0009	0.0009	0.0011	0.0011	0.0011
0.0011	0.0012	0.0013	0.0012	0.0013	0.0013
0.0017	0.0013	0.0017	0.0015	0.0016	0.0018
0.0015	0.0019	0.0020	0.0018	0.0023	0.0023
0.0023	0.0025	0.0026	0.0028	0.0029	0.0030
0.0031	0.0034	0.0036	0.0038	0.0046	0.0063

```
0.0031      0.0043      0.0044      0.0048      0.0055      0.0061
0.0070      0.0079      0.0082      0.0096      0.0114      0.0129
0.0162      0.0216      0.0276      0.0395      0.0896      4.4170
0.0952      0.0424      0.0303      0.0248      0.0193      0.0156
0.0141      0.0122      0.0122      0.0112      0.0101      0.0102

  THE PHASOR ANGLES, SINE BASED (in degrees):
-48.9164    -89.2255    -58.8345    133.6381   -113.0054   -171.5757
-157.1879    142.3019     55.1031   -127.4693    147.4653    -63.1094
144.2340      3.6785    132.1653   -157.0882    -87.8019   -167.5575
176.8319   -164.9223   -163.8944    179.6266   -175.2059   -155.0218
164.3547    148.9053    173.1435    158.6160    179.1543   -159.2321
-173.1428   -173.2159    175.9534    172.9241    173.3876   -173.0950
178.8686   -177.0840   -175.0782   -168.5033   -172.2980    175.7106
-176.1201   -172.1556   -178.8516    178.4293   -173.0506   -172.5790
-176.7243   -167.3837   -177.9281    175.2576   -179.1562    178.3286
-155.9026   -172.1384   -169.7943   -166.6364   -173.6483   -178.2757
-171.9280    176.1348   -173.1687   -174.4198   -177.1900   -172.2605
-172.9805   -174.9972   -172.1984   -170.1645   -168.8465   -161.1346
159.1965    178.4767   -176.5517   -175.0917   -177.3570   -176.4176
-171.3665   -176.4119   -177.5135   -174.8495   -172.4090   -173.3276
-170.3787   -173.5250   -172.7111   -170.5707   -167.0436   -173.3303
0.5018      5.0669      6.0584      8.1651      6.2304      5.0716
6.9613      7.3423     12.5157      9.3289     15.0424      5.8209


INPUT REAL POWER (from integration) ..... :   10.01933   10.01975  W
INPUT REAL POWER (from harmonics) ....... :   10.01561  W

INPUT APPARENT POWER (using V1 and I1)... :    44.4796  VA

 POWERS OF EACH HARMONIC
 -----------------------
  h       Pin

 90      10.0023

 LOSSES OF HARMONICS (Method A)
 The values below are for one transformer ONLY!
 ------------------------------
  h       Pcu             Ih       Rac
 90      10.0023      10.0509       0.0990

      h          Z          Xl       L (microHenry)
 ------------------------------------------
    90.0000   0.439420   0.428120    12.6180
```

APPENDIX B

DESCRIPTION AND DIMENSIONS OF INDUCTORS AND TRANSFORMERS

The losses, AC resistances (R_{AC_h}) and inductances (L_h) of 11 inductors and 2 transformers at different frequencies are measured. A brief description for each inductor and transformer is outlined below:

- **Inductors**

  1. **Inductor #1** has a rectangular core (shape I) and consists of laminated iron sheets. A stranded (not insulated strands) copper wire is wound along the long side of the core. This inductor was tested in three different configurations: with core, without core and in an unwound manner (one big loop with no core present).
  2. **Inductor #2** is the input filter inductor of the rectifier. It consists of two identical inductors connected in series. The structure of the core and that of the winding are similar to those of inductor #1.
  3. **Inductor #3** is the tank inductor of the rectifier. Thin rectangular copper sheets are wound on a ferrite material core (shape D). There are two air gaps associated with the D-shaped (compressed ferrite or powdered iron) core.

4. **Inductor #4** is the output inductor of the inverter. It consists of two identical inductors connected in parallel. The core (shape E) has laminated iron sheets and a square solid copper wire is placed on the center leg.
5. **Inductors #5, 6, 7** are the output filter inductors of the inverter. All have stranded wires. with individual strands insulated and transposed from each other (Litz wire). The cores of inductors #5 and #6 consist of laminated thin iron sheets while inductor #7 has a powdered iron core.
6. **Inductor #8** is the DC output filter inductor of the rectifier. Solid rectangular copper wire is wound on the center leg of an EI shaped core which consists of laminated, thin iron sheets.
7. **Inductor #9** is the damping inductor of the input filter of the rectifier. It is similar to inductor #1 except it has a solid circular wire. This inductor consists of four identical inductors connected in series.
8. **Inductor #10** is an air core inductor. A stranded (uninsulated strands) copper wire is used. No magnetic core is present in this inductor.
9. **Inductor #11** has an E-I shaped core which consists of laminated iron sheets. with a solid circular wire wound on the center leg.
10. **Inductors #12 and 13** have stranded (uninsulated strands) wires and have the same length as that of inductor #1. There is no magnetic core. and the wire has only one turn for each inductor.

- **Transformers**

1. **Sample tr#1**: Two 3-phase transformers between inverter and the power grid are connected in series. The one on the inverter side is a 3-phase, 3-legged, 45kVA, 480-208/120V, 60Hz transformer connected wye-delta (wye is on the inverter side). Solid rectangular copper wire is used on

the LV side, while solid circular copper wire is used on the HV side. The transformer on the utility side consists of a delta-connected bank of three 10kVA, single-phase transformers with 480V-240V, 60Hz. The HV side (480V) of the 45kVA transformer is tied to the HV side of the 30kVA transformer. The LV side of the 30kVA transformer is three-phase, short circuited, and sinusoidal voltages at different frequencies are applied to the any two phases at the LV side of the 45kVA transformer.

2. **Sample tr#2**: Single-phase transformer with an apparent power of 1.5kVA, 480V-3V, 60Hz. The LV side is short-circuited and voltage is applied to the HV side. The LV side winding consists of rectangular solid conductors with an area of $A = 18 \times 10 = 180mm^2$.

Figure B.1 and B.2 illustrate the types of cores used in the inductors and the construction of an inductor, respectively. Table B.1 lists the dimensions of each core. Different types of wires, e.g., solid, stranded, and Litz wires are used in the construction of these inductors. Wire properties are outlined in Table B.2 (see Figure B.2 for definitions).

Table B.1: Dimensions (in millimeters) of the cores (Figure B.1) of inductors.

inductor #	type	h	l	w	a	b	c	d	e	g
1	I	51	29	15	-	-	-	-	-	-
2	I	57	21	18	-	-	-	-	-	-
3	D	94	154	59	28	-	28	-	-	5
4	E	135	145	47	24	-	24	42	28	-
5	I	66	13	15	-	-	-	-	-	-
6	I	47	18	17	-	-	-	-	-	-
7	I	71	11	10	-	-	-	-	-	-
8	EI	127	190	88	31	31	31	64	31	9
9	I	54	10	10	-	-	-	-	-	-
10, 12, 13	no core is used in this inductor									
11	EI	51	76	25	13	13	13	26	12	0.4

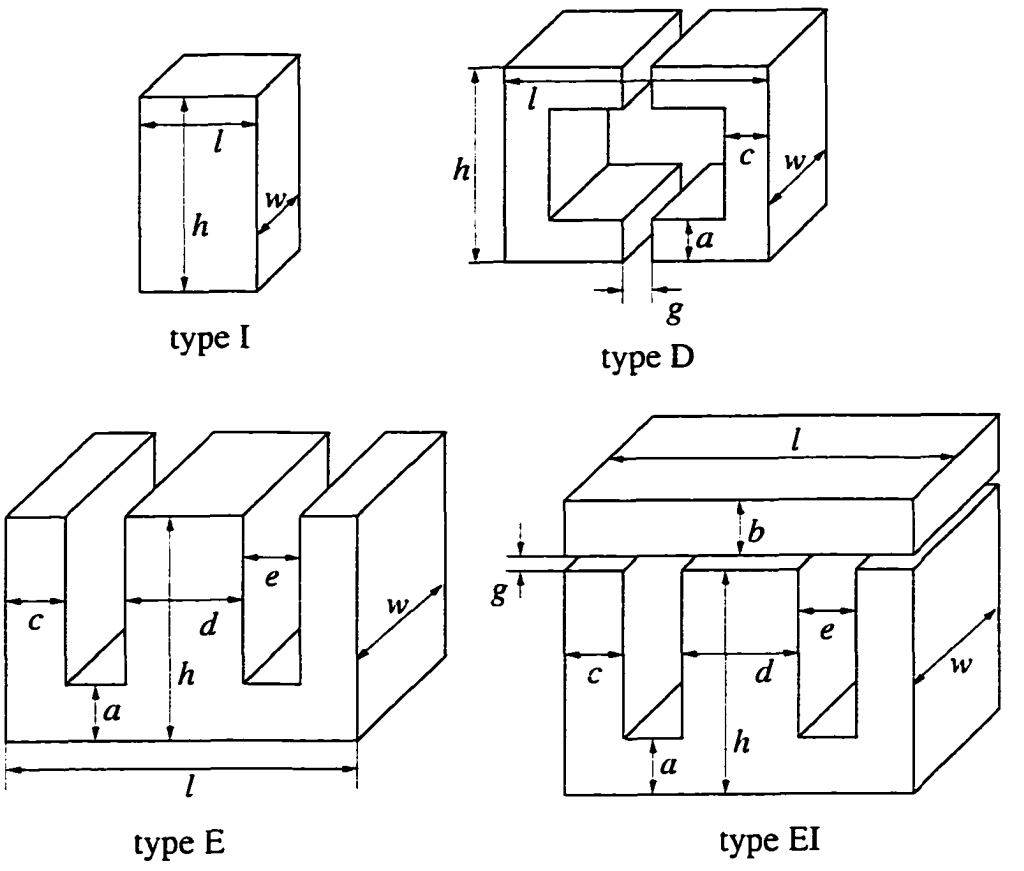

Figure B.1: Types of cores used in the inductors.

Inductor #6 consists of two of the same type of wires connected in parallel: therefore, the values given in Table B.2 pertain to one winding only.

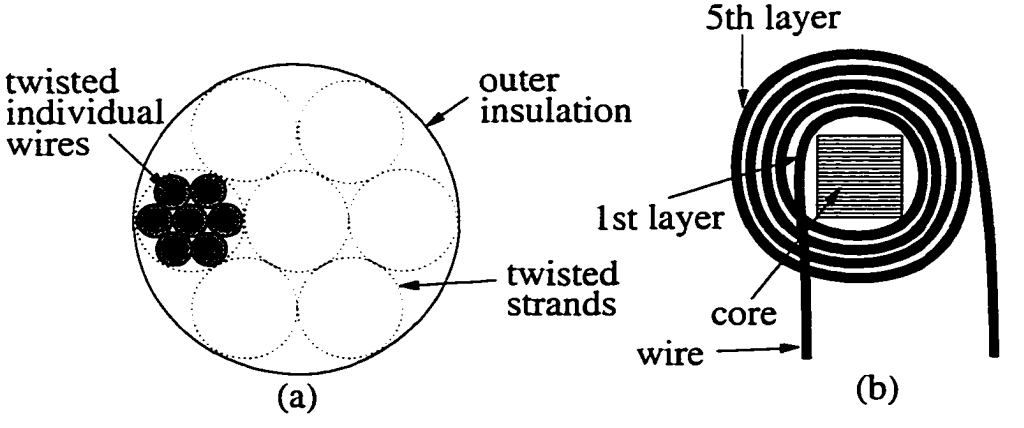

Figure B.2: Typical construction of a stranded wire (a) and an inductor (b).

Table B.2: Specifications of the wires used in the inductors.

inductor #	# of wire layers	# of turns in each layer	wire size	# of strands	# of wires within each strand	insulation between wires
1	5	9	8 AWG	19	7	no
2	5	7	6 AWG	19	7	no
3	7	1	43x0.5mm^2	2	1	yes
4	4	unknown	5x5mm^2	1	solid wire	
5	2	7	6 AWG	1	>100	yes
6	2	7	18 AWG	5	33	yes
7	2	10	6 AWG	1	>100	yes
8	5	8	7x4mm^2	1	solid wire	
9	2	13	13 AWG	1	solid wire	
10	2	6	6 AWG	7	1	no
11	4	unknown	32 AWG	1	solid wire	
12	1	1	4 AWG	7	1	no
13	1	1	8 AWG	7	1	no

APPENDIX C

CIRCUIT DIAGRAMS

C.1 Gating Circuit of Rectifier

The gating circuit of the rectifier is depicted in Figure C.1 including an 8-step A/D converter or piecewise amplifier, a Unitrode zero-current resonant integrated circuit (IC), UC3866N [83], and an optocoupler. The output current of the rectifier is measured thorough a 50A/50mV shunt and is amplified with a gain of 50. A low-pass filter is also used to reduce the high frequency switching ripples which are present in the output current. The amplified signal is then compared with 8 different voltage levels, between 0.3 volts and 2.24 volts, in 8 different comparators. A small amount of hysteresis is also employed to prevent chatter at each transition point. The outputs of the comparators are all at low state, where increasing output current will enable the output of the first comparator to reach a high state and a further increase in the output current will initiate the other comparators to enter the high state depending on their input voltage values. The output of all comparators are added together in an operational amplifier and the resultant voltage is connected to the noninverting input of the error amplifier inside the UC3866N IC.

The output voltage of the rectifier, measured by a voltage divider, is compared with a reference voltage in an error amplifier, and the error voltage is limited to V_{limit} by a limiter circuit. When the error voltage is less than the value of V_{limit}, the output of the operational amplifier is at its high state and the diode at the output is off, disconnecting

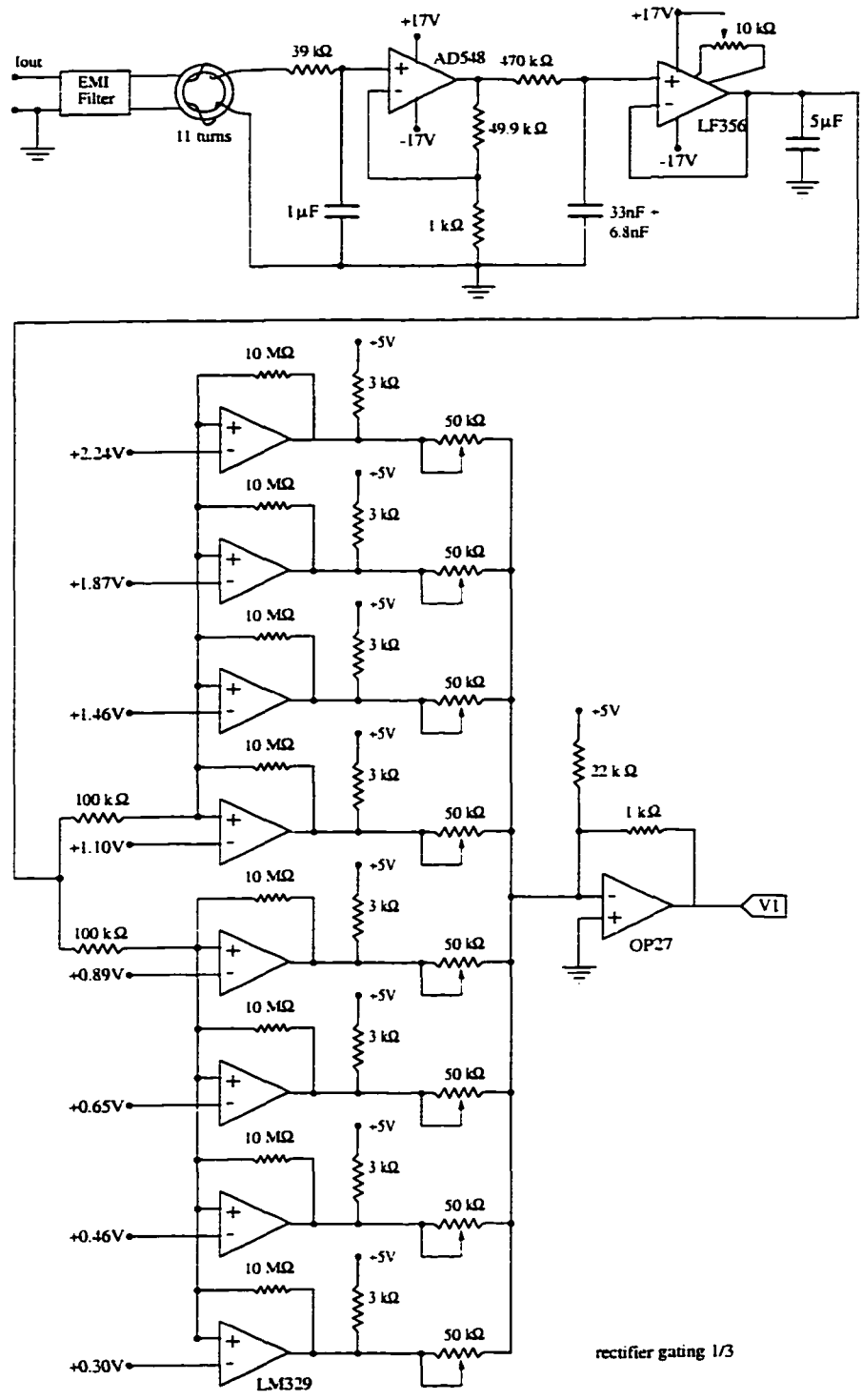

Figure C.1: Control circuit of rectifier.

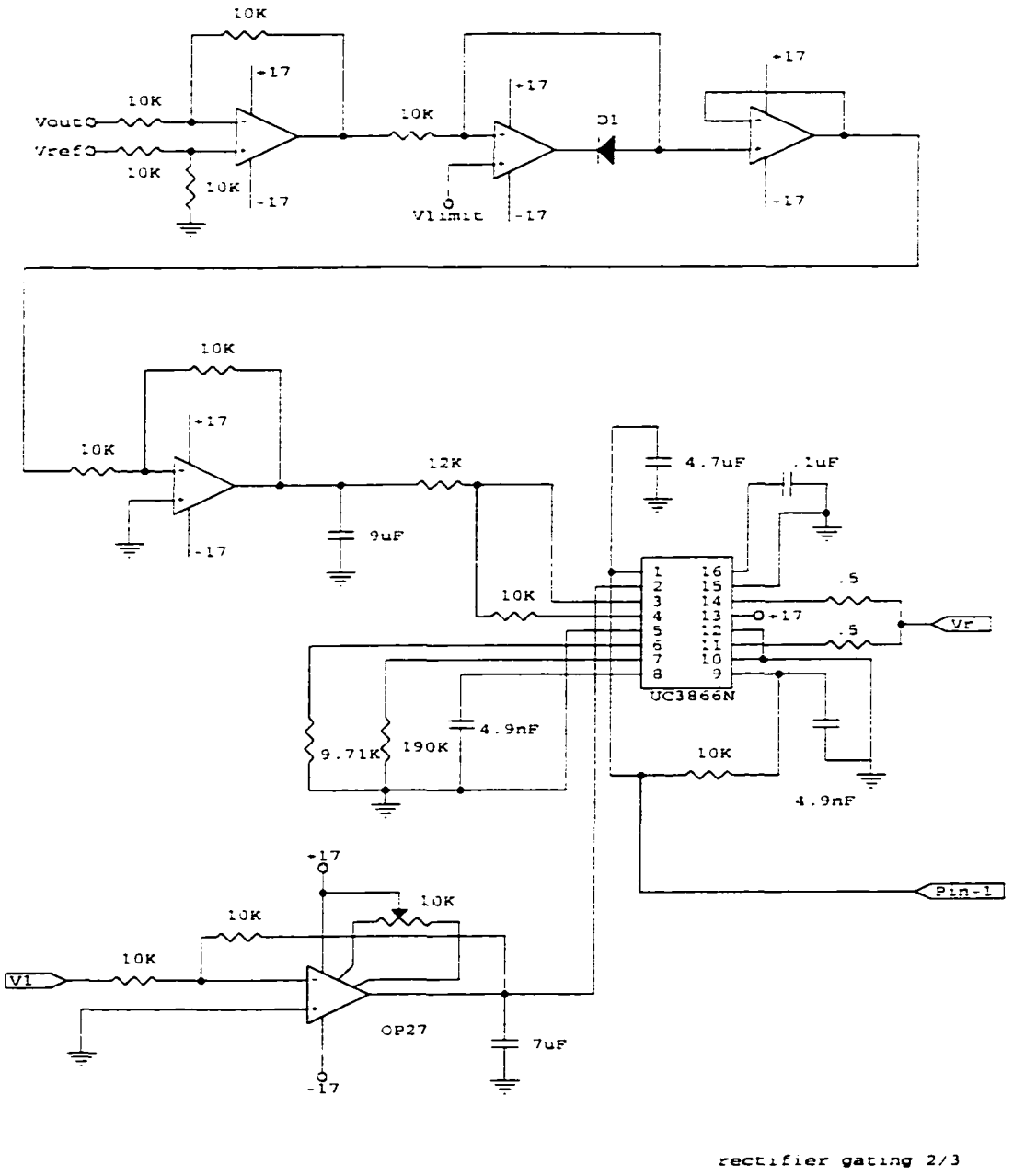

Figure C.1: Control circuit of rectifier, continued.

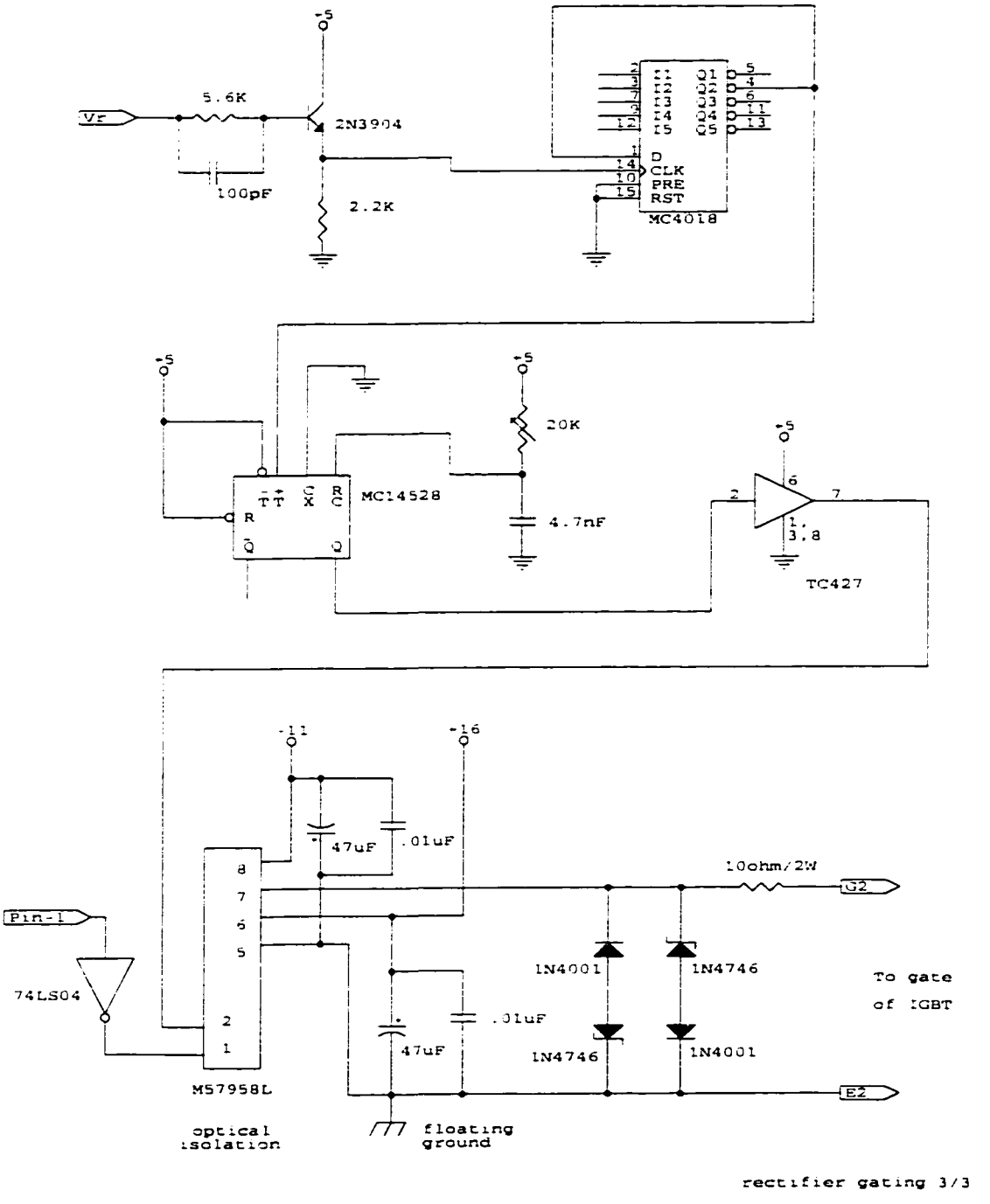

Figure C.1: Control circuit of rectifier,continued.

the operational amplifier from the circuit. The output voltage of the limiter circuit is now the same as its input voltage. When the error voltage is higher than V_{limit}, the output of operational amplifier approaches the negative supply voltage, thus turning the diode on: now the circuit is a simple voltage-follower whose output is the same as the voltage of the noninverting input, namely V_{limit}. The output of the limiter is inverted and connected to the inverting input of UC3866N.

The UC3866N IC consists of a voltage-controlled oscillator (VCO) driven by the output of the error amplifier. The resistors of $9.71k\Omega$, $190k\Omega$ and the capacitor of $4.9nF$, connected to pins 6, 7, and 8, respectively, are chosen to select the maximum and minimum switching frequency of the VCO, as explained in [83]. The constant on-time gating signals are available at both output pins of the UC3866N IC (pins 11 and 14), and the outputs are joined together by 0.5 Ω resistor as recommended by [83]. The magnitude of the output signal of UC3825 is equal to the supply voltage of 17 volts. However, the divider circuit requires a digital $5V$ level input (TTL), so the 17 volts are reduced to 5 volts by an emitter follower. The minimum and maximum output frequencies of the VCO can be adjusted from 10 kHz to 1 MHz. Since some operating points of the rectifier require lower switching frequencies than $10kHz$ (e.g., $6.5kHz$ to $24kHz$), a divider (MC14018, a divide-by-four counter) is employed to lower the frequency of the gating signal applied to the IGBT. The constant-width gating signal is then obtained by a monostable multivibrator (MC14528). Since the emitter of the IGBT is not at ground potential, the gating signal applied to the gate and emitter of IGBT must be isolated from the rest of the control circuit. Therefore, an optical isolation IC (M57958L) with a floating DC power supply is employed, where the amplitudes of the positive and negative pulses of the gating signal are equal to the positive and negative supply voltage of the isolator IC, respectively. The zener diodes of Figure C.1 (part 3) protect the gate from overvoltages by clamping the voltage to $\pm$18V.

C.2 Gating Circuit of Inverter

The control circuit of the inverter is shown in Figure C.2. The error voltage of one phase, the difference of the reference current and actual output current of inverter, is compared with a high-frequency ($5.76kHz$) triangular carrier wave form. The triangular wave from is obtained by integrating a square wave form, obtained from the power system frequency of nominal $60Hz$ using a phase-lock-loop (PLL) circuit as shown in Figure C.3. The frequency of the triangular carrier signal is $f_c = 60 \cdot 96 = 5.76kHz$.

Two different signals are obtained from the variable-width signal at the output of comparator (LM311) and applied to the gates of the upper and the lower IGBTs such that each transistor turns on alternately; that is, when the upper IGBT is turned on the lower IGBT is turned off. There is an $8\mu sec$ lock-out time delay between the two gating signals to prevent cross-conduction (short-circuiting the DC input voltage); i.e., the signals applied to upper and lower IGBTs are not turned on at the same time. The generation of the two signals with a lock-out time delay is outlined in Figure C.4. Since the emitter terminals of the lower IGBTs are at the same potential (DC ground), gating signals can be directly applied to these IGBTs through driver ICs (TC427). However, gating signals applied to each of the three upper IGBTs must be electrically isolated; therefore, each IGBT requires an additional power supply.

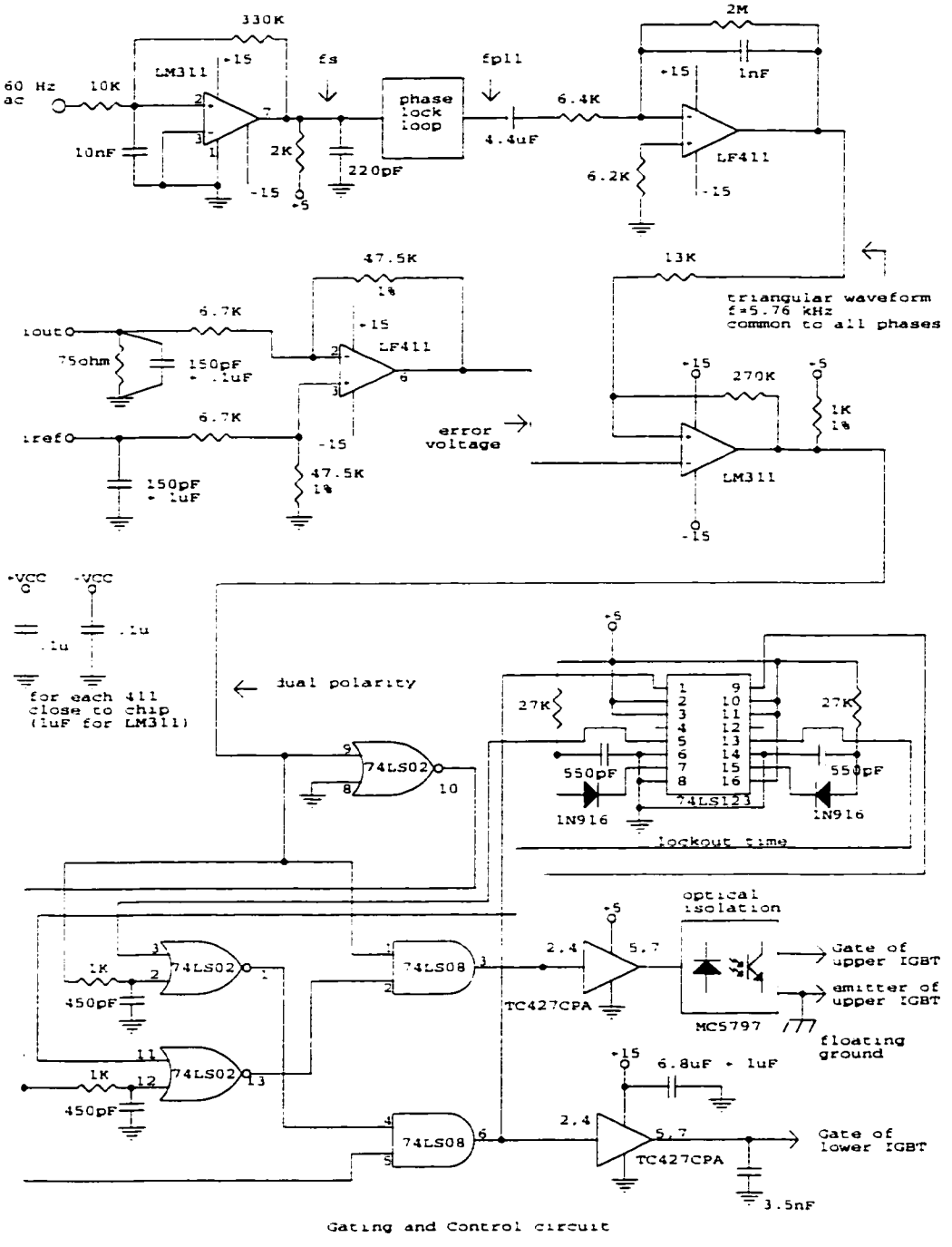

Figure C.2: Gating and control circuit of PWM inverter.

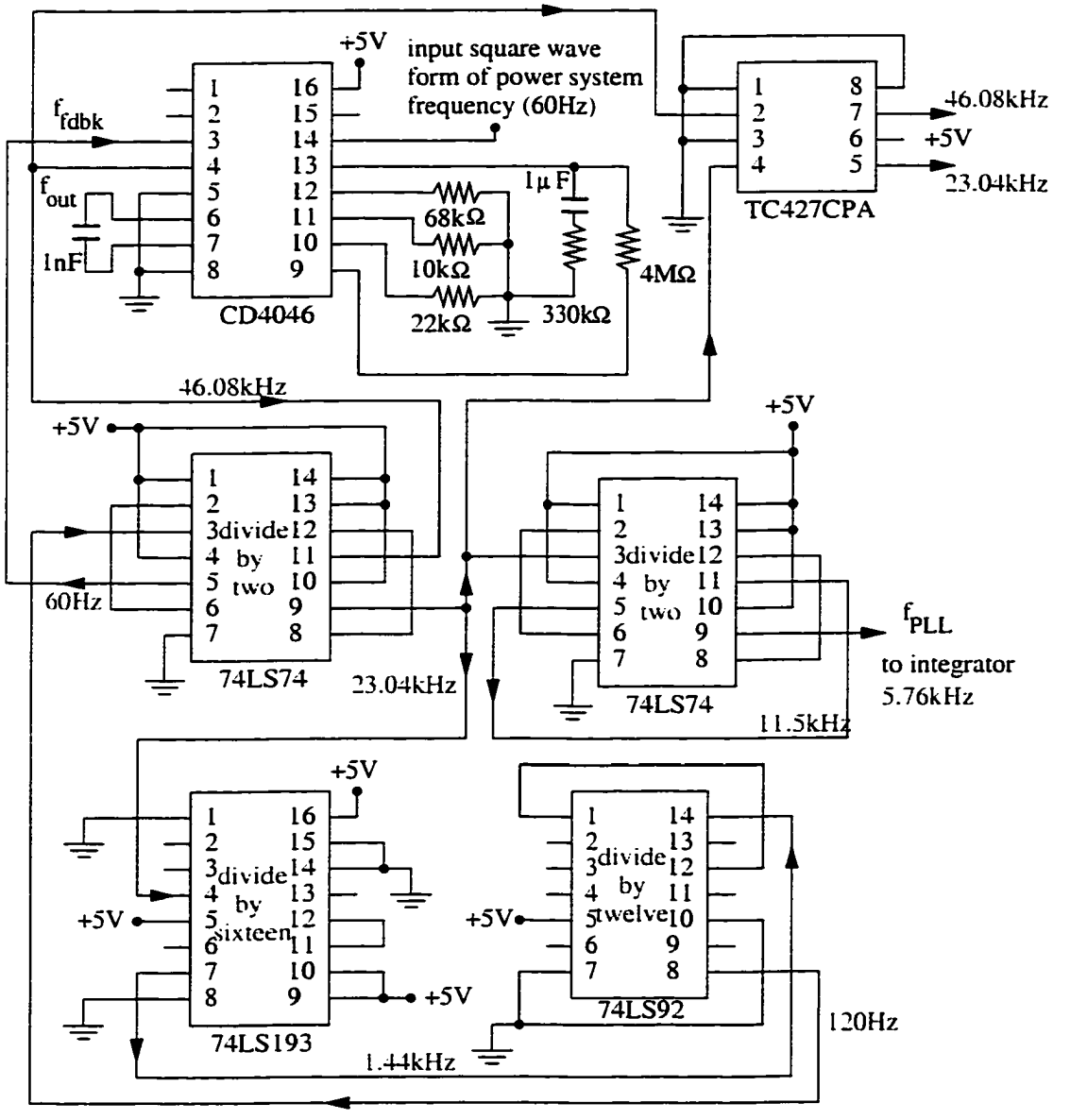

Figure C.3: Phase-lock-loop (PLL) circuit of Figure C.2

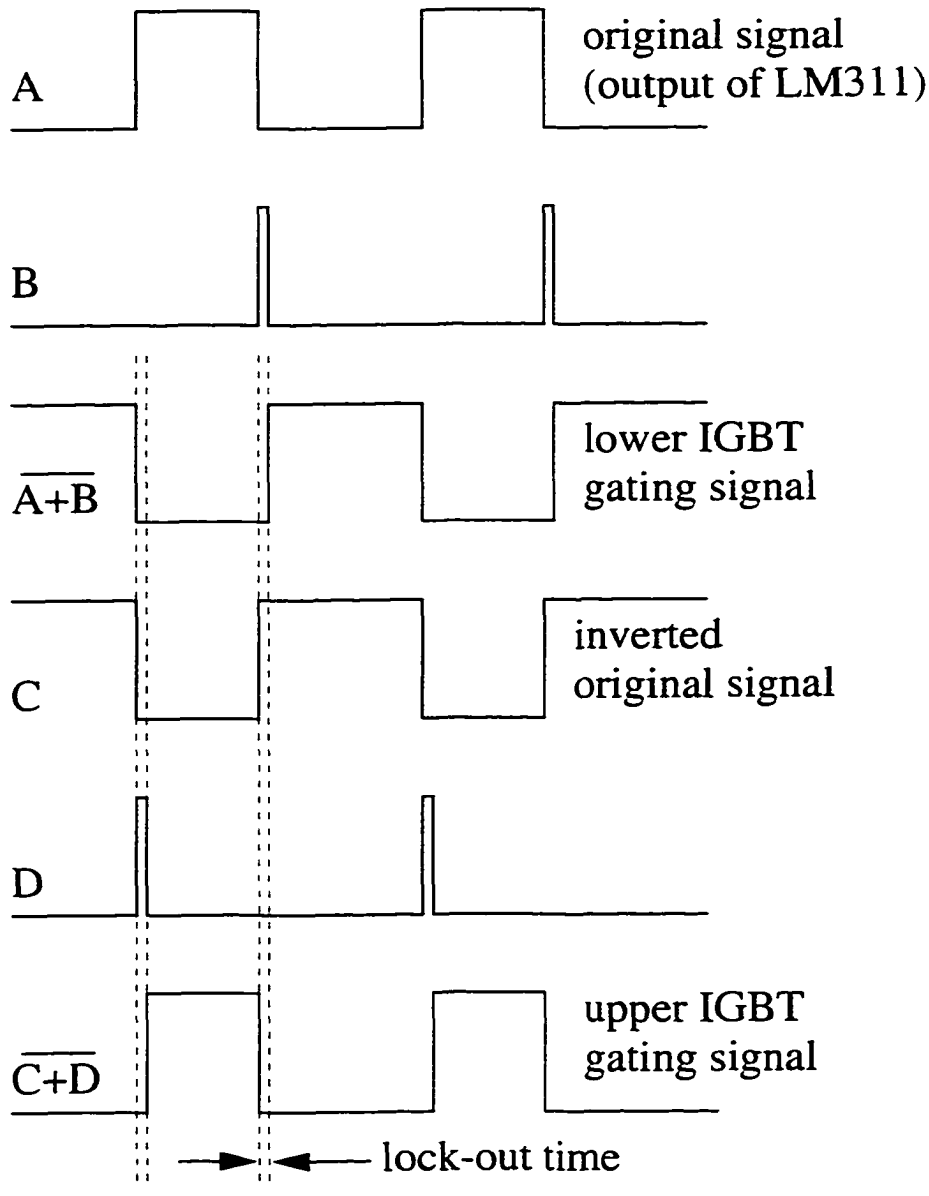

Figure C.4: Wave forms of lock-out time circuit.

C.3 Subcircuits of Synchronization Control Circuit

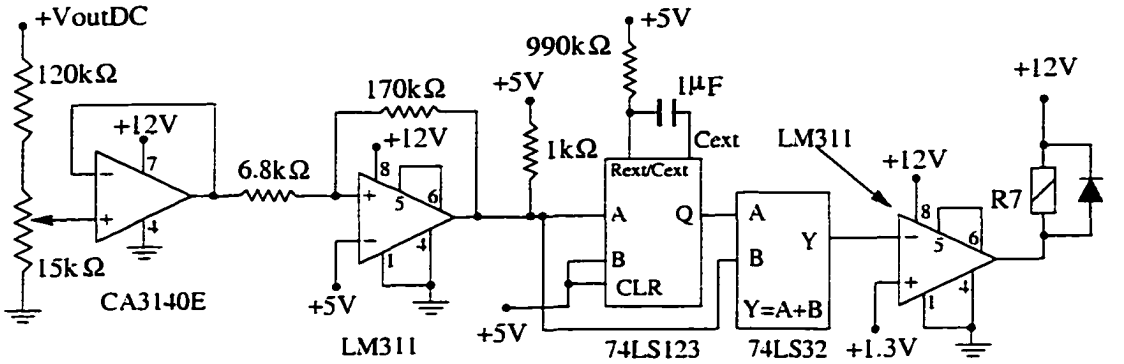

(a)

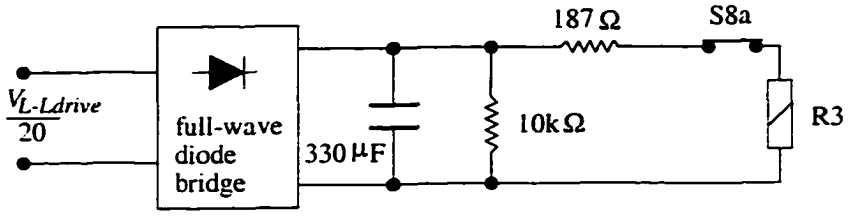

(b)

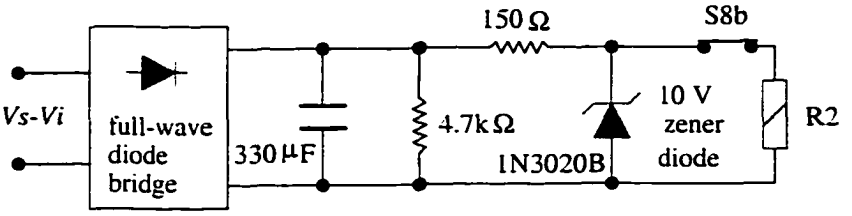

(c)

Figure C.5: (a) DC voltage amplitude control, (b) AC voltage amplitude control and (c) difference voltage subcircuits of Figure 4.6

APPENDIX D

FORTRAN PROGRAM FOR THE REACTIVE-POWER CONTROLLABILITY OF THE PWM INVERTER

```
      program inverter
      real f1,f2,eiiri1,eiiri2, eiile1,eiile2,eiihf,nt

      common /mag/ aimag(27), vph(27)

      open(unit=11, file='inv.dat', status='unknown')
      open(unit=15, file='trim.txt', status='unknown')

c      read magnetizing inductance vs phase voltage
      do i=1,27
         read(15,*) aimag(i), vph(i)
      enddo

c     enter inductance and resistor values for 60Hz
c     s is for system and i is for inverter output inductor
c
      nt = 240./208.

      rs  = 16.67e-3 / nt**2
      els = 88.e-6 / nt**2
      rtr = 56.25e-3
      eltr = 131.06e-6
      ri  = 28.3e-3 + rtr
      eli = 1.2e-3 + eltr

c      enter filter parameters here
      rf = 4.2e-3 / nt**2
      elf = 12.e-6 / nt**2
      ecf = 31.e-6 * nt**2

      freq = 60.
```

```
      pi=3.1415927
      rtod=180./pi

      om  = 2 * pi * freq

c  ###############################################################
c  analysis at high frequency
c       enter inductance and resistor values for 5.76kHz
c       s is for system and i is for inverter output inductor
c
      artr = 1.43
      aeltr = 100.95e-6
      ari  = 11.7 + artr
      aeli = 0.69e-3 + aeltr

c       enter filter parameters here
      arf = 46.7e-3 / nt**2
      aelf = 10.94e-6 / nt**2
      aecf = 31.e-6 * nt**2

      hfreq = 60.*96.
      hom =  2 * pi * hfreq

      xs  = hom*els
      axi  = hom*aeli
      axlf = hom*aelf
      axcf = 1./(hom*aecf)

c   enter rms current of inverter at 5.76kHz from measurement
      eiihf = 3.24
      zs = sqrt(rs**2 + xs**2)
      axf = axlf - axcf
      azf = sqrt(arf**2 + axf**2)
      azsf= sqrt((rs + arf)**2 + (xs + axf)**2)
      angzs = atan(xs/rs)*rtod
      angzf = atan(axf/arf)*rtod

      eifhf = (zs/(azsf)) * eiihf
      eishf = (azf/(azsf)) * eiihf

      avpccn = sqrt((eishf*rs)**2 + (eishf*xs)**2)
      atheta = acos((eishf*rs)/avpccn)
      abeta = acos((eifhf*arf)/avpccn)

      aphi = abeta - asin((eishf/eiihf)*sin(pi-atheta-abeta))

      aein1 = avpccn + eiihf*ari*cos(aphi) - eiihf*axi*sin(aphi)
```

```
      aein2 = eiihf*ari*sin(aphi) + eiihf*axi*cos(aphi)
      aein = sqrt(aein1**2 + aein2**2)
      adelta = asin(aein2/aein)

      write(11,*) 'high frequency results'
      write(11,*) '--------------------------'
      write(11,*)
      write(11,*) 'eiihf ............:', eiihf
      write(11,*) 'els, aeli, xs, axi .:', els, aeli, xs, axi
      write(11,*) 'ari, rs, aom  ......:', ari, rs, aom
      write(11,*) 'arf, axlf, axcf ....:', arf, axlf, axcf
      write(11,*)
      write(11,*) 'zs, azf  ...........:', zs, azf
      write(11,*) 'angzs, angzf  ......:', angzs, angzf
      write(11,*)
      write(11,*) 'eifhf, eishf .......:', eifhf, eishf
      write(11,*) 'atheta, abeta (deg).:', atheta*rtod, abeta*rtod
      write(11,*)
      write(11,*) 'avpccn, aein, ......:', avpccn, aein
      write(11,*) 'aphi, adelta (deg) .:', aphi*rtod, adelta*rtod
      write(11,*)
      write(11,*) '--------------------------'


c  ##############################################################


c   enter system voltage in here line-to-line
c
      eismax=0.0
      do 300 vll=245,245

      xs  = om*els
      xi  = om*eli
      xlf = om*elf
      xcf = 1./(om*ecf)

      esn=vll/sqrt(3.) / nt

c      enter epsilon value for stopping criteria
      emin=0.01

c      enter theta (as k) in degrees
c
      do 100 k=-16,88,4
c      do 100 k=-20,80,20
      theta=float(k)
```

```
        theta=theta/rtod
        ecur=0.0

c   eis is the current delivered to system, referred to primary
c   eis_primary = nt * eis_system, nt is the turns ratio of tr.
c
        do 200 eis=81,1,-5
c        do 200 eis=80,20,-10

        write(11,*)
        write(11,*) 'vll, esn, eis ....:', vll, esn, eis
        write(11,*) 'els, eli, xs, xi .:', els, eli, xs, xi
        write(11,*) 'ri, rs, om  ......:', ri, rs, om
        write(11,*)
        write(11,*) 'theta (rad, deg)..:', theta, theta*rtod
        write(11,*)

         vp1 = rs*eis*cos(theta)
         vp2 = xs*eis*sin(theta)
         vp3 = rs*eis*sin(theta)
         vp4 = xs*eis*cos(theta)
        vpccn = sqrt((esn + vp1 - vp2)**2 + (vp3 + vp4)**2)

        delta1 = acos((esn + vp1 - vp2)/vpccn)
        delta2 = asin((vp3 + vp4)/vpccn)

c        compute magnetizing current from i=f(vpcc) curve
c        also compute filter current
        eimag = f(vpccn)
        eif = vpccn/sqrt(rf**2 + (xlf-xcf)**2)
        beta = acos((eif*rf)/vpccn)
        eim = sqrt(eimag**2 + eif**2 +
     &              2 * eimag * eif * cos(pi/2. - beta))

        psph = esn*eis*cos(theta) + rs*(eis)**2
        qsph = -esn*eis*sin(theta) + xs*(eis)**2
        p = 3*psph*1e-3
        q = 3*qsph*1e-3
        spcc = sqrt(p**2 + q**2)

c       find phio
        phi=-pi/2
        dphi=0.00001
c       phi=0.1
c       dphi=0.00001

c        write(11,*) '----------------'
```

```
c        write(11,*) 'iteration starts'

        npts=float(pi/dphi)
        err=1.

        do 1 i=1,npts
        phi = phi + dphi
        thphi=theta-phi
c
c       positive sign in front of root
c
        f1a = esn + rs*eis*cos(theta) - xs*eis*sin(theta)
        f1b = rs*eis*sin(theta) + xs*eis*cos(theta)
        f1c = eis*cos(thphi)
        f1d = eis**2*(cos(thphi))**2 - (eis**2 - eim**2)

        if (f1d .ge. 0.0) then
         eiile1 = psph/(cos(phi)*f1a + sin(phi)*f1b)
         eiiri1 = f1c + sqrt(f1d)

         f1 = eiile1 - eiiri1
c
c        negative sign in front of root
c
         eiile2 = eiile1
               eiiri2 = f1c - sqrt(f1d)

         f2 = eiile2 - eiiri2

          if (abs(f1) .le. emin .or. abs(f2) .le. emin) then
            err1 = min(abs(f1),abs(f2))
            if (err1 .le. err .and. theta .ge. phi) then
              err=err1
              phio = phi
                if (abs(f1) .lt. abs(f2)) then
                   eii = eiiri1
                else
                   eii = eiiri2
                endif
              ifinal = i
              f1o = f1
              f2o = f2
              eiile1o = eiile1
              eiiri1o = eiiri1
              eiile2o = eiile2
              eiiri2o = eiiri2
            endif
```

```
c
c          write(11,*) 'minimum found'
c          write(11,*) 'i, phi, f1, f2 ..:',i, phi, f1, f2
c          write(11,*) 'eiile1, eiiri1 ..:',eiile1, eiiri1
c          write(11,*) 'eiile2, eiiri2 ..:',eiile2, eiiri2
          endif
         endif
1       continue

        write(11,*) 'iteration ends'
        write(11,*) '--------------'
        write(11,*)

        write(11,*)'FINAL RESULTS'
        write(11,*)
        write(11,*) 'ifinal, phio :',ifinal, phio
        write(11,*) 'eiile1o, eiiri1o, f1o ..:',eiile1o, eiiri1o, f1o
        write(11,*) 'eiile2o, eiiri2o, f2o ..:',eiile2o, eiiri2o, f2o

c        phio is the solution of phi
        e1 = ri*eii*cos(phio) - xi*eii*sin(phio)
        e2 = ri*eii*sin(phio) + xi*eii*cos(phio)

        ein=sqrt((f1a + e1)**2 + (f1b + e2)**2)
c
        eps=atan((f1b + e2)/(f1a + e1))
c
c
c        epsdel = eps - delta1
c        call adc(ein, epsdel, aein, adelta, sumein, angein)

c       dc voltage
         vdc = (pi/sqrt(2.0)) * ein + 100.
        write(11,*)

        write(11,*) 'vpccn,eimag,eim.....:', vpccn,eimag,eim
        write(11,*) 'vpccn,eif,beta(deg).:', eif,beta*rtod
        write(11,*) 'delta1,delta2 (rad).:', delta1, delta2
        write(11,*) 'delta1,delta2 (deg).:', delta1*rtod, delta2*rtod

        write(11,*)
        write(11,*)'psph, qsph .....,.....:',psph, qsph
        write(11,*)'p, q, spcc ...........:',p, q, spcc
        write(11,*)

        write(11,*)'phio (rad, deg)...:', phio, phio*rtod
        write(11,*)
```

```
        write(11,*)'eii, ein, vdc, vdch ....:', eii,ein,vdc,vdch
        write(11,*) 'eps (rad, deg) ..:',eps, eps*rtod
        write(11,*)
        write(11,*) '****************************************'

        if (vdc . le. 360) then
           if (eis .ge. eismax) eismax=eis
        endif

        if (vll .eq. 245) then
          if (vdc .le. 360 .and. eis .eq. eismax) then
            write(21,*) theta*rtod,phio*rtod,p,q,eis,vdc
            write(22,*) theta*rtod,vpccn,vll,ein,eii
c              write(21,*) theta*rtod,p,q,spcc,
c     &     vpccn,eimag,eif,eii,eis,phio*rtod,
c     &     ein,delta1*rtod,vdc
               endif

          if (eis .eq. 81) then
            write(25,*) theta*rtod,phio*rtod,p,q,eis,vdc
            write(26,*) theta*rtod,vpccn,vll,ein,eii
c              write(25,*) theta*rtod,p,q,spcc,
c     &     vpccn,eimag,eif,eii,eis,phio*rtod,
c     &     ein,delta1*rtod,vdc
           endif

          write(91,*) theta*rtod,phio*rtod,p,q,eis,vdc
          write(92,*) theta*rtod,vpccn,vll,ein,eii

        endif

        print*, theta*rtod,eis,p,q,vdc,vdcpwm,ein

200       continue
100      continue
300      continue
        stop
        end


        function f(x)
        real x
        common /mag/ aimag(27), vph(27)
        do 10 i=1,27
        xx=vph(i)
10        if (x.le.xx) goto 20
20        continue
```

```
if(i.gt.27) i=27
f=aprox(vph(i-1),xx,x,aimag(i-1),aimag(i))
return
end

function aprox(x1,x2,x3,y1,y2)
aprox=(y2-y1)*(x3-x1)/(x2-x1)+y1
return
end
```

IMAGE EVALUATION
TEST TARGET (QA-3)

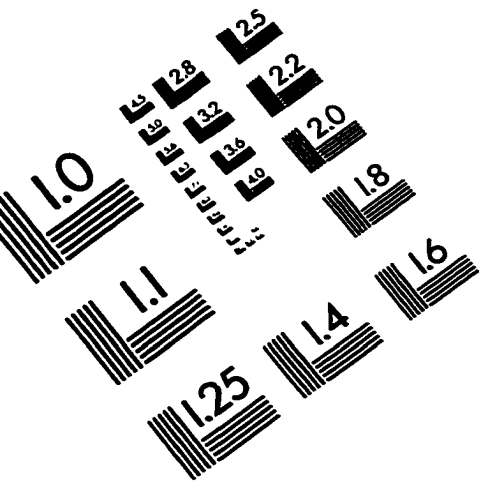

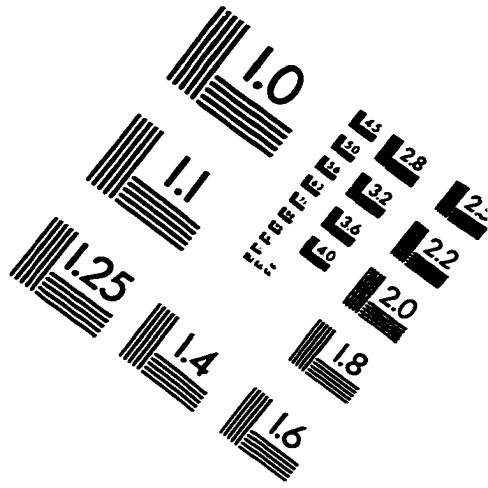

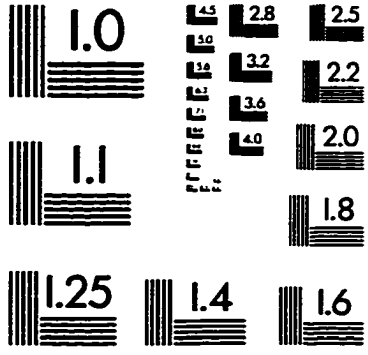

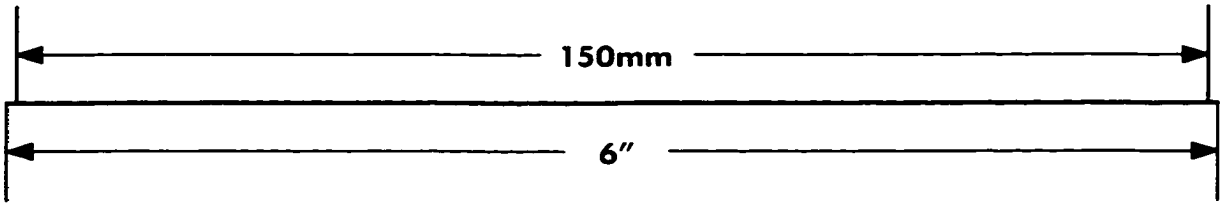

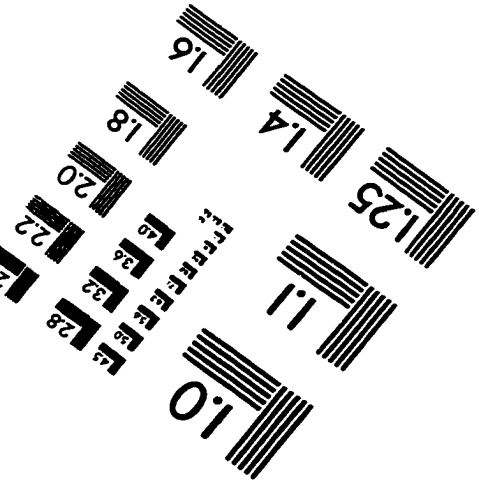

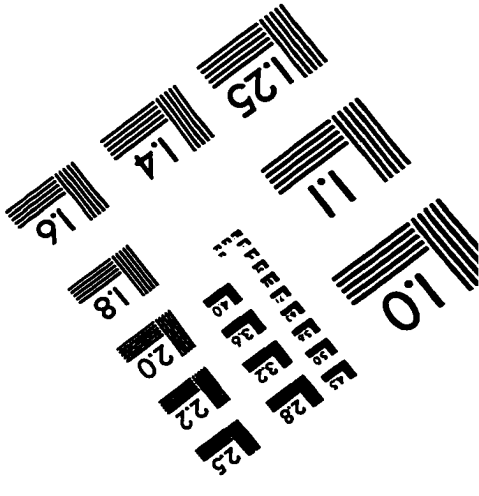

APPLIED IMAGE, Inc
1653 East Main Street
Rochester, NY 14609 USA
Phone: 716/482-0300
Fax: 716/288-5989